Dissertation

Patricia Erhard

Slurry-based 3D printing of ceramic casting cores

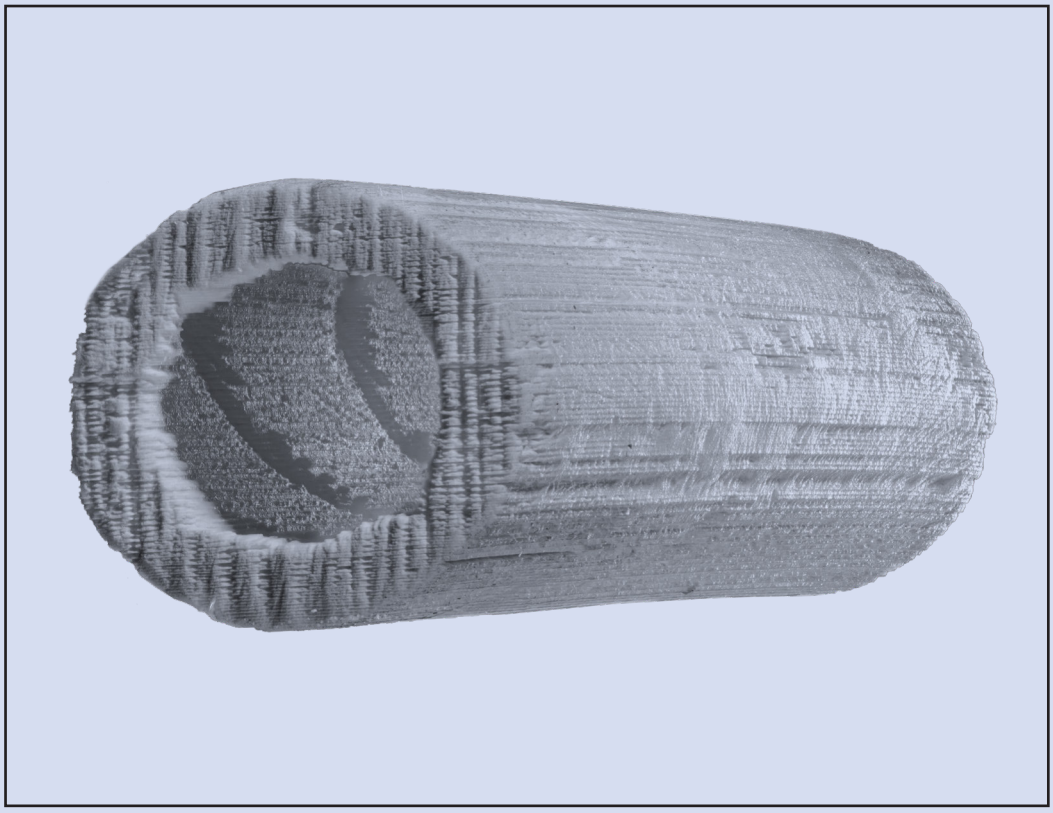

42
Maschinenbau

Lehrstuhl für
Umformtechnik
und Gießereiwesen

KOLLEMOSCH
Verlag & Kommunikation

Schriftenreihe Umformtechnik und Gießereiwesen

Technische Universität München
TUM School of Engineering and Design

Slurry-based 3D printing of ceramic casting cores

Patricia Erhard

Vollständiger Abdruck der von der TUM School of Engineering and Design der Technischen Universität München zur Erlangung einer

Doktorin der Ingenieurwissenschaften (Dr.-Ing.)

genehmigten Dissertation.

Vorsitz: Prof. Dr.-Ing. Rüdiger Daub

Prüfer*innen der Dissertation:

1. Prof. Dr.-Ing. Wolfram Volk
2. Prof. Dr. rer. nat. Tim C. Lüth
3. Prof. Dr.-Ing. Babette Tonn

Die Dissertation wurde am 27.02.2023 bei der Technischen Universität München eingereicht und durch die TUM School of Engineering and Design am 02.10.2023 angenommen.

Die Deutsche Nationalbibliothek verzeichnet diese Publikation in der Deutschen Nationalbibliografie; detaillierte bibliografische Daten sind im Internet über https://portal.dnb.de abrufbar.

Impressum:

Herausgeber: Lehrstuhl für Umformtechnik und Gießereiwesen (utg), TUM School of Engineering and Design, Technische Universität München

Layout und Gestaltung: utg

Umschlaggestaltung: Broy New Media.

Umschlagabbildung: Patricia Erhard
Druck und Bindung: KS Druck, Ebersberg

Verlegerische Betreuung:

Kollemosch Verlag & Kommunikation
Lutz Prauser
Hauptstr. 39
85656 Buch am Buchrain

ISSN: 2364-6942
ISBN: 978-3-9820746-6-5
www.tum.de

Vorwort

Diese Arbeit entstand im Rahmen meiner Tätigkeit als wissenschaftliche Mitarbeiterin am Fraunhofer-Institut für Gießerei-, Composite- und Verarbeitungstechnik IGCV und Doktorandin am Lehrstuhl für Umformtechnik und Gießereiwesen der Technischen Universität München. Mein besonderer Dank gilt meinem Doktorvater Herrn Prof. Dr.-Ing. Wolfram Volk, Ordinarius des Lehrstuhls und Institutsleitung des Fraunhofer IGCV, für die uneingeschränkte Unterstützung dieser Arbeit, das mir entgegengebrachte Vertrauen und die vielmals ansteckende Begeisterung für aktuelle und zuküftige Forschungsthemen. Frau Prof. Dr.-Ing. Babette Tonn und Herrn Prof. Dr. rer. nat. Tim C. Lüth danke ich für die Übernahme des Koreferats und Herrn Prof. Dr.-Ing. Rüdiger Daub für die Übernahme des Vorsitzes der Prüfungskommission.

Diese Arbeit basiert auf den Ergebnissen eines Kooperationsprojektes des Zentralen Innovationsprogramms Mittelstand (ZIM). Ein großes Dankeschön gilt Herrn Joachim Vogt vom Fraunhofer ISC/ Center HTL für den über das Projekt hinausgehenden intensiven und bereichernden fachlichen Austausch und der Firma voxeljet AG für die gute Zusammenarbeit in diesem und weiteren spannenden gemeinsamen Projekten.

Besonders danken möchte ich meinem Abteilungsleiter und Mentor, Herrn Dr.-Ing. Daniel Günther, für den Enthusiasmus an der Arbeit und die Bereitschaft, stets Erfahrungen und Expertenwissen zu teilen. Diese Arbeit wäre ohne seinen Ideenreichtum und die tatkräftige wissenschaftliche und technische Unterstützung nicht möglich gewesen. Ein herzliches Dankeschön geht zudem an Beatrix Kain für die in allen Belangen hervorragende administrative Unterstützung. Darüber hinaus möchte ich mich bei allen aktuellen und ehemaligen Kolleginnen und Kollegen am Fraunhofer IGCV, sowie den von mir betreuten Studierenden herzlich für die großartige Zusammenarbeit und die positive wie kreative Arbeitsatmosphäre bedanken. Ich blicke mit Stolz auf das, wozu wir unser Institut bisher gemacht haben, und freue mich darauf, was die Zukunft bringen wird.

Von ganzem Herzen bedanke ich mich bei Bernd, auf dessen liebevolle und geduldige Unterstützung ich immer zählen kann, sowie bei meiner Familie und Schwiegerfamilie für den großartigen Rückhalt.

Garching, im Oktober 2023 Patricia Erhard

Executive Summary

Binder jetting is a highly productive additive manufacturing method, where particle material is layer-wise applied to a build platform and selectively printed with a binder. The process enables, among other things, the production of complex casting cores made of sand, which are used to represent internal contours in metallic cast components. However, a conflict of objectives between the mechanical and thermal load-bearing capacity of sand cores during casting and their subsequent removability from the cast part leads to limitations in the exploitable design freedom of cavities.

Instead of dry, flowable quartz sand, a water-based ceramic slurry is used in this work. Through the suspension-based layer application and fine grain sizes, filigree green bodies of high surface quality are produced, whose mechanical and thermal properties can be adjusted in the subsequent sintering process.

This work's first focus is on developing a suitable hardware setup and corresponding process configurations to ensure homogeneous layer formation and stable process control. Based on this, the layer-by-layer drying of the dispersion medium is investigated by studying the cause-and-effect relationships of certain process parameters relevant to casting cores. Those parameters, which are decisive for both material properties and process efficiency, are layer thickness, drying intensity and drying period. Based on the scientific findings, the performance, potentials and challenges of the slurry-based 3D printing process are demonstrated against the background of the process chain in the foundry sector.

Compared to powder-based 3D printing with sand, the average roughness depths could be reduced by ~ 90 % to 1.2 µm. In a shrinkage-free sintering process, the final strength was adjusted to approximately 10 times higher with 25 MPa. Improved material properties were achieved with longer drying periods. This reveals a conflict of objectives between structural integrity and economic benefits. The high selectivity of the 3D printing process enabled an adequate level of detail to realise predetermined breaking lines in the internal geometry of hollow casting core structures. It was shown that by involving an appropriate structural design, the stresses arising during shrinkage of the solidifying metal alone can induce failure of the core. Mechanical de-coring of slurry-based 3D printed ceramic casting cores can thus be envisaged for more complex, filigree core geometries such as those required for the representation of efficient, close-contour cooling structures in high-performance cast components.

Kurzbeschreibung

Im Binder Jetting-Verfahren wird schichtweise Partikelmaterial auf eine Bauplattform aufgetragen und mit Binder bedruckt. Dieses hochproduktive additive Fertigungsverfahren ermöglicht unter anderem die Herstellung komplexer Gießkerne aus Sand, die zur Darstellung innenliegender Konturen in metallischen Gussbauteilen verwendet werden. Aufgrund eines Zielkonflikts zwischen der mechanischen und thermischen Belastbarkeit von Gießkernen im Gießprozess sowie der späteren Auslösbarkeit aus dem Gussteil sind der Gestaltung der Hohlräume in Gussbauteilen jedoch technische Grenzen gesetzt.

Anstelle von trockenem, fließfähigen Quarzsand wird im Rahmen dieser Arbeit ein wasserbasierter Keramikschlicker verarbeitet. Über einen suspensionsbasierten Schichtauftrag und die Verwendung feiner Korngrößen werden filigrane Grünkörper hoher Oberflächengüte erzeugt, deren mechanische und thermische Eigenschaften im nachfolgenden Sinterprozess eingestellt werden können.

Der erste Schwerpunkt dieser Arbeit liegt auf der Entwicklung eines geeigneten Hardwaresetups und einer Prozesskonfiguration zur Sicherstellung einer homogenen Schichtbildung und stabilen Prozessführung. Darauf aufbauend wird die schichtweise Trocknung des Dispersionsmediums und die Ursache-Wirkungsketten bestimmter für Gießkerne relevanter Parameter und Kennwerte untersucht. Die Parameter, die sowohl für die Materialeigenschaften als auch für die Prozesseffizienz entscheidend sind, sind Schichtdicke, Trocknungsintensität und Trocknungsdauer. Auf Basis wissenschaftlicher Erkenntnisse werden die Performance, die Potentiale und die Herausforderungen des schlickerbasierten 3D-Druck-Verfahrens vor dem Hintergrund der Prozesskette im Gießereiwesen dargelegt.

Gegenüber des konventionellen 3D-Drucks mit Sand konnten die mittleren Rautiefen um ~ 90 % auf 1.2 µm reduziert werden. Die Endfestigkeit wurde in einem schwindungsfreien Sinterprozess mit 25 MPa auf den ca. 10-fachen Wert eingestellt. Es wurden verbesserte Materialkennwerte bei längerer Trocknungsdauer und damit ein Zielkonflikt zwischen struktureller Integrität und wirtschaftlichen Vorteilen aufgezeigt. Die hohe Selektivität des 3D-Druckverfahrens ermöglichte es, Sollbruchstellen in der Innengeometrie hohler Gießkerne detailgenau abzubilden. Es wurde gezeigt, dass bei einer geeigneten geometrischen Auslegung allein die beim Aufschrumpfen des Metalls entstehenden Spannungen ein Versagen des Kerns induzieren können. Damit kann auch für filigrane Kerne wie sie z.B. zur Darstellung effizienter, konturnaher Kühlstrukturen in Hochleistungsgussbauteilen benötigt werden eine mechanische Entkernung schlickerbasiert 3D-gedruckter keramischer Gießkerne in Aussicht gestellt werden.

Contents

Prior Publications

During my doctoral studies, I contributed to the following publications. All relevant prior publications (*) are registered according to valid doctoral regulations.

Journal papers:

ERHARD, P.; TANJAVOORU, V.; HARTMANN, C.; VAN DEN BOSCH, L.; SEIDEL, A.; VOLK, W.; GÜNTHER, D. (2023). Simulation of Binder Infiltration in Additive Manufacturing of Sand Molds. In: *Advanced Engineering Materials,* **25**, 2300212.

ERHARD, P., TAHA, I., GÜNTHER, D. (2023): Influence of the Resin System and Sand Type on the Infiltration of 3D-printed Sand Tools. In: *Materials*, **16**, 5549.

ERHARD, P.; HARTMANN, C.; LI, R.; VOLK, W.; GÜNTHER, D. (2023). Advanced Procedures for Series production with 3D printed core packages. In: *International Journal of Metalcasting,* **17**, 2572-2583.

* ERHARD, P.; SEIDEL, A.; VOGT, J; VOLK, W.; GÜNTHER, D. (2022). Evaluation and optimisation of a slurry-based layer casting process in additive manufacturing using multiphase simulations and spatial reconstruction. In: *Production Engineering – Research and Development*, **16**, 43–54.

* ERHARD, P.; ANGENOORTH, J.; VOGT, J.; SPIEGEL, J.; ETTEMEYER, F.; VOLK, W.; GÜNTHER, D. (2021). Characterization of Slurry-Cast Layer Compounds for 3D Printing of High Strength Casting Cores. In: *Materials*, **14**, 6149.

GÜNTHER, D.; ERHARD, P.; SCHWAB, S.; TAHA, I. (2021). 3D Printed Sand Tools for Thermoforming Applications of Carbon Fiber Reinforced Composites—A Perspective. In: *Materials*, **14**, 4639.

Further publications:

ERHARD, P.; VOLK, W.; GÜNTHER, D. (2023). Slurry-based Binder Jetting of Ceramic Casting Cores. In: *2023 Annual International Freeform Fabrication Symposium (SFF Symp 2023)*.

SCHUSTER, D.; ERHARD, P.; GÜNTHER, D. (2023). Salt Cores for Advanced Manufacturing of Complex Fibre-Reinforced Composites. In: *Proceedings of the 17th European Conference on Spacecraft Structures and Environmental Testing (ECSSMET)*.

ERHARD, P.; BOOS, D.; GÜNTHER, D. (2023). In-Mold Coating in Pressing of Natural-Fiber-Reinforced Salt Cores for High-Pressure Die-Casting Applications. In: *Proceedings of the Munich Symposium on Lightweight Design 2021*. Springer Vieweg, Berlin, Heidelberg.

ERHARD, P.; GÜNTHER, D.; SEEBOLD, S.; MINKEL, G. (2022). Innovative salt cores for complex geometries. In: *Casting Plant & Technology*, **4**, 22-24.

ERHARD, P.; GÜNTHER, D.; SEEBOLD, S.; MINKEL, G. (2022). Innovative Salzkerne für komplexe Geometrien. In: *Giesserei*, **8**, 44-46.

ETTEMEYER, F.; ERHARD, P.; LECHNER, P.; SCHWEINEFUSS, M.; REINOLD, L. M.; LUSTIG, C.; SEHRSCHÖN, H.; VOLK, W.; GÜNTHER, D. (2021). Entkernverhalten anorganisch gebundener Sand-Binder-Systeme (Charakterisierung – Klassifizierung – Modellierung). In: *Giesserei-Special,* **1**, 18-23.

VOGT, J.; STEPANYAN, M.; ERHARD, P.; GÜNTHER, D.; SCHMALZL, S.; GLÄSER, S. (2021): Slurry-based Additive Manufacturing of Casting Cores. In: *InCeight Casting C8*, **1**, 123-130.

VOGT, J.; STEPANYAN, M.; ERHARD, P.; GÜNTHER, D.; SCHMALZL, S.; GLÄSER, S. (2021): Slurry-based 3D printing of Casting Cores. In: *Casting Plant & Technology*, **3**, 30-35.

VOGT, J,; STEPANYAN, M.; ERHARD, P,; GÜNTHER, D.; SCHMALZL, S; GLÄSER, S. (2021). Schlickerbasierte Additive Fertigung von Gießkernen. In: *Giesserei*, **11**, 51-57.

TONN, B.; TONN, L.; GOGOLIN, J.; NIELS, S. T.; DI MUOIO, G.; LECHNER,P.; HARTMANN, C.; ERHARD, P.; VOLK, W.; FROS, A. P.; FEHLBIER, M. (2021): Digitalisierung in der Gießereitechnik, Teil 2: Anwendungsbeispiele zur Prozessoptimierung. In: *Giesserei*, **7**, 34-42.

List of Symbols

Symbol	Unit	Meaning
α	-	Volume fraction
β_c	°	Chamfer angle
γ	mN/m	Surface tension
$\dot{\epsilon}$	Pa·s	Strain rate
ε_{ij}	-	Random error
η	mPa·s	Dynamic viscosity
θ	°	Contact angle
κ	mm^2/s	Thermal diffusivity
λ	mm^2/s	Thermal conductivity
μ	-	Constant in single-factor fixed effects model
ν	m/s	Droplet velocity
ρ	g/cm^3	Density
σ	MPa	Stress
σ_f	MPa	Fracture stress
τ	Pa	Shear stress
τ_i	-	Treatment or level effects
υ	m^2/s	Kinematic viscosity
Φ	-	Void fraction
a_p	-	Pore area surface fraction
b	-	Two-term model coefficient
c	mm	Half length of focal line
DR	l/hr	Deposition rate
E	GPa	Young's modulus
f	m^2/s	Power-law model parameter
F_d	N	Force induced by capillary flow
F_f	N	Buoyancy
F_g	N	Gravitational force

Symbol	Unit	Meaning
F_H	N	Adhesive force
F_{pp}	N	Interparticle force
$h_{filling}$	m	Slurry container filling height
h	mm	Height
H	µm	Preset layer height/ layer thickness
k	m^2	Permeability
K_c	$MPa \cdot \sqrt{m}$	Fracture resistance
l	m	Length
l_c	mm	Chamfer distance
$l_{ch,d}$	mm	Channel depth
$l_{ch,w}$	mm	Channel width
m	g	Weight
MR	-	Moisture ratio
n	-	Number of specimens
Oh	-	Ohnesorge number
p_c	Pa	Capillary pressure
$p_{rgh,in}$	Pa	Slurry inlet pressure
p_{slurry}	bar	Preset slurry pressure
P	-	P-value
PD	g/cm^3	Particle density
q	-	Power-law model parameter
r	µm	Radius
R	µm	Capillary radius
Ra	µm	Arithmetical mean roughness
res	µm	Print resolution
Re	-	Reynolds number
Rz	µm	Average roughness depth
s^2	-	Variance
S	-	Penetration coefficient

Symbol	Unit	Meaning
SR	-	Shrinkage ratio
t	s	Time
u	m/s	Velocity
T	°C	Temperature
$T_l(n)$	µm	Thickness of the n-th layer
V	mm³	Volume
w	mm	Width
We	-	Weber number
x	µm	Particle size
z	-	Two-term model coefficient
y_{ij}	-	Response variable

Index	Meaning
0	Reference
1, 2, 3, …	1st, 2nd, 3rd, …
lv	Liquid-vapour
min	Minimum
max	Maximum
mtx	Matrix
g	Green
s	Sintered
sl	Solid-liquid
sv	Solid-vapour
x, y, z	Coordinate directions

List of Abbreviations

Abkürzung	**Bedeutung**
AM	Additive manufacturing
ANOVA	Analysis of variance
CAD	Computer-aided design
CCT	Critical cracking thickness
CFD	Computational fluid dynamics
CJ	Continuous-jet
CRP	Constant rate period
DEM	Discrete element method
DOD	Drop-on-demand
DSC	Differential scanning calorimetry
EU	European Union
FEM	Finite element method
FRP1	First falling rate period
FRP2	Second falling rate period
Hexa	Hexamethylenetetramine
HPDC	High-pressure die-casting
HR	Hausner ratio
IPA	Isopropyl alcohol
LIS	Laser-induced slipcasting
LOI	Loss on ignition
MIT	Massachusetts Institute of Technology
PAV	Power adjustment voltage
PSD	Particle size distribution
PVA	Polyvinyl alcohol
RMSE	Root mean square error
SLA	Stereolithography
TG	Thermogravimetric analysis
VOF	Volume-of-fluid method

1 Introduction

The fundamental concepts of additive manufacturing (AM) were developed roughly 150 years ago. Those early technologies employed the layer-wise approach in the manual creation of parts, for instance, by cut-and-stack constructions, since modern computers have been involved in manufacturing technologies only since the mid-1960s. At the time of its initial commercialisation in the late 1980s, AM was referred to as rapid prototyping in conformity with its main applications. Ever since, multiple new processes, materials, and software tools have emerged in various applications of AM. Nowadays, approximately one-third of industry organisations employ AM systems for cosmetic and functional prototyping, and a second third for short-run production of end-use parts. One-sixth focuses on tooling applications, and another sixth addresses research, education and further applications. (Wohlers, 2022, pp. 48–55, Wohlers et al., 2022, pp. 22–30)

In contrast, metal casting dates back as early as 5000 – 3000 B.C. Initially, carved stones served as mould cavities. Even though various casting processes and advanced casting materials have evolved, in particular implying continuous advancements with respect to part design, part quality, and economic considerations for mass production, the basic principle of casting has remained the same. (Khan, 2017, pp. 1–10) The 3D printing technique, today known as the binder jetting process, is a highly productive generative procedure for manufacturing porous parts. The earliest associated patent application in the late 1980s already proposed implementing the technology in the casting process chain (Sachs et al., 1989). Binder jetting has thus been utilised to rapidly produce lost moulds for metal casting from its outset.

Meanwhile, 3D printed sand moulds, cores, and core packages have increasingly gained importance in gravity casting series production. However, since the processability of powders in the dry state is confined to coarse and thus flowable compositions, the complementarities of the so-called indirect metal AM process can still not be fully exploited: Since the surface area to volume ratio of foundry sands is too little to allow for sinterability, the load-bearing capacity of casting cores is limited to the adhesiveness and the temperature stability of the binder. Moreover, surface roughness is confined to the powder sizes used. (Sachs et al., 1998)

The objective of this thesis is to demonstrate the processability of fine powders dispensed in an aqueous suspension to allow for 3D printing of sinterable and, thus, high-strength ceramic casting cores on improved minimum feature sizes. Since drying strongly affects both material properties and process efficiency, the investigations focus on controlling the material properties

via drying configuration. Knowledge of the interfering factors of the drying process, which is the additional operational step in 3D printing machines required when replacing the dry powder with slurry, will help to establish a basis for industrial process design and facilitate future material and process developments.

The following initial theses on slurry-based binder jetting of casting cores provide a strong impetus for the research conducted herein:

- Slurry-based layer casting allows for the processability of small particle sizes and enables enhanced surface qualities, higher packing densities, and thus the sinterability of binder jetted parts.

- The mechanical properties of the printed parts can be adjusted via the sintering curve. Sintering shrinkage can be minimized via a suitable slurry composition.

- The extraordinary temperature resistance of sintered, and thus binder-free and high-strength casting cores can be exploited to enable filigree, self-supporting cores that do not exhibit hot distortion effects during casting.

- Sintered high-strength casting cores do not decompose during casting. Hence, de-coring needs to be achieved by applying hollow core structures and adapting the wall thicknesses used to the respective strength. Imprinted predetermined breaking points can be used to support collapsibility.

By extending the existing process knowledge on slurry-based 3D printing, in particular by studying the effect of the drying process crucial for both part quality and process performance, it is aimed to lower the hurdles for its industrial implementation in the environment of casting technologies.

2 State of the Art

This chapter introduces the fundamentals of additive manufacturing (AM). The basic principle of AM is clarified, and the associated technologies are classified into categories. The main focus of this chapter is placed on binder jetting technology. Here, binder jetting is categorised as powder-based and slurry-based binder jetting.

Both alternatives are presented in the context of casting technology to generate an understanding of the special requirements on processes and parts produced thereby. At the end of this chapter, the resulting research gap is summarised.

2.1 Additive Manufacturing – Basic Principle and Classification

Additive manufacturing is the general term for technologies generating physical 3D geometries from model data using a layer-based approach (DIN EN ISO/ASTM 52900) and has been recently incorporated in the classification of manufacturing processes of DIN 8580 in the main group of primary shaping (DIN 8580). AM processes comprise the following steps: From a software model representing the 3D geometry, a file readable by the respective AM machine is created, e.g. in STL file format. After transferring the file to an AM machine, the geometry may be manipulated regarding size, position and orientation. Before building the part, the machine parameters are set up according to the process, material constraints, and desired part properties. As soon as the mainly automated building process is completed, the parts can be removed but may need post-processing steps like cleaning or heat treatment prior to their end-use. (Gibson, 2021, pp. 3–6)

Multiple AM processes, similar and different in many respects, have been developed in parallel. Therefore, various attempts to classify the processes are available, e.g. in terms of materials, energy sources, types, and conveyance of feedstock (Kumar, 2020, pp. 21–26). The ongoing high number of AM-related patents issued, particularly the largest proportions within the category “AM hardware/ methods” and “AM materials”, points toward continuous innovation and investment in AM processes (Wohlers et al., 2022, pp. 287–288). The difficulty of differentiation in terminology and classifying all existing and future AM processes in clear categories follows logically (Kumar, 2020, p. 21).

DIN EN ISO/ASTM 52900 defines seven process classifications for additive manufacturing (Figure 2.1). Their approaches shall be introduced shortly: in binder jetting, the cross-sections of parts are formed by spraying a liquid bonding agent onto a powder bed. Directed energy

deposition processes provide the energy to merge materials, typically powders or wires, concurrently to their deposition. In material extrusion, printing material is drawn through a nozzle and deposited. Material jetting is a process in which material is selectively deposited in the form of droplets. In powder bed fusion, an energy source, like a laser or electron beam, is used to fuse the particles in the powder bed. Processes that merge sheets of material to form a part are called sheet lamination. Vat polymerization processes selectively cure liquid photopolymers contained in a vat. (Gibson, 2021, pp. 38–39)

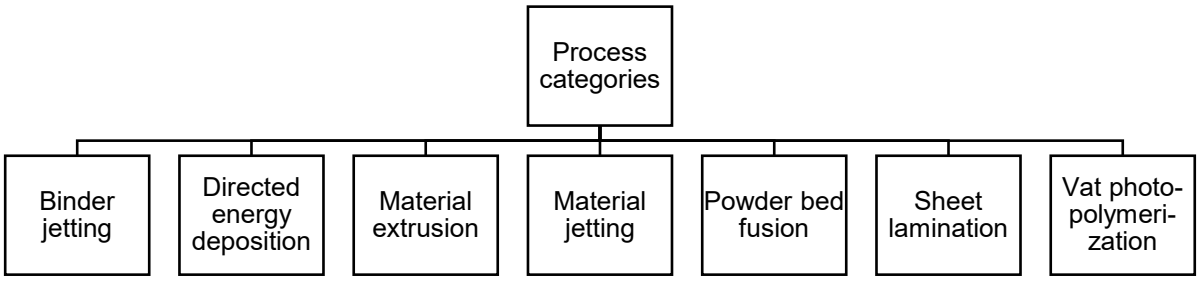

Figure 2.1: Additive manufacturing process categories (DIN EN ISO/ASTM 52900).

2.2 Powder-based Binder Jetting

Binder jetting technology was initially developed and patented at the Massachusetts Institute of Technology (MIT) (Sachs et al., 1989). DIN EN ISO/ASTM 52900 defines binder jetting as an „additive manufacturing process in which a liquid bonding agent is selectively deposited to join powder materials". Since this work focuses on the binder jetting process using a particle suspension instead of dry powder, the theoretical foundations treating the conventional powder-based process are given in this chapter before introducing the supplementary aspects associated with its slurry-based alternative in chapter 2.3.

2.2.1 Process Description

The binder jetting process is illustrated in Figure 2.2. It involves the following steps: Firstly, the build platform is lowered by a preset layer thickness. The free space between the underlying layer and the recoater created thereby is subsequently filled with powder. In the third step, an inkjet printhead selectively applies a binder to the new layer. The binder locally bonds the particles that constitute the respective cross-section of the part to be built – its infiltration enables the fusion with the print on the underlying layer. The process steps are repeated until the print job reaches its full height (Günther et al., 2021, p. 5).

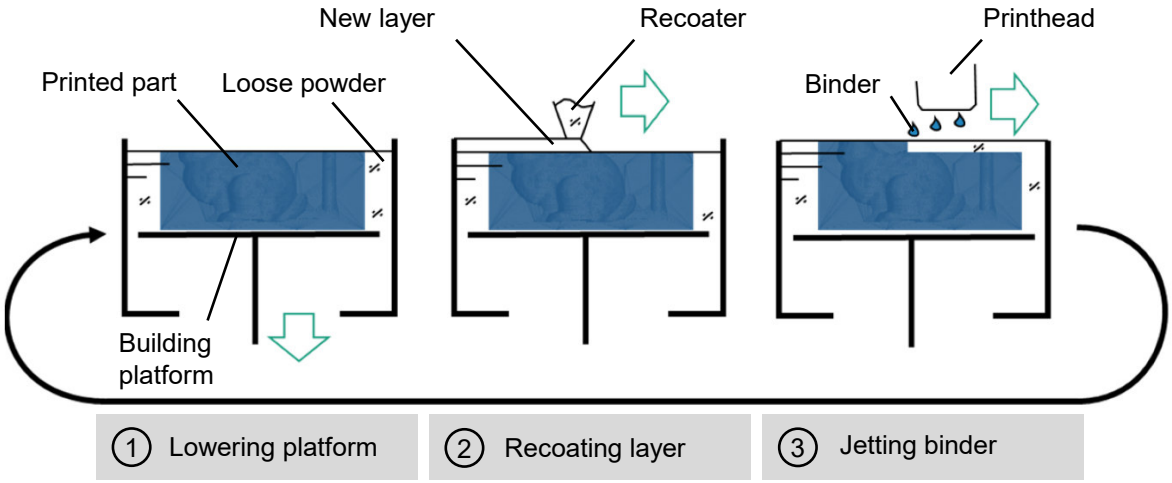

Figure 2.2: Schematic illustration of the process steps characterising the binder jetting process (after Günther et al., 2021, p. 5).

Two mechanisms of droplet generation are typically used in inkjet printing: continuous-jet (CJ) and drop-on-demand (DOD) inkjet printing. The first type generates a continuous stream of liquid binder droplets. An electric field deflects drops that are not needed to a gutter. Thereby recycling unused ink is possible for many applications that accept the risk of contamination during environmental exposure, e.g. graphics industry. CJ printers operate at drop generation rates in the range of 20 – 60 kHz. The drops are positioned by steering in flight or moving the substrate. (Derby, 2010, pp. 396–397)

DOD inkjet printheads produce individual drops when needed by promoting a pressure pulse in the fluid held in chambers next to the printing nozzles – either by a vapour pocket generated by a thin-film heater or by mechanical actuation from a piezoelectric transducer (Figure 2.3). Surface tension keeps the liquid inside the chamber when no pulse is applied. DOD systems typically generate drops at frequencies of 1 – 20 kHz. (Derby, 2010, pp. 397–399) CJ printheads can reach higher print rates than DOD. However, inks must be inductively chargeable to be deflectable to the gutter. For piezoelectric printheads, the rheological property is the central requirement in ink development, whereas in thermal inkjet printing, rapid dissolution of the vaporized liquid is crucial to allow for homogeneous binder ejection. (Mostafaei et al., 2020, pp. 19–20)

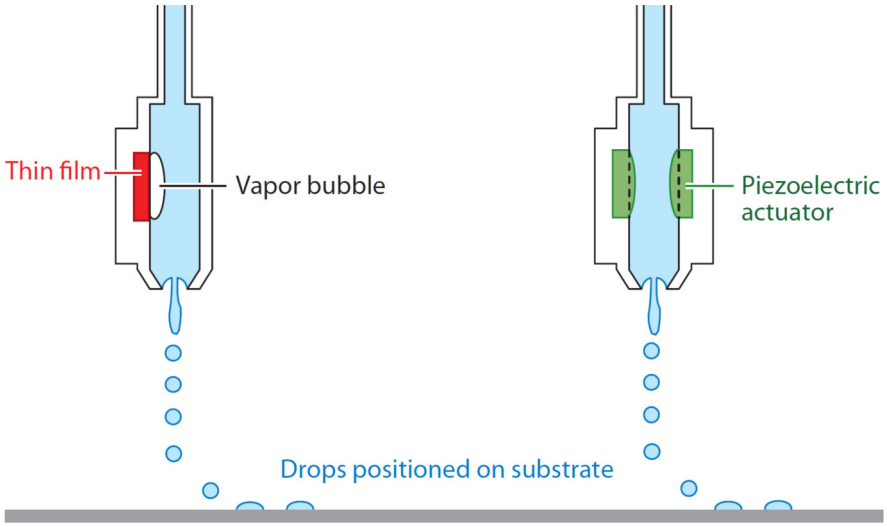

Figure 2.3: Schematic illustration of two drop generation principles for drop-on-demand (DOD) printing; (a) thermal inkjet, (b) piezoelectric inkjet (Derby, 2010, p. 398).

The process chain of producing BJ parts is shown in Figure 2.4. It starts from a 3D model of the part to be printed, prepared, and digitally processed to be readable by the respective 3D printer. Secondly, the binder jetting process is carried out. Figure 2.2 shows this step's generic operation sequence within a 3D printer. Some materials and processes require a curing step after binder jetting to dry the binder further and enhance the printed parts' green strength. In this case, the whole build box is typically transferred to a curing oven and undergoes a temperature treatment prescribed depending on the box volume, powder and binder system. After curing, the green parts show adequate green strengths to be handled securely. During depowdering, the loose powder is removed from the build box, and the parts are further cleaned, commonly by brushing, vacuuming or air-blasting. Some technologies require further densification steps to achieve high densities and enhance the mechanical properties. Sintering and infiltration are standard post-processing methods to achieve full density. For sintering, the post-processing cycle must be appropriately tuned to the material system used since every material composition, and grain size distribution shows specific sintering characteristics. Densification via infiltration typically ensures a high degree of dimensional accuracy, whereas sintering faces the challenge of shrinkage. (Mostafaei et al., 2020, pp. 7–9)

Figure 2.4: Schematic diagram of the regular process chain for binder jetting parts. Some binder jetting technologies do not require all steps. Steps that are not always needed are faded.

2.2.2 Binder Jetting Process Characteristics

Classifying and accommodating the binder jetting process characteristics in the AM technologies' framework underline the manufacturing method's importance. In the following, the benefits and drawbacks relative to other AM processes are categorised according to the crucial properties of production methods – efficiency, part properties, and versatility.

Process efficiency

The primary advantage of binder jetting relates to its high production rates. Since only the binder, which accounts for a small share of the total part volume, is dispensed through a printhead's nozzles, the process is relatively fast and build rates can be accelerated by increasing the number of printheads and thus nozzles used (Gibson, 2021, p. 248, Gokuldoss et al., 2017, p. 3). Large build volumes are commercially viable as no sealed chambers for vacuum or inerting are required (Mostafaei et al., 2020, p. 5). Extraordinary build rates, and thus cost-effectiveness, particularly for 3D geometries with added functionalities, are feasible (Gokuldoss et al., 2017, p. 3). By way of example, binder jetting machines processing sand for industrial series production of moulds and cores in the foundry industry achieve build rates up to 400 litres per hour which leads to costs of significantly less than 10 € per litre printed volume (Günther et al., 2021, p. 5). 3D printing has nowadays even begun to outperform conventional mould manufacturing processes not only in terms of lead times but also costs for larger production volumes (Sivarupan et al., 2021, p. 12). However, some applications, for instance, metal binder jetting applications, require costly and time-consuming post-processing steps like sintering or infiltration (Gibson, 2021, p. 249). Furthermore, adequate post-processing strategies still need to be developed for most materials (Mostafaei et al., 2020, p. 5).

Part Properties

Compared to other AM technologies, as-printed parts produced by binder jetting exhibit low relative densities. As a result, the green parts show significant porosity, and the mechanical properties are comparatively poor. Moreover, the dimensional accuracy and surface finishes are generally disadvantageous. (Gibson, 2021, pp. 248–249) However, since shaping via binder jetting is conducted at room temperature, defects related to high temperatures or temperature gradients, such as oxidation, can be avoided, and the quality of the loose supporting powder is hardly affected, making it highly recyclable (Mostafaei et al., 2020, p. 5).

Versatility

Concerning versatility, the main advantage of binder jetting is its exceptional compatibility with a wide range of powdered materials (Mostafaei et al., 2020, p. 5). Additives in binders even allow a two-material approach enabling customised adjustments of the mechanical properties (Gokuldoss et al., 2017, p. 3). Furthermore, there is no need for support structures for overhanging features as the part is supported by loose powder (Mostafaei et al., 2020, p. 5), decreasing geometric restrictions and expenses in finishing (Gibson, 2021, p. 249).

2.2.3 Influencing Factors in Binder Jetting Technology

With the current state of technology, it is impossible to predict the resulting part properties for most binder jetting applications as numerous mutually interfering factors occur. Many research results are not generalisable to other material systems, machines, etc. (Mostafaei et al., 2020, pp. 114–116). Multiple studies address the influence of material and process parameters on the properties of binder jetted parts, for instance, focusing on machine parameters (Bryant et al., 2020), powder characteristics (Yuasa et al., 2021), or printing parameters (Chavez et al., 2020) to improve the understanding of the process physics for specific applications. Figure 2.5 sums up the essential interfering factors within the complex material and process environment in binder jetting technology based on both comprehensive literature research and experience without claiming to be exhaustive.

The following details on important interrelationships in binder jetting affecting the part properties are provided: First, the powder-related factors influencing powder properties, characteristics and processes are presented. Secondly, the binder properties, characteristics and inkjet parameters are shown together with their interdependencies. Finally, the interaction between the binder and powder bed allows for an insight into the reciprocal effects of the process modules.

Powder Properties, Powder Characteristics and Powder Processing

Virtually any powdered material is processible in binder jetting technology (Mostafaei et al., 2020, p. 5). Particle size distribution (PSD) and morphology are considered decisive factors since they affect the packing density of powder beds and, thus, the quality of printed parts (Chen et al., 2022, p. 1). The flow properties of powders play an important role. The size and shape of particles affect the flow of powders (Utela et al., 2008, p. 2). Since the flowability of fine powders is limited, achieving high powder packing densities and satisfactory green densities required for full densification constitutes a major challenge in binder jetting (Bai et al., 2017, p. 2). Generally, the use of fine powder allows for a low part porosity. However, interparticle

forces and friction increase with decreasing particle diameters, leading to agglomeration and impeded flow behaviour. But yet, a sufficient level of flowability is necessary to enable a uniform powder deposition. (Diener et al., 2021, pp. 3–5)

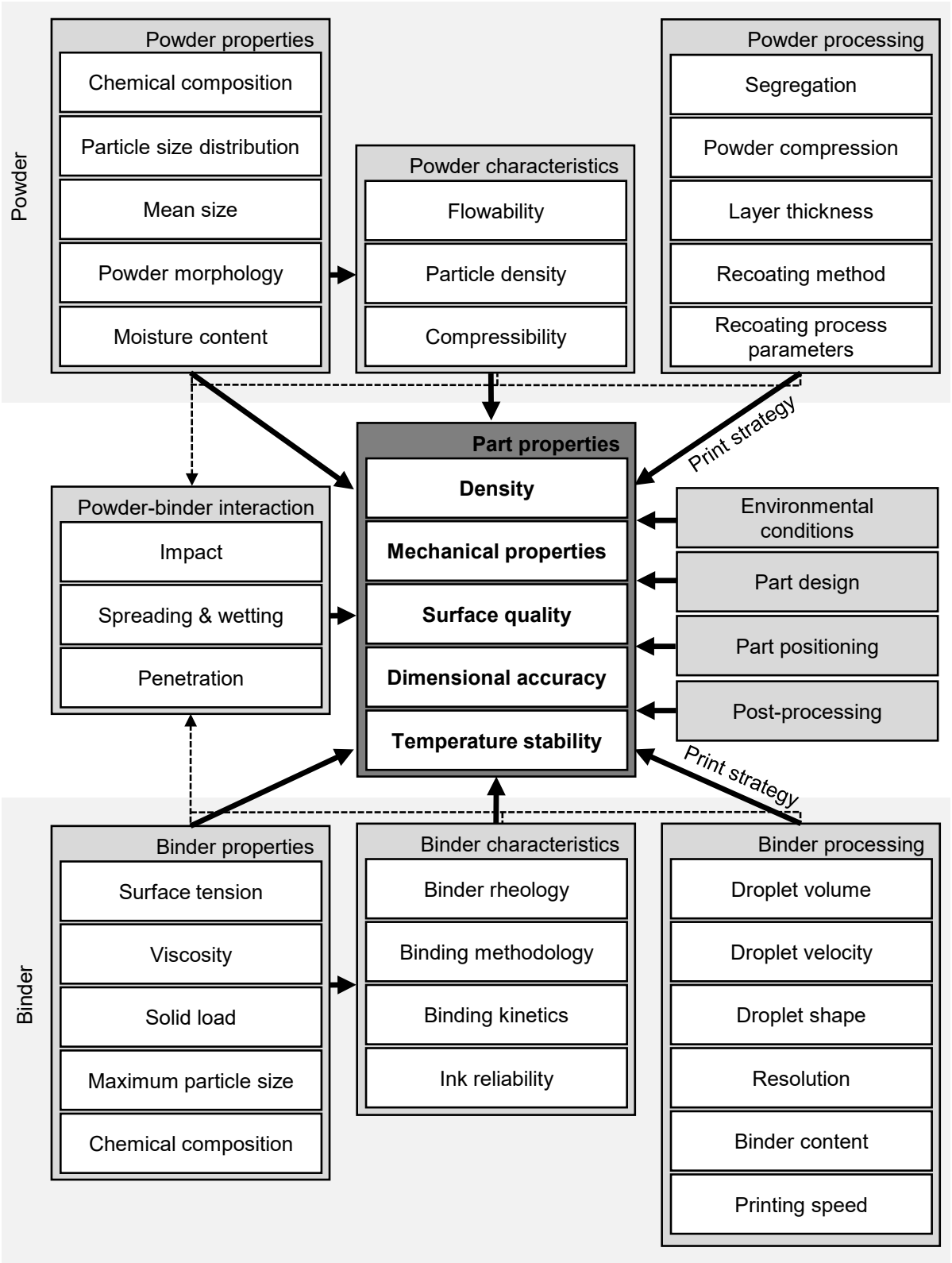

Figure 2.5: Influencing factors on part properties in binder jetting technology.

The flow properties of powders are not theoretically determinable by a function as they are affected by multiple influencing factors, e.g. PSD, particle shape, chemical composition, moisture and temperature (Schulze, 2008, p. 35). Typical relationships between flowability and powder properties are reported as follows (Vock et al., 2019, p. 388):

- A narrow PSD is favourable for achieving good powder flowability.
- Flowability increases with increasing particle sizes.
- Until saturation is reached, increasing moisture contents lead to decreasing flowability.

Bai et al. show an example of increasing powder packing and flowability simultaneously using bimodal powder mixtures (Bai et al., 2017, p. 6). Though, typically inhibited flow behaviour can be observed with increasing fines content (Schulze, 2008, pp. 237–238).

No universal statement on the impact of morphology on flow behaviour can be made. Coarse powders of smooth, spherical particles tend to flow better than rough, non-spherical particles. In contrast, rough particles may be favourable regarding the flowability of fine powders since adhesive forces play a crucial role. (Vock et al., 2019, p. 389)

Adhesive interparticle forces essentially affect the behaviour of bulk solids. Figure 2.6 shows the effect of particle size on various adhesive forces using the example of a spherical particle next to a wall. Forces due to liquid bridges – capillary forces in the presence of a wetting liquid – affect the adhesive forces the most, while van der Waals forces are dominant in dry, fine-grained bulk solids. Van der Waals forces act only within a small range. Therefore, the geometry of the particles' contact points pursuant to the particles' surface roughness and shape is decisive. Electrostatic forces play a relevant role in processing electrically conductive powders. However, electrostatic forces also apply to electrical isolators, e.g. during powder transport. (Schubert, 2012, pp. 214–220, Schulze, 2008, p. 211)

Moreover, Figure 2.6 compares the adhesive forces to the gravity-related forces caused by the particles' density labelled "weight" and complying with a density of 3 g/cm³ in this example. It shows interparticle adhesive forces becoming less important with increasing particle diameter since the particles' increasing weight ensures their high mobility (Schulze, 2008, pp. 139–140).

For process-technical reasons, the particle sizes in binder jetting are limited to the layer thickness used. A maximum particle size corresponding to half of the maximum layer thickness is recommended. (Diener et al., 2021, pp. 3–5) Hence, when processing coarse powder, increased layer thicknesses are required. Thus, the parts' surface finishes naturally become rougher (Chen et al., 2022, p. 1), even though new approaches allow for the smoothing of stair steps (Hartmann et al., 2022).

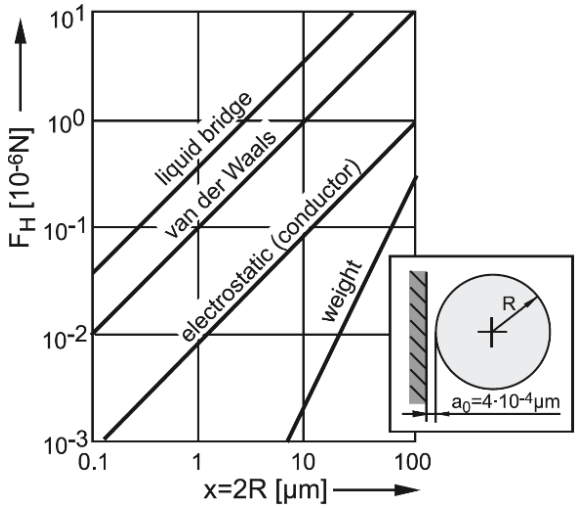

Figure 2.6: Influence of the particle size x on the adhesive force F_H compared to gravity-related force (Schulze, 2008, p. 26).

Furthermore, the requirements for flowability and sinterability are contradictory. While the enlarged specific surface area of fine powder leads to higher sintering driving forces, the interparticle forces within fine powders impede the particles' mobility. (Du et al., 2020, p. 5)

Powders differing in size, shape or density tend to segregate. Interparticle adhesion, apparent in fine powders, leads to limited mobility of particles and thus may prevent segregation (Schulze, 2008, p. 281).

The powder properties mentioned above affect not only flowability but also packing density, which is one of the key influencing factors in binder jetting technology. Packing density influences components' binder consumption, quality, integrity, sinterability, and final density (Miyanaji et al., 2019, p. 335). Powder morphology, powder mean size, PSD, interparticle forces, powder surface chemistry, and flowability impinge on the packing density (Mostafaei et al., 2020, 12-15). It is further known that the deformation history affects the behaviour of the powder (Schulze, 2008, pp. 115–124).

The following common relationships between packing density and powder properties or processing are reported (Mostafaei et al., 2020, pp. 12–15, Sohn, Moreland, 1968, p. 1):

- Broader PSD enables higher packing densities compared to narrow PSD.
- In fine powders, interparticle forces can lead to reduced powder packing densities. In the case of large particles, the packing density is independent of the particle size.
- The packing density depends on the layer depositioning method (e.g. roller/ rake) and parameters. Higher packing densities are achievable at a lower layer thickness.

Compressibility is the compaction related to consolidation stress in a powder bed (Diener et al., 2021, pp. 3–5). With increasing flowability, compressibility decreases (Schulze, 2008, p. 178). Commonly, the ratio between tapped and bulk density, known as Hausner ratio HR, is derived to describe the packing behaviour of powders subjected to compression. However, there are contrary reports regarding its applicability in AM (Spierings et al., 2016, pp. 11–12).

The method and parameters of powder spreading influence the layer properties. Powders are commonly processed via hoppers, rollers or blades at a definable recoating speed (Diener et al., 2021, pp. 5–9). Depending on the device used, relevant process parameters are, in particular, oscillator speed and blade angle or rotational direction and speed. Increasing the recoating speed is beneficial concerning costs (Diener et al., 2021, pp. 5–9, Mostafaei et al., 2020, p. 25). However, studies show a reduced dimensional accuracy, a lower powder bed density, and increased surface roughness with increasing recoating speeds (Miyanaji et al., 2018b, pp. 5–9, Myers et al., 2019, pp. 127–132).

Binder Properties, Binder Characteristics and Binder Processing

The binder liquid's core mission is penetrating interstitial spaces within the powder in each layer, forming bridges between the particles and thereby creating the desired shape. It has to fulfil various requirements to meet the demands of the binder jetting process: Rheology and stability during deposition have to be suited to processing via inkjet technology. Moreover, the binder must allow for sufficient wetting and penetration of the powder bed. The binding strength needs to ensure the structural integrity needed for further processing. Besides, minimising harmful chemical traces is desirable. Those competing demands make the selection or design of binder systems a challenging task. (Mostafaei et al., 2020, pp. 17–24)

Two basic binding strategies can be distinguished: Liquid-only binder systems provide all binding ingredients within the printing liquid and thus allow for flexibility and broad material compatibility. However, the binding components within the liquid entail a certain vulnerability regarding nozzle clogging. In contrast, binder systems containing in-bed components allow for a more reliable deposition since binding can only occur when interacting with the second component. Regarding chemical composition, common selection criteria are the binders' solid loading, thermal stability, volatility, and residuals during processing. Various binding methodologies are common, e.g. organic liquids, acid/base systems, inorganics or solvents. The binding kinetics strongly depend on the respective binding methodology. The ink's reliability is affected by the chemical composition, the rheological characteristics of the binding fluid, and its compatibility with the selected printhead. (Utela et al., 2008, pp. 99–102)

The rheological behaviour of an ink fluid is described by the Reynolds (*Re*), Weber (*We*) and Ohnesorge (*Oh*) numbers:

$$Re = \frac{v\rho l}{\eta} \tag{2.1}$$

$$We = \frac{v^2 \rho l}{\gamma} \tag{2.2}$$

$$Oh = \frac{\sqrt{We}}{Re} = \frac{\eta}{\sqrt{\gamma \rho l}} \tag{2.3}$$

Where v is the velocity, l a characteristic length, and ρ, η, and γ are the fluid's density, dynamic viscosity, and surface tension. Those physical constants grouped in the Re, We and Oh numbers describe relevant drop generation characteristics. (Derby, 2010, pp. 399–401) Figure 2.7 shows the limits of ink processing for a stable operation of DOD printheads. Sufficient kinetic energy has to be provided for drop formation, while splashing is avoided to allow for stable printing. *Oh* characterises the viscosity of the ink. DOD cannot process highly viscous media, whereas satellite droplet formation occurs at fluid viscosities that are too low. (Lohse, 2022, 354-365)

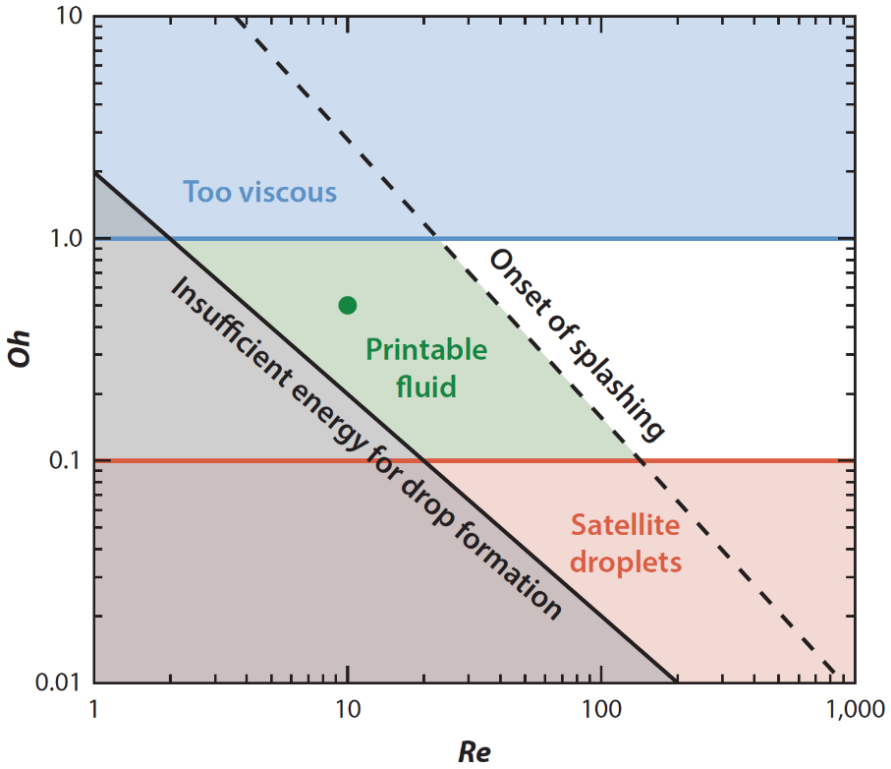

Figure 2.7: Domain for reliable inkjet fluids based on the Weber and Reynolds numbers (Lohse, 2022, p. 354).

The following rules outlined by Utela et al. (2008) can offer guidance in ink development for commercial inkjet print engines (Utela et al., 2008, pp. 99–102):

- Typical maximum dynamic viscosity η of 20 mPa·s – for special designs, maximum 100 mPa·s
- Minimum surface tension γ of 35 mN/m
- Maximum size of suspended particles/ polymer chains 100 times smaller than the nozzle diameter

Key printing parameters are droplet velocity, droplet size, droplet shape, resolution (spacing), and frequency (droplet inter-arrival time) (Colton, Crane, 2021, pp. 4–5, Staat et al., 2017, pp. 1–4). In particular, the binder content strongly influences the printed part's mechanical properties and dimensional accuracy. With increasing binder content, strength and dimensional distortion increase simultaneously (Patirupanusara et al., 2008, pp. 42–43, Yanez-Sanchez et al., 2021, pp. 15165–15167). A moderate droplet overlap is required for binder coalescence within the powder bed. However, balling defects occur when too much binder is deposited. Thus, droplet size, spacing, and layer thickness must be aligned carefully. (Colton, Crane, 2021, pp. 4–5)

Powder-Binder Interaction

The binder processing parameters mentioned above play a crucial role in powder-binder interaction. A series of infiltration kinetics occur: impact, spreading and wetting, and penetration (Mostafaei et al., 2020, pp. 23–24). Barui et al. (2020) observed a simultaneity of fluid surface spreading and infiltration and highly nonuniform penetration attributed to global changes in fluid drainage and pressure through porous media (Barui et al., 2020, p. 34262). Chun et al. (2020) reported increasing penetration depths with increasing capillary pressure within the powder, which was achieved by controlling the powder surfaces' porosity (Chun et al., 2020, p. 13).

Each droplet hits the powder bed at a distinct impact speed that supports binder spreading. Liquid bridges connecting particles are formed within a few microseconds. Further permeation into the non-saturated powder beneath (usually from 0.1 to 1 s) using the capillary force effect is mainly controlled by the respective properties of the powder bed and binder, e.g. binder viscosity and surface tension, and liquid-powder contact angle. Gravity is negligible due to the low mass of a single droplet. (Mostafaei et al., 2020, pp. 22–24)

2.2.4 Computational Models for Binder Jetting

Increasingly attention is given to modelling the binder jetting process computationally to gain an improved understanding of the process phenomena and save time and costs by replacing experiments. One focus is modelling the powder spreading to optimise the powder bed quality. Furthermore, the powder-binder interaction, including binder deposition, penetration and powder re-arrangement, is of vital interest, particularly for process development. (Mostafaei et al., 2020, pp. 104–111)

Modelling of Powder Spreading

Since numerous factors influence the packing density within the powder bed, an appropriate prediction of the packing behaviour of powders is desirable. The powder spreading process is normally modelled by the discrete element method (DEM). Attractive forces, such as adhesion and van der Waals forces, play an important role in particle-particle interaction and should therefore be considered in DEM simulations of fine powders (Parteli et al., 2014, p. 1). However, the relevance of certain forces on powders of different materials and PSD is still under investigation, e.g. particle-specific friction coefficients, fluid friction on air or forces due to liquid bridge formation (Parteli et al., 2014, pp. 4–5). Correlating the macroscopic behaviour of granular materials with their microstructure is still more a theoretical ideal wish than reality. However, multiple emerging material systems for 3D printing pave the way for systematic experimental research involving, e.g., different particle shapes. (Radjai et al., 2017, pp. 15–16)

Modelling of Powder-Binder Interaction

While particle-particle interaction dominates the powder spreading process, solid-liquid interactions must be considered as soon as binder droplets are jetted onto the powder bed. The infiltration of a liquid can be determined numerically by employing equations for computational fluid dynamics (CFD), i.e. Navier-Stokes equation. The particles are commonly implemented in a CFD model as boundary conditions, while the fluid's motion is tracked by the level-set or volume-of-fluid (VOF) method. (Mostafaei et al., 2020, pp. 108–111, Zhang, Prosperetti, 2005, p. 1)

2.2.5 Binder Jetting of Moulds and Cores for Metal Casting Applications

Integrating AM with the traditional metal casting process is also referred to as "indirect" metal AM (Hodder, Chalaturnyk, 2019, p. 653) or „multi-step metal AM". In contrast to "direct" AM, binder jetting allows for the production of tooling used to create the desired near-net geometry in the subsequent casting step. (Wang et al., 2019a, pp. 2–3) The efficiency of the binder jetting

process, in conjunction with the commercially available printing volumes of currently up to 4 x 2 x 1 m for sand systems, leads to extremely high production rates and practically no limits in weight and size of the respective casting parts (Kang, Ma, 2017, pp. 160–163).

The following shows the process chain of casting involving explicitly core and mould production by means of binder jetting technology. Moreover, the material systems typically used in indirect metal AM are specified together with the requirements on lost tooling produced by binder jetting related to its application in metal casting.

Overview of the Process Chain

Among the variety of casting processes, five categories of metal cast technologies were derived in DIN 8580: gravity casting, high-pressure die casting, low-pressure casting, centrifugal casting, and continuous casting. The first three abovementioned categories typically involve dies, whose geometry is the negative of the parts to be produced, into which metal melt is poured. An alternative classification of casting distinguishes between casting processes utilizing either lost moulds and reusable patterns, lost moulds and lost patterns, or permanent moulds (Klocke, 2018, p. 19). It thereby places the focus on the traditional strategies of mould making but excludes the alternative of direct mould manufacturing by binder jetting.

In the following, the process chain involving binder jetting of sand tools is outlined using the example of sand casting. Conventional mould-making strategies involve the manufacturing of patterns prior to mould production. Directly deriving the mould geometry from 3D CAD data reduces lead time and tooling costs (Bassoli et al., 2007, p. 149, Sama et al., 2020, p. 21). Moreover, the independency from patterns enables the part's and its casting system's design freedom. In particular, the functional performance can be enhanced by enabling undercuts. (Hackney, Wooldridge, 2017, p. 458)

The process chain of indirect metal AM, shown in a simplified form in Figure 2.8, starts with binder jetting of sand tools. Since sand tools are intended to be removable after casting, sufficient strength to withstand the loads during handling and casting is required, while easy destructibility after casting needs to be assured (Stauder et al., 2016, p. 2). Whereas the binder jetting specific part characteristics, particularly high porosity and low mechanical strength, are commonly disadvantageous for direct AM, those properties can be exploited as advantages in metal casting (Günther, Mögele, 2016, p. 54). The binder jetted sand tools are subsequently finished by de-powdering (removal of the unbound sand of the surrounding powder bed) (Almaghariz et al., 2016, p. 241) and, if appropriate, coated (Jakubski et al., 2005, p. 164). The unprinted powder can be recycled directly (Hawaldar, Zhang, 2018, p. 1039). The mould may be printed as a whole, including the gating system, the cores (used to shape the internal cavities)

and the outer mould (Snelling et al., 2015, p. 931), or assembled from modular components (Snelling et al., 2015, p. 925). The next step is the casting process, where molten metal – a wide range of alloys can be cast – is poured into the mould (Le Néel et al., 2018, p. 1328). The cores that outline the internal geometry of cast parts are removed after casting. De-coring is typically conducted by applying mechanical impulses before finishing the cast part by detaching the gating system and precision machining (Ettemeyer, 2021, pp. 14–17). Mitterpach et al. (2017) estimate a total demand of 6.3 tons of sand per each ton of ready castings of grey iron and emphasise the relevance of sand core reclamation on the life cycle assessment for foundries (Mitterpach et al., 2017, pp. 324–327). Recovery of foundry sands is typically performed by mechanical or thermal reclamation (Joseph et al., 2017, pp. 86–87).

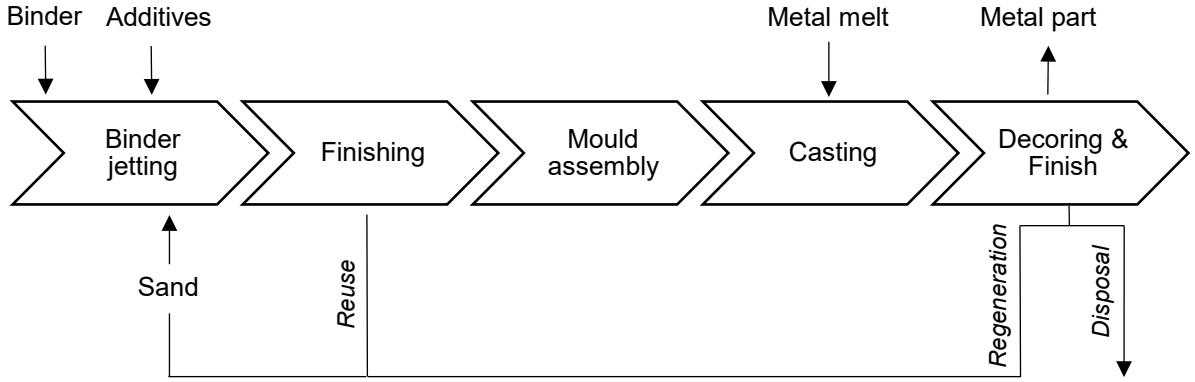

Figure 2.8: Simplified schematic process chain of indirect metal AM using sand moulds and cores and the corresponding material flow.

Materials for Binder Jetting of Moulds and Cores

The properties of casting moulds and cores strongly affect the cast parts' properties themselves – in particular, in the surface-near area. Concurrently, the characteristics of a binder jetted part strongly depend on the sand material used, its powder characteristics, and the binder material and proportion.

Conventional mould and core production involves the compression of pre-mixed sand-binder formulations against forming tools or patterns. Here, the grains are forced into an optimal orientation. Thus, finer powders are used in binder jetting compared to conventional forming methods of sand tools to reach similar surface quality levels. (Hodder, Chalaturnyk, 2019, p. 657) Sands produced for 3D printing applications are commonly sieved to average grain sizes of 140 – 250 µm (Upadhyay et al., 2017, p. 212). They typically show a more narrow PSD at smaller grain sizes and less angularity compared to traditional foundry sands (Hodder, Chalaturnyk, 2019, p. 653). However, when using fine grain sizes, negative side effects can occur, e.g. reduced gas permeability, increased binder consumption, or increased binder

spreading rate caused by the growth in powder surface area (Günther, Mögele, 2016, pp. 65–69, Mostafaei et al., 2020, p. 12).

Natural quartz sands composed of SiO_2 are foundries' most commonly used moulding materials due to their cost-effectiveness (Günther et al., 2021, pp. 5–7). When heated up, the mineral quartz exhibits the so-called quartz inversion point at 573 °C, where a rapid change in crystal structure appears. Quartz inversion is accompanied by an abrupt change in the expansion (from 0.26 to 0.45 % in length) and density (from 2.65 to 2.6 g/cm³). In contrast to other quartz crystal transformation processes, the transformation from the trigonal α-quartz to the hexagonal β-modification is always reversible. However, the abrupt volume changes within the casting process can result in severe casting defects. (Flemming, Tilch, 1993, pp. 40–41, Recknagel, Dahlmann, 2009, p. 8)

To overcome this obstacle or to further customise the moulding material properties in general, there are several artificial sand types available on the market: they may not exhibit quartz inversion or differ in thermal expansion, thermal conductivity and heat capacity, and thus facilitate the tailored modification of the cooling rate during solidification of the cast metal. (Sun et al., 2012, pp. 1886–1888) Hence, quartz sand may be replaced by artificial sand types with enhanced physical or chemical properties in order to fulfil the higher demands of the respective casting application. To name a few examples: materials of low thermal expansion coefficients can prevent sand expansion defects like veining and improve dimensional accuracy, isolating sands are used to realise thin-walled cast parts, and sands of high refractoriness avoid reactions between moulding materials and thermally burdened cast metals. (Recknagel, Dahlmann, 2009, pp. 11–15, Vasková et al., 2020, pp. 1–2)

Figure 2.9 illustrates two different sand types produced on unalike routes: the natural quartz sand GS14 RP (Strobel Quarzsand GmbH, Freihung, Germany) (Figure 2.9a) is one of the standards in 3D printing of sand cores and moulds. It shows an irregular shape with rounded edges at a relatively narrow particle size distribution. In contrast, the sintered mullite sand Cerabeads ES1450 (Hüttenes-Albertus Chemische Werke GmbH, Düsseldorf, Germany) (Figure 2.9b) consists of mainly spherical grains.

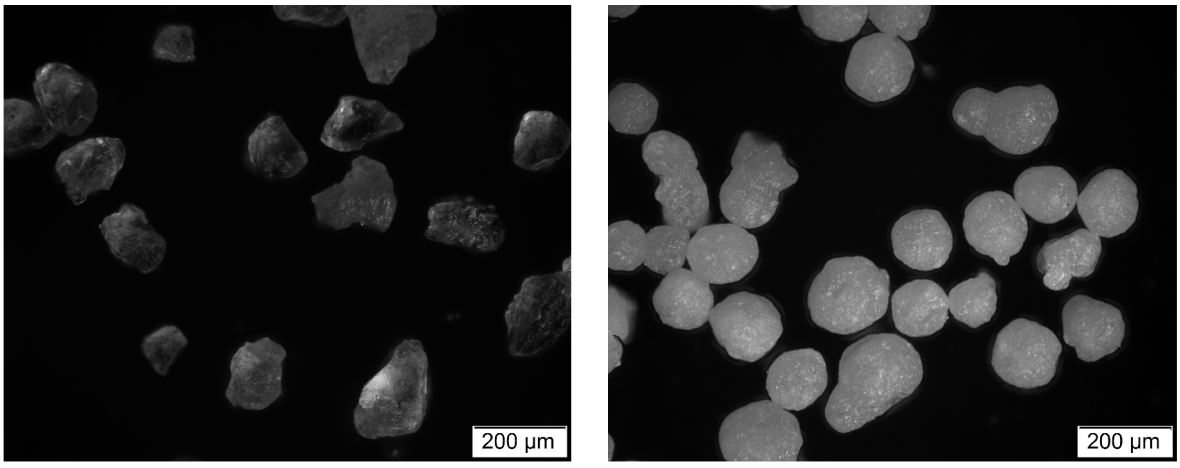

Figure 2.9: Dark field micrographs of (a) natural quartz sand GS14 RP and (b) sintered mullite sand Cerabeads ES1450.

The basic binder system categories relevant for binder jetting of moulds and cores are listed in Table 2.1, together with selected typical properties of sand moulds and cores produced utilizing those. Furan resin systems comprise a resin and an activator component. In contrast, the binding component within phenolic resins (phenol units) is contained in alcoholic or aqueous solutions and cross-linked at elevated temperatures. (Flemming, Tilch, 1993, pp. 86–93, Günther, Mögele, 2016, pp. 67–68) In the context of the increasing importance of preventing harmful emissions, inorganic silicate binders have already replaced organic binder systems for various casting applications. They can be cured physically by removing moisture. (Zaretskiy, 2016, pp. 88–89) Furan systems form the most gas, while inorganic sodium silicate binders evolve the least (Anwar et al., 2021, p. 1909). Depending on the binder system used, curing may be accomplished in several ways, e.g. self-hardening or microwave curing (Shi et al., 2021, p. 291).

Table 2.1: Relevant binder systems and properties of respective sand moulds and cores (after Günther, Mögele, 2016, p. 68).

	Furanic resin	**Phenolic resin**	**Inorganics**
Typical bending strength	2.5 MPa	3.5 MPa	3 MPa
De-coring	++	+	-
Pollutant emissions	High	High	No

Requirements On the Properties of Casting Cores and Characterisation Methods

Stauder et al. (2016) summarise fundamental sand core properties. These are arranged according to the casting progress in Figure 2.10. The requirements for the casting core, in

particular, depend on the production environment, the cast part's geometry, the quality demands, and the process design.

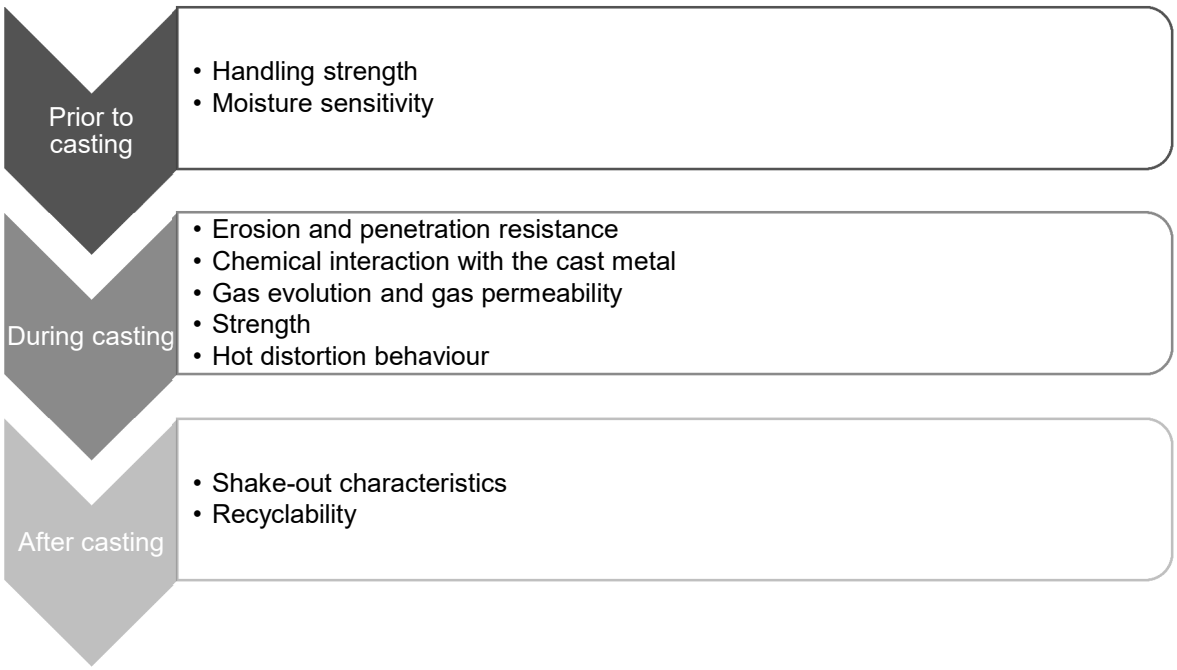

Figure 2.10: Fundamental relevant sand core properties categorised by the process stages in casting (after Stauder et al., 2016, pp. 1–2).

Dimensional accuracy is one of the most important parameters for evaluating moulds, cores, and the respective casting component (Hackney, Wooldridge, 2017, p. 462). Moreover, casting cores must withstand thermal and mechanical loads (Hasbrouck et al., 2020, p. 339). Already prior to assembly, casting cores need to show appropriate mechanical properties. Relevant mechanical properties include three-point bending strength but also scratch hardness.

Commonly, standard test bars measuring 22.4 x 22.4 mm in cross-section and 172 mm in length, described by the German Association of Foundry Specialists (BDG-Richtlinie P72), are used for measuring the three-point bending strength. Suitable characterisation equipment includes universal testing machines (Stauder et al., 2016, p. 191) or strength machines particularly designed for testing sand specimens (Anwar et al., 2021, p. 1905). The printed sand density is typically connected to the specimen's strength. It can be determined by associating the weight of a specimen measured by a balance of reasonable accuracy with its dimensions (Bryant et al., 2020, p. 4).

Scratch hardness describes a specimen's resistance to friability. It can be measured quantitatively by scratch hardness testers (Bryant et al., 2020, p. 5). It is a relevant property for handling purposes but can also indicate resistance to erosion during casting. Alternatively, the

hardness of sand moulds and cores can be obtained through the hardness B scale (Sadarang et al., 2021, pp. 1–2).

Sufficient refractoriness is needed to prevent sand-metal reactions. It can be characterised by the pyrometric cone equivalent, by determining the sintering behaviour according to the German Association of Foundry Specialists (VDG-Merkblatt P26), or by the help of heating microscopes. (Recknagel, Dahlmann, 2009, pp. 8–9)

Furthermore, casting cores need to remain dimensionally stable throughout the casting process to allow for the geometrical accuracy of the inner cavities. Binder systems are thus required to withstand the thermal loads during casting. While phenolic resins represent the organic binders with the highest temperature stability, inorganic binder systems show further improved temperature stability as they do not decompose. (Günther, Mögele, 2016, pp. 66–68) However, plastic deformation in inorganically bound sand cores occurs at their glass transition temperature (Vasková et al., 2020, pp. 11–12).

Loss of ignition (LOI) is a common test procedure for determining the weight loss of moulds and cores during casting and an indicator for gas generation (Anwar et al., 2021, p. 1905). Weight loss can be traced to the volatilisation of organics, the removal of chemically bound water or the dissociation of inorganic compounds when components emit in the gaseous phase. In LOI testing according to AFS 5100-12-S, the weight change of samples is determined before and after firing at 982 °C to calculate LOI:

$$\% \, LOI = \frac{B - C}{B - A} \, x \, 100 \qquad (2.4)$$

Where A is the starting weight of the empty crucible, B is the starting weight of the crucible containing the sample, and C is the weight of the crucible containing the sample after firing. (Joseph et al., 2017, p. 88)

A sufficient permeability of bonded sand is needed to allow for gas dissipation during casting. It can be determined using a permmeter measuring the airflow through cylindrical specimens (Martinez et al., 2020, pp. 1341–1343).

Finally, the surface finish is crucial as it directly affects the cast component's surface finish. Typically, a sand cast part shows an arithmetical mean roughness Ra of 12.5 to 25 µm (Snelling et al., 2013, p. 836) and an average roughness depth Rz between 30 and 360 µm. Casting components of high surface requirements are commonly produced by investment casting where Rz values between 6 and 30 µm are conceivable (Flemming, Tilch, 1993, p. 15). Investment casting achieves high dimensional accuracy and surface finishes by dipping precise wax patterns into ceramic slurries (Kumar, Karunakar, 2021, p. 1).

2.3 Slurry-based Binder Jetting

Moulds and cores produced by the powder-based 3D printing technique typically exhibit a relatively low density, stability, and surface quality. Since powders of small particle sizes result in limited flowability, the application area of powder-based binder jetting was found to be limiting. Firstly, the spreading of fine powders needs to be carried out at lower speeds leading to decreased productivity in binder jetting (Miyanaji et al., 2018a, pp. 505–506). However, most importantly, the production of high-density green parts to be sintered for application in technical ceramics is hindered (Zocca et al., 2017, p. 141). Thus, the layer-wise deposition of fine powders dispersed in a liquid was developed to overcome this constraint (Sachs et al., 1998).

2.3.1 Process Description

In contrast to the conventional binder jetting process, slurry-based 3D printing technology processes fine powders dispensed in a liquid to form and subsequently dry layers. Since capillary forces can draw the liquid phase of a slurry into a porous body, increased packing densities can be achieved by using fine particle suspensions (Zocca et al., 2015, p. 1995). The part contour is again defined by jetting the binder onto each layer. Figure 2.11 shows a diagram of the slurry-based binder jetting process. It comprises the following steps: First, a slurry is applied onto a substrate or the previously cast layer. Second, the powder bed is dried. The next step comprises printing the binder and, where appropriate, drying it. Those process steps are repeated until the part reaches its full height.

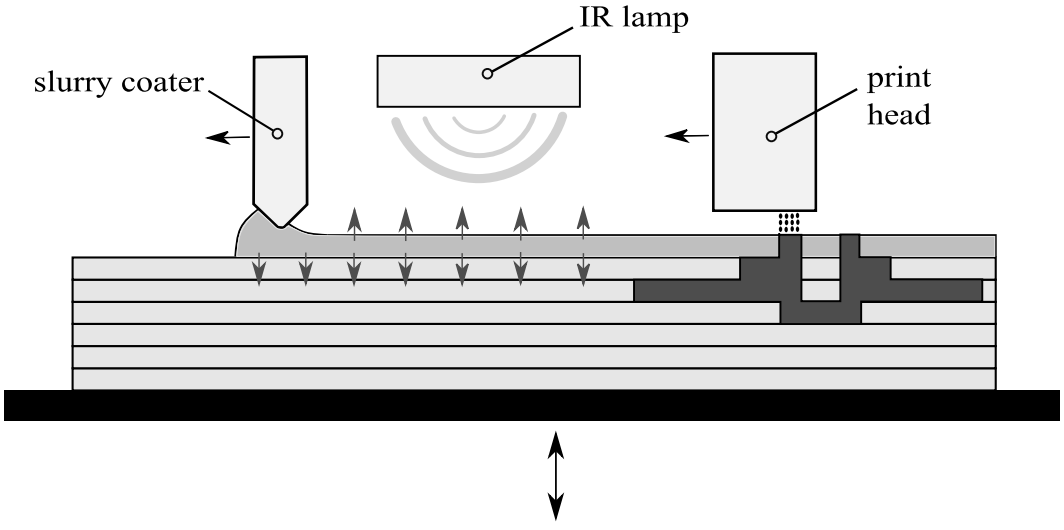

Figure 2.11: Diagram of the slurry-based 3D printing process (Erhard et al., 2022, p. 44).

2.3.2 Characteristics of Slurry-based Binder Jetting

Key differences between the powder-based and slurry-based 3D printing processes can be derived from solid-liquid interaction (Grau, 1998, p. 35):

- Processing of particles of diameter < 10 µm
- Deposition in the form of a slurry
- Cohesive behaviour of the powder bed

Consequently, the typically most critical steps are drying the layers during 3D printing and the post-processing step of de-powdering (Diener et al., 2021, p. 9). In the following, theoretical foundations describing the most important process steps of fabricating slurry-based 3D printed parts are given: layer casting, drying and infiltration with a binder. During post-processing, washout and sintering are particularly of interest.

Layer casting

The process of layer casting during slurry-based 3D printing can be described as a process combining characteristics of the technologies of tape casting, where a liquid suspension is spread as a thin layer, and slip casting, where the liquid phase of a slurry drains into a porous mould by capillary forces (Zocca et al., 2015, p. 1990). For alternative methods of layer forming, see chapter 2.3.3.

Figure 2.12 illustrates the forces acting on particles during layer casting. Apart from the force induced by capillary flow F_d, the gravitational force F_g, the interparticle force F_{pp}, and buoyancy F_f act on each particle. In contrast, in powder-based 3D printing, only gravitational and interparticle forces appear during layer deposition. Interparticle forces strongly dominate at smaller diameters as they scale as the second power of the diameter instead of the third power, as is the case for the gravitational force. Thus, small particles deposited in a dry state do not pack well when settling freely. Conversely, during layer casting, the fluid flow drags particles into points of maximum contact with already settled particles. Whereas those particles freely settle into favourable positions in a close-packing assemblage, they do not prevent concurrently floating particles from settling. (Zocca et al., 2015, p. 1995) The enhanced free settling can even lead to the absence of obvious layer interfaces in slurry-based AM (Zocca et al., 2015, p. 1990).

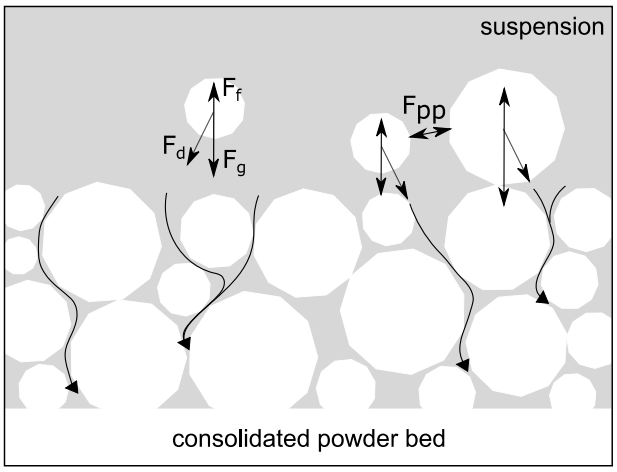

Figure 2.12: Illustration of the forces acting on particles during layer casting (after Zocca et al., 2015, p. 1995).

Capillary pressure p_c acts as the driving force for liquid migration (Grau, 1998, p. 35). Capillary pressure induced by a cylindrical pore can be described by means of the following equation

$$p_c = \frac{2\,\gamma_{LV}\,cos\theta}{r} \tag{2.5}$$

Where γ_{LV} is the surface tension of the liquid, θ the contact angle, and r the pore radius (Grau et al., 1999, p. 2081).

Young's equation describes the equilibrium at the contact of the liquid, vapour, and solid phase and thus the wettability of a solid by a liquid in a system:

$$cos\theta = \frac{\gamma_{SV} - \gamma_{SL}}{\gamma_{LV}} \tag{2.6}$$

Where γ_{SV} and γ_{SL} are the interfacial tensions between the solid and vapour, and the solid and liquid. However, surface roughness, irregularities, and porosity strongly affect the contact angle. (Alghunaim et al., 2016, p. 205, Zhang et al., 2021, pp. 1–2)

Washburn's equation predicts the flow of liquids under capillary pressure and, thus, the rate at which a liquid penetrates a small surface capillary:

$$l^2 = \left(\frac{\gamma}{\eta}\,\frac{cos\theta}{2}\right) rt \tag{2.7}$$

$$\frac{dl}{dt} = \frac{r}{\eta}\frac{\gamma}{4l}cos\theta \tag{2.8}$$

Where γ is the surface tension, η the viscosity, θ the contact angle, r the pore radius, and l the length of a column of liquid in the capillary at the time t. (Washburn, 1921, pp. 279–282)

In summary, capillary forces encourage high packing densities favourable for achieving high part densities within an economic sintering cycle. Following the equations listed above, capillary pressure in slurry-based 3D printing is particularly related to the porosity of the previously cast layer and the wettability of the solid material by the dispersing liquid. The liquid penetration rate is inversely proportional to the liquid's viscosity and the length of a capillary already filled and directly proportional to the radius of the capillary, the liquid's surface tension, and the cosine of the contact angle (Washburn, 1921, p. 280).

Drying

Since drying is one of the critical steps during slurry-based 3D printing, theoretical foundations and research work on drying are presented in this chapter.

The drying process not only plays an important role in designing an economical process. Also, properly optimised drying is considered crucial to enable uniformity and the absence of cracks, particularly when drying water-based suspensions (Briscoe et al., 1998, p. 1). Compared to other liquids, water shows a high latent heat of vapourisation. Thus an apparent high demand for energy needs to be met to enable the escaping of water molecules in the vapour phase (Brosnan, Robinson, 2003, pp. 4–8).

Stages of Drying When slurry is applied to an underlying layer, drying is accomplished from two directions simultaneously: The liquid is drawn into the pores of the porous layer underneath by capillary forces. In parallel, external heat sources can induce evaporation of the liquid from the top. (Diener et al., 2021, pp. 9–11) The following paragraph introduces the theory of thin-film drying, disregarding the influence of a porous substrate.

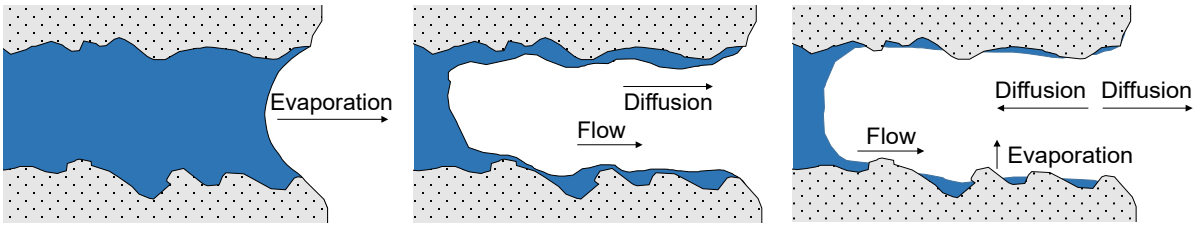

Figure 2.13: Scheme of the theory of drying - (a) representing the end of the constant rate period, (b) the 1st falling rate period, and (c) the 2nd falling rate period (Erhard et al., 2021, p. 6 after Scherer, 1990, pp. 6–8).

Drying processes in solids saturated with liquids start with the first stage of drying, the constant rate period CRP, where the evaporation rate is independent of time, and the surface is covered with a film of liquid. Capillary tension prevents exposure to the solid phase, and the solid undergoes shrinkage. The shrinkage of the suspension volume is proportional to the rate of evaporation. The end of CRP is reached as soon as the radius of the liquid meniscus equals the

pore radius within the network stiffened by shrinkage (Figure 2.13a). As soon as shrinkage is completed, further evaporation drives the meniscus into the body. Within the first falling rate period FRP1 (Figure 2.13b), the liquid recedes, and the pores become partially filled with air. The evaporation rate decreases, and the surface temperature increases to a value above wet bulb temperature but below ambient temperature since most evaporation happens at the exterior surface. The flux of the liquid to the surface reduces continuously. As soon as the liquid is removed predominantly by evaporation inside the body and diffusion of its vapour, the second falling rate period FRP2 (Figure 2.13c) begins. The sensitivity to external conditions decreases since the temperature of the surface approaches the ambient temperature. Even though the total stress on the network decreases, differential strain develops due to dissimilar compression in saturated and surface-near regions that can lead to warping. (Scherer, 1990, pp. 4–8, Rahaman, 2003, pp. 281–289)

Figure 2.14 illustrates the trends of surface temperature, water content, and drying rate on initially saturated samples at air temperature (Janetti, Janssen, 2020, p. 4).

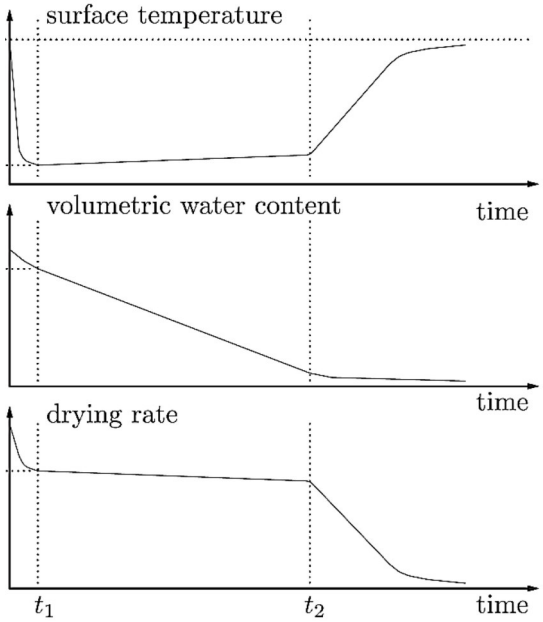

Figure 2.14: Illustration of the course of the average surface temperature, the volumetric water content and the drying rate. (Janetti, Janssen, 2020, p. 4).

Drying Defects Cracking is the most common drying defect in ceramics. Cracks can arise in connection with stresses resulting from excessive or differential shrinkage, typically at high drying rates or in thick bodies (Brosnan, Robinson, 2003, pp. 137–138). Reducing the probability of fracture may be accomplished by decreasing the capillary pressure, which is considered responsible for creating critical flaws. Conceivable options for reducing capillary pressure are decreasing the surface tension of the liquid, the cosine of its contact angle, or increasing the pore size and permeability (see equation (2.5)). (Scherer, 1990, pp. 10–12) Figure

2.15 illustrates a suspension's network strength and drying stress evolving in parallel during drying. Cracks develop in case a stress curve exceeds the network's strength curve. Murray (2009) proposes either a reduction of only the magnitude of stress (compression of the stress curve leading to lower maximum stress) or also a postponement of its development (an increase of the "open time") to avoid cracking. Multiple options to avoid differential stress include modifying the formulation of the components, e.g. using larger particles, volatile plasticisers or humectants, drying slowly, or applying thinner layers. (Murray, 2009, pp. 43–49)

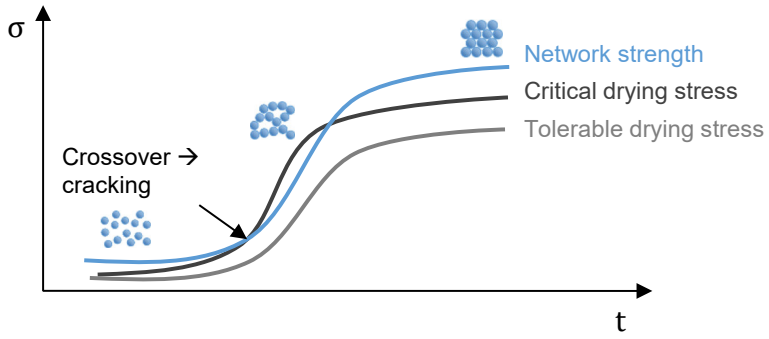

Figure 2.15: Stress development during drying (after Murray, 2009, pp. 38–39).

Hu et al. (1988) investigated the mechanics of cracking on thin films and and described the critical cracking thickness CCT as a function of the fracture resistance of a film material K_c, and the biaxial stress σ (Hu et al., 1988):

$$CCT = \left(\frac{K_c}{1.4\sigma}\right) \tag{2.9}$$

The critical layer thickness is thus suggested to be only dependent on stress evolving from capillary pressure and fracture resistance. The CCT was found to be independent of the drying rate but dependent on variations in film properties that affect either K_c or σ. CCT was found to be proportional to the polyvinyl alcohol (PVA) binder content that increases the fracture resistance of a film. (Chiu et al., 1993, p. 2263)

Excessive drying only from one surface of a drying product can also lead to warping. Within the early drying stage, capillary tension may develop on the drying surface, and liquid is drawn from the other surfaces to balance the hydrostatic pressure. If drying products exhibit a low permeability, this tension can lead to varying compressive forces on the solid and an upwards warping behaviour (Figure 2.16a). Warping in the reverse direction may occur at a later stage of drying. If the pores next to the surface are filled with air already, and the lower portion is still saturated with water, the lower network containing the liquid may be subject to compressive forces (Figure 2.16b). (Scherer, 1990, p. 7)

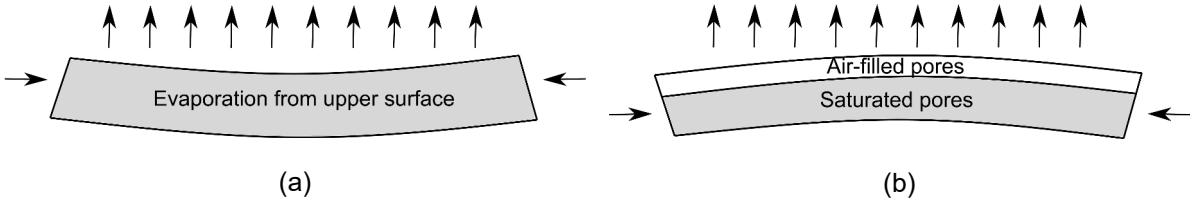

Figure 2.16: Demonstration of the reverse directions of warping in (a) early stages of drying and (b) later stages of drying (after Scherer, 1990, p. 7).

Drying shrinkage Shrinkage due to evaporation of a deposited thin slurry film's solvent must be accounted for to achieve the desired dimensional and shape accuracy of a green body. Hence, in contrast to powder-based 3D printing, the actual thickness of each layer is not automatically consistent with the layer heights preset in the machine parameters.

The thickness of the nth layer $T_l(n)$ can be calculated as follows:

$$T_l(n) = H(1 - SR^n) \tag{2.10}$$

Where H is the preset thickness of a layer and SR is the shrinkage ratio that depends on the volume content of the solvent in the slurry. The actual layer thickness is thus successively approaching the preset value. (Tian et al., 2012, pp. 364–366) Therefore, the higher the shrinkage ratio, the more base layers are needed to reach the preset layer thickness by low tolerance.

Binder infiltration

A binder used in slurry-based 3D printing is required to fulfil the following fundamental tasks (Grau, 1998, p. 137):

- Sufficient infiltration into a fine-grained powder bed
- Insolubility in the redispersion solvent to allow for part retrieval
- Sufficient strength
- Processability on inkjet printheads

Regarding binder absorption, the process of droplet penetration in rigid powder beds differs from that in loose powder beds. In powder-based 3D printing, the rapid deceleration at the impact of the droplet and its commingling with the powder happens simultaneously. Conversely, in slurry-based 3D printing, different size ratios between drop and particle exist. Here, droplets first hit the surface of a rigid powder bed and then penetrate it. Thus, compared to powder-based 3D printing, printed lines in slurry-based 3D printing tend to be rather flat but

wide. (Knezevic, 1998, p. 17) Since a rigid powder bed is tolerant to the ballistic impact of droplets, no deformation of the powder surface is expected. Moreover, the permeability and infiltration kinetics of cohesive powder beds strongly differ due to the proportionality of the infiltration kinetics to the pore size and the inverse proportionality of the permeability to the square of the pore size (Knezevic, 1998, p. 17, Grau, 1998, p. 146). Grau (1998) found the regions printed with an acrylic polymer emulsion to impact the kinetics of layer casting by a lowered void fraction, permeability, and contact angle. This effect led to bumps at the interface between printed and unprinted regions. Therefore, the ratio of the cosines of contact angles of unprinted and printed regions $\cos(\theta_{unprinted})/\cos(\theta_{printed})$ was suggested to match to enable similar casting rates. Changing the slurry solvent from water to a water/isopropyl alcohol blend (since water/isopropyl alcohol shows an improved wetting on the acrylic polymer emulsion used), or modifying the volume fraction of binder were suggested to prevent differential casting rates. (Grau, 1998, pp. 181–185) For detailed contiguities on binder characteristics and processing, the author refers to Moon et al. ‘s extensive study on important characteristics of inkjet binders for use in slurry-based 3D printing (Moon et al., 2002).

Wash-Out

Unlike in powder-based AM, green bodies produced by slurry-based AM cannot be easily removed from a loose powder bed. The powder compact surrounding the individual parts must rather be dissolved in a solvent that is water in the case of water-based slurries. (Mühler et al., 2015b, p. 22) The redispersion of the powder compact is mainly controlled by the number of particle-particle contacts and each contact’s strength. While the number of contacts depends on the particle sizes and the packing density, the strength can be influenced significantly by slurry additives. For example, polyethene glycol is believed to improve redispersion by forming soluble bridges between particles. (Grau, 1998, p. 15) Moon et al. studied the redispersion behaviour of different slurry compositions and demonstrated the challenge of enabling a spontaneous redispersion of powder compacts and, thus, a damage-free part retrieval. In particular, polymeric components in the slurry and a high packing density of the powder compact were found to strengthen particle-particle bonds and, thus, impede redispersion. (Moon et al., 2000)

Since the dissolution of the powder compact is preceded by its swelling, inhomogeneous volume expansion may occur. Moreover, the manufactured part may act as a diffusion barrier for the solvent, making the wash-out process even more critical in slurry-based AM. (Mühler et al., 2015a, p. 115, Mühler et al., 2015b, p. 22) When using slurry-based binder jetting technology, the wash-out medium must not dissolve or weaken the binder. Furthermore, the

printed part must exhibit sufficient strength to resist the wash-out process successfully. (Grau, 1998, p. 137)

Spray rinsing is suggested to support material removal: no or a mild spraying intensity may be used to achieve a smoothening effect by leaving material on the surface. More intense spraying allows for removing all residuals from the manufactured body (Mühler et al., 2015b, p. 22).

To realise the full potential of slurry-based binder jetting, easy removal of undercut material (particularly from long and thin channels to produce hollow and filigree casting cores for cooling channels) is desirable, as well as the reuse of the redispersed particles to enable an integral material cycle.

Sintering

Sintering is the process of densifying a green body using the macroscopic driving force of the reduction in surface energy during heating. The part density achievable by sintering a green part and its shrinkage mainly depend on the green body's density, the material system and the sintering curve. (Du et al., 2020, p. 11, Zocca et al., 2017, pp. 144–146) Since, compared to powder-based binder jetting, slurry-based 3D printing uses relatively small-sized particles and enables an increased packing density, greater surface-to-volume ratios and green part densities, the technology generally allows for enhanced sintering when using the same temperature profile. Common procedures to enhance sinterability in slurry-based 3D printing may include adding a second material system to decrease the sintering temperature and realise liquid phase sintering. (Bourell et al., 2020, pp. 123–124, Vogt et al., 2021b, pp. 33–35) Generally, a high green density of > 50% is required for achieving a high sintered density: the higher the green density, the lower the density change (shrinkage) during sintering to a defined sintered density. Sintering can also lead to shape distortion due to gravity effects, temperature gradients, or liquid-phase formation (Du et al., 2020, p. 11). For a comprehensive overview of the theories and principles of sintering, the author refers to Rahaman (Rahaman, 2007).

2.3.3 Layer Forming Methods

The layer forming method defines the roughness of each layer of slurry (Cima et al., 2001, p. 219) and directly influences the technically feasible process parameters. Various layer-forming methods for slurry-based 3D printing have been investigated from the technology's outset (Caradonna, 1997, pp. 30–33):

- Slurry jetting
- Spray deposition
- Tape casting

Slurry jetting uses small inkjet nozzles to give precise control of the slurry to be deposited. However, the drawbacks were found to be reliability issues due to clogged nozzles and relatively poor surfaces. Spray deposition uses atomizing nozzles that can be rastered across the building plate to create the layer. Only comparatively simple hardware is necessary to realise spray deposition. The difficulty within this method is a low control of the flow rate and, thus, of the resulting layer thickness. The tape casting approach, sometimes also referred to as layer-wise slurry deposition, uses a doctor blade to spread a pool of slurry. (Caradonna, 1997, pp. 30–33) Most recent publications adopt the tape casting approach (e.g. Tian et al., 2012, Mühler et al., 2015a). Yen (2015) designed a novel coat hanger geometry based on tape casting and slot-die casting, including a slurry-feeding mechanism that enables a reliable and uniform distribution (Yen, 2015). Vogt et al. (2021a) recently announced pursuing a nozzle-based strategy (Vogt et al., 2021a, pp. 42–43).

2.3.4 Materials and Applications of Slurry-Based Additive Manufacturing

A series of fundamental and extensive studies on slurry-based 3D printing was conducted at the Massachusetts Institute of Technology (MIT) in Cambridge, USA, in the late 90s and early 2000s. Cima et al. (2001) report the successful production of components without foreseeable material limitations. Alumina, titania, silica, silicon nitride, and WC-Co have been investigated (Cima et al., 2001, p. 222). Moreover, a research team around the Clausthal University of Technology and BAM Federal Institute for Materials Research and Testing in Berlin, Germany, investigates slurry-based additive manufacturing of ceramics since the late 2000s. Table 2.2 gives an overview of materials previously processed by slurry-based AM methods without claiming to be exhaustive.

Table 2.2: Overview of studies on slurry-based additive manufacturing.

AM method	Particulate material	Solvent	Layer thickness in µm	References
N/A	SiO_2	Polyvinyl alcohol	10-80 µm	(Yen, 2015)
Laser sintering	Al_2O_3-SiO_2	Water	100 µm	(Gahler et al., 2006)
Laser sintering	Porcelain	Water	100-200 µm	(Tian et al., 2009, Tian et al., 2012, Mühler et al., 2015a)
Binder jetting	Al_2O_3	Water	20-50 µm	(Grau, 1998)
Binder jetting	WC-Co	Isopropyl alcohol	35 µm	(Oliveira, 2002)
Binder jetting	Al_2O_3	Water	50 µm	(Zocca et al., 2017)
Binder jetting	Porcelain	Water	N/A	(Lima et al., 2018)
Binder jetting	SiC/ SiSiC	Water	100 µm	(Zocca et al., 2019, Diener et al., 2022, Diener et al., 2023)

2.3.5 Potential for Application in Casting Technology

Due to the relatively low costs, binder jetted sand moulds and cores are already part of large series production of cast parts in engine production (Günther et al., 2021, p. 6). However, the application of complex cores is limited to certain applications by reason of inadequate properties like a high volume of porosity and shrinkage and low strength (Huang et al., 2019, p. 1).

Two relevant use cases of high-strength ceramic casting cores are presented shortly:

- The insertion of sintered, highly temperature-stable ceramic cores into ceramic shells in investment casting is state-of-the-art in producing near-net shape turbine blades. Complex interior cooling geometries are particularly needed for superalloy airfoils in gas turbine engines. In investment casting, shells are produced by repetitively coating a wax pattern with a refractory ceramic slurry, stuccoing, and drying the respective layer. (Kanyo et al., 2020, pp. 1–2) Multiple steps are involved in manufacturing the patterns and, subsequently, the moulds and cores: e.g. two sets of injection moulding tooling may be required – the first to fabricate the ceramic core, the second to mould a wax pattern around the core. (Bae, Halloran, 2011, pp. 1–2) A single, patternless process directly producing an integrally cored ceramic mould not only allows for reduced

tooling costs, less material waste, and shorter lead times. It also enables advanced dimensional accuracy and structural control. (Kanyo et al., 2020, p. 16) Stereolithography (SLA) technology has accomplished AM of complex investment casting cores and integrally cored metal casting moulds (Halloran, 2016, pp. 20–22). Since lead times can be improved by 89 % and production costs by 60 % compared to investment casting involving hard tooling, AM of burn-out patterns is also used in investment casting (Wang et al., 2019b, p. 648). The removal of the ceramic cores in hollow turbine blade manufacturing is commonly accomplished by leaching (Zhu et al., 2019, pp. 1–2).

- Lost cores in high-pressure die casting (HPDC) must withstand high injection velocities and pressures. Thus, advanced high-strength casting cores are needed in HPDC. Despite their high strength, cores still need to be mechanically removable after casting, e.g. by water jetting. An EU research project developed the production process of a ceramic water jacket core of a closed-deck aluminium engine block by dry pressing and sintering (López de Sabando, 2019). Two crucial challenges have been faced: first, the porosity required in core removal allowed for penetration of aluminum melt. Second, there were strength issues. A subsequent coating and infiltration addressed those (Merchán et al., 2019). Overall, the cycle time of de-coring was not feasible for mass production, mostly due to the complexity of the core.

These studies reveal the conflict between a casting core's strength and its removability on the one hand and the demand for an economical process for manufacturing complex high-strength casting cores on the other. Compared to SLA, slurry-based binder jetting is an interesting alternative for manufacturing integrally cored moulds in investment casting, particularly in terms of economic efficiency (reduced material costs, increased build-up rates, increased build volumes, reduced sintering times). Slurry-based binder jetting shows higher cycle times than the powder-based alternative due to the additional process step of drying the slurry solvent. Conventional advantages of scalability and flexibility in terms of material systems and high complexity apply regardless. Besides high strength, improved surface qualities and thermal resistance are required to realise filigree, self-supporting core structures for contour-close cooling channels, e.g. in manufacturing electric motors. A potential application of slurry-based binder jetted casting cores in all gravity and low-pressure casting technologies is considered technically challenging but feasible.

2.4 Research Gap

Due to the increasing interest in additive manufacturing technologies, powder-based binder jetting and its material-dependent factors of influence on the process and the resulting part characteristics have been extensively investigated and transferred to industrial application. Comparatively, few studies address the slurry-based alternative whose process complexity is expanded by the additional process step of drying. Even though the literature points out the importance and characteristics of drying regarding the stress development in ceramic films, no previous studies on layer-wise drying are known to the author.

The effect of the drying conditions on the part quality in slurry-based 3D printing is not yet revealed in the literature. However, they strongly affect not only the material properties but also the process performance. Among the AM methods, preference for the binder jetting process is frequently given if a high cost pressure calls for economic efficiency. To be able to respond to this demand which is of particular importance in casting technologies also, drying needs to be studied with respect to the effects on part quality on the one hand side and process performance on the other side which is – compared to conventional powder-based 3D printing – heavily influenced by the additional process step of moisture removal.

To allow for the potential integration of slurry-based 3D printing in the process chain of casting, the technology's crucial influencing factors need to be determined with respect to the requirements of casting cores. Finally, so far, it is not known that slurry-based 3D printing has been utilised for producing high-strength casting cores before. The potentials and challenges specifically associated with the process chain integrating this technology in the conventional casting process are thus to be revealed.

3 Objectives and Approach

Although the latest state of science and technology reveals rising interest in an improved understanding of materials and processes in binder jetting technology, few studies on slurry-based binder jetting have been conducted. Since the little literature on slurry-based 3D printing focuses on processing various materials rather than studying the influences of the process parameters, 3D printing itself still raises decisive unresolved issues. Notably, no prior study is known to tailor the process to fit the demands of casting applications. The central task of the present work is to elaborate fundamental knowledge on processing an environmentally friendly water-based ceramic slurry in binder jetting in view of the potential application in indirect metal AM. The extended process chain to be investigated thus involves the 3D printing process itself, the post-processing steps of curing, wash-out and sintering, and the casting and de-coring process.

Figure 3.1 gives an overview of the overall approach and structure of the present work. The first objective is to elaborate the procedures of stable processing of a defined ceramic slurry material system in a 3D printing test setup. Those allow for reliable process control and homogeneous powder bed formation, a key prerequisite for profound process-specific investigations. For this purpose, both CFD simulation and experimental work are utilised, enabling a stable process control, a suitable hardware and software configuration of the test setup, and, thus, the fabrication of constant quality prints. Secondly, understanding the sub-process of layer-wise drying is considered decisive for controlling slurry-based binder jetted casting cores' properties. The drying conditions each individual layer cast from a ceramic suspension is subjected to are crucial to enable a defect-free layer buildup. The resulting microstructure, powder packing density, strength, dimensional accuracy, surface quality, and the economic viability of the overall process are regarded as dependent on drying. In contrast, the binder system's function is of minor interest, as its task is mapping the contour instead of providing the final strength. Hence, a tailored process management is to be elaborated specifically with regard to drying.

The overall aim of this work is a scientific contribution to the process development of slurry-based 3D printing with a strong focus on generating knowledge utilisable for transfer to industry. It is thus of particular importance to consider the central product and process demands relevant for potential implementation in the foundry sector. Against the background of state of the art in 3D printing and drying technology, the following central research hypotheses to be

confirmed within this study assume a contradiction between economic efficiency and beneficial material properties:

- Excessive drying provokes the formation of major flaws and thus reduces strength.[1]
- High drying periods lead to improved compaction and thus result in increased density and strength.
- Low layer thicknesses enable improved compaction and thus result in increased density and strength.
- High residual moisture contents lead to lateral binder migration.

From an economic perspective, the energy required for drying each layer is preferably input rapidly at a sufficient radiation power. Drying slowly, conversely, is known to prevent typical drying-related defects. High strength and density are considered advantageous material properties for casting cores since those encourage flexibility in design. Furthermore, the absence of major defects indicated by strength is conducive to process reliability. Binder migration is to be avoided in order to allow for dimensional accuracy. While applying lower layer thicknesses enables high surface qualities and filigree designs, it implies a higher number of layers to be deposited subsequently and, thus, higher processing efforts.

Correlations between crucial process parameters indirectly determining the technology's economical viability and important quality-related material properties shall be drawn up in this work. The variety of casting processes and the diversity of casting products involve specific requirements. A quantification thereof is essential to allow for an evaluation of individual target attainability in spite of the assumed conflict of ambivalence between profitability and part quality.

Moreover, all requirements within the expanded process chain must be elaborated carefully. However, the process steps of sintering and casting are considered state of the art and thus only provide the prerequisites for the overall process consistency. Finally, the applicability of the

[1] Drying is considered to be excessive from the total energy input per layer configured to such an amount that drying-related material defects arise. Excessive drying can be induced by either exposing the layers to too high stages of radiated power and thus realising rapid drying or by exceeding the drying duration above a tolerable period. Since both a newly developed material system and 3D printing test setup are subject to the present investigation, those limits are to be specified.

slurry-based 3D printing process to achieve high-strength casting cores is to be demonstrated along the process chain of indirect metal AM.

The structure of this work follows the framework of scientific questions as outlined above and illustrated in Figure 3.1.

Chapter 4.1 describes the materials initially customised to the requirements of slurry-based 3D printing of casting cores. To allow for a comprehensive process understanding, investigations are particularly drawn up aiming at ensuring a reliable process control by elaborating a suitable hardware and process parameter configuration for homogeneous layer formation and allowing for the control of the material properties by means of drying setup. Chapters 4.3, 4.4 and 4.5 specify the simulation and experimental methods. A CFD simulation model developed to predict cast layers' homogeneity and surface quality is introduced, as well as the lab scale slurry-based 3D printing test setup (chapter 4.2). Appropriate, experimentally elaborated process specifications and the factors affecting the drying conditions within the test setup are presented along with the experimental design.

Chapter 5.1 provides the results of the validation of the simulation model and its application in the advancement of the coater geometry used in the test setup. Moreover, chapter 5.2 outlines the results of the experiments on the control of material properties via drying configuration and discusses those against the background of already published knowledge. A fundamental process understanding is derived from these results (chapter 5.3), facilitating control of the final part properties by specifically controlling the drying conditions within the binder jetting process while explicitly considering the reciprocal influence on the production process efficiency mandatory for a future technology scale-up.

Finally, the knowledge gained is applied in an overall process demonstration in chapter 6. A collapsible core structure tailored to aluminium gravity casting of a contour-close cooling application is designed and realised. As a second use case, the applicability of slurry-based 3D printed digital codes for part tracking purposes is suggested. Finally, the potentials and challenges of implementing slurry-based 3D printing in the conventional processes of metal casting, as unveiled in this work, are summarised.

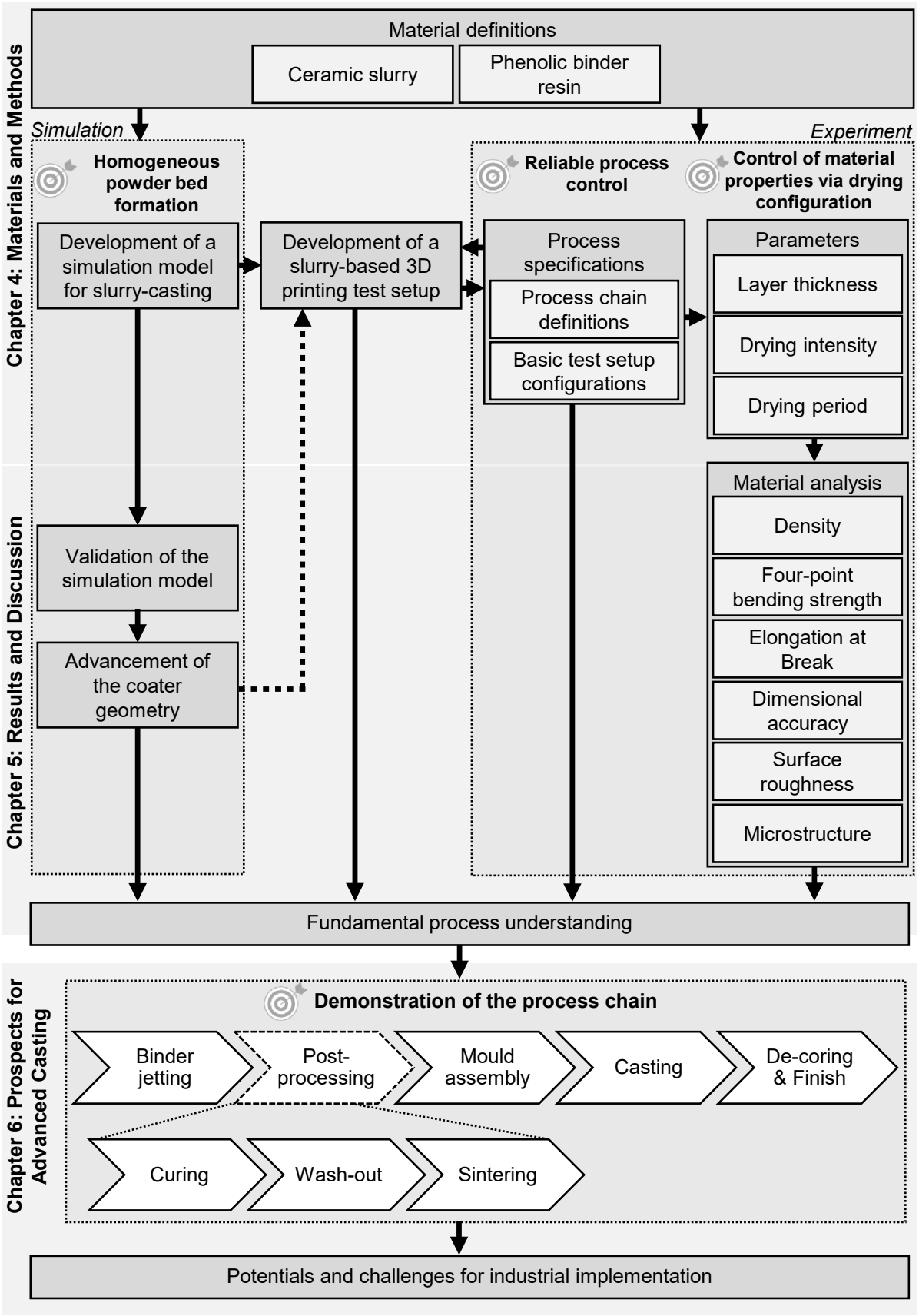

Figure 3.1: Big picture of the present thesis.

4 Materials and Methods

This chapter describes the materials utilised for investigations on the slurry-based 3D printing process in general and the layer-wise drying process in particular. The lab-scale slurry-based 3D printing setup, its configuration, the parameters involved in the basic 3D printing sequence, and the simulation model for slurry-casting are introduced. Moreover, the methods of fabrication and analysis of specimens are depicted, as well as the overarching process chain.

4.1 Materials

The consolidated powder bed, referred to as powder compact, is formed from an aqueous silica slurry. A thermoset resin insoluble in water after curing is used as a binder. Both are specified in the following.

4.1.1 Slurry

Quartz was selected as the raw material powder due to its benefits in regard to costs and availability. Quartz powder is the standard moulding material in light metal and iron sand casting. Slurry development and characterisation were carried out at Fraunhofer ISC/ Center HTL. In contrast to the coarse-grained sand used in standard processes, a fine quartz flour (Sikron SF600, Quarzwerke GmbH, Germany, d_{50} value 3 µm, d_{95} value 10 µm) is appropriated herein. 44 vol.- % of quartz flour is suspended in ~ 55 vol.- % of deionised water with the addition of ~ 1 vol.- % organics, resulting in a suspension with a density of 1.725 g/cm³. The organics are composed of polysaccharides as the viscosity modulating agent, a dispersing agent, a defoamer, and a preservative. The slurry is prepared on a roller for 12 h with the help of 12 mm alumina beads. For 7 days, no considerable sedimentation is noticeable. (Vogt et al., pp. 124–127) Nevertheless, the slurry is stored on a roller for at least 24 h prior to processing to avoid segregation. Figure 4.1 depicts the rheological characteristics of the slurry.

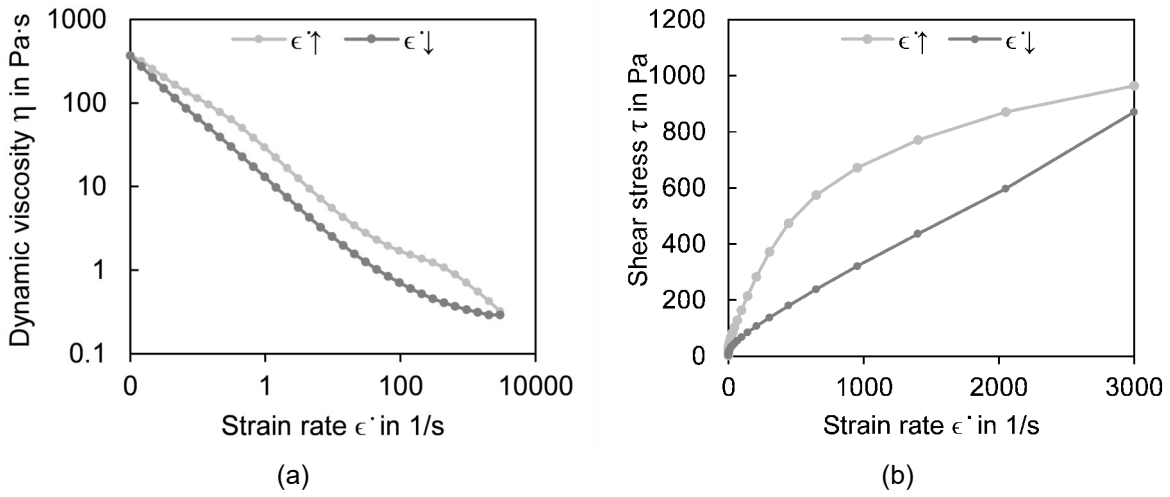

Figure 4.1: Rheological properties of the quartz slurry at T = 20 °C determined by a rotational rheometer (MCR301, Anton Paar GmbH, Germany); (a) dynamic viscosity and (b) shear stress in dependence on the strain rate.

4.1.2 Binder System

The binder systems' main function in slurry-based 3D printing is defining the shape of the part to be fabricated. Hence, the binder needs to ensure bonding between the fine particles of the powder compact. However, the strength of the bond is of minor importance since the consolidation during sintering defines the part strength. Still, sufficient green body strength is required to ensure secure handling during wash-out.

In brief, the following requirements have to be met for application in the slurry-based 3D printing process presented herein:

- Appropriate rheological properties for reliable processing in inkjet printheads
- High selectivity, even when exposed to residual moisture in the powder compact
- Sufficient bonding of particles to allow for appropriate handling strength
- Insolubility in water after curing

The binder system selected for this study conforms to all those prerequisites. It consists of a solid phenolic novolak resin dissolved in isopropyl alcohol (IPA) and the curing agent Hexamethylenetetramine (Hexa) described in a patent description of Hüttenes-Albertus Chemische-Werke GmbH, Düsseldorf, Germany (Egeler et al., 2012). Phenolic resins are the condensation products of phenol and formaldehyde. Novolak is a non-self-curing phenolic resin that is soluble in solvents and storable. Adding Hexamethylenetetramine enables the transition to the non-soluble end stage when applying heat or acids. (Pöhlmann, 2006, pp. 14–16)

Different resin-to-solvent ratios have been tested for their processability in an inkjet printhead. Table 4.1 shows the fluid parameters for each alternative, determined by viscometer SV-10 (A&D Co., Ltd, Tokyo, Japan), and the optical contact angle goniometer and drop shape analysis system OCA 25 (DataPhysics Instruments GmbH, Filderstadt, Germany). All those three compositions fit the area of reliable inkjet fluids stated in fluid theory on inkjet technology (Figure 4.2).

Table 4.1: Fluid parameters of different resin-to-solvent ratios (mean values over five measured values).

	Weight proportions of resin to IPA		
Fluid parameter	**1:4**	**1:6**	**1:8**
Dynamic viscosity in mPa s	9.4	5.6	4.4
Surface tension in N/m²	24.5	22.9	21.2
Contact angle in °	29.8	25.5	24.0

Due to the fast volatilisation of the solvent, the reliability of the printhead SL 128-AA (Fujifilm Dimatix, Inc., Santa Clara, USA) was found to decrease with increasing resin contents. The weight ratio of resin to IPA is thus set to 1:8. It allows for a purge-free operation time of ~ 40 min compared to ~ 15 min for the 1:6 alternative and ~ 30 s for the 1:4 mixture.

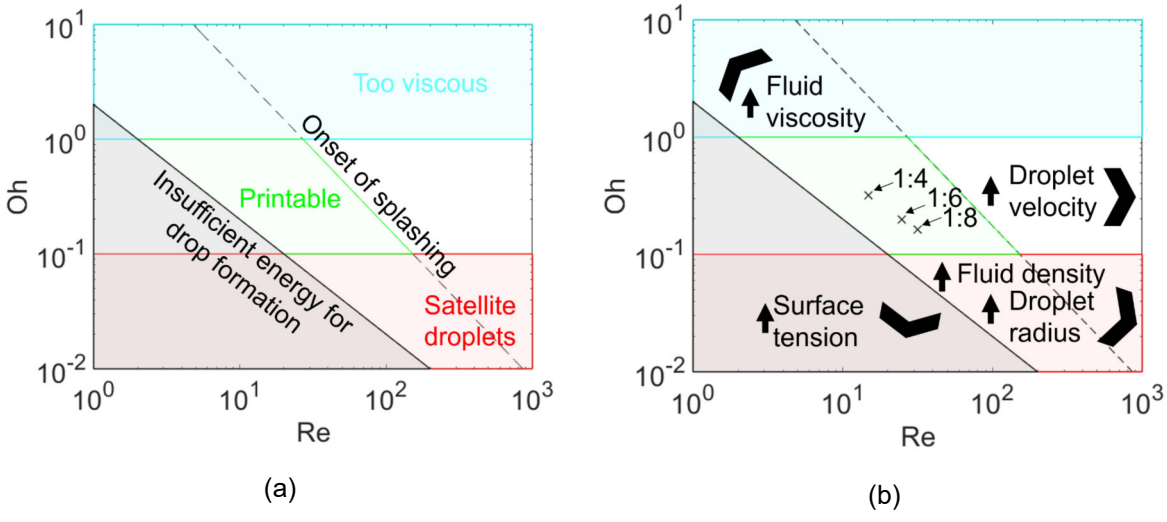

Figure 4.2: (a) The domain for reliable inkjet fluids based on the Weber and Reynolds numbers (after Lohse, 2022, p. 354), and (b) assignment of the binder compositions and visualisation of the directional effects of the contributing factors.

Using fluids of higher resin content is conceivable when utilising the purge function every few layers. The resin proportion of the ink actually provides the binding effect, while the solvent IPA is a non-functional component that, however, also needs to be ejected by the printhead.

High resin loads are economically desirable in industrial processes on account of the printhead and binder effectivity. Since a purge function was found compulsory for printhead reliability in print jobs exceeding 50 layers (e.g. to realise the complex geometries presented in chapter 6), the test setup was upgraded by a printhead cleaning unit subsequently to the performed parameter study on drying conditions. However, to provide consistency, the 1:8 resin is used in all experiments performed in the context of this work.

4.2 Slurry-based 3D Printing Test Setup

In the following section, the 3D printing test setup is introduced as well as the process sequence implemented to allow for reliable process control.

4.2.1 Hardware Implementation

The experimental test setup (Figure 4.3) comprises three moveable axes driven by stepper motors: the x-axis for the coating module; the y-axis, which is mounted on the same base as the coating module and enables slight shifts of the printhead from layer to layer to avoid cumulating printing defects; and the z-axis for lifting and lowering the build platform. The printhead SL 128-AA (Fujifilm Dimatix, Inc., Santa Clara, USA) is mounted at an angle of 16° to the coating direction, resulting in a fixed print resolution of 140 µm in the y-direction. The test setup is controlled via a programmable logic controller (PLC) based on SIMATIC S7 (Siemens AG, Munich, Germany), accessible by a standard PC via ethernet. The control program on the PC allows a specification of the process steps using a high-level definition language.

The coating module includes the coating head with an inner structure responsible for slurry distribution along the coating width and the pneumatically operated slurry feeding system (Figure 4.4a). A coater cleaning unit consisting of a continuously rotating roller immersed in water is positioned so that the coater rests on the cleaning unit while drying each layer. Thereby, slurry residues are prevented from drying in and clogging the coater.

An IR emitter (IRD X230L, Optron GmbH, Garbsen, Germany) is mounted in a fixed position on the coating module, ensuring homogeneous heating of the sample during drying (Figure 4.4b). A suitable position of the IR heater was determined by examining the temperature homogeneity within the building area with a PI400i thermal imaging camera (Optris GmbH, Berlin, Germany): the distance between the respective layer and the filament of the IR lamp was set to 65 mm.

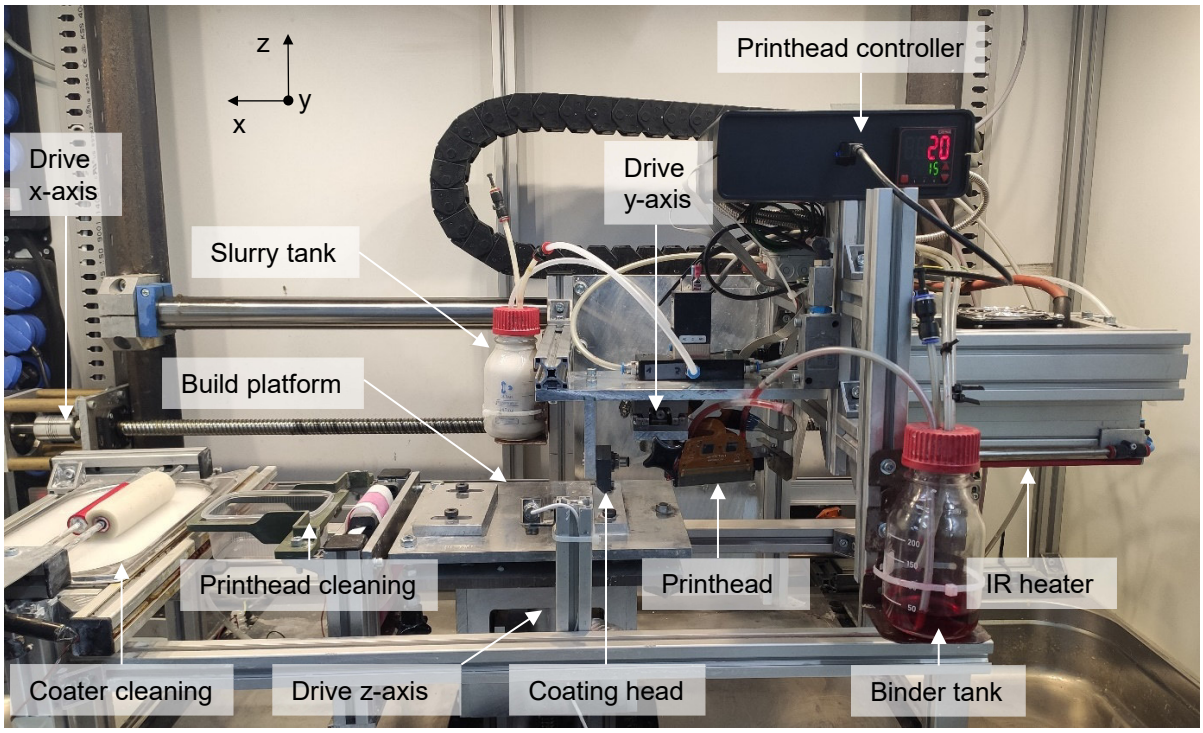

Figure 4.3: Slurry-based 3D printing setup.

A pyrometer (CT-SF22, Micro-Epsilon Messtechnik GmbH & Co. KG, Ortenburg, Germany) is mounted above the build platform and records the radiant energy of a freshly applied ceramic layer during drying. The IR radiator's infrared radiation superimposes the layer's radiation. In addition, the emission coefficient of the layer changes over time due to moisture loss. Therefore, the temperature values displayed by the pyrometer are treated as digital values representing a specific drying state only. A type K thermocouple is ducted through a hole drilled through the substrate and connected to a universal measuring amplifier (QuantumX MX840B, Hottinger Brüel & Kjaer GmbH, Darmstadt, Germany) to monitor the actual temperature in the lowest layer.

The printhead is operated with 1.96 mbar negative pressure on the binder tank to avoid unwanted leakage from the open nozzles and to allow for defined droplet formation by piezo-electric actuation (Figure 4.4c). As mentioned above, the test setup was upgraded by a printhead cleaning station subsequently to the parameter study to enable the fabrication of larger parts. Layer-wise printhead cleaning is accomplished by applying 0.45 bar pressure on the printhead tank above a purge basin and wiping off binder residuals using a coiled non-woven material.

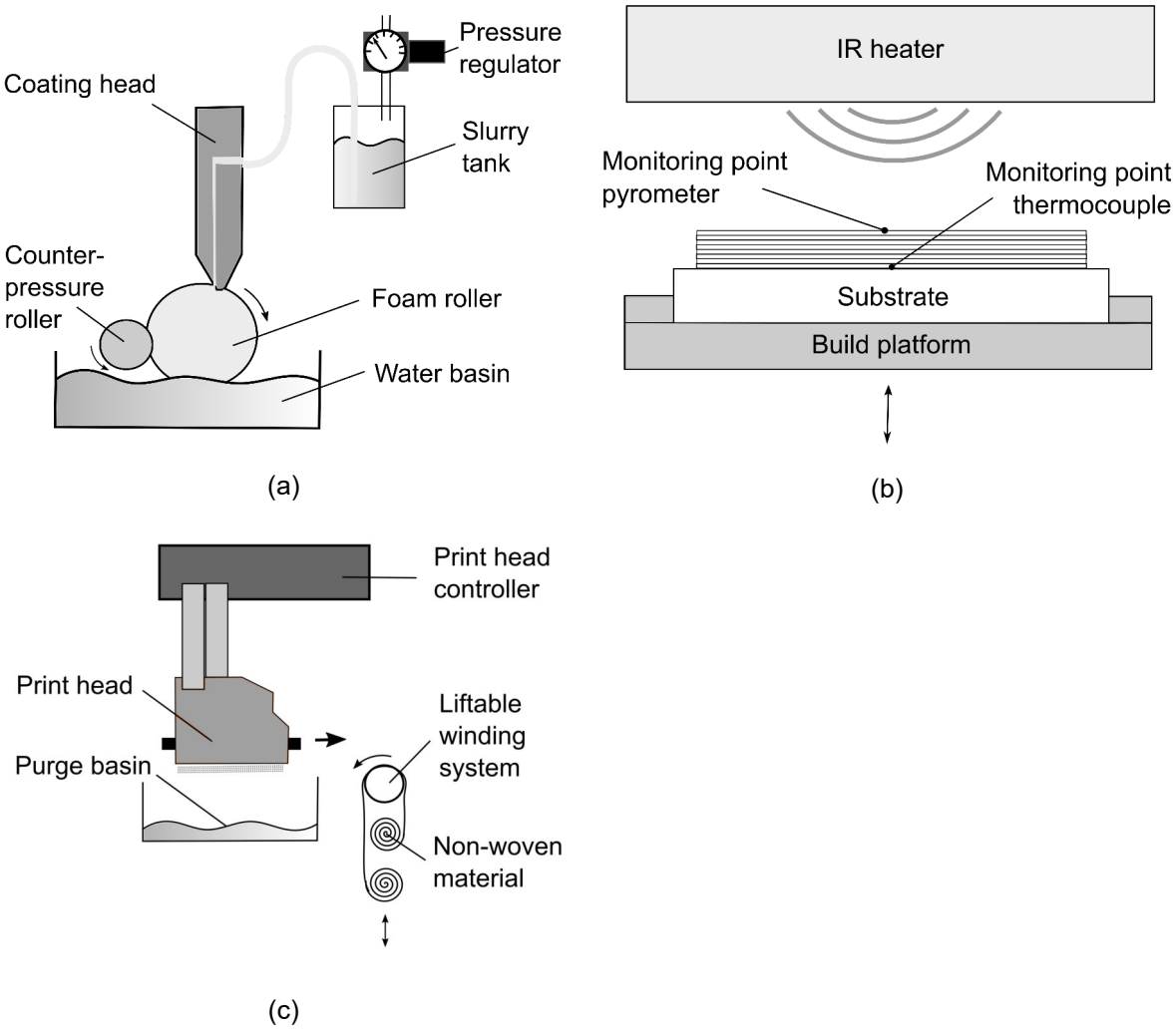

Figure 4.4: Schemes of the test setup's sub-systems: (a) coating head feeding and cleaning system, (b) drying arrangement, (c) printhead feeding and cleaning system.

4.2.2 Process Sequence

The investigated process for the fabrication of ceramic layer compounds is shown in Figure 4.5. It follows the sequence:

(a) The gap between the coater and the build platform is set to the predefined layer height. A coater applies slurry to the build platform. The slurry's delivery rate corresponds to the coating speed and the layer height. It is thus fed according to demand only with a small surplus of material.

(b) An IR radiator is centred above the build platform, heating the layer for a defined period of time to remove moisture from the freshly applied layer.

(c) The build platform is lowered.

(d) The printhead selectively applies the binder onto the powder compact whilst returning to the starting position.

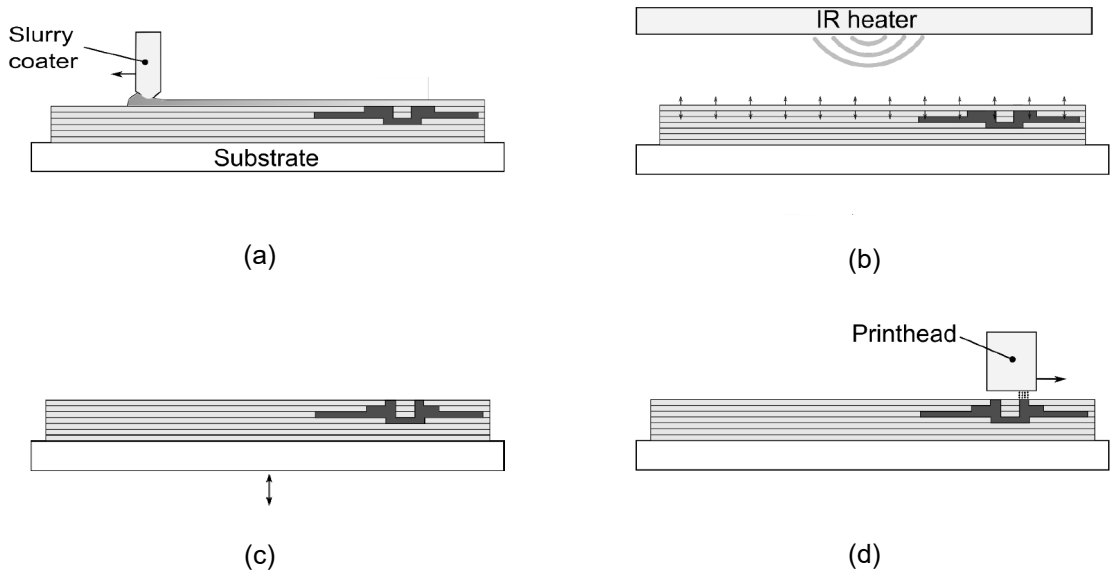

Figure 4.5: Slurry-based 3D printing sequence realised in the test setup: (a) layer casting, (b) drying, (c) lowering of the build platform, (d) printing.

In detail, the process implementation in the test setup comprises the following essential consecutive steps, which are implemented in the software to control the actuators of the slurry-based 3D printing test setup:

1. The printhead moves to a starting position in the y-direction (y-axis movement).
2. The coater moves to a starting position in the x-direction which is one end of the build platform (x-axis movement).
3. The layer height is adjusted to the prescribed value (z-axis movement): 50 µm or 75 µm.
4. Slurry material is supplied motionless during the pre-load time (slurry feed).
5. Slurry material is spread along the build platform (x-axis movement, slurry feed).
6. The coater is cleaned by swaying it back and forth above a rotating coater cleaning roller (x-axis movement).
7. The layer is dried for a prescribed drying period (IR-heater): 15 s, 35 s, 55 s, or 75 s.
8. The slice data for the respective layer are loaded.
9. The printhead is shifted by a prescribed distance in accordance with modified sliced data to avoid the accumulation of nozzle defects throughout the total part/ specimen height (y-axis movement).
10. The build platform is lowered by 1 mm (z-axis movement).

11. The printhead is purged, and the nozzle plate is cleaned from binder residuals to enable good printing image qualities.
12. The printhead moves back to the starting position together with the coater. The binder is selectively applied onto the dried layer (x-axis movement).

Those steps are repeated until the print reaches its prescribed full height. The drying intensity, or radiated power, is set to a prescribed power adjustment voltage of 3.8 V, 4.2 V, or 4.6 V (chapter 4.4.3) prior to starting the print job using a hardware control dial.

4.3 Process Specifications

An overview of the process chain investigated herein is given in Figure 4.6. The slurry-based binder jetting process step plays a key role within this elaboration and is most intensively studied in the experimentation. However, the post-processing steps of curing, wash-out, and sintering are to be adapted to suit the material system and integrated into the experimental studies to allow for a consistent characterisation of the specimens' properties. The application of ceramic cores in casting technology involves the process steps of mould assembly, casting, and de-coring. Those are demonstrated subsequently in a proof-of-principle trial (chapter 6) using the 3D printing parameters elaborated hereinafter (chapter 5). This chapter focuses on the process specifications enabling reliable process control. It states the process modules, their characteristics, and the constants utilised for conducting experiments on the layer-wise drying process. The crucial parameters or configurations used are marked in **bold** to facilitate fast perception.

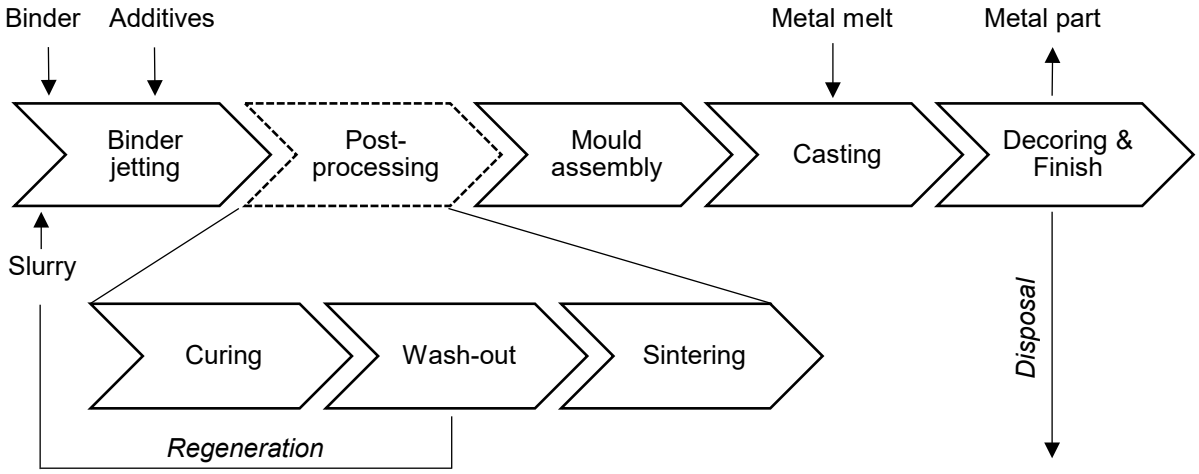

Figure 4.6: Simplified schematic process chain of indirect metal AM using slurry-based 3D printed cores and corresponding material flow.

4.3.1 Slurry-Based Binder Jetting

The process sequence of slurry-based 3D printing realised in the test setup is described in chapter 4.2 and illustrated in Figure 4.5. Sorption-capable **calcium silicate boards** (MONALITE® M1T, Etex Building Performance GmbH, Ratingen, Germany) are used as substrates for layer casting. The slurry container is filled with **250 ml of slurry**, which is sufficient for a build-up of 10 mm.

As typical for powder-based binder jetting also, starting layers are applied before printing the first layer to allow for uniform and consistent conditions throughout the print job. In slurry-based binder jetting, starting layers ensure not only the homogeneity of layers but also the compensation of shrinkage due to solvent evaporation and, thus, the dimensional accuracy in the building direction. The number of starting layers required for the desired shape is calculated from (2.10). The maximum shrinkage ratio SR_{max} to be considered here equals the liquid proportion of the slurry used (55 vol-%). The actual thickness of the 11th layer after drying $T_l(11)$ is calculated to reach a minimum of 99.86 % of the preset value, which is 49.93 µm for 50 µm, and 74.90 µm for 75 µm layers. From layer 11 on, the lower and upper layers already show a comparable thickness. **Ten base layers** are thus considered sufficient concerning the dimensional accuracy of specimens and kept constant throughout the experiments. Since the slurry's liquid phase drains into the subjacent porous layers straight after its outflow from the coater, no horizontal shrinkage is apparent.

The **slurry pressure is set to 0.95 bar**. For technical reasons, a delay of slurry outflow occurs during pressure build-up using pneumatic control elements. Hence, a constant **pre-load time of 800 µs** is set, which is the minimum time needed to form a slurry front using the implemented hardware as determined experimentally. The pre-load time avoids the so-called saw-tooth effect occurring in case the coater is already moving before the gap height is covered by slurry through the entire length of the coater. The slurry is supplied and fed through the coater prior to its movement by applying the pre-load time.

Since the coating unit is guided on only one machine side shaft and carries not only the coater but also the printhead, the printhead control unit, and, in particular, the IR heater as an overhung load, oscillating forces can occur. The test setup was found to operate close to the resonant frequency at low coater velocities, resulting in higher average roughness depths (e.g. Rz > 20 µm for velocities < 40 mm/s). Figure 4.7 visualises macroscopic observations at different coating velocities under the same drying conditions. Periodic irregularities were detected at velocities lower than 100 µm. A coating velocity of 100 mm/s was found to go well with a layer thickness H of 50, or 100 µm. By contrast, a fragmentary filling of the layer during coating was found at a velocity of 120 mm/s. Thus, the **coating velocity u is set to 100 mm/s**.

(a)	(b)	(c)	(d)	(e)
u = 40 mm/s;	u = 80 mm/s;	u = 100 mm/s;	u = 100 mm/s;	u = 120 mm/s;
H = 100 µm	H = 100 µm	H = 100 µm	H = 50 µm	H = 50 µm

Figure 4.7: Determination of a suitable coating velocity at identical drying conditions (target layer temperature of 70°C). (a)-(b) Periodically visible impurities at low coating velocities due to oscillating forces in the test setup; (c)-(d) no visible inhomogeneities at a coating velocity of 100 mm/s; (e) incomplete layer at a velocity of 120 mm/s.

Since a high selectivity of the print was found during the production of specimens, the y-axis and the image shift mechanism were installed for the production of higher specimens and parts only, intending to achieve higher image qualities using the same printhead installation. Hence, steps 1 and 9 of the process sequence specified in chapter 4.2.2 apply only to experiments described in chapter 6.

Table 4.2 summarizes the process parameters kept constant throughout this work. The velocities of the respective axes are also set constant during the process: The **velocity of the x-axis is set to 100 mm/s** following the coating velocity for all further movements. The **velocities of the y- and z-axis are set to 1 mm/s**. A **printhead voltage of 75 V** results in a stable droplet mass of 33 ng. For quality purposes, the average weight of a droplet is measured by weighing 128 x 50000 droplets prior to each print using the balance Practum 513-1S (Sartorius AG, Göttingen, Germany). Moreover, the number of clogged nozzles is counted by passing a paper strip under the printhead activated for a defined number of droplets (2000 per nozzle). The printhead condition is rated sufficient if the measured droplet mass complies with a tolerance of ±10 % around the value of 33 ng and less than 10 of 128 nozzles do not perform as intended. Since the printhead angle is fixed in the test setup, the **printhead resolution in the y-direction is 140 µm**. However, the printing resolution in the x-direction can be adjusted in the software. The binder content can be set by adjusting the printing resolution in the x-direction. The binder system's central function herein is the mapping of the contour. Therefore it must be primarily ensured that the layers are properly bonded to sufficient handling strength and dimensional accuracy. Since only a green part to be sintered is printed, the final mechanical properties of the casting cores are adjusted in the sintering process.

A binder-to-powder ratio of 11 wt.-% is set (assuming a bulk density of 1.4 g/cm³ from Erhard et al., 2021), resulting in a **printhead resolution $res_{x,50}$ of 20 µm for layer heights of 50 µm, and $res_{x,75}$ of 30 µm for layer heights of 75 µm**. When substracting the volatile proportion of the binder, a binder-to-powder ratio of 1.25 wt.-% remains. A green body thus contains a total proportion of organics of < 2 wt.-%.

Table 4.2: Overview of process parameters set constant.

Constant	Value	Unit
Number of base layers	10	-
Slurry pressure	0.95	bar
Pre-load time	800	µs
Coating velocity	100	mm/s
Printhead voltage	75	V
Binder-to-powder ratio	11	wt.-%

4.3.2 Curing & Wash-Out

An appropriate curing temperature is to be found to ensure a strong cross-linking network in the binder. The curing agent used is Hexamethylenetetramine, a reaction product of formaldehyde and ammonia able to split off those substances in a reverse reaction. The degree of cure describes the number of crosslinking points compared to its theoretical maximum possible number. Since the curing process is time- and temperature-dependent, and crosslinking may be superimposed by thermal decomposition, it isn't easy to specify the degree of cure. Hence, no characterisation method is available to directly determine the cross-linking point arrangement. (Pöhlmann, 2006, pp. 18–24) Consequently, the property of three-point bending strength is experimentally determined at different curing temperatures to allow for an application-specific evaluation of curing.

For this purpose, sand specimens of the dimensions 22.4 x 22.4 x 172 mm from a foundry-specific standard (BDG-Richtlinie P72) are produced by compacting a sand-binder mixture in a mould. Five specimens are generated for each curing temperature: 220 °C, 260 °C, and 300 °C. The standard foundry sand GS14 RP (Strobel Quarzsand GmbH, Freihung, Germany) is used. The mass ratio of novolak resin to sand is set to 2 %. All specimens are cured for 1 h in the muffle furnace LE14/11/R7 (Nabertherm GmbH, Lilienthal, Germany). Figure 4.8 shows the specimens' colour change towards dark brown, and the respective three-point bending strength determined based on the appropriate foundry standard (BDG-Richtlinie P71) on Zwick Z020 universal testing machine (ZwickRoell GmbH & Co. KG, Ulm, Germany).

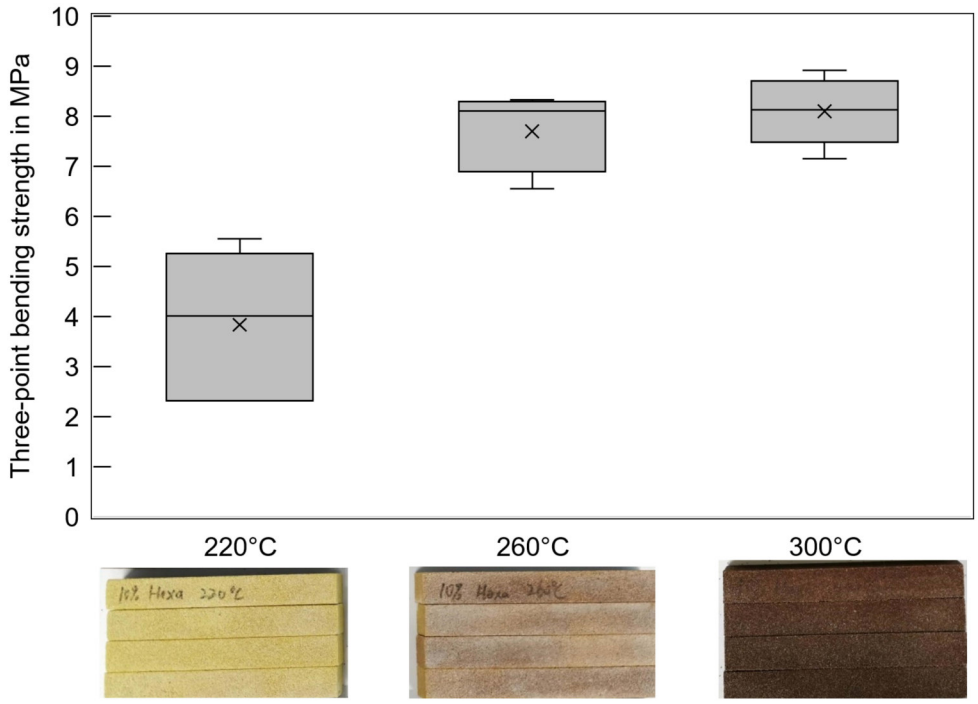

Figure 4.8: Three-point bending specimens cured at different temperatures for 1 h.

The high dispersion of the bending strength values for the curing temperature of 220 °C provides evidence that the cross-linking reaction is still ongoing at 220 °C after the curing time of 1 h. At a curing temperature of 260 °C, the strength is set to double compared to 220 °C, whereas the standard deviation is halved. Further, minor achievable strength and standard deviation improvements are detected for a curing temperature of 300 °C. However, the dark brown colour indicates conversion reactions that do not initiate further molecule growth. According to Pöhlmann, 300 °C is the onset temperature of thermal decomposition (Pöhlmann, 2006, pp. 19–20). Hence, a **curing temperature of 280 °C for 1 h** is prescribed.

Whereas in powder-based 3D printing the unprinted regions can be easily cleared from loose powder, powder beds fabricated by slurry-based 3D printing show relevant cohesive strengths. Grau (1998) found the redispersion behaviour dependent on the number of particle-particle contacts, which, in turn, varies inversely with the cube of the respective particle size. Thus, part retrieval is a major challenge, and the redispersion behaviour of the powder bed and its sintering characteristics must lead to an acceptable trade-off. (Grau, 1998, pp. 69–75)

The slurry composition's small portions of organics (see chapter 4.1.1), e.g. polysaccharides, inhibit the redispersion behaviour. Figure 4.9 compares the redispersion behaviour of powder bed samples cured in the muffle furnace LE14/11/R7 (Nabertherm GmbH, Lilienthal, Germany) for 1 h. The samples are put in a water bath and found to dissolve into smaller flakes after treatments at higher curing temperatures. An influence of the organic slurry additives on the redispersion behaviour is thus evidenced. However, all specimens form plate-like structures

instead of being redispersed homogeneously. The need for a material-specific wash-out process that accounts for anisotropies within the layer-wise built-up specimens is thus indicated. The part retrieval process is considered particularly important regarding an overall economic process, as well as to allow for the fabrication of complex, hollow casting core structures. **Thus, the wash-out during the drying process evaluation (chapter 5) is conducted by placing the cured and cooled-off powder bed in a water bath, manually brushing off powder residuals from the specimens, and drying the individual specimens from water at 50 °C for 5 h.** Further investigations of the wash-out of complex geometries are shown in chapter 6.1.2.

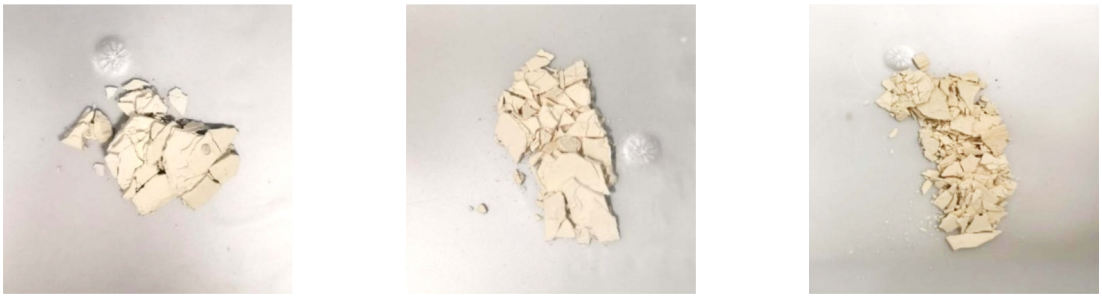

Figure 4.9: Qualitative comparison of the redispersion behaviour of a powder compact in water after thermal treatment. The degree of shattering is found to raise with increasing curing temperatures.

4.3.3 Sintering

A sintering process tailored to the prescribed slurry system is developed at Fraunhofer ISC/ Center HTL. The raw materials used in this study comply with the material system QS6 (Figure 4.10). Further optimisation regarding processability in slurry-based 3D printing and shelf life includes variations of the solid content and viscosity modulating agent content only.

Vogt et al. (2021b) analysed QS6 slip-cast specimens by thermooptical measurements and sintering tests. While sintering at a temperature of 1200 °C for 5 h led to low bending strength of approx. 4.5 MPa, a decisively improved strength was found when raising the sintering temperature to 1300 °C. Further improvements in strength were proved feasible when adding kaolin as a sintering aid. (Vogt et al., 2021b, pp. 33–35)

Studies on slurry additives, raw materials, and the sintering process exceed this study's scope. Inflation of approx. 0.7 % caused by cristobalite formation was measured for specimens from slurry QS6 (Figure 4.10a) sintered at 1300 °C for 5 h instead of shrinkage. The target **sintering temperature is set to 1275 °C, and the dwelling time to 5 h** to account for this overmodulation.

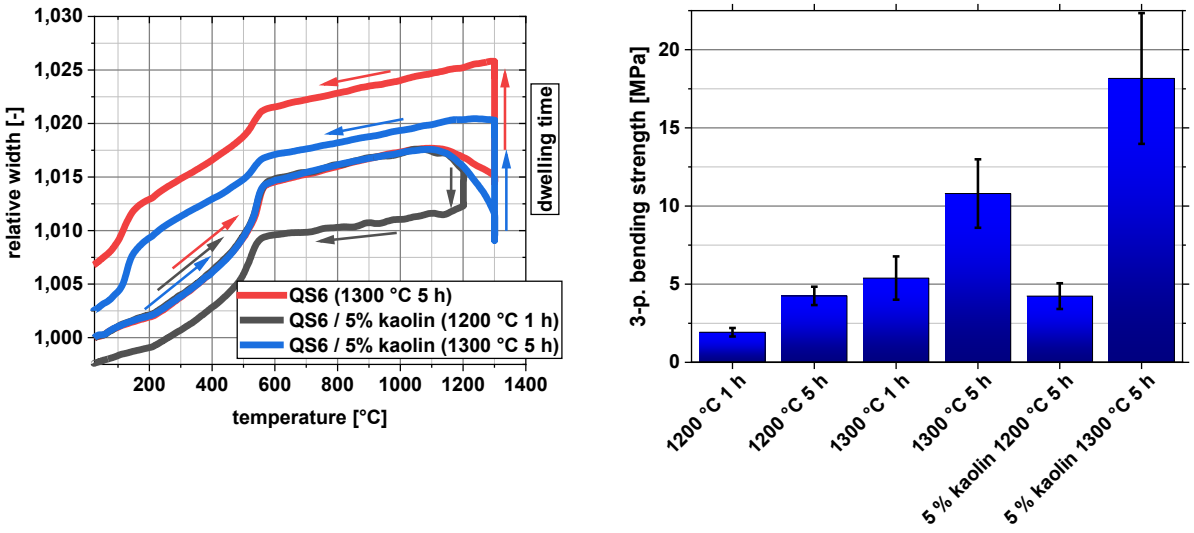

(a) (b)

Figure 4.10: Results characterising the sintering behaviour of a similar slurry composition QS6: (a) in-situ analysis of thermal treatment cycles with and without kaolin as a sintering aid. (b) Three-point bending strength of specimens fabricated by slip-casting, sintered at different temperatures and dwelling times (Vogt et al., 2021b, pp. 34–35).

Sintering is performed in the Top 60 furnace (Nabertherm GmbH, Lilienthal, Germany) on the following course: Debindering is accomplished by heating up using a low heating rate of 60 °C/h until a temperature of 650 °C is reached. From 650 °C to 1275 °C, the temperature is raised by 150 °C/h. After the dwelling period of 5 h, the furnace is cooled down at a cooling rate of 150 °C/h as long as procurable without active cooling. Further investigations on the sintering behaviour of slurry-based 3D printed specimens are shown in chapter 6.1. The prescribed sintering course and the actually occurring temperature course are visualised in Figure 6.12a.

4.4 Experimental Configuration

The central task of the present work is to elaborate a qualitative, deterministic process model relating target product properties of ceramic casting cores to configurable process variables in the layer-wise drying process. By identifying the respective cause-effect chains when processing a water-based slurry system, a systematic understanding of the effect of different input variables on critical quality attributes in the production process is to be gained. Moreover, the collation of experiences on the process capability and performance aims at tailoring a slurry-based 3D printing process to the requirements in the field of indirect metal AM.

4.4.1 System Description

Figure 4.11 depicts the system description of the investigation described herein: the process modules appear in the centre of the illustration with input values on the left and output values on the right sides. The qualitative process model to be developed will describe relationships between the process factors and their effects on process efficiency and the material properties, as highlighted in **bold**.

Chapter 2.3.2 presents the fundamentals of drying theory that provide the basis for the investigations on the layer-wise drying process in slurry-based 3D printing conducted herein. By specifying the process variables pursuant to the research hypotheses presented in chapter 3, the relationships known from drying theory concerning single layers are incorporated into this study to confirm their validity in slurry-based 3D printing.

Cracks are formed by stress resulting from shrinkage. The magnitude, as well as the direction of the effect of stress, vary with the drying conditions. Both absolute and differential shrinkage is to be considered due to their interference with crack formation. The magnitude of stress is known to increase in proportion to the thickness of a layer and the rate of evaporation, meaning that stress development is reduced when applying thinner layers and drying slowly. Differential strain forms due to dissimilar compression of saturated and surface-near regions and develop either in an early or a late stage of drying in contradicting directions. Hence, varying the process parameters of layer thickness, drying intensity, and drying period is considered appropriate to study the quality-critical process step of drying. Since the capillary pressure affected by a layer's permeability is known to induce flaws, an interaction of those process variables must be carefully observed.

Temperature measurements continuously monitor the binder jetting process. Figure 4.4b displays the measuring points used for in-process monitoring. The thermocouple identifies the absolute temperature evolution on the lower end of the building area. The pyrometer sensor allows observation of the respective layer surface's IR emissions. The author's previous contribution (Erhard et al., 2021) demonstrated process control via layer temperature. Herein, pyrometer measurements are only utilised for in-process monitoring and quantification of the duration of the individual sub-processes or machine movements, enabling reliable conclusions on the cycle times.

Key characterisation methods involve the measurement of density, four-point bending strength and elongation at break. The density is considered decisive for assessing the compaction. The probability of the appearance of cracks or major flaws can be evaluated by analysing the four-point bending strength. The observations are to be backed up by microscopic examinations. The

emerging spill-over effect of binder migration dependent on the drying conditions is observed by measuring the dimensional accuracy. Surface roughness measurements allow for a first evaluation of the future application areas of slurry-based 3D printed cores in the casting industry.

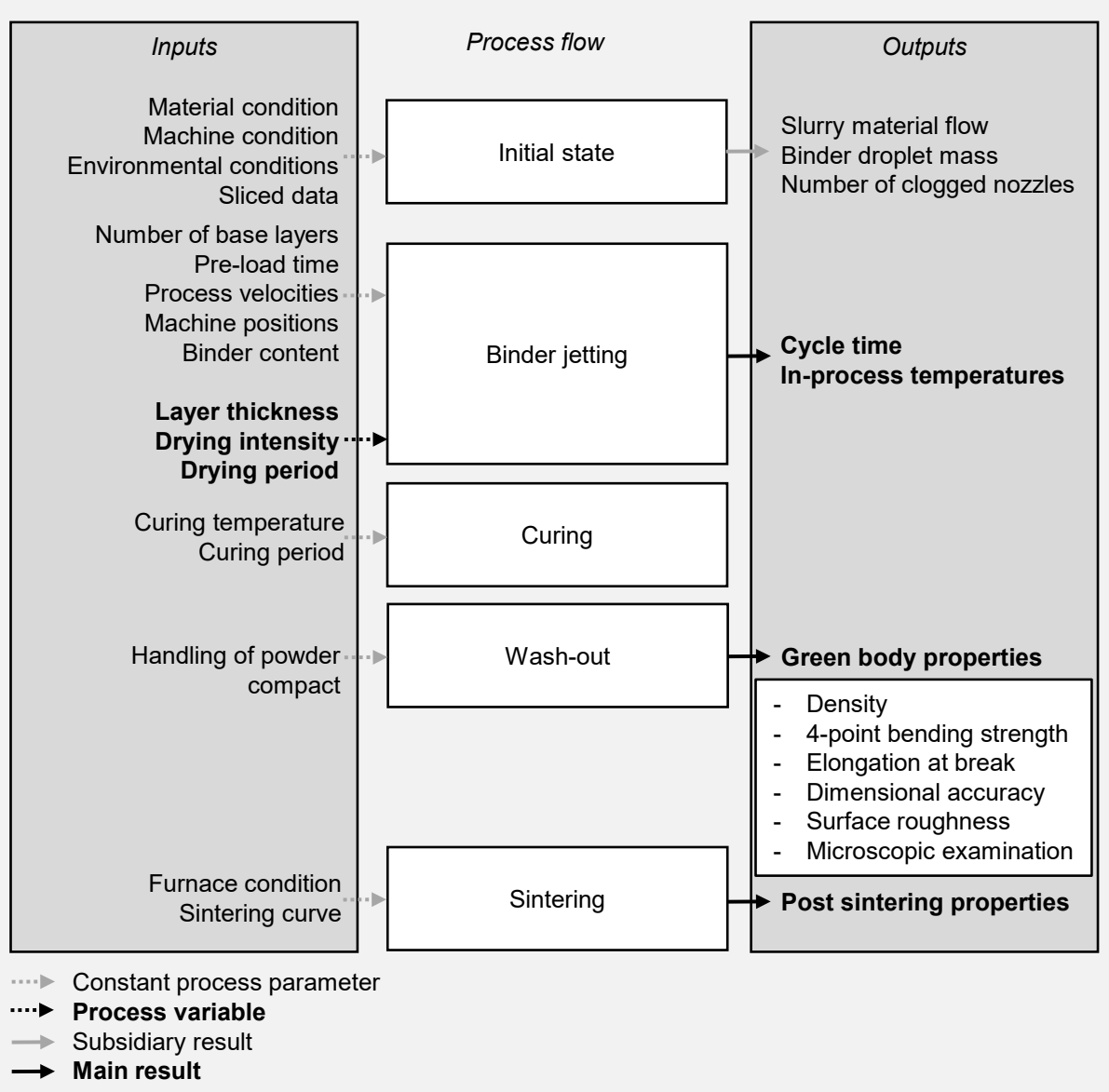

Figure 4.11: System description.

4.4.2 Specimens' Geometries

The shape of the test specimen A (Figure 4.12a) to be used is specified as a cuboid of 2.5 x 2 x 25 mm in analogy to standard DIN EN 843-1, embodiment A. The standard commonly applies to advanced technical ceramics and specifies methods for determining the nominal bending strength of monolithic high-performance materials at room temperature. Specimen type A is used to evaluate dimensional accuracy, density, four-point bending

strength, surface roughness, and microstructure and is thus the key type of specimen within this investigations. All measurements are conducted on the same set of specimens for each experimental run. Hence, the determined properties can be easily allocated and compared with each other in chapter 5.2.

Specimens B (Figure 4.12b, right) are cylinders with a diameter of 5 mm and a height of 10 mm. Those are used for conducting thermooptical measurements and measuring the density using the principle of Archimedes.

Specimens C (cylinders with a diameter of 11 mm and a height of 2 mm as illustrated in Figure 4.12b, left) allows for measuring the thermal conductivity and sintering activity. The investigations on the sintering behaviour are described in chapter 6.1.3.

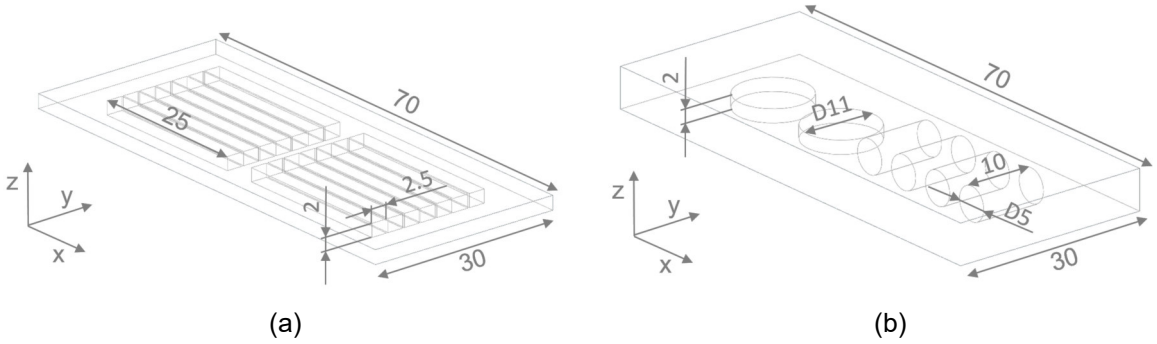

Figure 4.12: Specimens used for the experiments in this work and their orientation in the build volume. (a) Specimens A, (b) specimens B (right), and specimens C (left).

4.4.3 Experimental Design

A factorial experiment concept involves runs on all possible level combinations of the factors used. A full factorial approach is conducted herein. Hence, the interaction between all factors is included in the investigation. (Montgomery, 2009, pp. 4–7)

Three factors are being considered for the experiment that impact the drying conditions in slurry-based 3D printing. Table 4.3 shows an overview of those together with the respective levels, leading to a total number of 24 runs. To collect observations on the layer-wise drying process to the fullest extent, the factors are studied at 2, 3, or 4 levels, depending on the range of the process window. However, conventional full factorial designs suggest an identical number of levels for each factor (Antony, 2014, p. 63). The process window has been determined together with the factor's responses in preliminary screening studies (e.g. Erhard et al., 2021). It represents the limits of stable processing on the test setup utilised. The drying intensity is indicated as the IR power adjustment voltage PAV corresponding to a specific radiated power. The radiated power has been determined by the power meter HLP-200B (Jilin Yongli Laser Technology Co., Ltd., Changchun, China).

Table 4.3: Overview of process variables for investigating the layer-wise drying process.

Process variable	Level 1	Level 2	Level 3	Level 4
Layer thickness	50 µm	75 µm	-	-
PAV	3.8 V	4.2 V	4.6 V	-
Radiated power	0.73 W/cm²	0.97 W/cm²	1.18 W/cm²	-
Drying period	15 s	35 s	55 s	75 s

Each run is conducted under the same experimental conditions. In each run, 14 specimens are printed: 7 for analysis in the green state and 7 for analysis in the sintered state (Figure 4.12a).

4.4.4 Material Characterisation Methods

Reliable material characterisation methods allow for a quantitative determination of material properties and, thus, objective comparisons of technological properties. Those enable the targeted development and optimisation of materials, processes, and products. In Chapter 2.2.5, requirements on the properties of casting cores and standard characterisation methods are specified. Flemming, Tilch (1993) sum up the basic requirements of moulding materials: mechanical strength, thermal stability, dimensional accuracy, and surface quality. Hot distortion is a typical fault that can arise when exposing filigree cores produced from sand-binder mixtures to elevated temperatures and mechanical loads during casting. The process investigated herein involves a sintering step and, thus, a sustained high-temperature operation. During sintering at 1275 °C, no creep is observed. Even a long-term exposure to 1650 °C only causes minor deformation, implying the possibility of application in steel casting. However, the hot distortion of sintered ceramic casting cores is not relevant in aluminium casting applications due to the low pouring temperatures (< 800 °C) and is not further analysed herein.

This work processes a material system not yet utilised in casting applications. Furthermore, until now, no common standards exist in testing specimens fabricated by the slurry-based 3D printing process. Hence, the specimens and the testing methods are adapted, taking into account application-specific requirements and established standards on a cross-application basis. The following section presents the characterisation procedures utilised within this work.

Dimensional Accuracy

The length of the green or sintered cuboids (specimens A) and the dimensions of specimens B and C are measured using a standard calliper gauge (DIN EN ISO 13385-1, reading accuracy

0.01 mm, tolerance 20 µm). The cross-section is determined using a micrometre (DIN 863-1, reading accuracy 0.01 mm, tolerance 2 µm).

Density

The weight m is determined by a Secura 125-1S analytical balance (Sartorius AG, Göttingen, Germany). It shows a linearity of 0.1 mg and a repeatability of 0.02 mg. The density ρ follows:

$$\rho = \frac{m}{V} \tag{4.1}$$

The density of specimens A is determined directly by measuring the specimens' weight and their dimensions based on DIN EN ISO 18754, method B, after drying to constant mass (uncertainty of measurement 1%). Specimens B are analysed for their particle density PD, open porosity OP, and bulk density ρ using the principle of Archimedes:

$$PD = \rho_{H2O} \frac{m_{dry}}{m_{dry} - m_{floating}} \tag{4.2}$$

$$OP = \frac{m_{wet} - m_{dry}}{m_{wet} - m_{floating}} \tag{4.3}$$

$$\rho = PD \cdot (1 - OP) \tag{4.4}$$

This method is recommended for highly reliable density determinations. Here, Spierings et al. (2011) found a measurement accuracy and repeatability of ±< 0.1%.

Four-Point Bending Strength

Inherent flaws rule the mechanical behaviour of ceramics. Since the size distribution of flaws is decisive for failure, a considerable scatter is characteristic to occur in strength testing of ceramics. Moreover, since the likelihood of the occurrence of a major flaw in a larger body is higher, the strength of a ceramic part is always dependent on its absolute size. Due to stress concentration in flaws, failure in ceramics occurs in tension rather than compression. Hence, compressive fracture strength is typically 10-15 times higher than tensile fracture strength. Though tensile testing is an uncommon procedure for ceramics due to their brittleness and difficulties in the specimens' preparation and the alignment in the testing machine relating thereto. Instead, bending testing enables a cost-effective determination of tensile strength using simple sample geometries. (Carter, Norton, 2016, pp. 304–313)

Three- and four-point bending setups using cuboid specimens are most commonly used to determine uni-axial tension in ceramics. Since a comparatively low portion of the specimen is exposed to the maximum stress in three-point testing, ASTM C1161-18 recommends four-point

flexure testing for most material characterisation purposes. Though, three-point flexure testing offers the advantage of the simplicity of test fixtures and application procedure (ASTM C1161-18). The adequacy of uni-axial bending testing is discussed controversially in scientific literature. Compared to bi-axial bending testing, where the load is applied on a disc-shaped specimen supported by balls or rings, the effective surface area is smaller (Börger et al., 2002, pp. 1425–1428), and there is a risk of measuring the edge effects modifiable during finishing (With, Wagemans, 1989, p. 1538). However, numerous difficulties are associated with the testing assemblies or the proper use of the analytical equations – uni-axial testing is the widely performed standard in strength testing of ceramics (Morrell, 2007). Both three-point and four-point testing have evolved into popular characterisation methods for additively manufactured ceramics (Lakhdar et al., 2021, pp. 8–11). Lechner (2021) showed clearly differentiating fracture probabilities: four-point bending testing leads to overall lower fracture stresses, confirming that the comparatively larger volume subjected to stress is more likely to contain a major flaw or critical stress concentration (Lechner, 2021, pp. 73–74).

Four-point bending test is preferred over a three-point bending test here since a larger portion of the specimen is subjected to the bending moment applied – with regard to much higher effective volumes in the industrial application of casting cores. The four-point bending strength is determined based on the standard DIN EN 843-1 using the Inspekt table 100kN universal testing machine (Hegewald & Peschke Meß- und Prüftechnik GmbH, Nossen, Germany) and a 5 kN load cell (accuracy class ISO 7500-1).

Surface Roughness

The surface roughness of the sintered cuboids (specimens A) is measured on the specimens' lower surfaces parallel to the coating direction using the MarSurf M400 surface measuring instrument (Mahr GmbH, Göttingen, Germany) and the BFW A 10-45-2/90° probe arm.

Homogeneity and Defects

Micrographs are captured using a BX53M microscope (Olympus Europa SE & Co. KG, Hamburg, Germany).

Sintering Behaviour

Specimens B are utilised in the green state for the in-situ analysis of the sintering behaviour. Figure 4.13a shows the basic layout of a thermooptical measurements (TOM) device as developed at Fraunhofer ISC/ Center HTL. The design variant TOMMI_last is used, allowing for the in-situ analysis of the relative width of specimens on a measurement uncertainty of

0.4 µm. Since the investigated process follows a layer-wise buildup strategy, the physical characteristics of specimens differ, corresponding to the orientation on the build platform. In order to analyse the anisotropic shrinkage behaviour, the specimens' relative dilation is investigated both parallel and orthogonal to the layer interfaces (Figure 4.13b) on identical temperature courses using heat-up and cooling rates of 2 – 5 K/min and a dwell time of 1 h.

In addition, specimen C is used to determine the thermal diffusivity during heat-up to 1300 °C using a TOM device. The measurement allows for parallel analysis of the debinding progress and the onset of sintering.

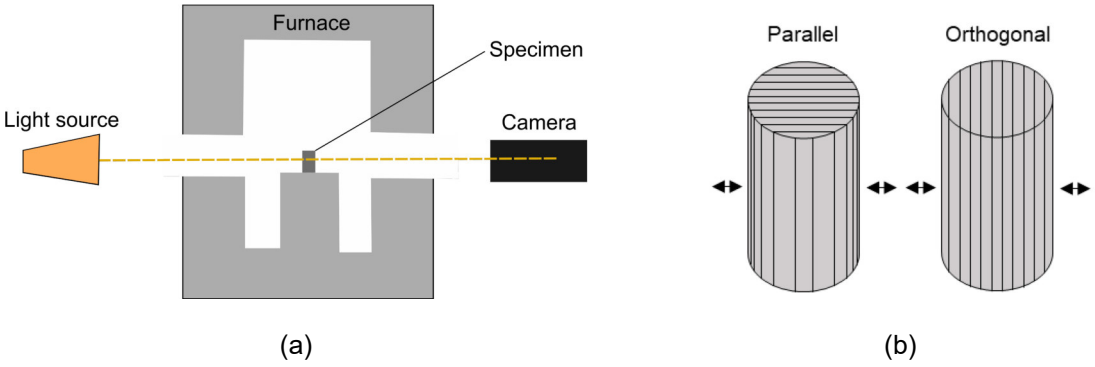

Figure 4.13: (a) Basic layout and measurement principle of a thermooptical measurement (TOM) device (after Vogt et al., 2022), (b) Schematic representation of the direction-dependent investigation of shrinkage using 3D printed cylindrical specimens.

4.4.5 Statistical Analysis

Comparisons are drawn for data assessed at different levels, and a statistical analysis is conducted by applying the "Analysis of Variance" method, also known as ANOVA. More precisely, a single-factor ANOVA for the fixed effects model is applied. In statistical inference, ANOVA is a procedure utilised for testing the equality of treatment means. The single-factor fixed effects model describes the response variable y_{ij} as a linear function of the model parameters:

$$y_{ij} = \mu + \tau_i + \varepsilon_{ij} \begin{cases} i = 1, 2, \dots, a \\ j = 1, 2, \dots, n \end{cases} \tag{4.5}$$

With the constant μ, the treatment or level effects τ_i and the random error ε_{ij}. (Montgomery, 2009, pp. 63–64)

The model errors are assumed to be normally distributed random variables with a mean zero and a variance s^2 constant for all levels. Thus, for hypothesis testing, the observations are presupposed to be mutually independent. (Montgomery, 2009, pp. 63–70)

The P-value approach is adopted here, assessing the significance level of null hypothesis truth. The P-value is the smallest level of significance, leading to a rejection of the null hypothesis. In engineering sciences, a fixed significance level testing is frequently applied, rejecting the null hypothesis to be tested at a specified level of typically $5 \cdot 10^{-2}$. The P-value is the probability of finding results at least as extreme as the observed value of the statistic when the null hypothesis is true. Hence, it gives additional information on the weight of evidence against the null hypothesis and enables an analysis of data without formally preselecting a level of significance. (Montgomery, 2009, p. 38) The P-value allows for reasonable conclusions about making a Type I error (a false positive finding) by rejecting the null hypothesis. A P-value of $5 \cdot 10^{-2}$, which still is the common standard criterion for significant findings, means that the null hypothesis is falsely rejected in 5 % of the analyses. (Travers et al., 2017, pp. 210–211) Schmidt, Osebold (2017) anticipate a specific quality of significance according to Table 4.4 that is used for the assessments within this study.

Table 4.4: P-values and the related significance levels (after Schmidt, Osebold, 2017, p. 154)

P-value	Significance Level
$P > 5 \cdot 10^{-2}$	Not significant
$P \leq 5 \cdot 10^{-2}$	Significant
$P \leq 1 \cdot 10^{-2}$	Very Significant
$P \leq 1 \cdot 10^{-3}$	Highly Significant

The P-value resulting from ANOVA is incorporated in the respective data visualisations together with the number of specimens n each boxplot refers to.

4.5 Coating Simulation

This section introduces the CFD model and simulation setup developed for simulating the slurry-based layer casting process with a significant contribution of Alexander Seidel's master thesis (appendix A2), supervised by the author. It has been published previously, together with the results shown in chapter 5.1 in Erhard et al., 2022.

To the author's knowledge, there is no published work by other researchers on numerical simulation of the slurry-based 3D printing process, nor on the subprocess stage of slurry-based layer casting. Thus, this elaboration builds upon recognitions from tape casting, which is the manufacturing method with the maximum overlap with the subprocess investigated herein. Tape casting is a wet forming technique where the ceramic slurry is spread over a surface using

a doctor blade to form a thin layer (Jabbari et al., 2016, pp. 1–2). The resulting layer properties in tape casting depend on similar parameters like a slurry's rheological behaviour, layer height, and coating velocity. In contrast, this work aims to develop a slurry device for selective instead of continuous application of slurry, as proposed previously by Yen (2015).

4.5.1 System Description

The CFD model based on the open-source environment OpenFOAM developed by OpenCFD Ltd. aims at predicting the homogeneity of a cast slurry layer with defined parameter sets or coater geometries using the Volume-Of-Fluid (VOF) method. Homogeneity is considered crucial to ensure stress-free drying and high surface qualities. Hence, the CFD approach is proposed to allow faster process developments in slurry-based 3D printing. The numerical solver interFoam is used in OpenFOAM in version v1912 to capture the behaviour of the two fluid phases, air and slurry, and their interface. InterFoam utilises the VOF method in combination with the Continuum-Surface-Force (CSF) method. It extends the conventional Navier-Stokes and continuity equation by adding a convection term for the volume fraction of the first phase α. (Deshpande et al., 2012) For further details on modelling multiphase flows by those methods, the author refers to specialist literature, e.g. Brackbill et al., 1992 or Nieves-Remacha et al., 2015.

As a starting point, a physical setup of a coater geometry, hereafter referred to as "waterfall coater", is given (Figure 4.14). Its ability for precise slurry application was confirmed experimentally before the simulation study. Conversely to the movement in the experimental test setup, layer casting itself is modelled by moving the substrate parallel to the slurry outflow – first, in a linear acceleration phase, and, next, in a phase of constant coating velocity.

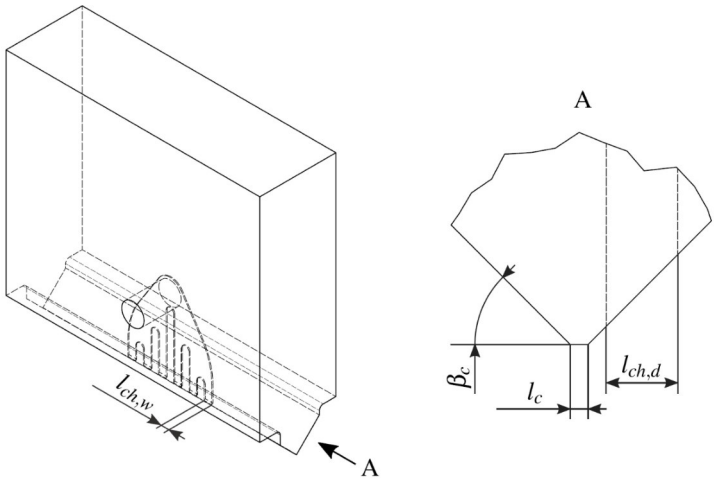

Figure 4.14: Geometry of the waterfall coater (Erhard et al., 2022, p. 44). The gaps between the channels equal the channel width of 3 mm.

The coater is fed with slurry from a pressure-tight container via plastic tubing (inner diameter 4 mm, length 600 mm). The targeted slurry outflow is to be controlled via a pressure reducing valve connected to the container. The slurry pressure p_{slurry} is set to the constant value of $9.5 \cdot 10^4$ Pa.

4.5.2 Boundary Conditions and Discretisation

To decrease the computational demand in the simulation, the pressure drop along the slurry tubing of the experimental setup for a filling height $h_{filling}$ of 70 mm of the container is calculated in a pre-processing sub-simulation. The resulting pressure at the inlet $p_{rgh,in}$ of $3.1732 \cdot 10^4$ Pa is set as a fixed boundary condition in the subsequent sub-simulation.

Figure 4.15 shows the simulation domain for a gap height h_g of 0.1 mm. An atmospheric condition is prescribed, and the noSlip boundary condition is assigned to the substrate and the cavity wall patches treating those as impermeable surfaces with zero velocity. A locally refined mesh represents the coater geometry's near-gap region, including an evaluation plane for the spatial reconstruction method (chapter 4.5.4). A velocity u is inscribed at the substrate patch for a simulation time of 2.5 s to model the coater movement.

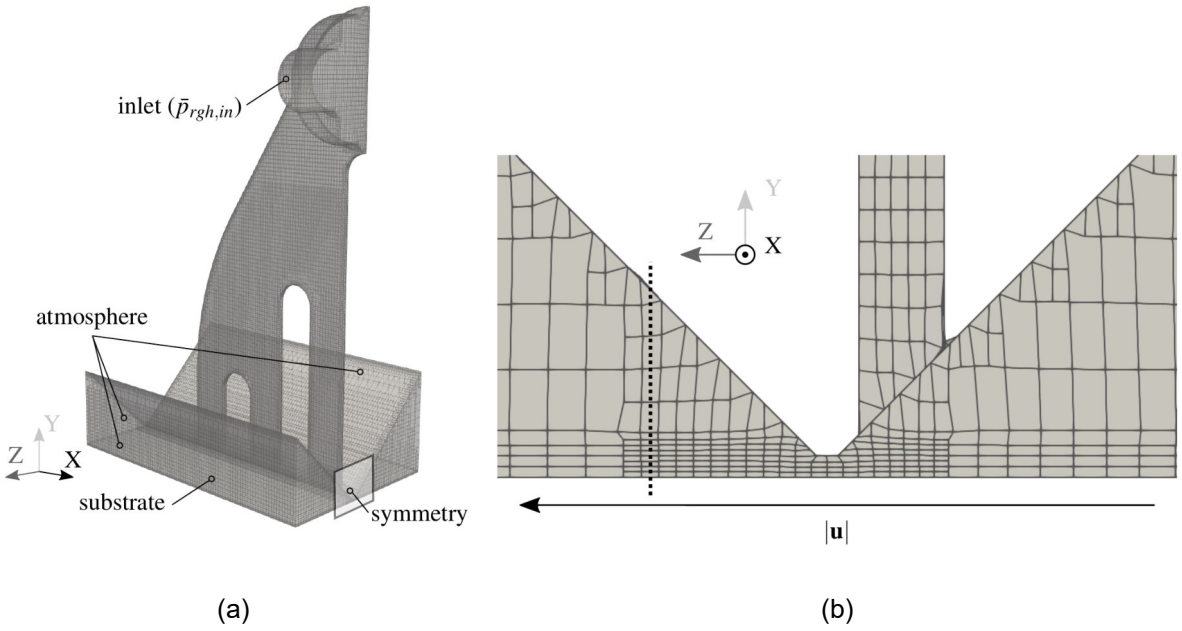

Figure 4.15: Simulation domain for the coating process. (a) Overview of boundaries. (b) The details in the near-gap region for a gap height h_g of 0.1 mm. The dotted line corresponds to the evaluation plane for the spatial reconstruction. (Erhard et al., 2022, p. 46)

4.5.3 Rheology model

Ceramic slurries are usually considered non-Newtonian fluids (Chantaramee et al., 2008, p. 3182), showing shear-thinning behaviour (Nagasawa et al., 2015, p. 1432). Hence, a power-law rheology model is applied for the slurry phase, whereas the air phase is modelled as a Newtonian fluid.

The power-law model is defined as follows (Westermaier, Kowalczyk, 2020, p. 138):

$$\upsilon = f\,\dot{\epsilon}^{q-1}, \text{ with } \upsilon_{min} \leq \upsilon \leq \upsilon_{max} \qquad (4.6)$$

with υ being the kinematic viscosity, υ_{min} and υ_{max} the lower and upper viscosity limits from experimental data gained in rheology measurements (Figure 4.1), $\dot{\epsilon}$ the strain rates. f is the consistency index numerically equal to the kinematic viscosity at a shear rate of 1/s, and q is the power-law index describing the rheology of the fluid (where q = 1: Newtonian, q < 1: shear thinning, q > 1 dilatant) (Ansari et al., 2020, pp. 2–3). Using a non-linear Levenberg-Marquardt least-squares approach, the parameters f and q are fitted to the experimental data measured employing rheometry with a root mean square error RMSE of $9.81 \cdot 10^{-4}$ m²/s. Table 4.5 shows an overview of the parameters used to model the rheology.

Table 4.5: Summary of the rheology parameters used by the interFoam solver. The properties of air are adapted and simplified from Wagner et al., 2010.

	γ in N/m	ρ in g/cm³	υ in m²/s		f in m²/s	q in -
			υ_{min}	υ_{max}		
Slurry	$7 \cdot 10^{-2}$	1.7254	$1.772 \cdot 10^{-4}$	$2.139 \cdot 10^{-1}$	$1.228 \cdot 10^{-2}$	$3.794 \cdot 10^{-1}$
Air	-	0.001	$1.48 \cdot 10^{-5}$		-	-

4.5.4 Spatial reconstruction

A method for evaluating the slurry layer quality in the entire building area is developed based on the coating simulation. The need for a high mesh resolution in the coater gap on the one hand and careful handling of economic simulation resources on the other leads to a demand for an advanced method when examining the entire length of the slurry layer (which is of magnitude 10^2 bigger than the gap height).

Figure 4.16 shows the spatial reconstruction method proposed for evaluating the entire slurry layer during short computing periods. The slurry was found to form a downstream meniscus during the deposition process before remaining within a small range. The evaluation plane is set perpendicular to the coating direction within the high-mesh resolution area but far enough

away from the coater to not be influenced by the downstream meniscus (Figure 4.15). The spatial reconstruction method evaluates the volume fraction α, herein referred to as the liquid slurry phase volume fraction, of each cell within this evaluation plane for each timestep in grayscale snapshots. Those are subsequently saved in a video file. α = 1 is described by black pixels, α = 0 by white pixels. By amalgamating the data from the grayscale snapshots and the respective positional information, a three-dimensional dataset of the α values for the reconstructed layer is generated. An isosurface can be created on which α is equal at every point. The method of spatial reconstruction is used to evaluate the surface quality of the slurry layer. The arithmetic mean roughness Ra is calculated from the resulting surface data averaged to its mean values along the coating direction representing the average surface heights in the observed area.

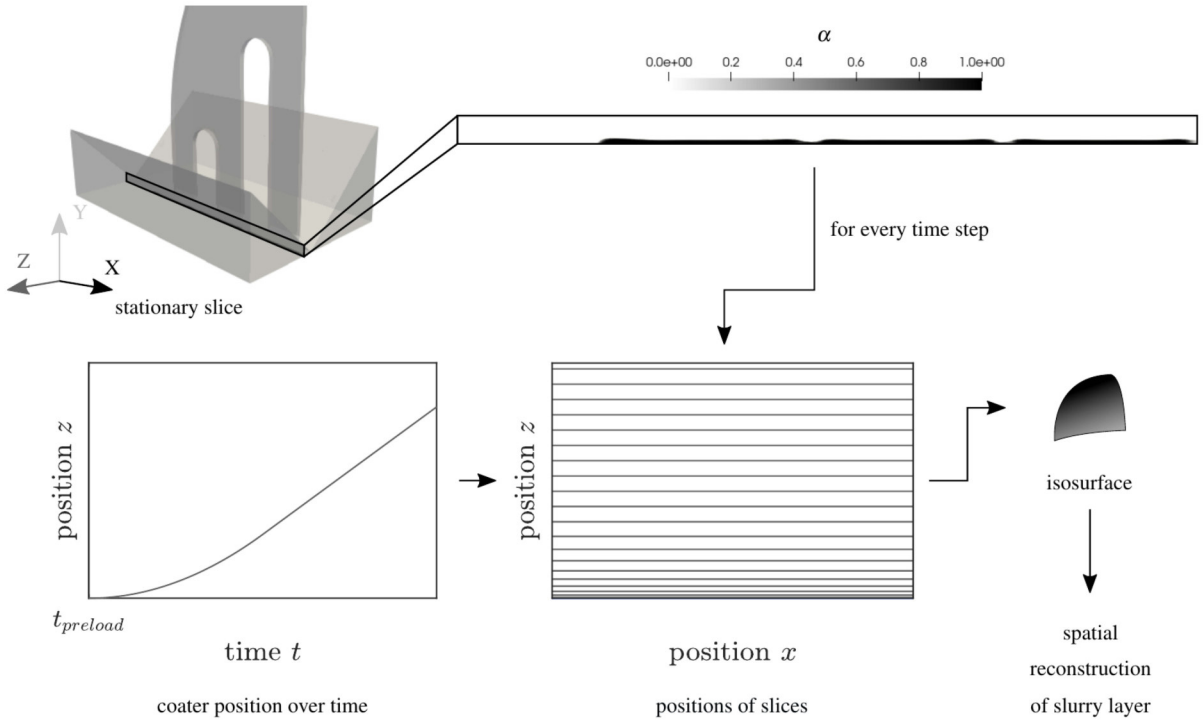

Figure 4.16: Reconstruction of a slurry layer based on temporal data (Erhard et al., 2022, p. 47).

4.5.5 Validation Approach

The slurry-based 3D printing setup, as described in chapter 4.2, is used to determine the degree of accurate representation of experimentally observed phenomenons by comparing experimental results to the data associated with the simulation models. Coating experiments, simulations and spatial reconstructions are carried out for five different parameter sets, varying the coating velocity u and the gap height h_g according to Table 4.6 and keeping the material, the slurry outflow, the drying conditions, and the building height constant.

Table 4.6: Summary of the parameters varied in the validation experiments.

Specimen/ simulation No.	u in mm/s	h_g in mm
1	55	0.1
2	65	0.1
3	80	0.1
4	95	0.1
5	97.5	0.075

Dimensioned and perspectively corrected photographs are used to compare the simulation and the experimental results. The specimens' photographs and the reconstructed outlines are saved as new image files with a resolution of $1 \cdot 10^{-4}$ mm/px and overlaid graphically. MarSurf M400 surface measuring instrument (Mahr GmbH, Göttingen, Germany) and the BFW A 10-45-2/90° probe arm are used to evaluate the surface roughness.

4.5.6 Advancement of the Coater Geometry

Since weaknesses of the waterfall coater geometry have been identified, the simulation approach described above is applied iteratively for alternative coater geometries. The advancement of the coater geometry aims to increase the process and part quality and lower the hurdles for scale-up and industrial application. In particular, improvement is proposed to reduce cycle times, increase reliability, and reduce excess material.

The initial reference geometry for advancement is a coat hanger design known from polymer sheet production (Carneiro, Nobrega, 2012, pp. 114–120, Han, Wang, 2012). The advancement process is carried out using three major iterations of the geometry: a single-step coat hanger design with sharp cavity edges, a single-step coat hanger design with rounded cavity edges, and the final two-step coat hanger with rounded cavity edges. The focus is set on adapting the distribution chamber geometry at the slurry inlet since it is a key item for minimising low-velocity regions and thus allows for stable coating.

Subsequently, the simulation methods described above are used to determine an appropriate parameter set for the new coater design.

5 Results and Discussion

5.1 Homogeneous Powder Bed Formation

Verification is the process of assessing the correctness and numerical accuracy of a model solution. By validating, the physical accuracy of the mathematical model is assessed, comparing computational results and experimental data and thus proving the credibility of a simulation model. (Oberkampf, 2010, pp. 13–14) In the following chapter, the simulation results of the computational model described in chapter 4.5 are shown based on the parameter study set up as a first validation approach.

5.1.1 Prediction of the Slurry Front Formation and Slurry Flow

Simulation No. 1 from the validation experiments is chosen as the exemplary simulation set to verify the accurate implementation of the model. The respective process parameters are listed in Table 4.6. Figure 5.1a depicts the result: the isosurface for $\alpha = 0.5$ is shown, as well as the streamlines starting in the distribution channels (coloured according to the respective velocity magnitude u). An upstream meniscus in front of the coating head forms during the preloading process. A snapshot from the experimental setup shows a similar behaviour (Figure 5.1b).

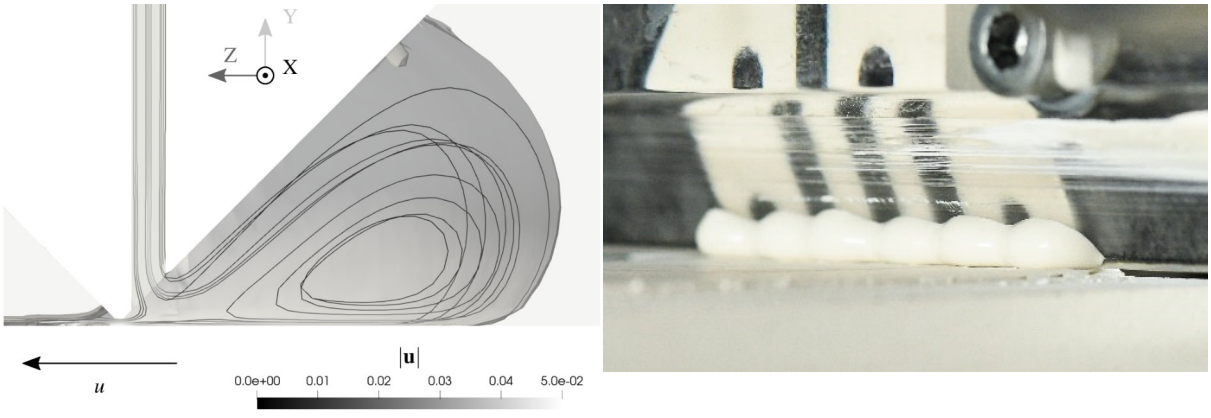

Figure 5.1: (a) Simulation result for simulation No. 1 at t = 2.25 s showing the isosurface for α = 0.5 and the streamlines within the slurry phase. (Erhard et al., 2022, p. 47); (b) photograph showing the formation of the continuous slurry front from single beads at t ~1.5 s.

By examining a single stream line, the path of recirculation of a mass-less particle is tracked. A superposition of a transversal movement – from the coater channel towards the area between two channels necessary to form the continuous slurry front – and circulation is shown in Figure

5.2, resulting in a helix shape with a time-dependent radius and slope. A particle is found to be emitted through the channel in the first place. It then circulates inside the upstream meniscus while heading transversely towards the area where no direct outflow of slurry occurs. As soon as the particle gets close enough to the substrate, it passes the coating gap and is deposited. However, since the slurry is treated as one phase only in the simulations, the spiral movement of a real particle is presumed to depend on its individual size and shape. Superimposing capillary and transverse forces caused by recirculation are expected to cause irregularities during particle settlement and may lead to lower powder bed densities. These observations are taken into account when developing an improved coater geometry.

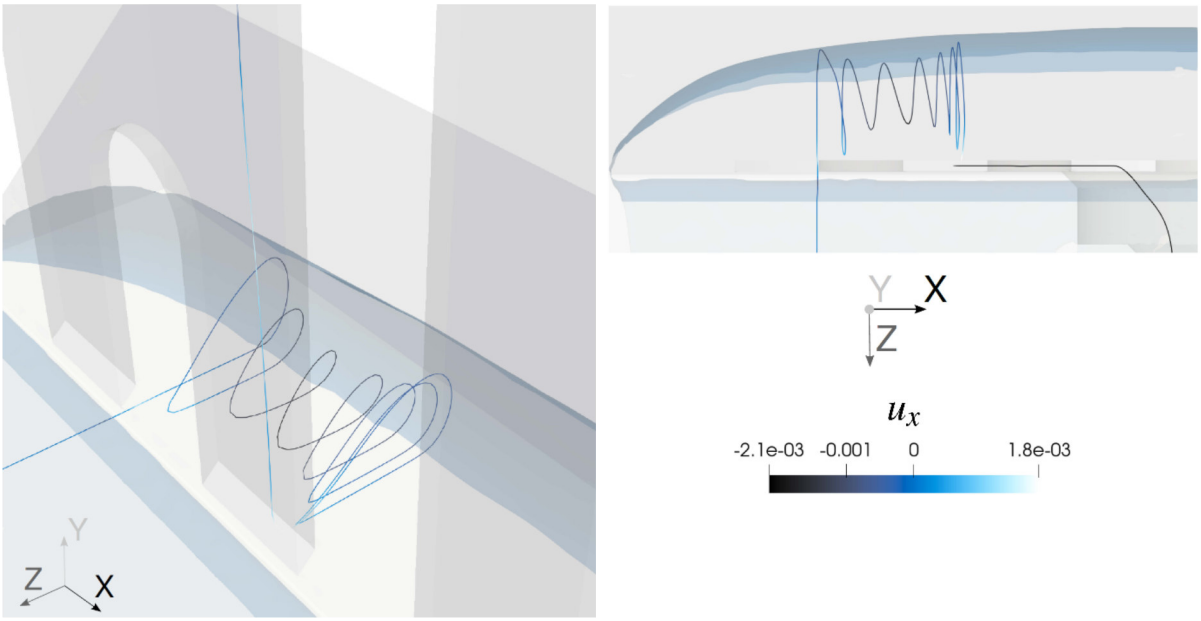

Figure 5.2: Tracking of an exemplary particle – the simulation shows a transversal circulating movement.

The pressure at the coater inlet leads to a computed flow rate of 196 mm³/s for the waterfall coater geometry, whereas experimental measurements show flow rates of 202 to 226 mm³/s. Hence, in this respect, deviations in the range of 3 - 13% are observed. Those are assigned to the relatively low accuracy of the pressure gauge (scale spacing of 0.05 bar, precision category 2.5) used. Overall, the simulation results are found to fit the experimental observations well.

5.1.2 Visualisation of the Layer Topology by Spatial Reconstruction

Figure 5.3 shows the result of the spatial reconstruction of simulation No. 1. A rugged top and bottom interface and minor holes are found. This effect is assumed to be caused by the simulation setup modelling the slurry casting on an impermeable surface. Air entrainment accumulating in front of the coating gap is suspected to occur at the flow front of the upstream meniscus, resulting in α values smaller than 1, and, thus, in holes appearing in the deposited

layer. In contrast, multiple layers are coated one by one in the real setup. A layer cast from slurry represents an absorbent substrate. Hence, it enables capillary forces to induce a microfluid flow into the underlying layers. However, the spatial reconstruction shows the fluid flow creating an outer lip higher than the centre region of the slurry layer. Since air entrainments can hardly influence the outer lip due to the boundary effects, evaluating the slurry layer width based on the spatial reconstruction method is considered justifiable.

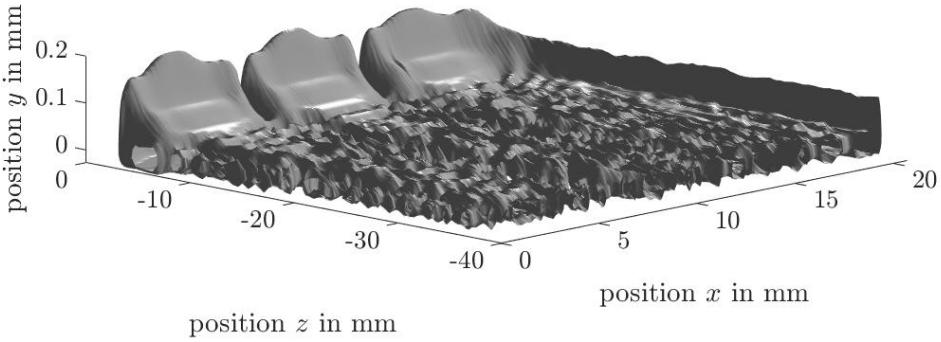

Figure 5.3: Spatial reconstruction for the waterfall coating head geometry for simulation No. 1 at $\alpha = 0.5$ (Erhard et al., 2022, p. 48).

5.1.3 Validation Results

The approach to validating the CFD simulation model is specified in chapter 4.5.5. In the following, the simulation results and experimental data are checked for consistency. Thereby, the outlines of the experimental and simulation runs and the resulting surface roughness data are compared.

Evaluation of the Outlines

Figure 5.4 shows an overlay of the respective outlines of the simulation results analysed by the spatial reconstruction method and the dimensioned photographs of the fabricated specimens. Since the first layer of each specimen was cast at velocities $<< u$ to compensate for a potential unevenness of the substrate by overfeeding, a single broader layer for each specimen is visible below the actual layers to be evaluated. The constant simulation time of 2.5 s for each simulation and the varying coating velocities considered in each simulation case (Table 4.6) lead to different lengths of the reconstructed layer and thus outlines to be evaluated (Figure 5.4, dashed outlines determined by spatial reconstruction). The outline of a single slurry layer is found to agree well with the specimens for varying velocities u and gap heights h_g. As can be seen, the overall width of the slurry layer can be predicted well. Moreover, the slurry accumulations at the beginning of the coating process are accurately represented. A slight deviation in shape between the experimental and simulation result is visible in all specimens

regarding one detail: a more abrupt increase in width at the beginning of the layer is found when analysing the simulation results compared to the experimental ones. This effect is attributed to the non-constant acceleration apparent in the test setup. Whereas a constant acceleration to the coating velocity u is prescribed in the simulation setup, the physical axes are accelerated and decelerated following a linear slope in order to reduce mechanical loads.

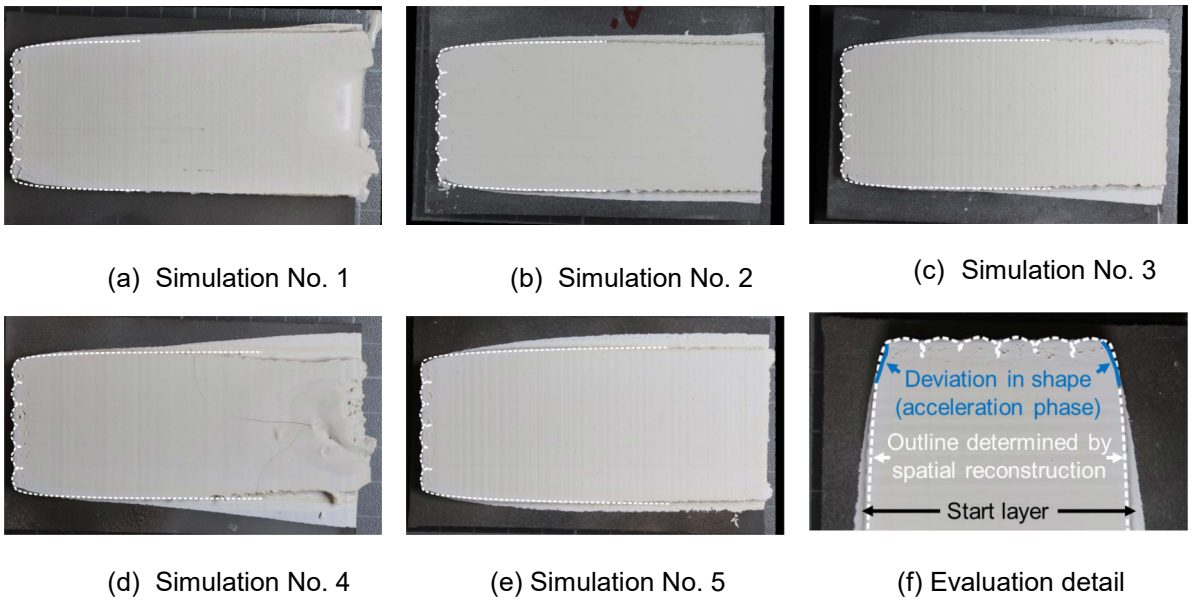

Figure 5.4: Overlay of the outlines determined by spatial reconstruction and the perspective-corrected images of the physical specimens (Erhard et al., 2022, p. 50).

Evaluation of the Surface Roughness

Only the top side of the computational reconstructed slurry layer was evaluated and compared with surface measurements on the physical specimens. When comparing the simulation and experimental results, it has to be noted that the surface of the physical specimens is formed to their final shape by multiple layers instead of one single in the case of the simulation. That might lead to averaging, overlay, or blurring effects. An evaluation line for surface measurement of the physical specimen is chosen orthogonal to the coating direction. The position of the surface measurement cannot be set up precisely. However, three measurements at varying positions along the coating area showed a standard deviation of only 0.044 µm. Hence, deviations along the physical specimen are rated negligible. To assess the simulation results, the surface roughness Ra is determined by evaluating the surface topology along three different planes perpendicular to the coating direction and calculating the mean of those values.

Both the reconstruction and the physical specimens were found to show valley and plateau regions. Obviously, more slurry is deposited directly behind a channel than in the inter-channel regions. Furthermore, grooves along the coating direction are formed in the experiments that are also visible in the reconstruction.

In the VOF method, a distinction between the phases is made by judging a cell's respective volume fraction α. The interface of the phases lies within the volume of a cell if $0 < \alpha < 1$. In the presented model, setting α to 0.5 ensures that a cell centre is assigned to the slurry phase if more than half of the cell is filled with slurry. By altering α to a value of 0.25, the influence of the air entrainment can be reduced since additional cells are assigned to the interface's slurry side in this case. However, this approach needs to be examined critically: underestimated α values will result in a loss in the significance of the results.

The results of the surface roughness evaluation in Figure 5.5 compare the computed simulation data for both $\alpha = 0.5$ and $\alpha = 0.25$ and the experimental data for varying coating velocities. All Ra values are determined in the same order of magnitude ($2\ \mu m < Ra < 8\ \mu m$). Considering the experimental data, the average roughness Ra is shown to increase along with the substrate velocities u. Nevertheless, the simulation results do not follow this trend for both α values but indicate an inverse behaviour. For $\alpha = 0.25$, a good approximation for $u < 65$ mm/s is achieved. However, substantial discrepancies were determined for higher velocities. That effect is assigned to the higher impact of air entrainment with increasing velocities. Moreover, the simplified material model may have caused the discrepancy: the constant shear thinning flow behaviour, as implemented herein, may induce smoothing. At the same time, the slurry's viscosity is presumed to increase rapidly when in contact with the underlying absorbent layers. Thus, the present model is found to be capable of predicting only the magnitude of Ra. Further work on an advanced material model involving an altering viscosity behaviour and a permeable substrate is suggested.

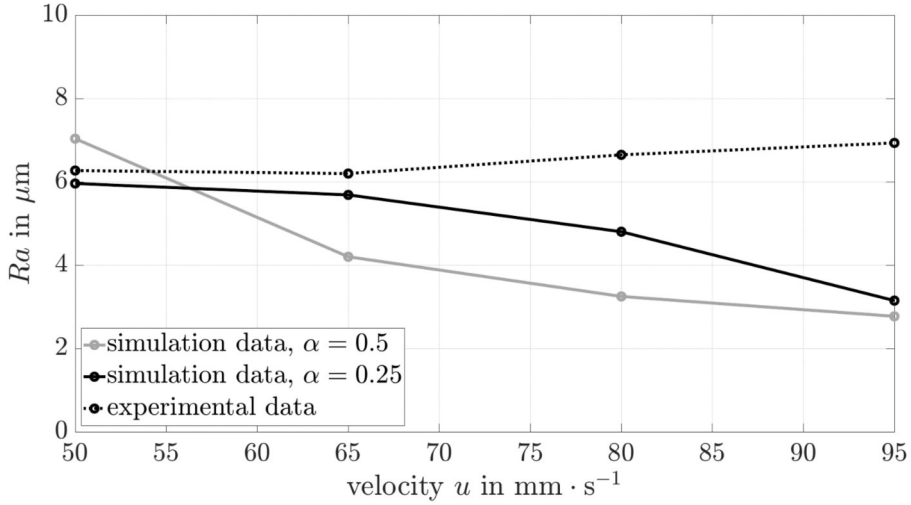

Figure 5.5: Comparison of the calculated and experimentally determined average surface roughness Ra as a function of coating velocity for h_g = 0.1 mm (Erhard et al., 2022, p. 51).

5.1.4 Advancement of the Coater Geometry

As described above, the following weaknesses of the waterfall coater geometry have been identified: material recirculation and transverse forces, surface inhomogeneities, and a non-uniform velocity distribution at the outlet. Furthermore, during the practical trials, a tendency of clogging coming from regions of low velocities within the inner coater geometry has been observed, as well as a high portion of excess material. Those weaknesses that clearly constitute an obstacle to industrial implementation and scale-up are to be compensated by improving the coater geometry.

Three major geometrical modification steps with multiple sub-iterations were carried out on the CAD design of a scaled coat hanger known from polymer sheet production. In particular, simulation identifies low-velocity regions on the shoulder's edges. Hence, the contour of the shoulders is progressively rounded to enable uniform slurry distribution and cleanability of the inner geometry by water backwashing. The resulting geometries of the coat hanger cavities are depicted in Figure 5.6. A detailed sketch of the final geometry and the related geometry parameters are included in the appendix (Figure A 1, Table A 1).

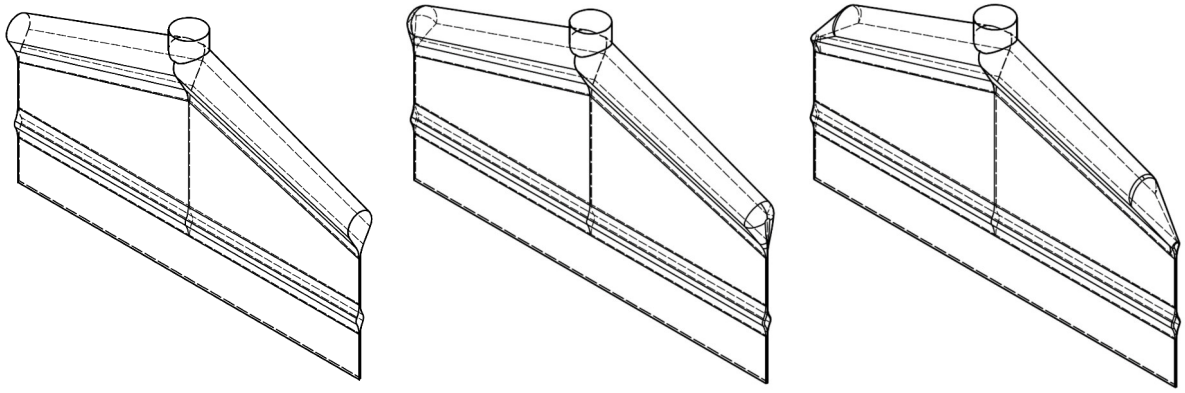

Figure 5.6: Illustration of the major iteration steps in coating head geometry advancement.

The simulative methods introduced above enable the iterative determination of an appropriate parameter set for the advanced coating head geometry, referred to as coat hanger design. When applying a substrate velocity of u = 65 mm/s at a slurry pressure p_{slurry} = 1.4 bar for a filling height $h_{filling}$ = 70 mm, and a gap height h_g = 0.1 mm, the preloading step was shown to be no longer needed since those parameters allow for the formation of a continuous slurry front of constant magnitude during movement. Thus, the cycle time can be reduced by eliminating the preloading phase, and acceleration and deceleration procedures can be omitted in the process sequence. Moreover, by realising the slurry-on-demand deposition, no more slurry recirculation occurs, enabling the minimisation of excess material. Figure 5.7 illustrates the streamlines in

the slurry phase using the coat hanger design. Particles emitted through the coater outlet are shown to be deposited without circulation, following the shortest path possible to the coater gap.

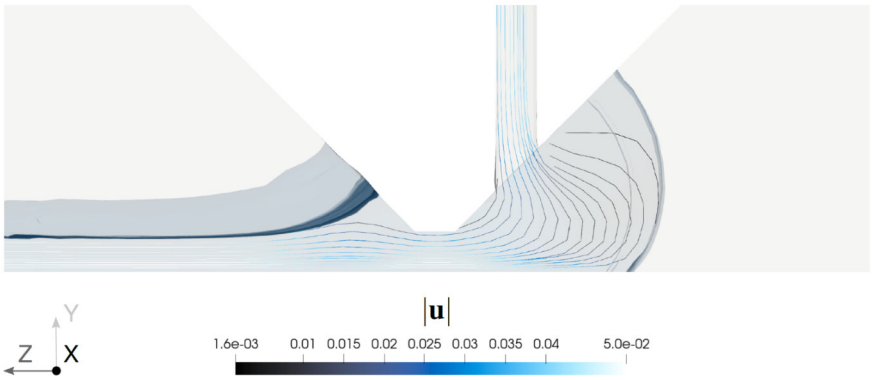

Figure 5.7: Illustration of the streamlines in the slurry phase using the enhanced coating head design.

Another important achievement of the enhanced design is the prevention of air entrainment and, thus, more homogeneous layers of increased surface qualities. The surface's improved homogeneity is obvious when comparing the spatial reconstruction of a layer fabricated by the enhanced design (Figure 5.8) and the corresponding simulation using the waterfall coating head (Figure 5.3). Neither plateaus and valleys nor grooves occur when using the enhanced design since a continuous outlet instead of a channel structure is implemented. The averaged roughness Ra of the enhanced design resulted in Ra = 0.79 µm, which equals a decline of around 80 %. Nevertheless, it has to be noted that a two-phase suspension of ceramic particles and water is implemented as a one-phase fluid in the simulation. Hence, the achievable surface roughness, in reality, will be further influenced by particle settling and drying dynamics, although those were disregarded within this study.

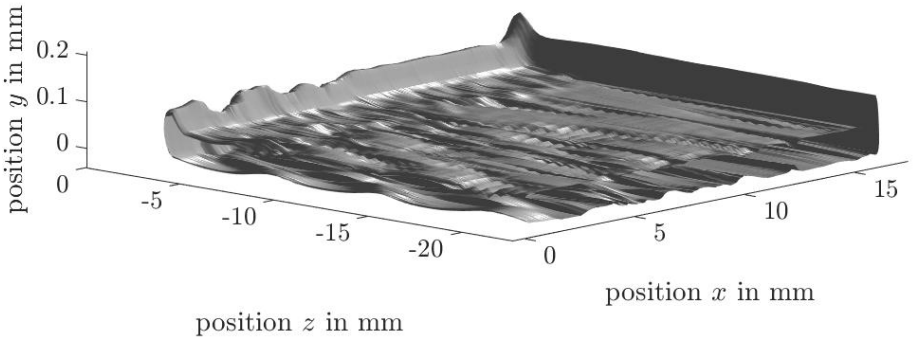

Figure 5.8: Spatial reconstruction for the enhanced coating head geometry for h_g = 0.1 mm and u = 65 mm/s at α = 0.5 (Erhard et al., 2022, p. 52).

Overall, the CFD model enables the prediction of the magnitude of surface roughness, providing a useful tool for indicating inhomogeneities or defects. Inversely, it can be utilised for optimising geometries and proposing appropriate parameter sets for stable processing. The study conducted herein is assessed as an initial validation approach for the suggested methods. Future work is proposed on implementing an advanced material model and proving evidence on the resulting properties of the cast layers based on a larger test series.

However, reflecting upon the coating geometry's advancement, a great added value has been created by developing a coater geometry enabling a customised fluid flow using the suggested methods. The suggested parameter set is implemented in a slightly modified form for technical reasons. Still, practical experiments using the coat hanger design confirmed the added value of those carefully aligned parameter sets. First, the cleanability of the coater cavity has improved significantly since deposits of hardened slurry are prevented by design (minimised regions of low velocities). Second, the homogeneity has increased. Third, slurry access material has decreased, enabling a slurry-on-demand process that allows selective coating applications in future developments.

5.2 Control of Material Properties via Drying Configuration

In this chapter, the results from experiments described in chapters 4.3 and 4.4 using the test setup described in chapter 4.2 are analysed and discussed with regard to the theoretical background summarised in chapter 2.3.2.

In particular, by doing so, the central research hypotheses concerning the control of materials' properties by means of drying shall be tested for their truth. It is analysed whether excessive drying provokes major flaws that reduce strength. Moreover, the investigations shall reveal a potential dependence of compaction on the drying periods and layer thicknesses. Finally, secondary effects resulting from varied drying conditions shall be carefully observed, in particular concerning binder migration and surface qualities.

Chapter 4.4.3 introduced the full-factorial experimental design applied in this study with its factors and levels or treatments. Table 5.1 gives an overview of the comprehensiveness of the results deduced thereof. As indicated by the ×-mark, some treatment combinations did not produce quantitatively evaluable results. The respective specimens broke during handling prior to their analysis, so no quantitative observations were feasible in this case.

However, as shown in Table 5.1, these treatment combinations involve either both high radiation outputs and long drying periods at the lower level of layer thickness or the lowest radiant power and drying period at the higher level of layer thickness. Thus, it can be

qualitatively concluded that those treatment combinations exceed the feasible process window. More precisely, the failure of the experiments conducted on a layer thickness of 50 µm in combination with high drying intensities and periods early indicates the potential truth of the research hypothesis in chapter 3, stating that excessive drying during layer formation leads to major flaws. Conversely, by drying a layer of 75 µm for only 15 s at the lowest drying intensity, a too-high residual moisture content within the layer buildup is believed to cause insufficient densification and blurring of the binder. Nevertheless, those qualitative observations are to be confirmed by quantitative investigations of the successful treatment combinations in the subsequent subchapters. However, when analysing the data, it is essential to remember that the unquantifiable data lead to a distortion of the results at first glance. Consequently, each visualisation of data contains information on the number of data sets directly compared with each other. Occasionally, green bodies were damaged during transport, resulting in a sample number n as low as 2 for strength analysis. For data integrity reasons, these results are shown with a note of caution on interpretation.

Table 5.1: Overview of the treatment combinations in the full-factorial experimental design. Parameter combinations marked with 'x' did not lie within the feasible process window. Damage during transportation occurred at sintered specimens of the run marked with '✓'.*

		Drying time			
Layer thickness	**Drying intensity**	**15 s**	**35 s**	**55 s**	**75 s**
50 µm	3.8 V	✓	✓*	✓	✓
50 µm	4.2 V	✓	✓	×	×
50 µm	4.6 V	✓	×	×	×
75 µm	3.8 V	×	✓	✓	✓
75 µm	4.2 V	✓	✓	✓	✓
75 µm	4.6 V	✓	✓	✓	✓

5.2.1 Influence of the Layer Thickness

In order to reveal relationships between the layer thickness and crucial material properties, the data are examined extensively at different degrees of detail. This chapter starts from the hypothesis that improved density, four-point bending strength, and elongation at break can be achieved by reducing the layer thickness. When reducing the layer thickness, the residual moisture content within a layer to be printed onto is lower if the drying intensity and period remain unchanged. Thus, secondly, this chapter deals with the hypothesis of increased moisture contents leading to increased binder migration at higher layer thicknesses.

Density

The density is determined in the green and sintered stage. The two chosen levels of 50 and 75 µm are set due to their proven ability to be processed with the same constant parameter set for slurry deposition (in particular pressure, preloading time, and coating velocity) and thus to avoid an increased cross-sensitivity. Figure 5.9 shows a general conspectus of the results, including the scatter. The number of specimens n relates to each box plot in a diagram and is specified as an absolute number or an interval. The example in Figure 5.9 indicates that each of the four box plots in the diagram is generated by merging data from 21 to 33 specimens of different process parameters in respect of the two other process variables (here, drying intensity and drying time). The quantity of specimens of each box thus varies by reason of a differing quantity of test series included. In this case, only 21 data points are available for the box plots of 50 µm layers because of the missing quantitative data of experimental runs marked with × in Table 5.1. By contrast, all except one run on 75 µm layers, in total eleven runs with three data points for each run, led to an increased number of quantitatively analysable results. Moreover, the P-values of the respective series are given: P_g for the green series and P_s for the respective sintered ones.

Figure 5.9 indicates a significant decrease in density when increasing the layer thickness for both green and sintered specimens. Overall, the green series show higher absolute densities than the respective sintered ones. This is attributed to two effects: first, the green body contains not only the quartz particles but also the binder and the organic slurry additives that account for approximately 2 wt.-% of the total weight. Second, even more decisively, the material system tends to inflation during sintering. This effect is extensively discussed in chapter 6.1.3.

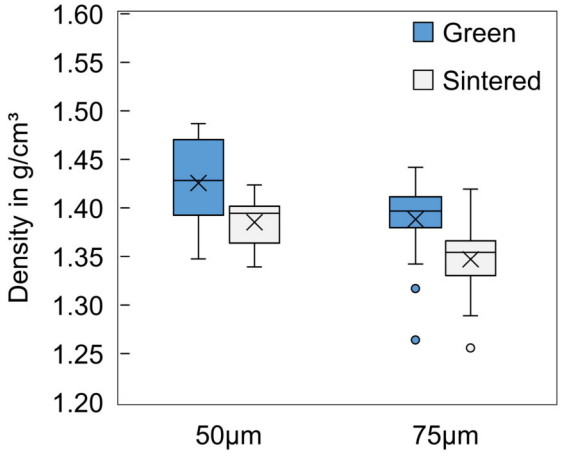

$P_s = 9.82 \cdot 10^{-5}$; $P_g = 4.13 \cdot 10^{-3}$; n = [21;33]

Figure 5.9: Density distributions for varying layer thicknesses.

When directly comparing associated parameter sets (Figure 5.10), a correlation between the layer thickness variable and density property is confirmed. Decreasing layer thicknesses significantly enhanced the density of green and sintered specimens fabricated by slurry-based 3D printing. When altering the layer thickness from 75 µm to 50 µm, an average increase in the green density of 5.8 % or in the sintered density of 4.8 % was detected. Thus it can be concluded that lower layer thicknesses lead to improved densities of the printed parts.

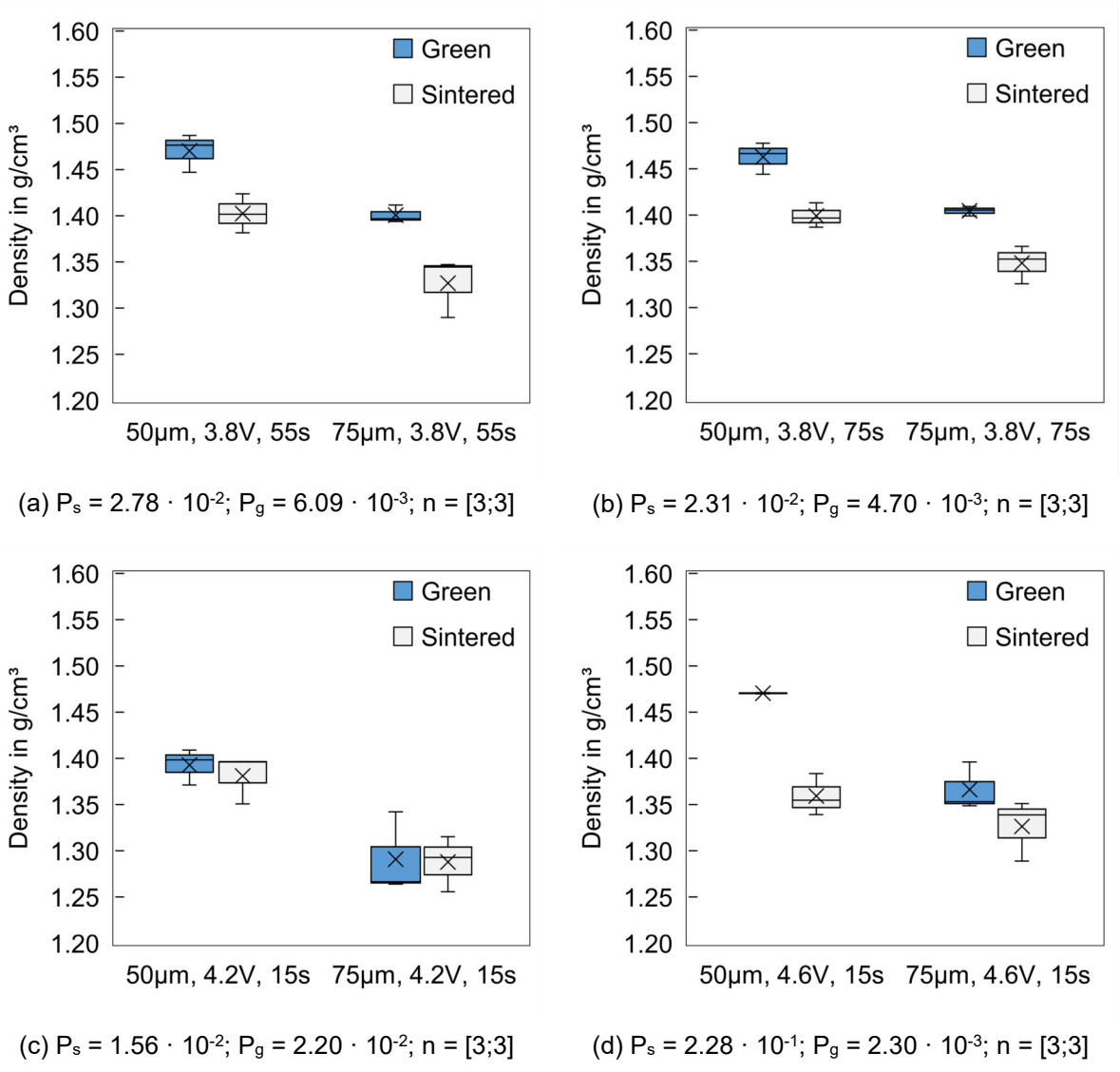

(a) $P_s = 2.78 \cdot 10^{-2}$; $P_g = 6.09 \cdot 10^{-3}$; n = [3;3]

(b) $P_s = 2.31 \cdot 10^{-2}$; $P_g = 4.70 \cdot 10^{-3}$; n = [3;3]

(c) $P_s = 1.56 \cdot 10^{-2}$; $P_g = 2.20 \cdot 10^{-2}$; n = [3;3]

(d) $P_s = 2.28 \cdot 10^{-1}$; $P_g = 2.30 \cdot 10^{-3}$; n = [3;3]

Figure 5.10: Direct comparison of density distributions with varying layer thicknesses at defined drying intensities and drying periods.

Discussion The drying conditions applied to a layer substantially differ for varying layer heights as drying is accomplished simultaneously by evaporation from the top and capillary forces acting from underneath. A higher proportion of the total particle carrying liquid forming one layer is believed to be immediately soaked into previously deposited layers instead of being subsequently evaporated when using lower layer thicknesses.

The time of depleting a droplet t on a constant drawing area can be calculated by

$$t = \left(\frac{V_0}{{r_d}^2 \, \pi \, a_p \sqrt{\frac{\gamma_{LV} cos\theta R}{2\eta}}} \right)^2 \tag{5.1}$$

where V_0 is the total liquid volume, r_d the drawing radius, a_p the pore area surface fraction, γ_{LV} the surface tension of the liquid-vapour interface, θ the contact angle of the liquid on the solid, R the capillary radius, and η the dynamic viscosity. (Denesuk et al., 1993, pp. 116–117) Equation (5.1) does not account for gravity effects. However, such simplification of the general equations of capillary flow derived by Washburn (1921) is suggested to model liquid infiltration in porous substrates since only distances in micro-scale are involved vertically (Holman et al., 2002, p. 432, Hilpert, Ben-David, 2009, p. 207).

Since the total liquid volume using 50 µm layers corresponds to two-thirds of the total volume using 75 µm layers and the material constants and the drawing area are considered almost constant, the infiltration time t is estimated to reduce approximately by one-third when using the 50 µm layers. Thus, by applying the same coating velocity, additional slurry may be delivered, filling the gap created simultaneously with water removal by capillary forces and thus increasing the overall solid content in CRP, where shrinkage is equal to the loss of fluid (Scherer, 1990, p. 7).

Moreover, densification depends on the permeability of the underlying layer and the slurry viscosity. Pivinskii et al. (1973) investigated the forming rates of quartz ceramics in slip casting and identified the porosity of the mould as a significant factor affecting the forming rate. The mould porosity, in turn, was directly related to its moisture capacity. Furthermore, the packing density of the forming product was found to decrease with increasing suspension viscosities. (Pivinskii et al., 1973)

In summary, when depositing thinner layers onto each other, multiple effects are assumed to superimpose: first, water removal by soaking may be accomplished in a shorter period. Thus, a higher proportion of backfill during layer casting can be realised using the same coating velocity. Second, since the absolute liquid volume to be removed during drying is lower, a more advanced moisture removal can be realised, leading to an increased moisture capacity which encourages capillary dehydration of the next layer to be deposited. Higher capillary forces result in an advanced particle arrangement and, thus, in increased packing densities. Moreover, the distance between the previously cast layer and the farthest newly deposited particle is lower. Hence, since the upper proportion of the newly cast layer is subjected to higher capillary forces than a thicker layer's upper section, improved densification is expected.

Four-point Bending Strength

Since the strength of brittle materials depends on the size of a flaw, the flaw distribution, and the specimen's geometry, the strength of ceramics must be evaluated statistically (Danzer et al., 2007, p. 3). A proofed statistic on bending strength distributions requires a large number of specimens that this study cannot provide. However, the analysis of bending strength on the same set of specimens as used for density determination will provide the first indication of critical flaws, e.g. interconnected pores, emerging at certain parameter combinations in slurry-based 3D printing. In particular, a potential correlation between the packing density and the bending strength achieved by sintering is to be determined.

Figure 5.11 shows the bending strength distributions of all specimens assigned to the respective layer thickness preconfigured in the process control. The results indicate a reduction of bending strength by increasing layer thicknesses which fits with the results on density determination. The green bending strength is relevant for handling issues only and is strongly dependent on the binder content. In contrast, the sintered bending strength is a mechanical property of the ready-to-use casting core. In view of the sintered strength, a high dispersion is found at both levels of layer thicknesses (Figure 5.11). Nevertheless, the sintered specimens fabricated with 50 µm layers significantly deviate from those with 75 µm. The decrease in green strengths with increasing layer thicknesses at a constant binder content is consistent with own further research on binder jetting technology and that carried out by others, e.g. by Vaezi, Chua (2011) (Vaezi, Chua, 2011, pp. 279–280).

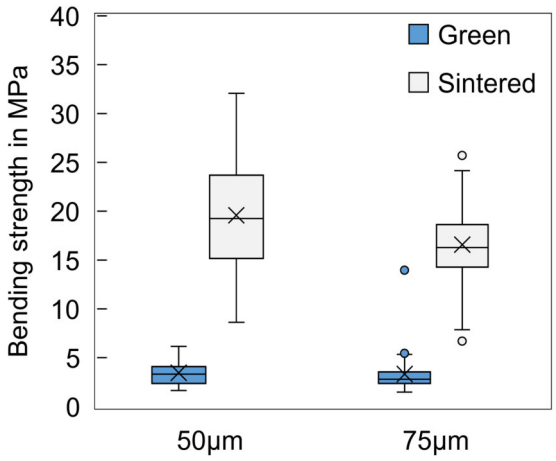

$P_s = 4.58 \cdot 10^{-3}$; $P_g = 8.01 \cdot 10^{-1}$; n = [20;62]

Figure 5.11: Bending strength distributions for varying layer thicknesses.

When directly comparing associated parameter sets in Figure 5.12, a high level of significance is shown for results of specimens fabricated at drying periods of 55 or 75 s (Figure 5.12a and

Figure 5.12b) only, indicating a clear correlation between bending strength and layer thickness on sintered specimens when using PAV = 3.8 V. Since the specimens of 50 µm layers showed higher packing densities as well, this behaviour meets the expectations. However, this observation cannot be made at selected parameter sets of higher drying intensities and lower drying periods (Figure 5.12c and Figure 5.12d). The microstructural analysis at the end of this sub-chapter reveals major defects for both parameter sets visualised in Figure 5.12d, leading to equally low bending strengths.

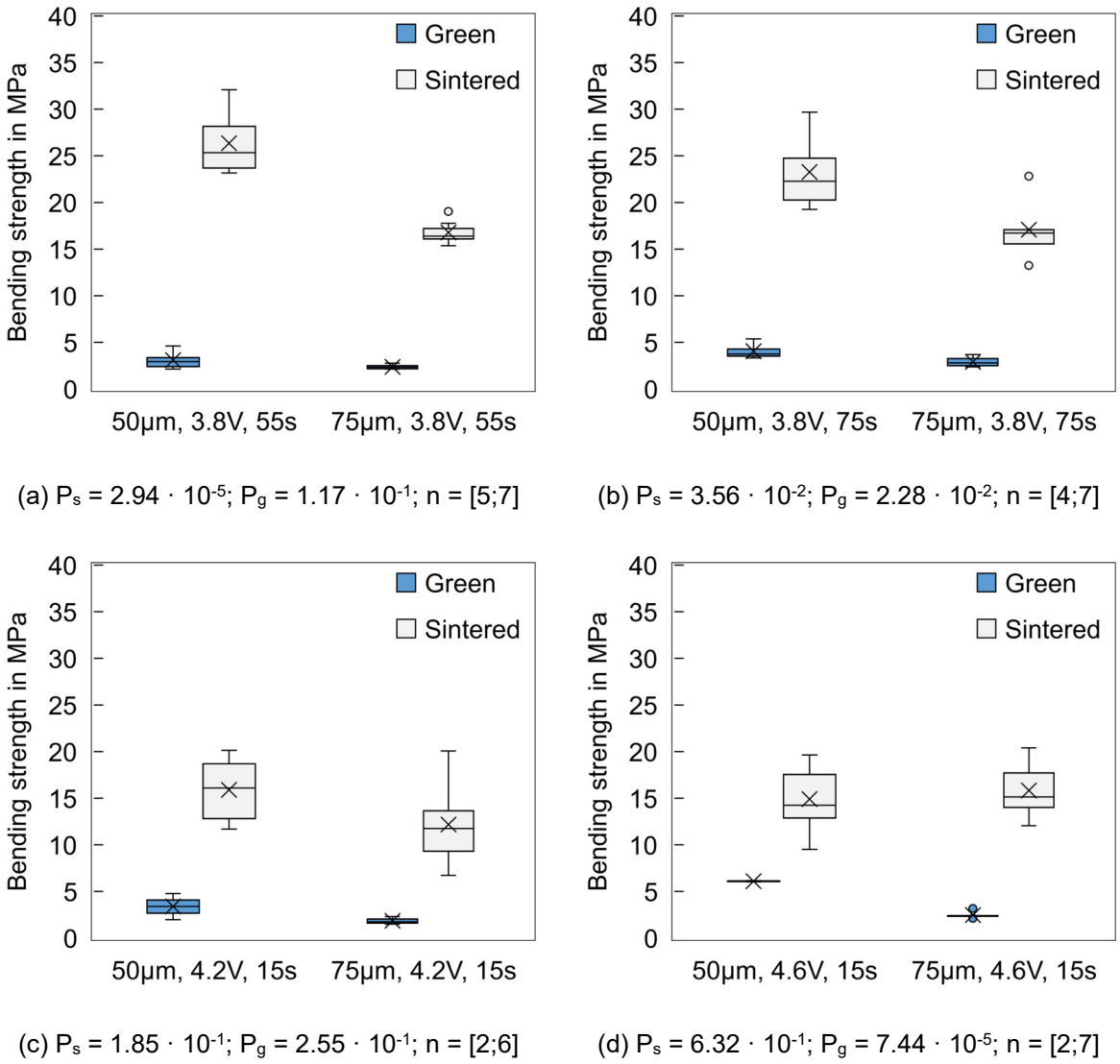

(a) $P_s = 2.94 \cdot 10^{-5}$; $P_g = 1.17 \cdot 10^{-1}$; n = [5;7]

(b) $P_s = 3.56 \cdot 10^{-2}$; $P_g = 2.28 \cdot 10^{-2}$; n = [4;7]

(c) $P_s = 1.85 \cdot 10^{-1}$; $P_g = 2.55 \cdot 10^{-1}$; n = [2;6]

(d) $P_s = 6.32 \cdot 10^{-1}$; $P_g = 7.44 \cdot 10^{-5}$; n = [2;7]

Figure 5.12: Direct comparison of bending strength distributions with varying layer thicknesses at defined drying intensities and drying periods. Note of caution for interpretation: The data of green bodies shown in (c) and (d) are incomplete (n=2) due to specimen break prior to testing.

Discussion An improved packing density is known to positively affect the mechanical properties attainable during sintering. Coincidently, at higher densities a reduced pore volume

appears. The global pore concentration created during processing affects the sinterability and, thus, indirectly, the mechanical strength.

Two fundamental types of defect may constitute the origin of failure during the four-point bending test: pores and cracks. The shape of the pores determined by the surface energies as driving forces is also of major relevance when intending enhanced mechanical properties. Pores are known for their ability to coalesce (Carter, Norton, 2016, p. 284). Moreover, due to the pores' characteristic of concentrating stress, the strength of a porous polycrystalline ceramic is known to decrease more rapidly than its density (Carter, Norton, 2016, p. 289). Cracks are known to develop preferably due to excessive or differential shrinkage at high drying rates or in thick bodies (Brosnan, Robinson, 2003, pp. 137–138). Hence, low layer thicknesses are recommended in order to avoid stresses caused by shrinkage (Murray, 2009, pp. 43–49). To sum it up, the results showing an increased probability of enhanced bending strength when applying layers of 50 µm instead of 75 µm conform to expectations provided in the literature: both density and strength were found to improve with a reduction in layer thickness. The not significantly deviating results when using PAV = 4.6 V indicate a flaw generation induced by drying intensity independent of the layer thickness. Since major flaws liable for failure are apparent in both levels of layer thickness, the increased density in specimens from a layer thickness of 50 µm cannot contribute to enhanced strength.

Overall, a significant increase in strength was achieved by sintering. Depending on the binder system and content, conventional 3D printed sand parts for foundry applications show bending strengths of 2.5 to 3.5 MPa (Günther, Mögele, 2016, p. 68), corresponding approximately to the strength attained in slurry-based 3D printed green bodies. Conversely, on average, bending strengths above 15 MPa were measured on sintered specimens.

Elongation at Break

Since no displacement transducer or strain gauge was installed, the uniaxial testing machine equipment did not allow for precise deflection measurements as provided in DIN EN 843-2. Thus, Young's modulus cannot be derived from the bending tests' results. However, fracture occurred at forces within the range of 4.5 to 19 N when testing sintered specimens, making the determination of the elongation at break as a criterion for brittleness feasible. The material property of elongation at break included herein reflects the displacement of the specimens in the direction of the applied load at fracture. It is recorded as the maximum machine displacement during a bending test experiment. As described in DIN EN 843-2, alternative methods or specimens' geometries are recommended for enhanced material characterisation.

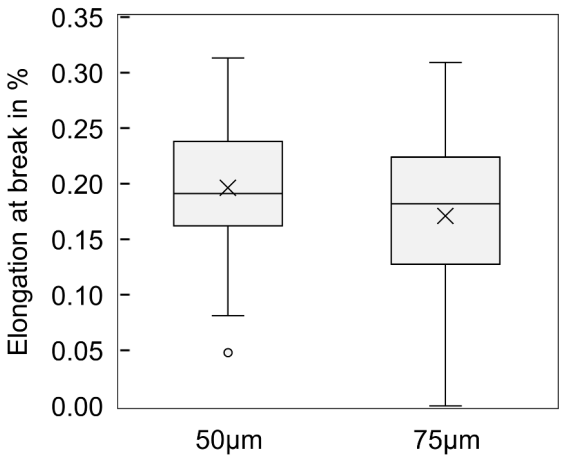

$P_s = 8.76 \cdot 10^{-2}$; n = [31;62]

Figure 5.13: Elongation at break distributions for varying layer thicknesses.

Figure 5.13 shows an overview of the results involving all experimental runs. A very large scattering is observed – not merely due to the grouping of individual trials on different parameter sets but also to the principal behaviour of ceramics in mechanical testing. The elongation at break is the characteristic material property quantifying a specimen's deformation capacity. Compared to metals, the brittleness of ceramics causes very small absolute deformation and significantly larger scattering since it is dependent on the flaw size (Munz, 1999, p. 137) and the probability that the most critical defect size and shape (Zhang, Yang, 2019, pp. 10–11) is apparent in the effective surface area under maximum tensile stress during mechanical testing and thus the initiator of fracture. Due to the large scattering, no significant deviation between the 50 µm and 75 µm can be derived from the overview in Figure 5.13. The mean elongation at break is only slightly lower for the specimens of 75 µm layers.

The direct comparisons in Figure 5.14b, Figure 5.14c, and Figure 5.14d provide significant results indicating a lower elongation at break value at 75 µm compared to 50 µm for selected parameter sets. In summary, the specimens tend to have a higher elongation at break at a lower layer thickness. This trend agrees with the previously determined higher density and bending strength values for lower layer thicknesses. Data on Young's modulus may be recorded in future investigations to prove evidence.

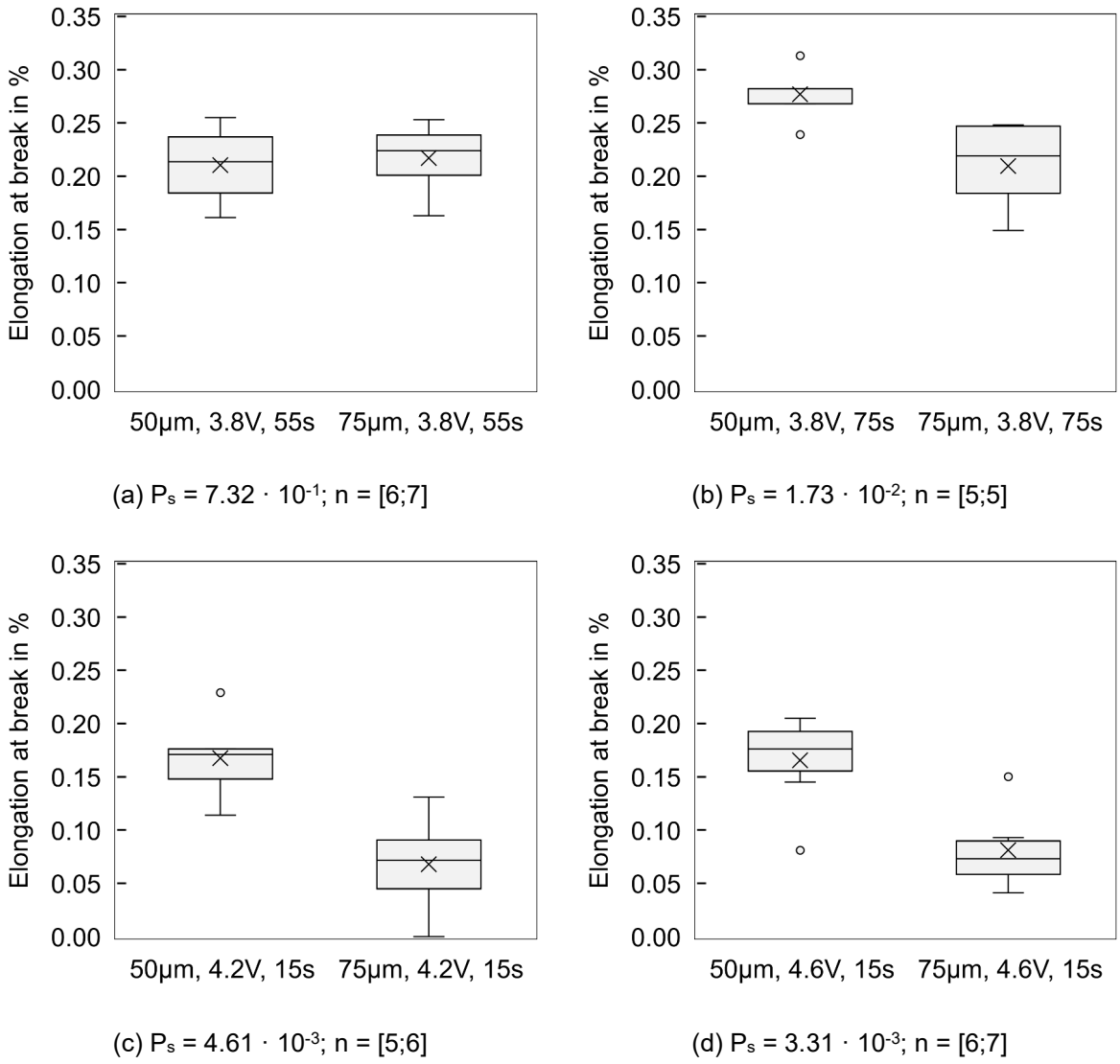

(a) $P_s = 7.32 \cdot 10^{-1}$; n = [6;7]

(b) $P_s = 1.73 \cdot 10^{-2}$; n = [5;5]

(c) $P_s = 4.61 \cdot 10^{-3}$; n = [5;6]

(d) $P_s = 3.31 \cdot 10^{-3}$; n = [6;7]

Figure 5.14: Direct comparison of elongation at break distributions with varying layer thicknesses at defined drying intensities and drying periods.

Discussion Within bulk ceramics, reduced strength is typically caused by imperfections or flaws such as pores, large grains, or cracks acting as stress concentration sites (Bengisu, 2001, pp. 218–219). Griffith established a theoretical strength theory, calculating the fracture stress σ_f in the case of plane stress to

$$\sigma_f = \sqrt{\frac{2E\gamma}{\pi c}} \tag{5.2}$$

With the Young's modulus E, the surface free energy γ, and the half length of the focal line c quantifying the imperfection's size (Griffith, 1921). The theoretical relationship between stress and strain proposes an increase in strength with increasing elastic modulus, which, in turn, is expected to correlate with its substitute elongation at break. Since specimens showing enhanced

strength mostly also have elevated elongation at break values, a relationship between stress and elongation at break is confirmed here. It is assumed that the global dislocation motion is impeded to the same extent due to the identical material system and sintering process applied, and thus due to a constant intrinsic flaw size being the grain boundaries. The deformation capacity tends to be impeded severely by raising the layer thickness. It can be reasonably resumed that the likelihood of occurrence of a critical flaw is higher within the outermost 75 µm layers that are exposed to the most extreme stress level than within a 1.5-fold amount of 50 µm layers involving a higher number of layer interfaces. The number of layer interfaces within a highly stressed volume is found to be not decisive for fracture probability but rather the linkage of individual layers or in-layer defects. Early failure is assigned to the formation of more critical flaws when applying unfavourable drying conditions (here: increasing the layer thickness) that are more likely to occur in the maximum load zone in four-point bending testing.

Dimensional Accuracy

Herein, the specimen's width is analysed in order to evaluate the dimensional accuracy in the green and sintered stage. The green width is considered a decisive criterion for investigating lateral binder migration effects that are also related to vertical effects. The width of the specimens' geometry can be examined at a higher precision than its height using the measurement method described in chapter 4.4.4 and is thus preferred for analysing binder migration. The difference between green and sintered specimens is particularly interesting since the deformation caused by sintering effects also impacts the final cast part dimensions.

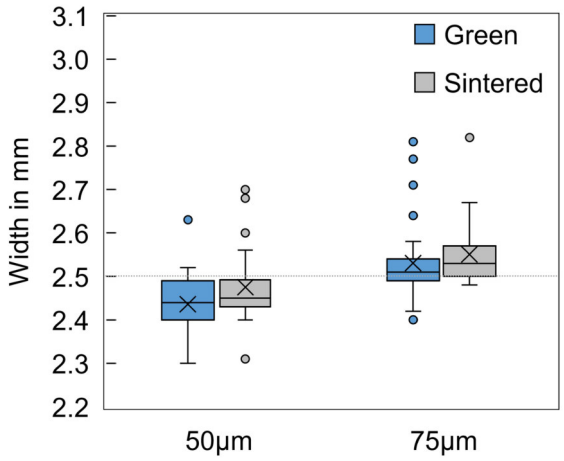

$P_s = 1.80 \cdot 10^{-3}$; $P_g = 1.47 \cdot 10^{-4}$; n = [20;33]

Figure 5.15: Specimens' width distributions for varying layer thicknesses.

Figure 5.15 shows the distributions of the specimens' widths categorised in 50 µm and 75 µm layers. The dotted horizontal line indicates the specimens' target width. Some outliers are

visible for all categories. A sample measurement series was performed by different personnel to determine the bias of the inspection worker using the same micrometre gauge. Deviations of less than 4.4 % were found. Hence, the outliers are assigned to the material adherences on the specimens' sides that are removed manually, and the dependence of the adhesive forces on the roughness profile of the side faces. An unevenness in the z-direction, characteristic for layer-wise built-up specimens, and local printing defects caused by random single nozzle failures may provide a setting for adherences. On average, the specimens of 50 µm layers did not reach the preset value of 2.5 mm, while the specimens of 75 µm layer height averagely overran this value. The width of 75 µm layer height specimens can be significantly distinguished from the width of 50 µm specimens.

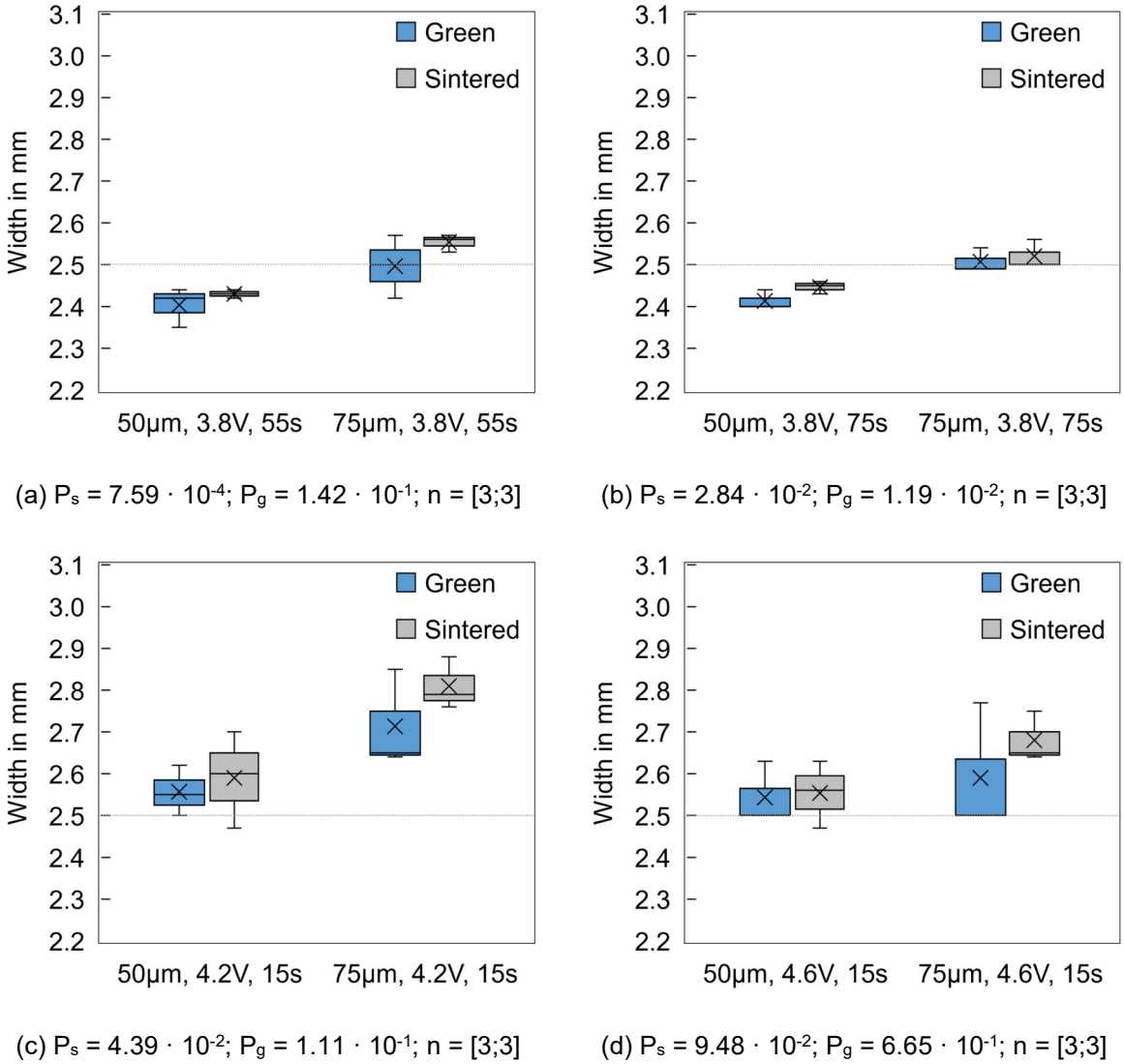

(a) $P_s = 7.59 \cdot 10^{-4}$; $P_g = 1.42 \cdot 10^{-1}$; n = [3;3]

(b) $P_s = 2.84 \cdot 10^{-2}$; $P_g = 1.19 \cdot 10^{-2}$; n = [3;3]

(c) $P_s = 4.39 \cdot 10^{-2}$; $P_g = 1.11 \cdot 10^{-1}$; n = [3;3]

(d) $P_s = 9.48 \cdot 10^{-2}$; $P_g = 6.65 \cdot 10^{-1}$; n = [3;3]

Figure 5.16: Direct comparison of specimens' width distributions with varying layer thicknesses at defined drying intensities and drying periods.

The same conclusion can be derived when directly comparing corresponding parameter sets and varying the parameter of layer thickness only (Figure 5.16). The results show the same trend and mostly a significant relationship between sintered specimens' width and layer thickness.

Discussion The increased number of outliers and the observation of not reaching the intended width is attributed to the manual wash-out process. During wash-out, the specimens are subjected to abrasion in all directions since the brush glides along the specimens' surfaces with its hair, eventually even carrying abrasive ceramic particles intensifying this abrasive effect. The correlation between layer thickness and specimens' width implies that the binder jetting process shows a significantly higher selectivity at a lower layer thickness and, thus, a proceeded drying stage. Nevertheless, it is to be noted that the binder content was adjusted to the same overall percentage for both layer thicknesses by aligning the droplet spacing. Parab et al. (2019) showed the coalescence of consecutive binder droplets in real-time observations via high-speed X-ray imaging. One cannot rule out that by arranging the droplets closer to the consecutive one in one direction (to increase the overall binder content), the binder impact, spreading, and infiltration behaviour change simultaneously. (Parab et al., 2019, pp. 6–7) A detailed statement and investigation of the sintering process explaining the reason for marginally wider sintered specimens compared to the respective green specimens are provided in chapter 6.1.3.

Surface Roughness

Since the surface properties are of major importance in casting applications, possible relations between the drying parameters and the specimens' surface qualities are examined. The average surface roughness Ra is analysed, as well as the corresponding average roughness height Rz. The requirements for casting cores' properties concerning surface quality are detailed in chapter 2.2.5. Yet, Rz values between 6 and 30 µm, conventionally only achievable by investment casting (Flemming, Tilch, 1993, p. 15), are targeted when applying slurry-based 3D printing in casting core applications.

Figure 5.17 reveals no relation between the layer thickness and the surface quality of specimens A determined on the upper-level plane surface. However, an average surface roughness Ra of 1.4 µm or an average roughness height Rz of 10.8 µm is detected. Logically, if surface properties are determined along the z-direction (at an angle of 90°) or at angles > 0° and < 90° to the layer's level, higher surface roughnesses will be observed due to the discrete layer thicknesses that form stair steps.

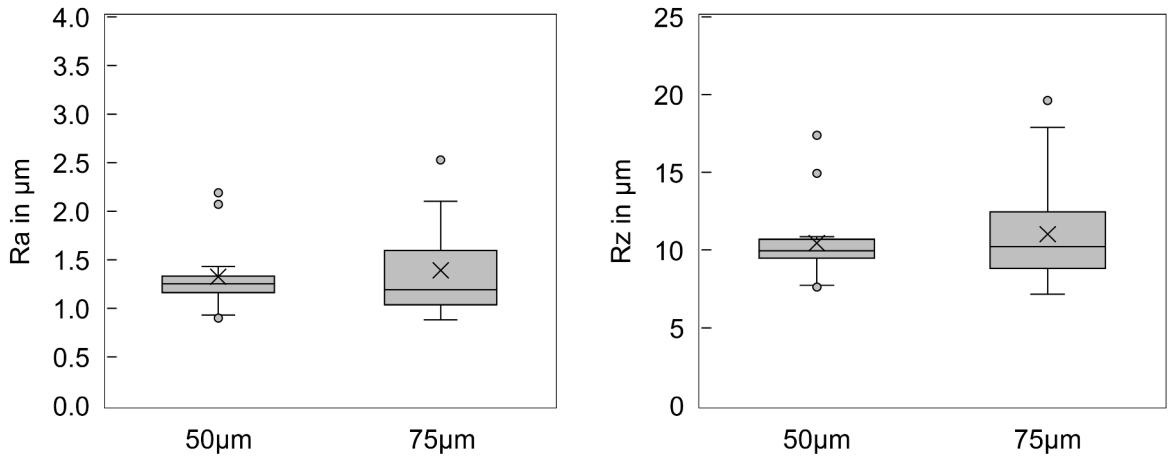

(a) $P_s = 5.92 \cdot 10^{-1}$; n = [21;33] (b) $P_s = 4.85 \cdot 10^{-1}$; n = [21;33]

Figure 5.17: Specimens' roughness distributions for varying layer thicknesses.

Discussion Even though the values show a relatively high spread, the enormous potential of the slurry-based 3D printing technique is confirmed by the magnitude of Ra and Rz identified within this study. For comparison – sand cores fabricated via powder-based 3D printing using the typical foundry material systems GS14 RP (medium grain size 0.13 mm) in conjunction with furan resin lead to Ra = 23.9 µm and Rz = 117.9 µm when using the same measurement device. The average Ra has thus improved by 94.3 %, and the average Rz by 90.8 % using the slurry-based 3D printing method.

Homogeneity and Defects

Figure 5.18 shows the microstructure of specimens of varying layer thickness at a drying intensity of PAV = 3.8 V and a drying period of 55 s. The bright lines show the layer interfaces that exhibit lower local densities. Even though the number of highly porous interfaces is naturally higher using a lower layer thickness (Figure 5.18a), the global porosity proportion is found to be far lower. Apart from porosity, no major flaws are detected when comparing these parameter sets. Hence, the increase in elongation at break and bending strength with decreasing layer thicknesses can be assigned to the globally increased density.

In contrast, Figure 5.19 reveals major flaws for both layer thicknesses when applying PAV = 4.6 V and a drying period of 15 s. Defects as large as 500 µm are visible in great numbers at both layer thicknesses. This observation indicates the independence of that type of anomaly in the microstructure from the layer thickness and, thus, the total water content to be dried off. The constant bending strengths for different densities are explained by considering the relevance of flaws in the failure of ceramics.

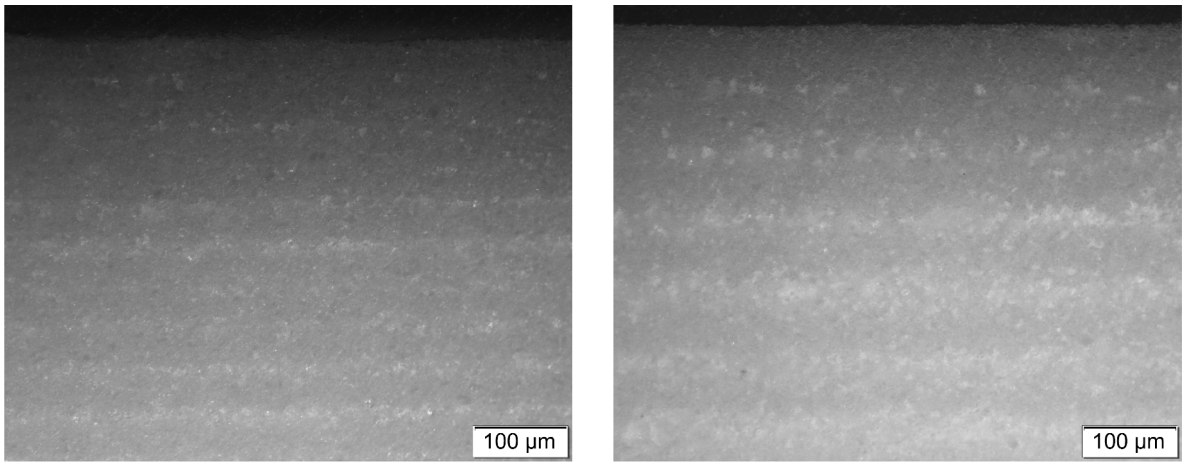

(a) 50 µm, 3.8 V, 55 s (b) 75 µm, 3.8 V, 55 s

Figure 5.18: Micrographs showing the microstructure of specimens of varying layer thickness fabricated at PAV = 3.8 V and a drying period of 55 s.

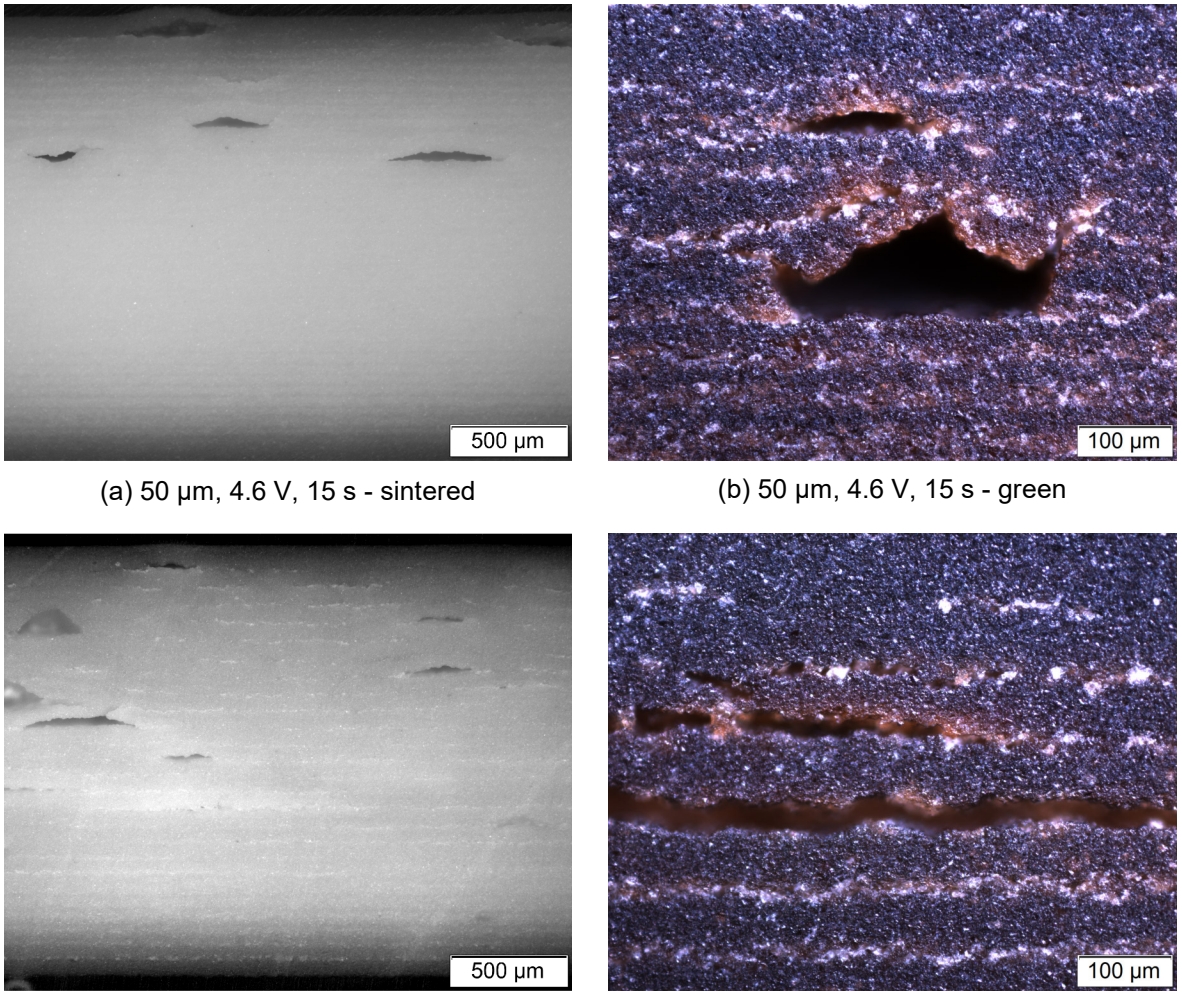

(a) 50 µm, 4.6 V, 15 s - sintered (b) 50 µm, 4.6 V, 15 s - green

(c) 75 µm, 4.6 V, 15 s - sintered (d) 75 µm, 4.6 V, 15 s - green

Figure 5.19: Micrographs showing the microstructure of specimens of varying layer thickness fabricated at PAV = 4.6 V and a drying period of 15 s.

Discussion Figure 5.18 reveals two defect-free specimens showing diverging mechanical properties due to varying proportions of porosities and densified regions. Densification is thus confirmed to be preferably attainable by reducing the layer thickness, and to be directly relatable to the mechanical strength in case no flaws bigger than usual pores occur.

Three characteristic forms of flaws are visible in Figure 5.19. The commonest, the plano-convex defect shape with lengths between 50 and 500 µm is found. Some flaws resemble more a hat shape (Figure 5.19b) in cross-section, others more a plate- or tube-like structure (Figure 5.19d). Since those types of defects occur only when using high drying intensities and low drying periods simultaneously, they may originate from moisture accumulation at the bottom sides of the layers while the surface of the layer subjected to direct radiation is already dry. Exceeding radiation power might lead to a prompt drying of the surface-near region of the respective layer. If the pores in the bottom region of the layer are still filled with water simultaneously, shrinkage of the bottom part occurs only subsequently to shrinkage of the surface-near part. Hence, the layer might be subjected to compressive forces causing local warping (Figure 2.16). Alternatively, the in total incompletely solidified layer might be subjected to shear forces causing thrust deformations as known from tectonics in geology. When an already solidified and poorly permeable cover layer is created by excessive radiation while a high residual inner moisture content is retained at the layer interface, the partially solidified layer may not yet be securely attached to the previous layer. Applying a new slurry layer onto a layer containing trapped moisture may lead to shear-off.

A detailed explanation of the flaw development mechanism cannot be verifiably demonstrated at this point. However, since those flaws appear only after a certain building height (approximately from 20 layers of 50 µm or 10 layers of 75 µm), likely, enclosed moisture is gradually growing with increasing layer heights for these parameter sets.

5.2.2 Influence of the Drying Intensity

Analogous to the previous examinations, plausible interrelations between the drying intensity and selected material properties are to be discovered in this chapter in different degrees of detail. In particular, the following research hypothesis is addressed here: “Excessive drying provokes the formation of major flaws, and thus leads to reduced strength.” Drying intensity can be related to energy input per time or drying speed and is considered particularly relevant with respect to the binder jetting process efficiency.

Density

Figure 5.20 presents an overview on data on specimens' densities for different drying intensities. With respect to density, no significant deviations were detected when investigating the effect of varying drying intensities. No direct correlation between the process parameter of drying intensity and the material property of density can be deduced.

Discussion While capillary flow leads to rapid water drainage, the comparatively low power output of the IR lamp generates only moderate evaporation that does not result in spontaneous vaporisation. Additionally, the IR lamp operates in a chronologically downstream process step. The non-existence of a link between drying intensity and density is mainly assigned to the energy input of the IR emitter acting only after the particle arrangement due to capillary forces is completed.

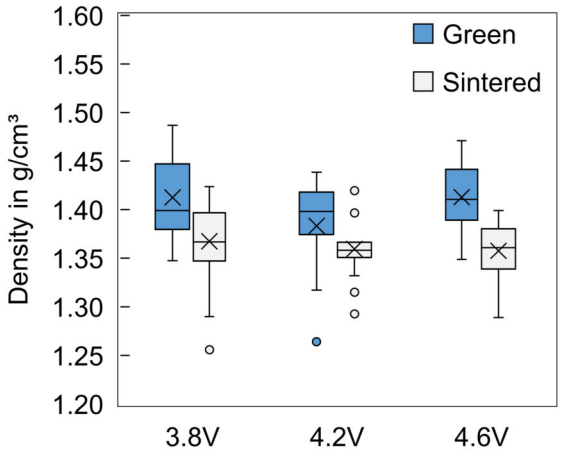

$P_s = 2.91 \cdot 10^{-1}$; $P_g = 1.06 \cdot 10^{-1}$; n = [15;21]

Figure 5.20: Density distributions with varying drying intensities.

Four-point Bending Strength

During preliminary investigations, it was noted that accumulated pores forming flaws of critical size lead to reduced strengths of specimens (Erhard et al., 2021). Herein, it is studied if higher drying intensities increase the probability of major flaw formation in sintered specimens.

A consistently increasing green strength with higher drying intensities can be observed at a high level of significance (Figure 5.21). In particular, the green strength of specimens fabricated at PAV = 4.6 V can be clearly distinguished from those produced at PAV = 4.2 V. One outlier even shows a green strength as high as 14 MPa. Only a minor distinction is derived when comparing PAV = 4.2 V and PAV = 3.8 V. Conversely, Figure 5.21 shows a trend towards

decreasing sintered bending strengths with increasing drying intensities at a high significance level.

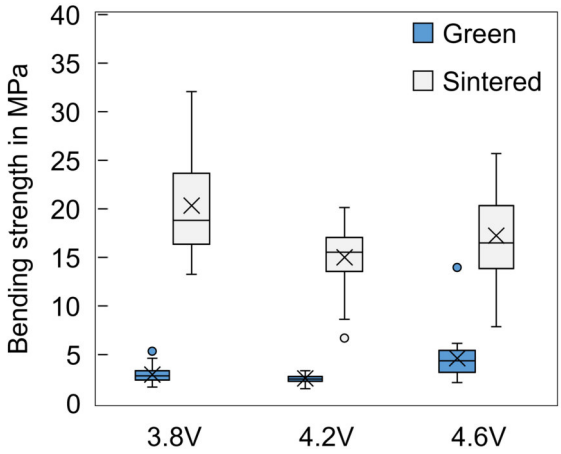

$P_s = 3.13 \cdot 10^{-5}$; $P_g = 1.17 \cdot 10^{-5}$; n = [21;32]

Figure 5.21: Bending strength distributions for varying drying intensities.

The direct parameter comparison visualised in Figure 5.22a shows the sensitivity of a 50 µm experiment to flaw formation at high drying intensities, even at a low drying period. The vulnerability of 75 µm layers when simultaneously using high drying periods and drying intensities is evidenced in Figure 5.22d. However, increased bending strengths in the sintered state can be achieved by increasing the drying intensity for 75 µm layers and applying drying times of 35 or 55 s (Figure 5.22b, Figure 5.22c). All direct comparisons show enhanced green strengths at increasing drying intensities, even though not all runs provided significant results due to the low sample number.

Discussion Since a classic example of a thermosetting resin is used in this work, a dependence of the thermal process management on the curing of the binder is reasonably assumed. Consequently, increasing bending strengths with increasing 3D printing process temperatures are confirmed by these findings.

No influence of drying intensity on green or sintered density has been found. Though, packing density is crucial to impact the achievable strength during sintering. The effect of reduced sintered strength when using higher drying intensities and either depositing 50 µm layers or simultaneously allowing the layer to dry for an exaggerated long period is attributed to a higher probability of flaw formation due to excessive drying. Excessive drying is expected to lead to high differential shrinkage and, thus, to stress development and crack formation. Moreover, high process temperatures are suspected of causing planar pore formation on the layer interfaces.

Furthermore, it has been shown that by coordinating the parameters of drying intensity, drying period, and layer thickness, equivalent sintered strength can be achieved for both levels of layer thickness. It thus can be stated that sufficient drying is to be guaranteed in slurry-based 3D printing to achieve high strength – this may be accomplished by increasing the drying period, by reducing the layer thickness, or, particularly economically advantageous, by increasing the drying intensity.

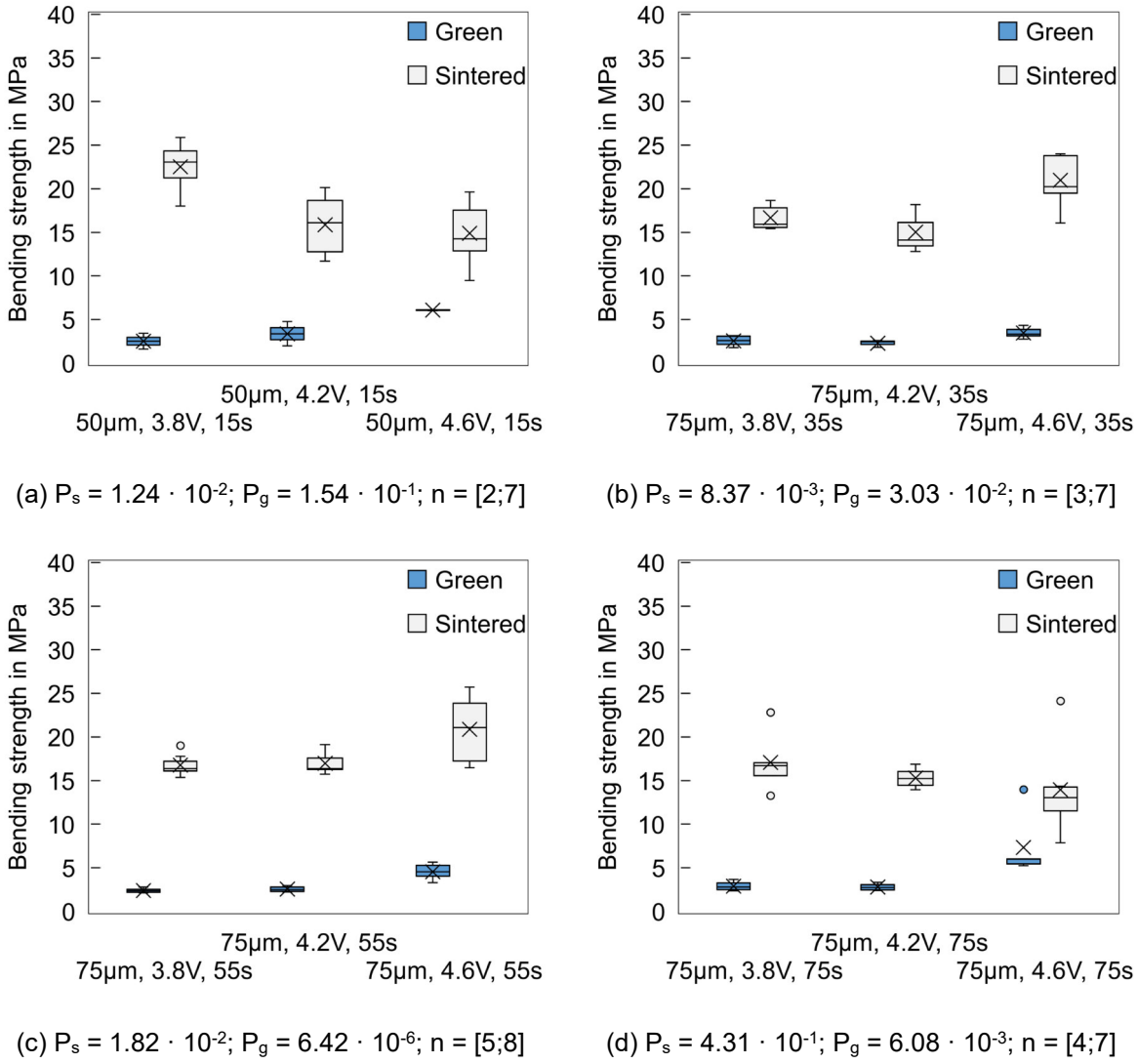

(a) $P_s = 1.24 \cdot 10^{-2}$; $P_g = 1.54 \cdot 10^{-1}$; n = [2;7]

(b) $P_s = 8.37 \cdot 10^{-3}$; $P_g = 3.03 \cdot 10^{-2}$; n = [3;7]

(c) $P_s = 1.82 \cdot 10^{-2}$; $P_g = 6.42 \cdot 10^{-6}$; n = [5;8]

(d) $P_s = 4.31 \cdot 10^{-1}$; $P_g = 6.08 \cdot 10^{-3}$; n = [4;7]

Figure 5.22: Direct comparison of bending strength distributions with varying layer thicknesses at defined drying intensities and drying periods.

Elongation at Break

When analysing the elongation at break of sintered specimens, a slight decrease in elongation at break with increasing drying intensities is found at an immense spread (Figure 5.23).

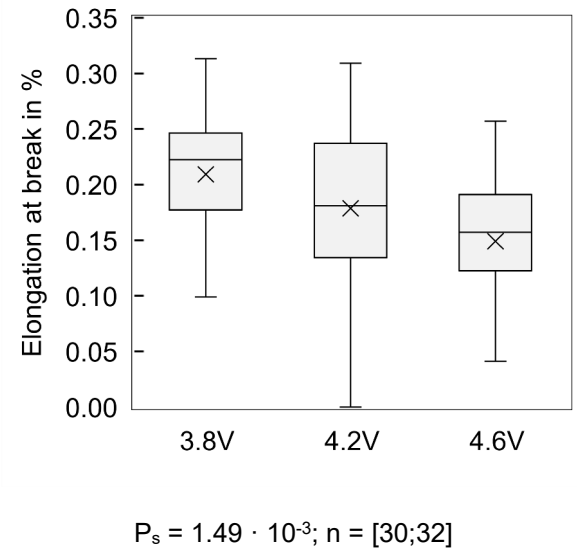

Figure 5.23: Elongation at break distributions for varying drying intensities.

When comparing directly related parameter sets (Figure 5.24), no uniform trend can be derived. No influence of the drying intensity on the deformation capacity can be derived here.

Discussion The results cannot consistently confirm the typical relationship between stress and elongation at break stated by Griffith (1921). The discrepant results refer to runs applying 75 µm layers and drying periods of 35 and 55 s. Here, the specimens generally exhibit enhanced bending strengths at a lower elongation at break when applying PAV = 4.6 V compared to PAV = 4.2 V. Inherent flaws are known to form stress concentration sites promoting brittle failure (Bengisu, 2001, p. 244). Thus, it is presumed that those specimens exhibit flaws of unfavourable size or shape at a disadvantageous place.

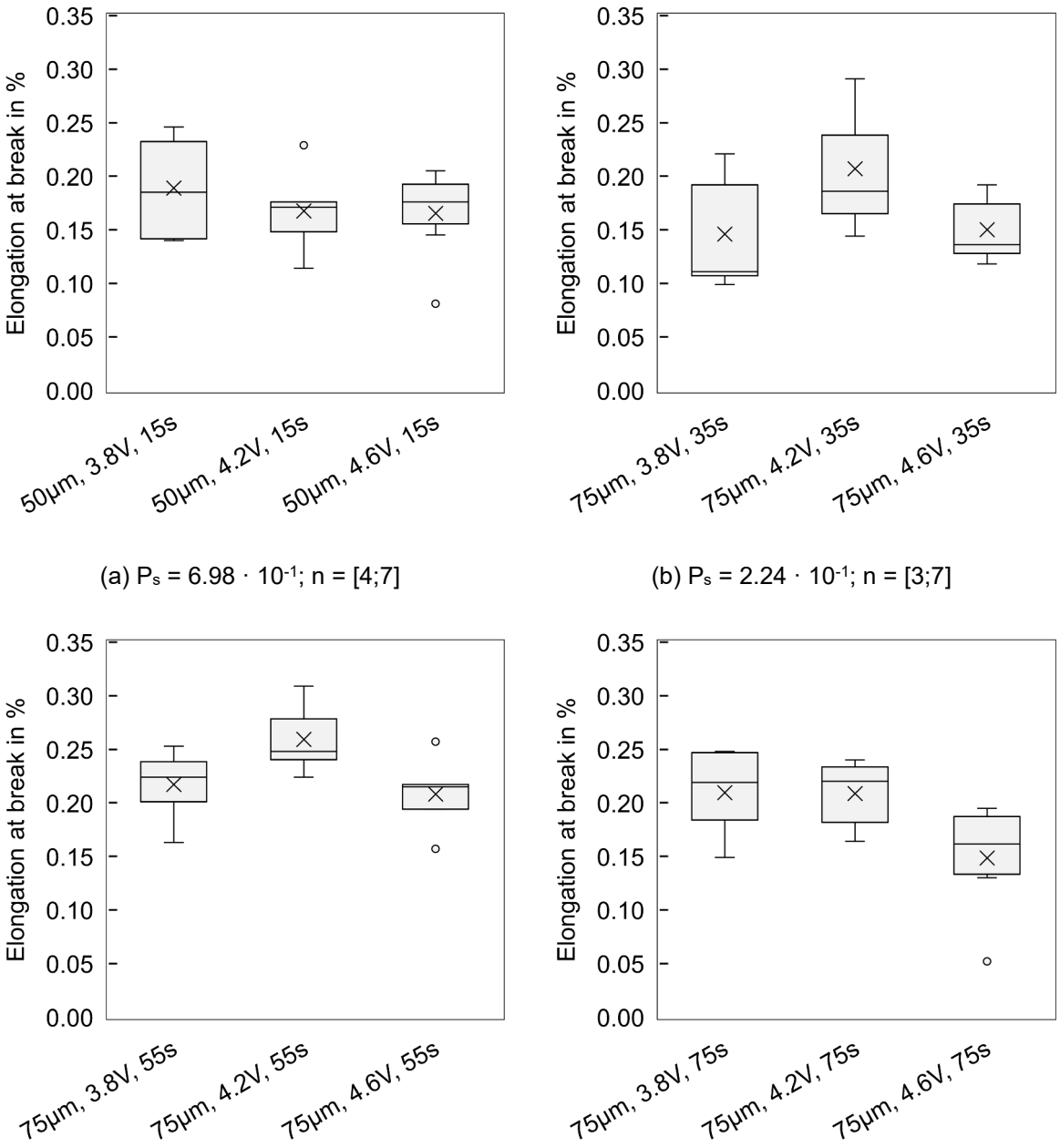

(a) $P_s = 6.98 \cdot 10^{-1}$; n = [4;7]

(b) $P_s = 2.24 \cdot 10^{-1}$; n = [3;7]

(c) $P_s = 4.14 \cdot 10^{-2}$; n = [5;7]

(d) $P_s = 5.25 \cdot 10^{-2}$; n = [5;6]

Figure 5.24: Direct comparison of elongation at break distributions with varying layer thicknesses at defined drying intensities and drying periods.

Dimensional Accuracy

The specimens' width is analysed to deduce a relationship between the drying intensity and binder migration. At higher drying intensities, higher energy inputs are applied. Thus, lower drying intensities may promote binder migration. Figure 5.25 indicates an overall contrary trend. However, it is to be noted that this diagram is compiled from only quantifiable data sets – the data comprising the boxplots for 4.6 V involve data from runs at higher layer thicknesses or lower drying periods. In contrast, the 3.8 V runs also yielded quantifiable results at 50 µm and longer drying periods.

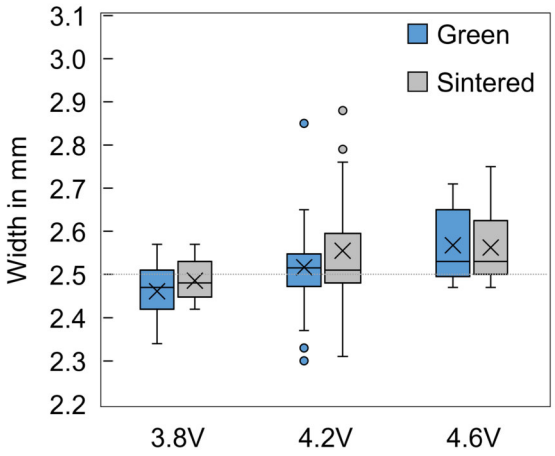

$P_s = 4.29 \cdot 10^{-2}$; $P_g = 6.90 \cdot 10^{-3}$; n = [15;21]

Figure 5.25: Specimens' width distributions with varying drying intensities.

Figure 5.26 shows the direct comparisons of selected parameter sets. No correlation between drying intensity and dimensional accuracy is determined.

Discussion There is no evidence that drying intensity affects either densification or binder migration. Though, porosity is believed to influence binder migration strongly. The literature reveals the crucial impact of the packing density on fluid infiltration behaviour (Barui et al., 2020, p. 34258). However, further research is needed to allow for a breakdown of counter-acting effects: Migration is presumed to increase with increasing moisture contents within the powder bed. However, the overall rise in temperature (chapter 5.2.4) may promote infiltration by raising the binder's viscosity or impede infiltration by hindering molecular motion due to an ongoing glass transition.

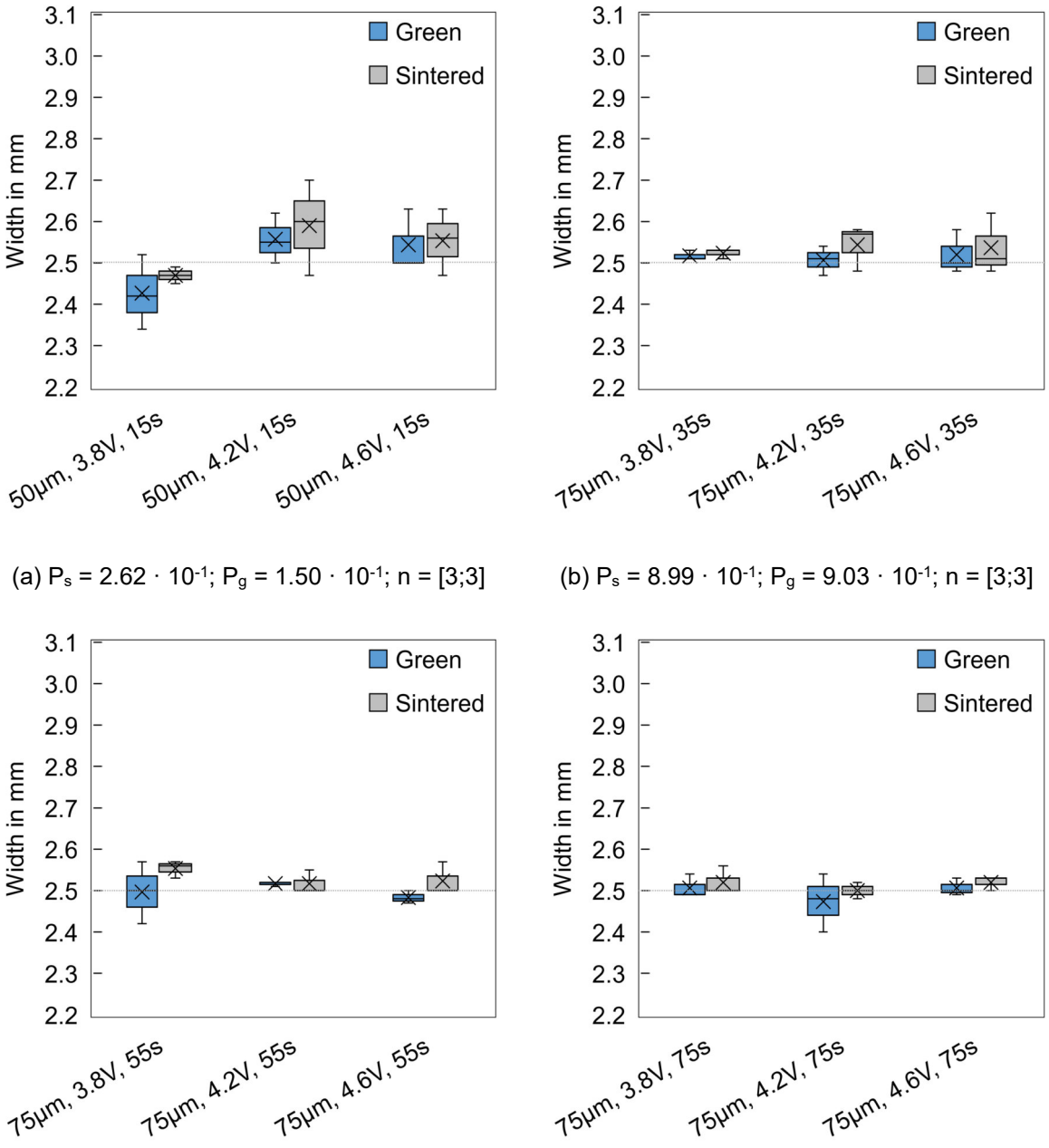

(a) $P_s = 2.62 \cdot 10^{-1}$; $P_g = 1.50 \cdot 10^{-1}$; n = [3;3]

(b) $P_s = 8.99 \cdot 10^{-1}$; $P_g = 9.03 \cdot 10^{-1}$; n = [3;3]

(c) $P_s = 3.69 \cdot 10^{-1}$; $P_g = 6.69 \cdot 10^{-1}$; n = [3;3]

(d) $P_s = 5.64 \cdot 10^{-1}$; $P_g = 6.10 \cdot 10^{-1}$; n = [3;3]

Figure 5.26: Direct comparison of specimens' width distributions with varying layer thicknesses at defined drying intensities and drying periods.

Surface Roughness

Figure 5.27 shows increasing plane-level surface roughnesses with increasing drying intensities at a high significance level. A medium average surface roughness Ra of 1.1 µm at PAV = 3.8 V compared to 1.7 µm at PAV = 4.6 V means an improvement of Ra by 33.5 %. Coincidently, Rz is found to improve by 28.3 % when applying the lowest level of drying intensity compared to the highest one selected in this study.

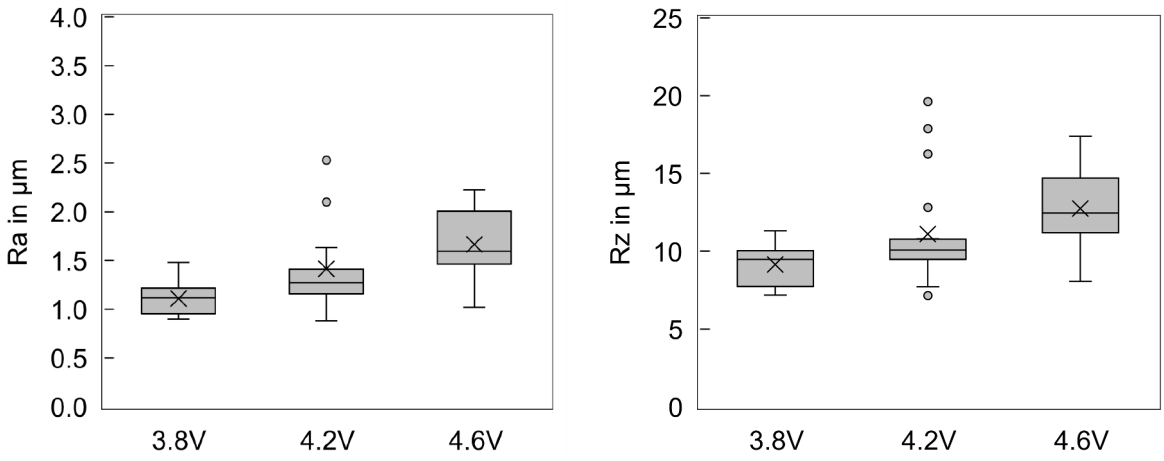

(a) $P_s = 1.50 \cdot 10^{-4}$; n = [15;21] (b) $P_s = 5.05 \cdot 10^{-4}$; n = [15;21]

Figure 5.27: Specimens' roughness distributions for varying drying intensities.

Discussion The results reveal a clear relationship between drying intensity and surface roughness. In thin film technologies, a correlation between drying rate during solvent evaporation, particle packing, and permeability has been reported (Reyes et al., 2007, pp. 356–357). Reyes et al. (2007) found a great difference in the particle arrangements with varying drying rates causing a nonlinear deterioration of surface qualities with increasing drying velocities (Reyes et al., 2007, pp. 361–367). Herein, the drying intensity is the process variable mostly influencing the drying rate. An impaired particle arrangement may be a reasonable explanation for reduced surface qualities when drying intensity increases. However, since no impact on density is shown coincidently, higher temperatures are more likely to cause surface imperfections by promoting adhesions on the coating head.

Homogeneity and Defects

In Figure 5.28, a comparison of the microstructure of specimens fabricated at different drying intensities is shown. It is demonstrated that the specimens dried at the lowest level of drying intensity do not exhibit any major flaws (Figure 5.28a, Figure 5.28b). In contrast, the specimens fabricated at the drying intensity of 4.6 V show multiple major flaws, preferably on the upper side of the specimen.

Discussion In chapter 5.2.1, major defects are found at both levels of layer thickness when applying the highest drying intensity and a drying period of 15 s. This effect was assumed to originate from moisture inclusions leading to differential stresses within the layer or thrust deformations. Figure 5.28 compares a 50 µm layer specimen dried at the lowest level of drying intensity to the corresponding specimen dried at the highest drying rate. Since the specimen dried at PAV = 3.8 V does not show any flaws, it is supposed that – in contrast to the higher

level of drying intensity – no rapid solidification appears here, but a more homogeneous moisture removal throughout the whole layer. That may lead to low differential stresses and enhanced structural stability of the layer, even though its overall moisture content during printing is high.

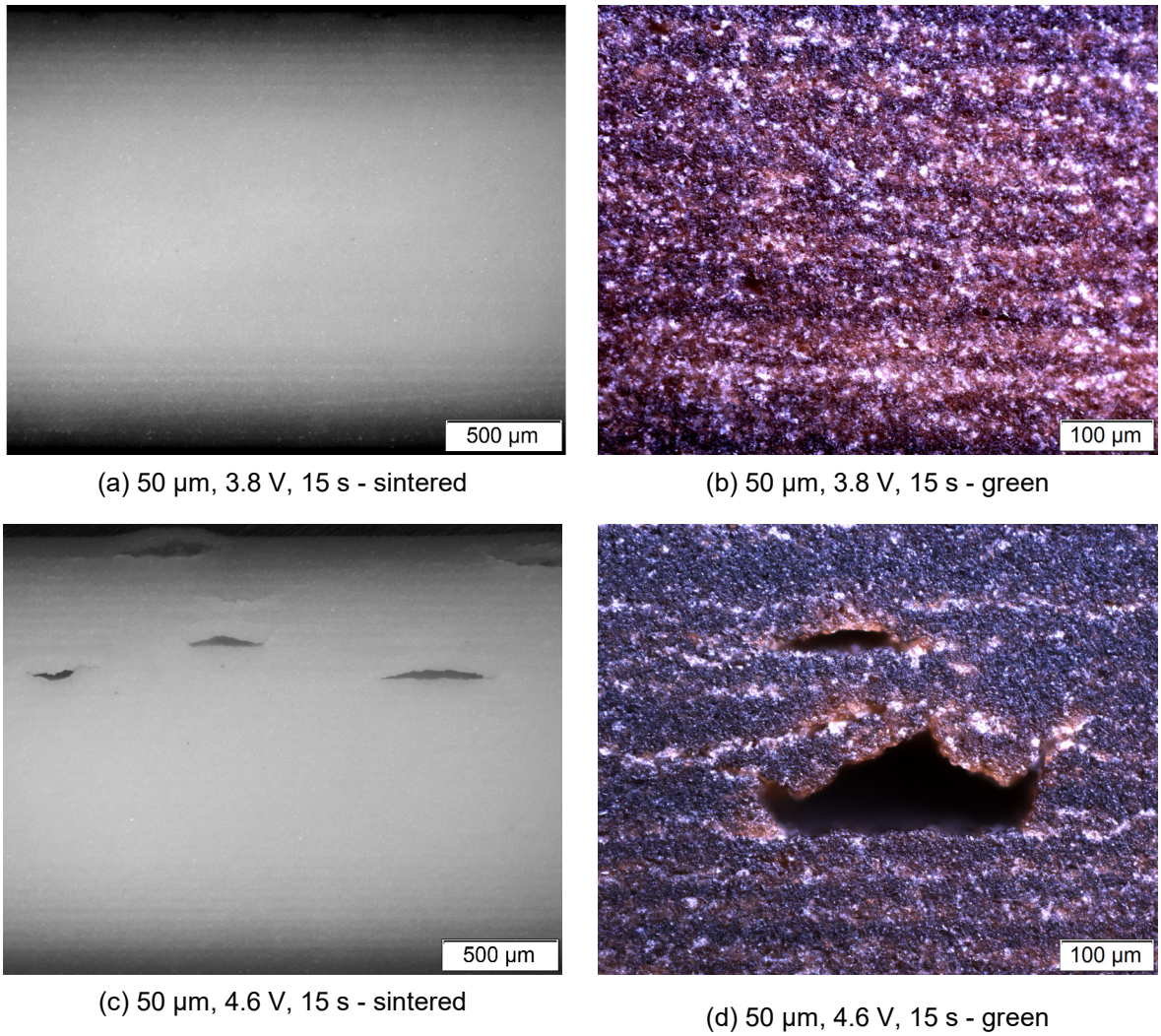

(a) 50 µm, 3.8 V, 15 s - sintered

(b) 50 µm, 3.8 V, 15 s - green

(c) 50 µm, 4.6 V, 15 s - sintered

(d) 50 µm, 4.6 V, 15 s - green

Figure 5.28: Micrographs showing the microstructure of specimens of varying drying intensities fabricated at the layer thickness of 50 µm and a drying period of 15 s.

5.2.3 Influence of the Drying Period

Drying is considered "excessive" when applying conditions that, in total, expose every layer to a high level of infrared radiation. Thus, along with the breakdown of the effect of the parameter drying intensity, the analysis is extended, focusing on the period of IR exposure – the drying period. The first research hypothesis addressed in this chapter states the increasing formation of defects when drying excessively. Secondly, greater progress in drying is regarded as favourable for improving compaction. In the following, both hypotheses are investigated for their truth.

Density

Figure 5.29 shows an overview of density data gained at different drying periods. With increasing drying periods, an increase in both sintered and green density is found until a drying period of 55 s. When drying for 75 s, a slight decrease in density is observed.

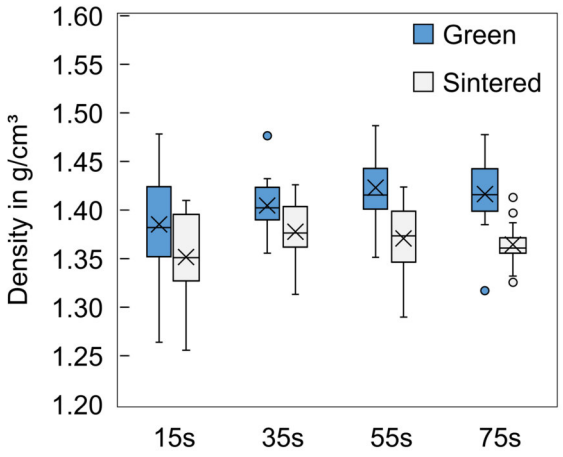

$P_s = 2.73 \cdot 10^{-1}$; $P_g = 1.62 \cdot 10^{-1}$; n = [12;16]

Figure 5.29: Specimens' width distributions with varying drying periods.

In direct comparisons (Figure 5.30), the trend of increasing densities with increasing drying periods is confirmed. All runs show the highest densities at a drying time of 55 s, whereas when drying for 75 s, a loss in density is found. The most significant finding in Figure 5.30b enables clear differentiation of densities assessed for varying drying periods.

Discussion While drying intensity and density did not show any interferences, significant deviations in density are found with varying drying periods. The duration of energy input for evaporation purposes is observed to affect densification and, thus, the global microstructure. Densification in slurry-based 3D printing is known to be attainable by either capillary flow or drying shrinkage. Capillary pressure as the driving force for densification during layer casting is indirectly proportional to the pore radius and the infiltration velocity (chapter 2.3.2). Moreover, an enhanced moisture capacity far off the pore saturation level allows for fast dehydration and thus enables increased packing densities. Conversely, drying shrinkage results in particle arrangement during drying itself. However, shrinkage during drying is mainly assigned to the constant rate period CRP, which is generally short compared to drying completely (Janetti, Janssen, 2020, p. 3). During CRP, a constant drying rate is accompanied by a linear moisture loss and hardly any temperature increase due to evaporation enthalpy (Figure 2.13).

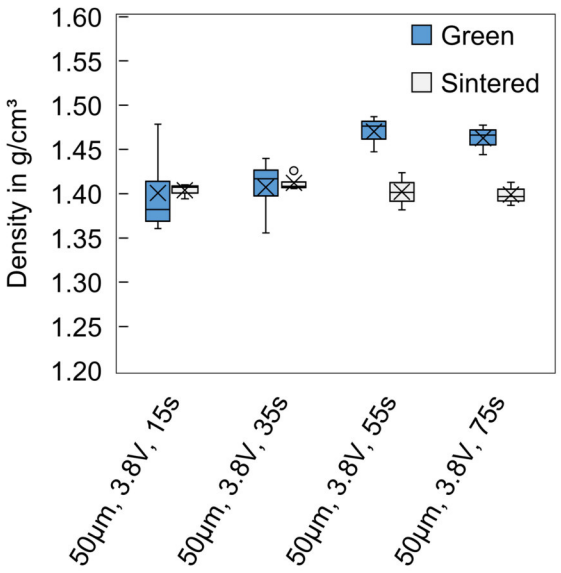

(a) $P_s = 6.21 \cdot 10^{-1}$; $P_g = 6.91 \cdot 10^{-2}$; n = [3;3]

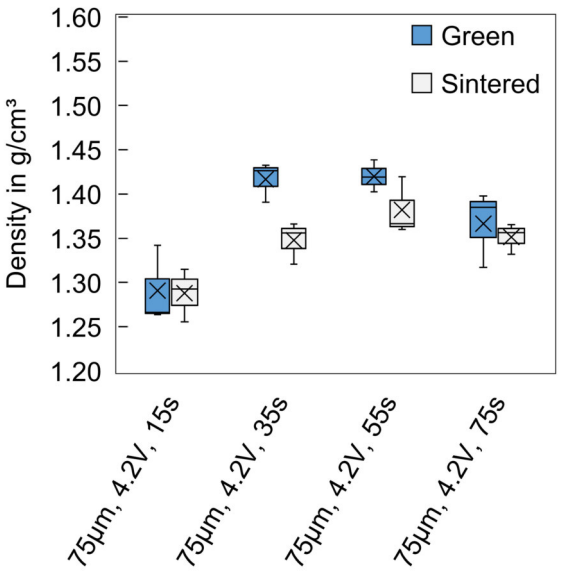

(b) $P_s = 1.51 \cdot 10^{-2}$; $P_g = 5.47 \cdot 10^{-3}$; n = [3;3]

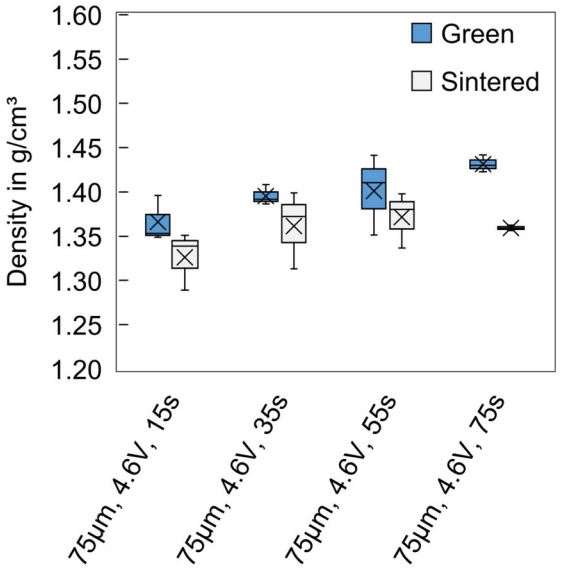

(c) $P_s = 3.86 \cdot 10^{-1}$; $P_g = 1.03 \cdot 10^{-1}$; n = [3;3]

Figure 5.30: Direct comparison of specimens' width distributions with varying drying periods at defined layer thicknesses and drying intensities.

Compaction via capillary flow is assumed to be more spontaneous than the drying process's total duration. However, since a more proceeded drying stage will influence moisture capacity and capillary flow, capillary effects and drying are believed to interact and superpose during layer-wise drying. When exceeding FRP1, relevant temperature increases above ambient temperature are expected locally at the exposed surface, which is believed to cause rapid solidification instead of regular capillary flow when applying the subsequent layer. When reaching the drying period of 75 s, relevant temperature increases are observed (chapter 5.2.4)

that may lead to a rapid moisture release impeding capillary flow or blistering during the deposition of a new layer.

Four-point Bending Strength

Analogous to the findings on the density, Figure 5.31 shows significantly increasing sintered bending strengths with increasing drying periods only until a drying period of 55 s is reached while the green strength is further increasing.

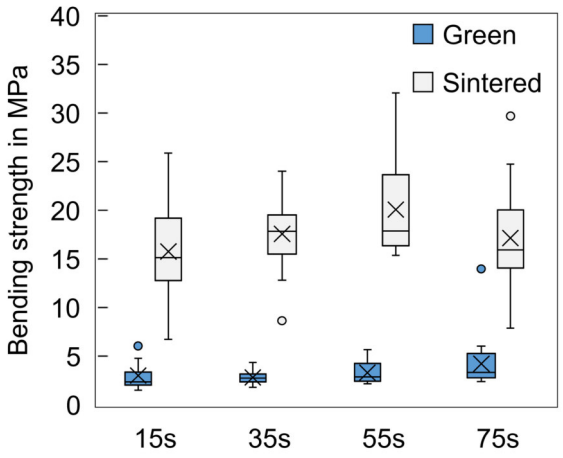

$P_s = 1.35 \cdot 10^{-2}$; $P_g = 5.17 \cdot 10^{-2}$; n = [14;28]

Figure 5.31: Bending strength distributions with varying drying periods.

When directly comparing associated parameter sets (Figure 5.32), the growth in sintered strength with increasing drying periods until certain drying progress is confirmed. Moreover, all parameter combinations showed enhanced green strengths at higher drying periods.

Discussion Higher process temperatures attained by extended drying periods are found to lead to an enhanced level of curing of the thermoset resin used in this study and, thus, to higher green strengths. This context is discussed in greater detail in chapter 5.2.4. However, the sintered strength is affected by the sintered microstructure only. The improved packing density detected above correlates with the mechanical strength. The higher packing density, and thus the reduced pore volume directly leads to enhanced bending strengths.

Contrary to the drying intensity effects assessment, a direct correlation between density and bending strength can be revealed. The enlarged process window can explain that effect. While the heat flux generated by the respective drying intensity can only be varied by a factor of 1.6, radiation is varied from 15 s to 75 s representing a factor of five.

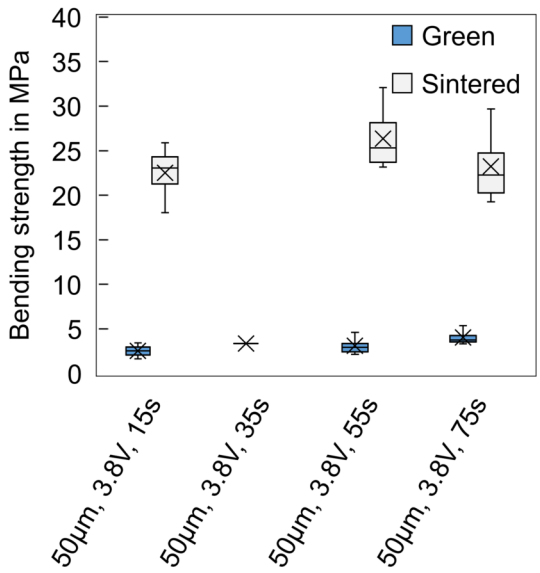

(a) $P_s = 2.42 \cdot 10^{-1}$; $P_g = 3.60 \cdot 10^{-1}$; n = [0;6]

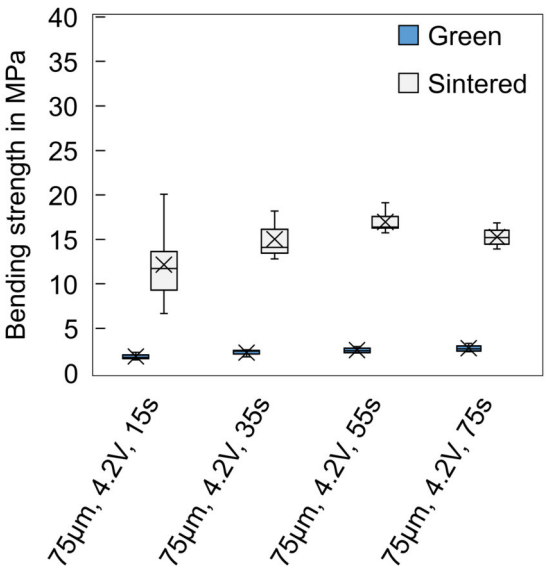

(b) $P_s = 6.71 \cdot 10^{-3}$; $P_g = 4.72 \cdot 10^{-2}$; n = [3;6]

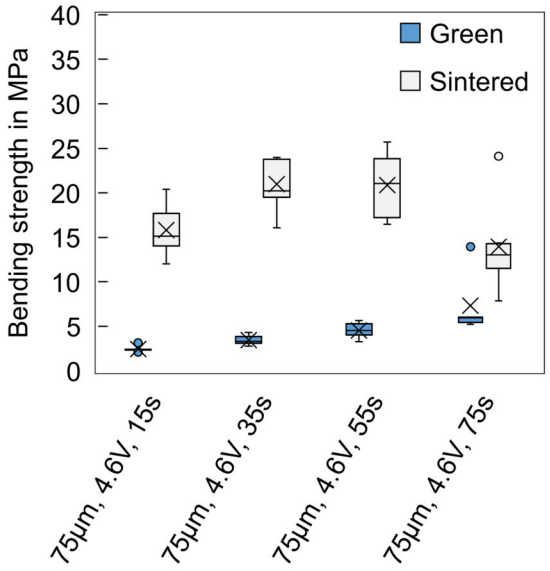

(c) $P_s = 1.11 \cdot 10^{-2}$; $P_g = 3.01 \cdot 10^{-3}$; n = [5;8]

Figure 5.32: Direct comparison of bending strength distributions with varying drying periods at defined layer thicknesses and drying intensities. Note of caution for interpretation: The data of sintered bodies shown in (a) are incomplete (n=0) due to transport damage.

Elongation at Break

Figure 5.33 shows the elongation at break distributions of sintered specimens depending on the drying duration. In accordance with the strength development displayed in Figure 5.31, a significantly increasing elongation at break with increasing drying periods until a drying period of 55 s is found.

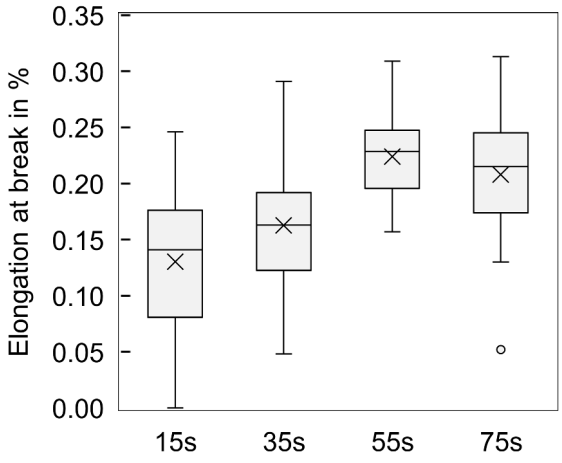

$P_s = 1.45 \cdot 10^{-7}$; n = [19;28]

Figure 5.33: Elongation at break distributions with varying drying periods.

In Figure 5.34, direct comparisons confirm the increasing elongation at break at a constantly high level of significance until a certain level is reached. Only Figure 5.34a reveals higher elongation at break values at the drying period of 75 s compared to the respective 55 s run, even though the measured strength is found higher at 55 s (Figure 5.32a).

Discussion The typical relationship between strength and elongation at break is confirmed in Figure 5.33 and Figure 5.34. The courses meet the expectations in light of the strength development with increasing drying periods, as detected in Figure 5.31 and Figure 5.32. In summary, the material properties of density, bending strength, and elongation at break assessed within this chapter prove two research hypotheses to be true: First, high drying periods have been found to improve compaction and lead to higher density and strength. Second, excessive drying generated by applying exceedingly high drying periods leads to major flaws and, concurrently, to reduced strength and elongation at break distributions.

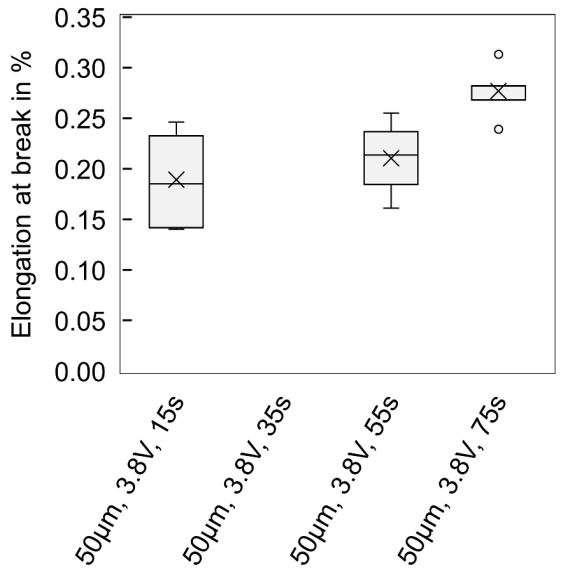

(a) $P_s = 2.43 \cdot 10^{-2}$; n = [0;6]

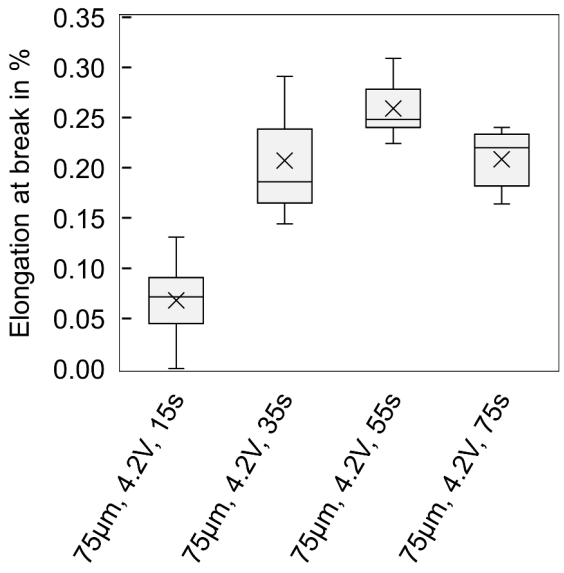

(b) $P_s = 5.54 \cdot 10^{-6}$; n = [3;6]

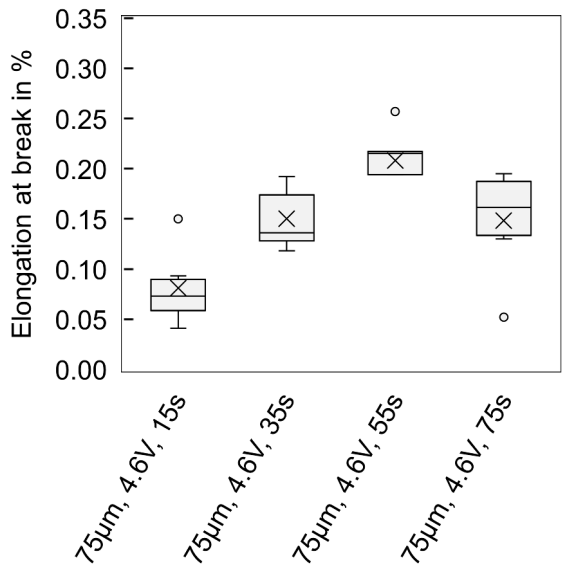

(c) $P_s = 3.46 \cdot 10^{-4}$; n = [5;7]

Figure 5.34: Direct comparison of elongation at break distributions with varying drying periods at defined layer thicknesses and drying intensities. Note of caution for interpretation: The data of sintered bodies shown in (a) are incomplete (n=0) due to transport damage.

Dimensional Accuracy

The specimens' width is analysed to assess the correlation between the drying progress and binder migration (Figure 5.35). At the lowest level of drying period, 15 s, an increased width and a high spread of data are found. In contrast, as long as sufficient energy for evaporation of the slurry solvent is provided (which is the case when drying for at least 35 s), the specimens' width is determined to be a constant value close to the target.

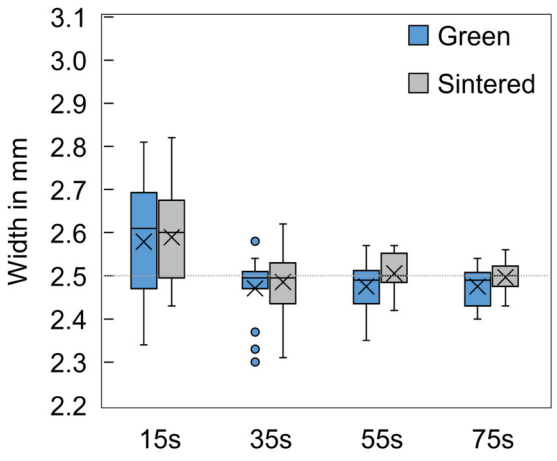

$P_s = 3.56 \cdot 10^{-3}$; $P_g = 5.12 \cdot 10^{-3}$; n = [12;16]

Figure 5.35: Specimens' width distributions with varying drying periods.

When comparing directly related parameter combinations, cross-links between layer thickness and drying periods are noticed regarding lateral binder migration. Figure 5.36 shows the effect of lateral binder migration only at the higher layer thickness level in combination with the lowest drying period level.

Discussion Since relevant deviations from the target specimens' width are measured when both a high amount of water is supplied and the drying period is selected to be short, a relationship between residual moisture contents and lateral binder migration is assumed. The migration phenomenon itself is known to be more sensitive to the diffusion coefficient that describes the transport of a substance due to particle movement than to the conductivity of the substrate (Farkas et al., 1991, p. 1045). Farkas et al. (1991) compared the binder infiltration profile during the drying of paper and found binder particles in more distant sites when drying slowly (Farkas et al., 1991, pp. 1042–1045). Klinov, Anashkin (2019) investigated diffusion in binary aqueous solutions of alcohols and found an almost doubled diffusion coefficient of IPA when increasing the temperature within this study's relevant temperature range from 40 °C to 60 °C (Klinov, Anashkin, 2019, p. 5). The high diffusion rate of IPA, the solvent in the binder system used, at elevated temperatures is suspected of leading to the high selectivity of binder application and impeded migration.

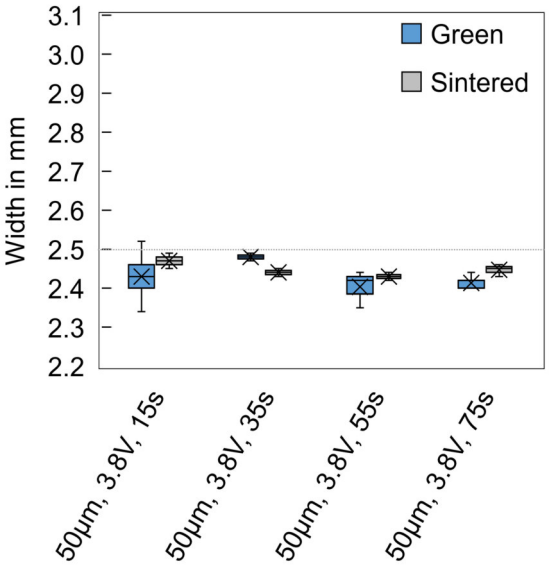

(a) $P_s = 3.91 \cdot 10^{-2}$; $P_g = 4.61 \cdot 10^{-1}$; n = [3;3]

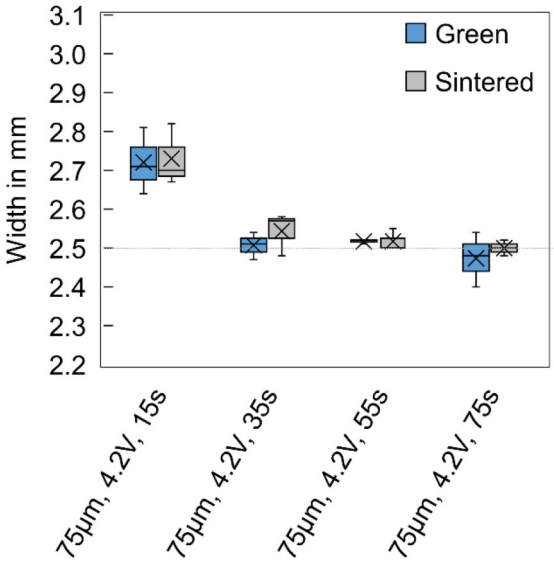

(b) $P_s = 1.98 \cdot 10^{-3}$; $P_g = 3.12 \cdot 10^{-3}$; n = [3;3]

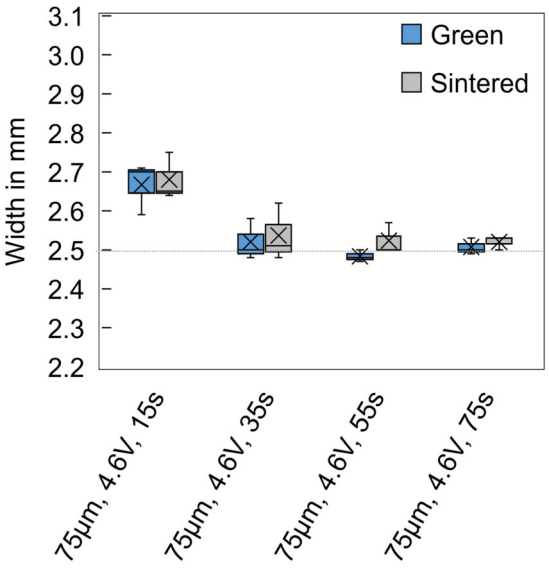

(c) $P_s = 2.97 \cdot 10^{-1}$; $P_g = 3.81 \cdot 10^{-3}$; n = [3;3]

Figure 5.36: Direct comparison of specimens' width distributions with varying drying periods at defined layer thicknesses and drying intensities.

Surface Roughness

Figure 5.37 shows the development of the plane-level surface roughness with increasing drying periods. While from 35 s, a constant level of Ra ~ 1.2 µm, or Rz ~ 10 µm, is observed, the drying period of 15 s is shown to be clearly unfavourable with respect to surface quality.

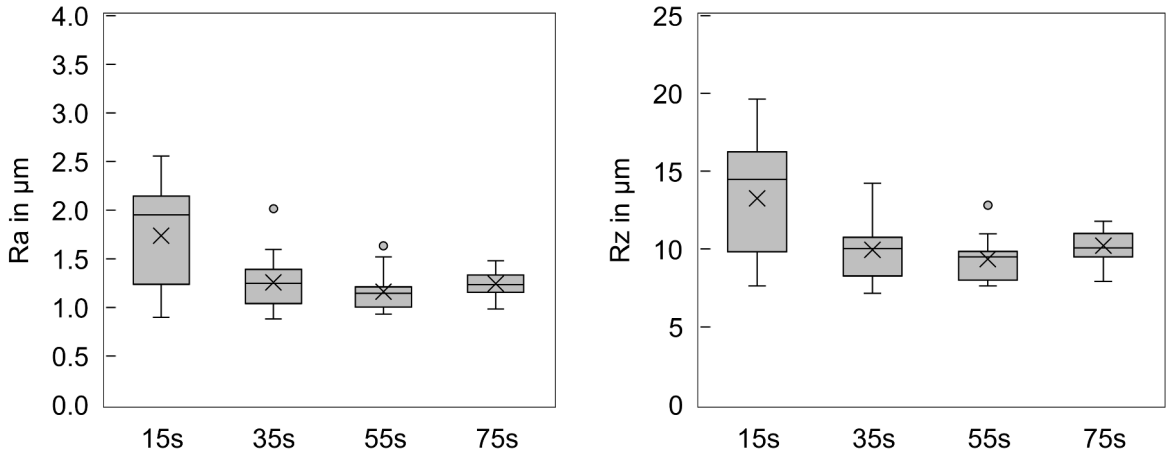

(a) $P_s = 3.22 \cdot 10^{-4}$; n = [12;15] (b) $P_s = 5.72 \cdot 10^{-4}$; n = [12;15]

Figure 5.37: Specimens' roughness distributions for varying drying periods.

Discussion As shown above, low drying times in combination with high drying intensities lead to major flaw generation assigned to inhomogeneous moisture distribution within the layer. Those major flaws of sizes up to 500 µm are also suspected to reduce surface qualities.

Homogeneity and Defects

Figure 5.38 demonstrates that the specimen dried for only 15 s at PAV = 4.6 V shows large flaws, which complies with the expectations from the mechanical testing results. In contrast, the specimens dried for 55 s indicate no impairments within the microstructure. However, interlayer cracks are observed when drying excessively (for as long as 75 s).

Discussion The microstructural analysis shows that the drying period needs to be carefully adjusted to further drying-related parameters to avoid differential stresses. It has been evidenced that an excessively long drying period is disadvantageous in many respects, as well as a low drying period in combination with high drying intensities.

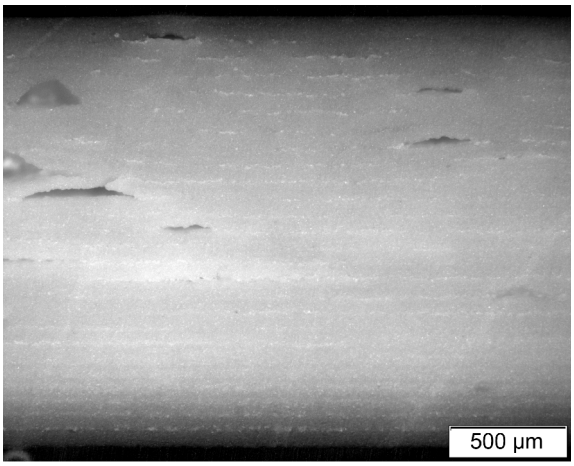

(a) 75 µm, 4.6 V, 15 s - sintered

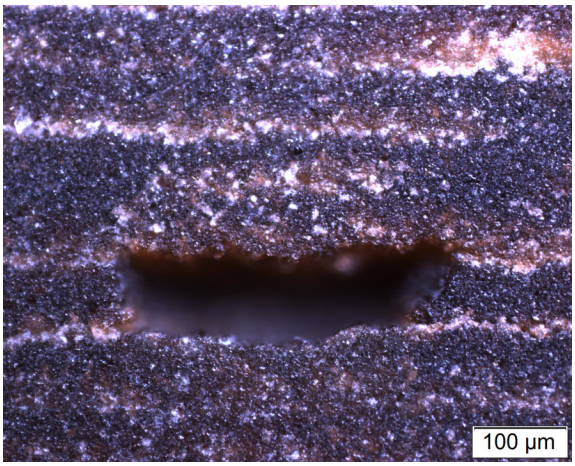

(b) 75 µm, 4.6 V, 15 s - green

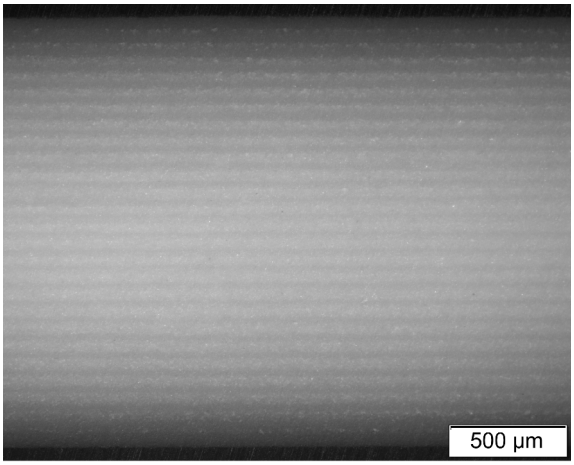

(c) 75 µm, 4.6 V, 55 s - sintered

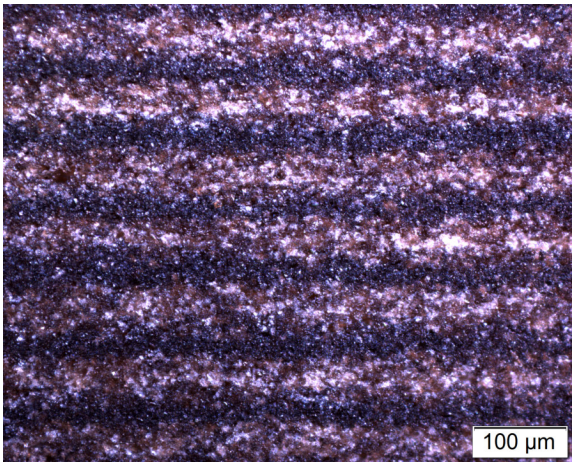

(d) 75 µm, 4.6 V, 55 s - green

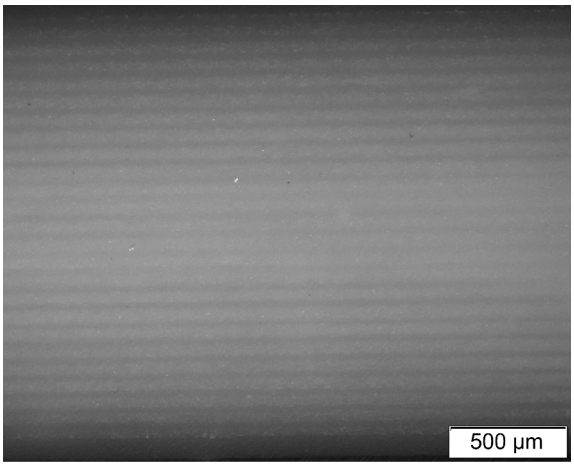

(e) 75 µm, 4.6 V, 75 s - sintered

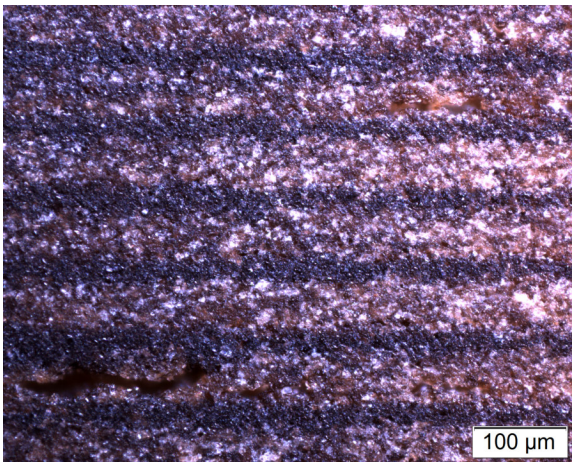

(f) 75 µm, 4.6 V, 75 s - green

Figure 5.38: Micrographs showing the microstructure of specimens of varying drying periods fabricated at the layer thickness of 75 µm and PAV = 4.6 V.

5.2.4 Temperature Evolution and Influence of the Layer Temperature

The temperature evolution during drying obtained by a thermocouple positioned below the respective specimens (Figure 4.4b) is analysed to verify the above-mentioned results. Figure 5.39 indicates whether an advanced drying stage is reached as expected when varying layer thickness, drying intensity, and drying period. All parameters are found to be significantly deviating. As anticipated, higher drying intensities and, thus, a higher radiated power output or higher drying periods clearly lead to higher layer temperatures (Figure 5.39b, Figure 5.39c).

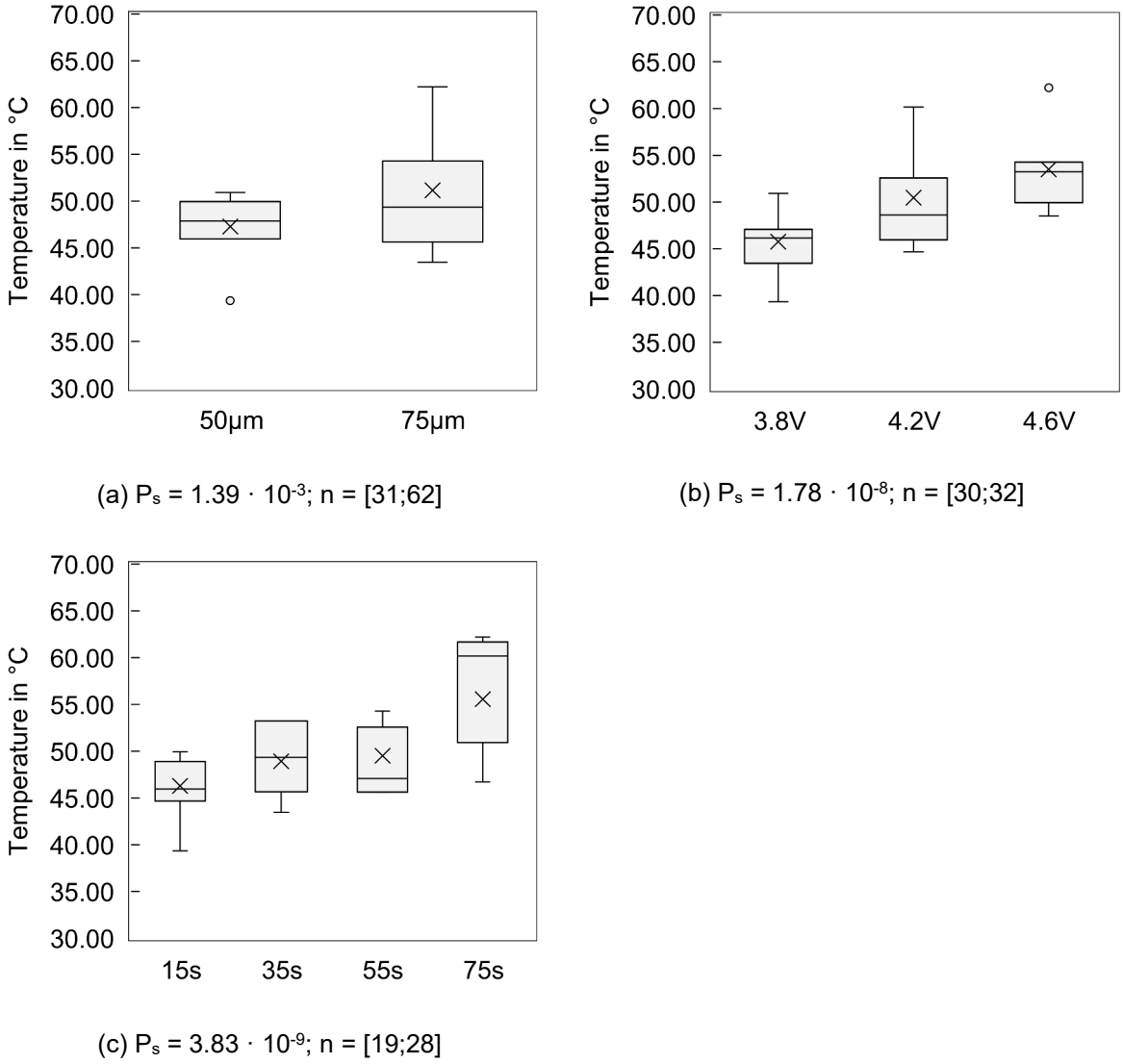

(a) $P_s = 1.39 \cdot 10^{-3}$; n = [31;62]

(b) $P_s = 1.78 \cdot 10^{-8}$; n = [30;32]

(c) $P_s = 3.83 \cdot 10^{-9}$; n = [19;28]

Figure 5.39: Temperature evolution during drying – dependent on (a) the layer thickness, (b) the drying intensity, and (c) the drying time.

Since only 50 µm specimens fabricated at a low drying intensity or a low drying period led to green bodies stable enough to allow for material analysis (Table 5.1), the overall temperatures attained when using a higher layer thickness were slightly higher than the respective ones of the lower level of layer thickness (Figure 5.39a). Though, directly comparable parameter sets

show 1.5 °C higher temperatures at the lower layer thickness. Consequently, a proceeded drying stage is evidenced to be attainable by lowering the layer thickness, by increasing the power to be radiated, or by increasing the duration of radiation exposure.

Figure 5.40 shows diagrams of the average density, strength, and elongation at break attained at different layer temperatures, coloured corresponding to the parameter drying intensity. While increasing temperatures tend to enhance green bodies' densities and strengths (Figure 5.40b, Figure 5.40d), no clear relationship between the temperatures and both densities and strengths in the sintered state can be derived (Figure 5.40a, Figure 5.40c). However, Figure 5.40e reveals a tendency towards higher elongation at break values at higher layer temperatures.

Discussion When drying ceramic films, most of the shrinkage and drying stresses are known to occur during CRP, which is the initial stage of drying in which the pores are still filled with the liquid phase (Scherer, 1990, p. 1). However, temperature increases above the wet bulb temperature arise only during FRP1 and FRP2. In this study, reaching the elevated drying stages of FRP1 and FRP2 is accomplished by increasing the drying periods and rate or by reducing the layer thickness. Due to reciprocal influences, enhanced data reliability and conclusiveness are achieved by directly drawing conclusions between material properties and input parameters instead of temperature data attained by process monitoring. The layer temperature development is considered particularly dependent on the residual moisture of the powder compact and its distribution.

Moreover, cooling due to evaporation is continuously superimposed with heat transfer which, in turn, is strongly dependent on the pore fluid's thermal properties. Thus, future research may focus, in particular, on applying advanced methods from heat and water transport physics to the slurry-based 3D printing process. Chapter 5.2.5 introduces the requirements for modelling these complex processes in the future.

The green bodies' increasing densities and strengths with elevated temperatures are attributed to the curing behaviour of the novolak system. Differential scanning calorimetry (DSC) is a thermal analysis method measuring the heat flow from or into a small material sample during a prescribed temperature program and is thus a characterisation method appropriate for investigating the polymerisation of thermoset resins (Focke et al., 1991, p. 1665). Various studies have investigated the curing of phenolic resins using this method. Chun-Chiao, Jie (1988) report a softening of novolak resin from 50 °C (Chun-Chiao, Jie, 1988, p. 175). Maji et al. (2014) observed an endothermic polymerization reaction from ~ 67 °C (Maji et al., 2014, p. 588).

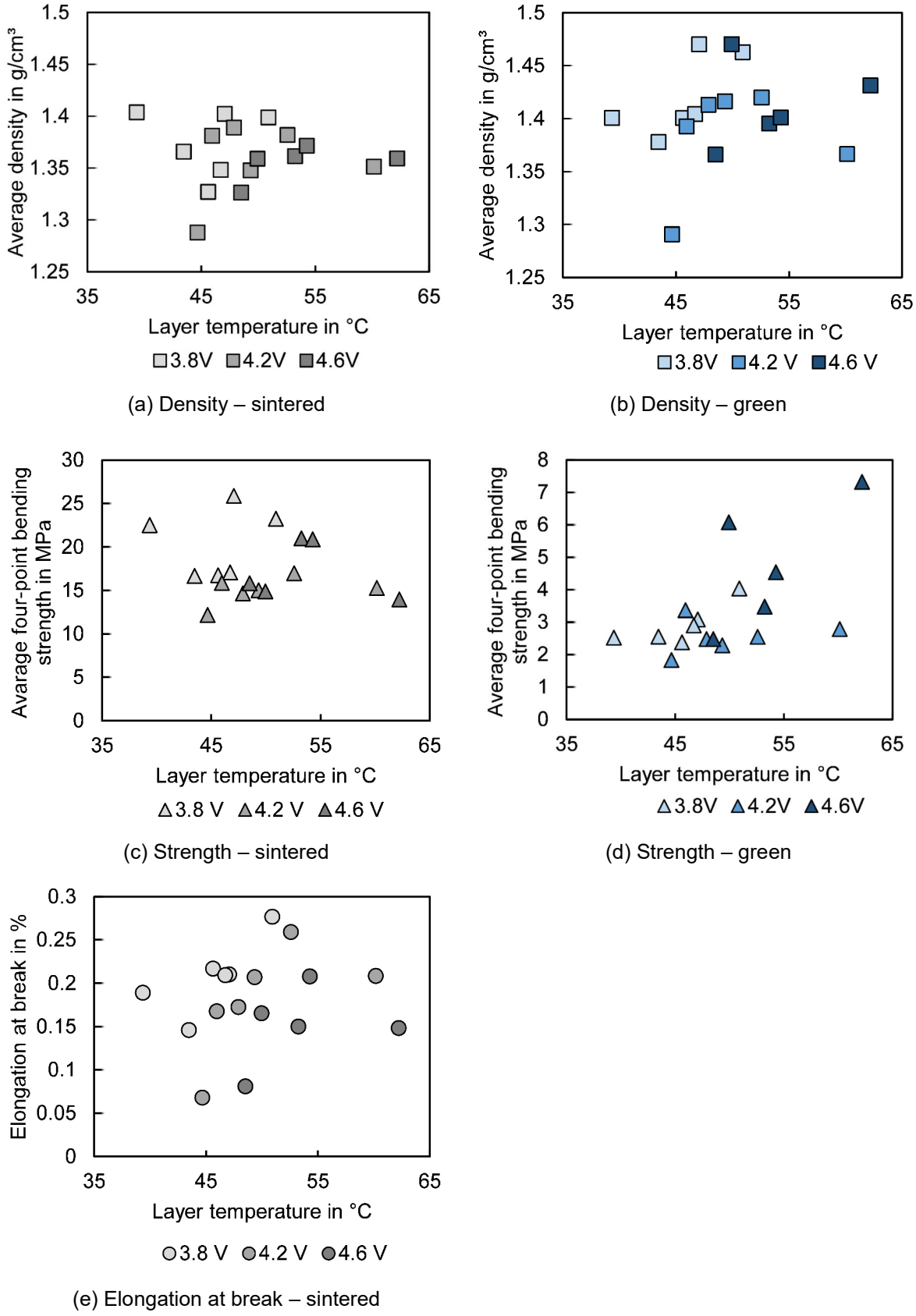

Figure 5.40: Averaged values of selected material properties attained dependent on the temperatures evolving at different drying intensities.

When analysing a chemically similar system, Pöhlmann (2006) found an endothermic peak at ~ 58 °C and assigned it to relaxation during the glass transition that occurs prior to the exothermic cross-linking from 140 °C (Pöhlmann, 2006, pp. 30–34). The authors interpret the endothermic reaction as relaxation accompanied by vaporisation, implying viscosity changes or an impeded molecular motion that may prevent binder migration.

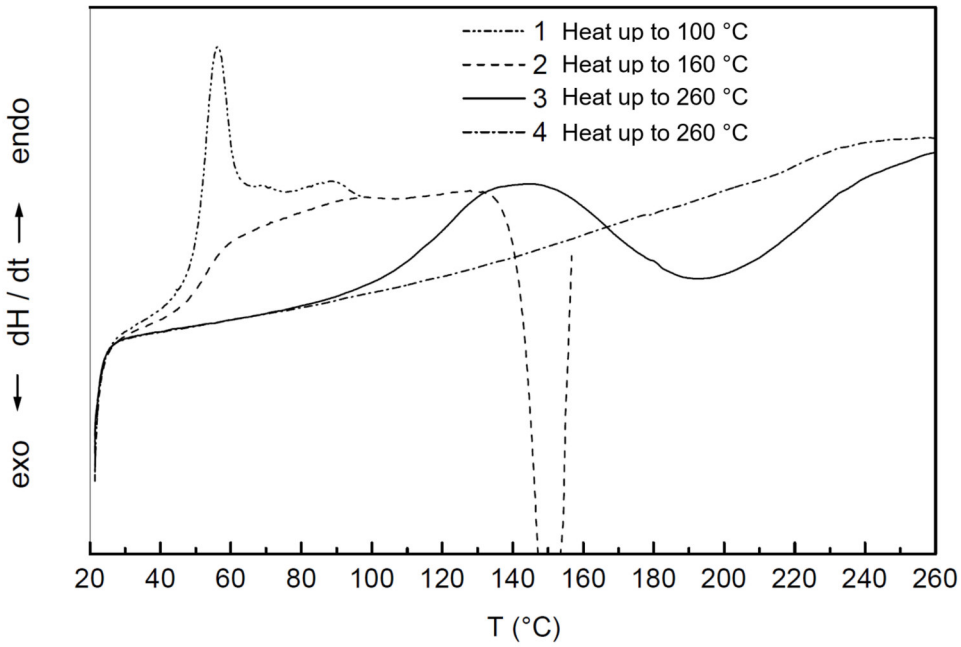

Figure 5.41: DSC curve of Novolak/ Hexa 90/10 wt.-% (Pöhlmann, 2006, p. 31).

5.2.5 Requirements for Model Development

Due to the strong influence of the drying conditions on the specimens' properties demonstrated above and the potential of the slurry-based 3D printing process to allow for the processing of almost every material system, model development for the slurry-based layer casting and drying process is considered important for further advancements in process development. Given this thesis's complexity and wide scope, merely the requirements for model development are discussed that provide a basis for model development on future industrial machines. This chapter is divided into subchapters concerning the drying of thin layers, transport processes and heat transfer in porous media. It is suggested to develop an advanced model capable of linking thermodynamic and fluid mechanic models to allocate the interacting mechanisms within the iterating process steps in slurry-based 3D printing.

Drying of Thin Layers

Typically, there is an exponential relationship between a thin film's weight and the drying time. Varying authors have proposed different models. Akpinar et al. (2004) summarised 14 different expressions. Due to the inadequate measurement accuracy of the measurement equipment

available for this study (Kern PCB 1000-2, Kern & Sohn GmbH, Balingen, Germany), the best fit with experimentally determined data on a slurry volume in the magnitude of 100 - 200 times higher than one layer in slurry-based 3D printing has been investigated exemplary for those models by regression analysis (Figure 5.42). The two-term model suggested by Henderson was found to represent the best fit with the experimentally determined data.

$$MR = b_1\, e^{-z_1 t} + b_2\, e^{-z_2 t} \tag{5.3}$$

With the moisture ratio MR, the time t, and the model coefficients $b_1 = 6.374 \cdot 10^4$, $b_2 = 1605$, $z_1 = 2.004 \cdot 10^{-4}$ and $z_2 = 4.651 \cdot 10^{-4}$. For developing an advanced material model, further data acquisition is needed in accordance with the actual layer volume and different drying times. The author suggests using a fully enclosed measurement setup and a microbalance.

Chiu, Cima (1993) utilise an optical interference technique to analyse substrate deflection and, thus, stress development during the drying of ceramic films. However, no prior work is known to the author addressing a layer-wise approach taking into account the strongly differing behaviour when applying thin films on porous layers, eventually retaining moisture.

Those methods will assist in identifying a slurry's drying behaviour but need to be coupled through differential equations to enable a process model considering the layer-wise build-up. However, even more advanced methods and models are to be qualified to provide a model that covers aspects regarding the development of the microstructure during drying, as described by Breinlinger (2015).

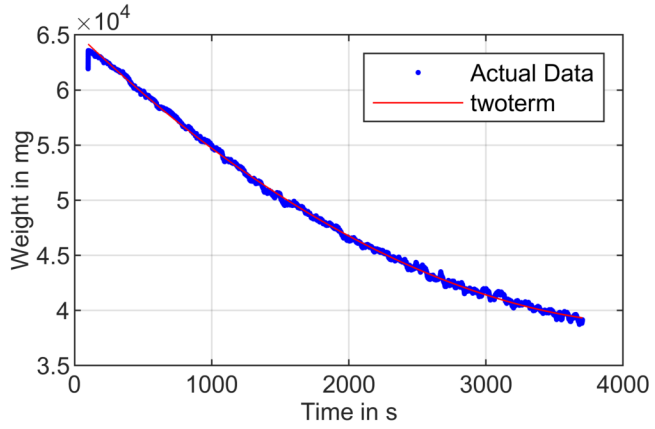

Figure 5.42:Regression analysis of experimental data to determine an appropriate drying model.

Transport Processes in Porous Media

Grau (1998) suggests using Washburn's equation to calculate the infiltration times in slurry-based 3D printing. Chapter 2.3.2 gives an introduction to modelling the infiltration times. The infiltration time t can be accordingly calculated by:

$$t = \frac{h^2 \eta}{2 \Phi k p_c} \tag{5.4}$$

With the liquid column height h, the liquid viscosity η, the void fraction Φ, the permeability k, and the capillary pressure p_c. The author refers to Grau 's detailed example calculations on the slurry-based layer casting process, including the application of the colloidal filtration model developed by Aksay, Schilling (1984) that accounts for particle consolidation on the interface to a porous substrate, mould or layer (Grau, 1998, 175-193), and Washburn's equation (Grau, 1998, 222–224).

However, with today's advanced computing capacities, solving the flow and transport problems might be preferentially conducted using simulation tools. Besides multiple commercial tools (e.g. Flow-3D), open-source simulators like DuMu^x allow for the modular setup of multi-domain simulations solving partial differential equations in porous-medium flow (Koch et al., 2021, pp. 423–424). Fetzer et al. (2017) account for both heat and water flux in a hydro system application using DuMu^x by presenting a simulation of evaporation from wet soil surfaces. Investigating the adaptability of those existing models to slurry-based 3D printing will be a highly interesting task in future research.

Heat Transfer in Porous Media

One can describe the temperature variations within a bulk solid containing a pore fluid by the so-called heat penetration coefficient S (Buntebarth, 2020, p. 3):

$$S = \frac{\lambda_{fluid} \sqrt{\kappa_{mtx}}}{\lambda_{mtx} \sqrt{\kappa_{fluid}}} = \frac{\sqrt{\lambda_{fluid} \rho_{fluid} c_{fluid}}}{\sqrt{\lambda_{mtx} \rho_{mtx} c_{mtx}}} \tag{5.5}$$

With the thermal conductivity λ and the thermal diffusivity κ of the fluid (λ_{fluid} and κ_{fluid}) and of the matrix (λ_{mtx} and κ_{mtx}).

The thermal conductivity of a slurry mixture can be approximately calculated to be around 3 W/(mK). In contrast, the powder compact's thermal conductivity (the pores are filled with air instead of water) is estimated to be around 1.3 W/(mK). Analogously, the thermal diffusivity is estimated to lower from around 1.4 mm²/s to around 0.4 mm²/s. A calculation of the heat penetration coefficients S of the theoretical limits within the application in slurry-based 3D printing, which are the slurry consisting of quartz and fully saturated with water S_{Slurry} (5.6)

and the powder compact with pores that are fully saturated with air $S_{Compact}$ (5.7) results in a factor of 270 higher heat penetration coefficient in case of the slurry. (Buntebarth, 2020, pp. 3–5) Even though the experiments described above run within tighter limits, the thermal properties can be stated as widely changing during drying. Given the reciprocal influences of temperature development, the drying parameters, and the resulting layer properties, a temperature-dependent model needs to account for the kinetics of both heat and transport flux. Its implementation using advanced simulation tools is recommended due to the problem's complexity.

$$S_{Slurry} = \frac{0.6\ \frac{W}{m\ K}\sqrt{3.57\frac{mm^2}{s}}}{7\frac{W}{m\ K}\sqrt{0.14\frac{mm^2}{s}}} = 0.43 \tag{5.6}$$

$$S_{Compact} = \frac{0.026\ \frac{W}{m\ K}\sqrt{3.57\frac{mm^2}{s}}}{7\frac{W}{m\ K}\sqrt{20\frac{mm^2}{s}}} = 0.0016 \tag{5.7}$$

5.3 Consequences for Industrial Core Production

In chapter 5.2, the effects of the drying conditions on the material properties are analysed, and the cause-effect chains are discussed. In the interests of clarity, it is discussed briefly how the newly gained knowledge on the control of materials' properties via drying configuration can be exploited for adjusting the slurry-based 3D printing process parameters according to the requirements in an industrial environment – with a special focus on material properties and economic efficiency.

5.3.1 Control of Casting Cores' Properties via Drying Conditions

Figure 5.43 summarises the effect of increasing the drying parameters layer thickness, drying intensity, drying period, and temperature on the crucial material properties of casting cores. It becomes clear that raising the layer thickness causes unfavourable changes in all material properties except for the surface quality measured on the plane surface. Though, as discussed above, 3D parts' surface properties are necessarily connected with the layer thickness.

The positive effect of increasing the drying period to a certain extent is likewise evidently demonstrated. When increasing the drying intensity, no unambiguous conclusion can be drawn since elongation at break, and surface quality are shown to be lower. In contrast, four-point bending strength even increases in some instances.

Moreover, higher process temperatures lead to higher green densities and strengths and tend to allow for increased elongation at break values in sintered state. However, no evident conclusion can be drawn here for the reasons extensively discussed in chapters 5.2.4 and 5.2.5.

		Layer thickness ↑	Drying intensity ↑	Drying period ↑	Temperature ↑
Density	Green	↓	○	↑*	↑
	Sintered	↓	○	↑*	○
Four-point bending strength	Green	↓	↑	↑*	↑
	Sintered	↓	50 µm ↓ 75 µm ↑	↑*	○
Elongation at break	Sintered	↓	↓	↑*	↑
Dimensional accuracy	Green	↓	○	↑	○
	Sintered	↓	○	↑	○
Surface quality	Sintered	○	↓	↑	○

* Peak at 55 s

Figure 5.43: Summary of the effects of the investigated drying conditions on the resulting material properties.

Conclusion and implications It has been shown that in slurry-based 3D printing, lower layer thicknesses improve materials' properties in terms of density, mechanical strength, ductility, dimensional accuracy, and surface quality. The drawback of lower layer thicknesses is solely the total increase in 3D printing process time and cost due to increased axes movements for the same print job. Since higher initial densities are achieved that facilitate densification during sintering, this disadvantage might be attenuated by time savings in post-processing. Since no further improvements are possible with increasing the drying periods above 55 s, it is recommended to dry at maximum up to this period. An overall rating of the investigated parameter sets (Figure 5.44) visualises possible trade-offs in process settings by assigning ratings from one to ten in linear gradations to each parameter set except for the sets using the exaggerated drying period of 75 s. When applying short process times, comparatively disadvantageous properties are to be expected, whereas superior strength, surface quality, and dimensional accuracy are attainable with a trade-off in process time.

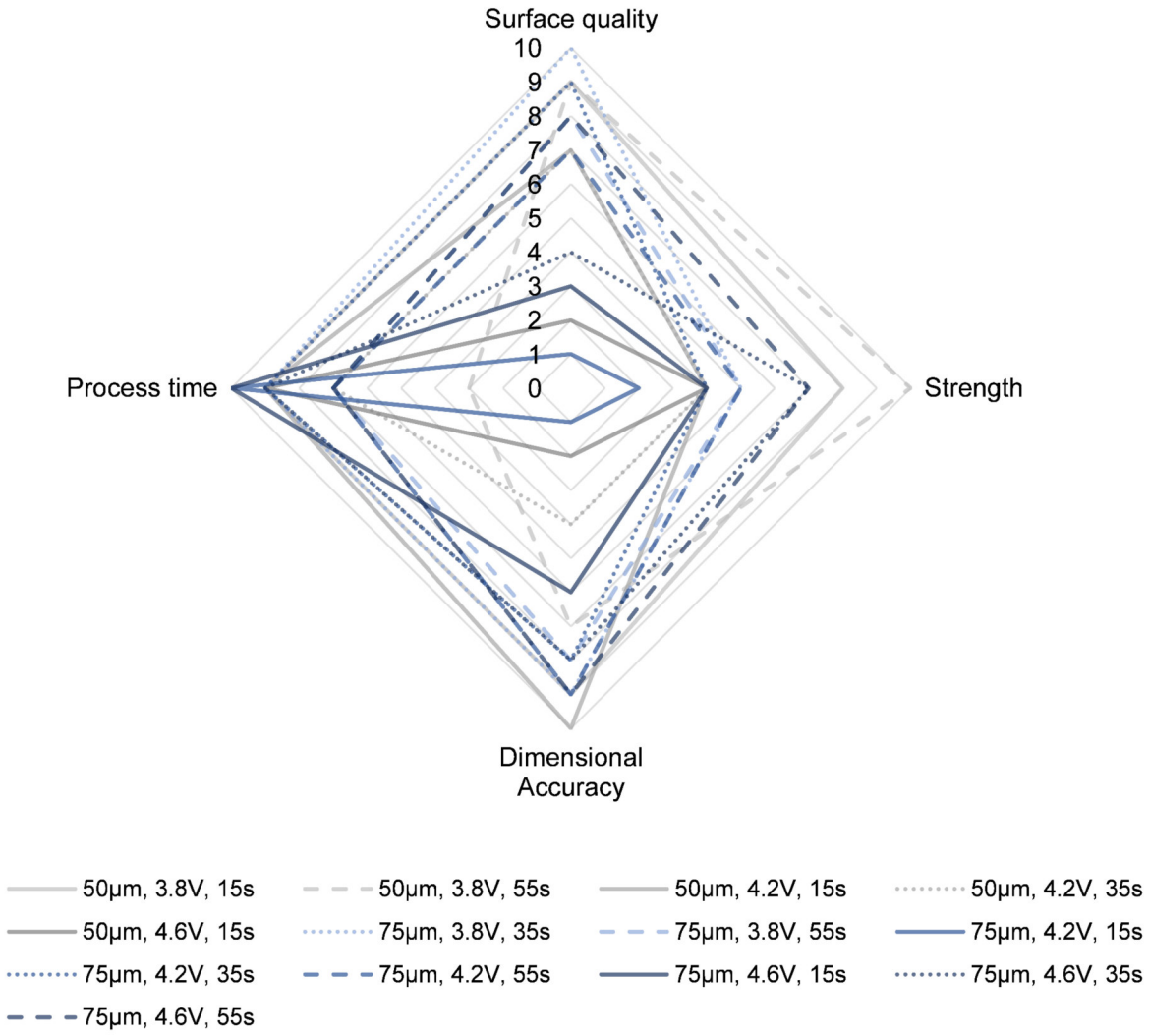

Figure 5.44: Overall rating of the investigated parameter sets regarding process times, surface quality, strength, and dimensional accuracy. The data is linearly normalised to scale values between 0 (unfavourable) and 10 (favourable).

5.3.2 Economic Efficiency Analysis

This subchapter focuses on the economic efficiency of the slurry-based 3D printing process investigated herein. Thereby, hints on feasible optimisations in terms of efficiency are elaborated. Exemplary, the effect of thinner layers on process times is calculated on the base of the given test setup environment and abstracted to an industrial machine.

A total print job embraces base and finish layers enabling consistent conditions all over the print job height and print layers that actually compose the later green part. In this work, the number of base and finish layers n_{Base} and n_{Finish} were fixed following the elaboration of the process specifications for reliable process control (chapter 4.3). The number of print layers n_{Print} can be calculated by deviding the total job height h_{Job} by the layer thickness H used. Typically, n_{Print} is automatically output by the slicing software.

Similarly, all layers require the step of layer casting and drying. Though, when printing onto layers, additional time-consuming steps are involved, such as the layer-wise cleaning of the printhead or a slowed-down movement to ensure the desired printing frequencies. The equations (5.8) – (5.10) allow for the calculation of the process times during slurry-based 3D printing on the test setup utilised herein:

$$t_{Printjob} = (t_{Layercasting} + t_{Drying}) \cdot (n_{Base} + n_{Print} + n_{Finish}) + n_{Print} \cdot t_{Printing} \quad (5.8)$$

$$t_{Layercasting} = t_{Coating} + t_{Coatercleaning} + t_{Machine} \quad (5.9)$$

$$t_{Printing} = t_{Printheadcleaning} + t_{Dataload} + t_{Nozzleshift} \quad (5.10)$$

With the variables as listed and quantified in respect of the test setup in Table 5.2.

Table 5.2: List of variables for process time calculation.

Variables		Quantification	Specification
$t_{Printjob}$		~	Eq. (5.8): Total print job duration
$t_{Layercasting}$		16.3 s	Eq. (5.9): Duration of depositioning one layer and returning to the starting position
	$t_{Coating}$	1.3 s	Duration of layer deposition
	$t_{Coatercleaning}$	2.0 s	Duration of the coater cleaning operation
	$t_{Machine}$	13 s	Empty machine movement times
t_{Drying}		~	Drying period
$t_{Printing}$		12.1 s	Eq. (5.10): Extra time for printed layers
	$t_{Printheadcleaning}$	6.0 s	Duration of the printhead cleaning operation
	$t_{Dataload}$	5.0 s	Duration of data load
	$t_{Nozzleshift}$	1.1 s	Duration of lateral printhead movements
n_{Base}		10	Number of base layers
$n_{Print} = \frac{h_{Job}}{H}$		~	Number of print layers
n_{Finish}		5	Number of finish layers

When excluding the drying period, the layer time $t_{Layer} = t_{Layercasting} + t_{Printing}$ of the test setup is 28.4 s, and its printing area is 40 x 80 mm. In comparison, an exemplary industrial binder jetting machine for sand printing VX1000-S (voxeljet AG, Friedberg, Germany) allows for a layer time of only 12 s when equipped with multiple stacks of printheads (Quitter, 2019). It can print onto an area of 1000 x 600 mm (Gibson, 2021, p. 246).

The deposition rate DR as the key performance indicator for slurry-based 3D printing efficiency can be calculated as:

$$DR = \frac{l \cdot w \cdot H}{t_{Layer} + t_{Drying}} \tag{5.11}$$

With the machine-dependent length and width of the printing area l and w.

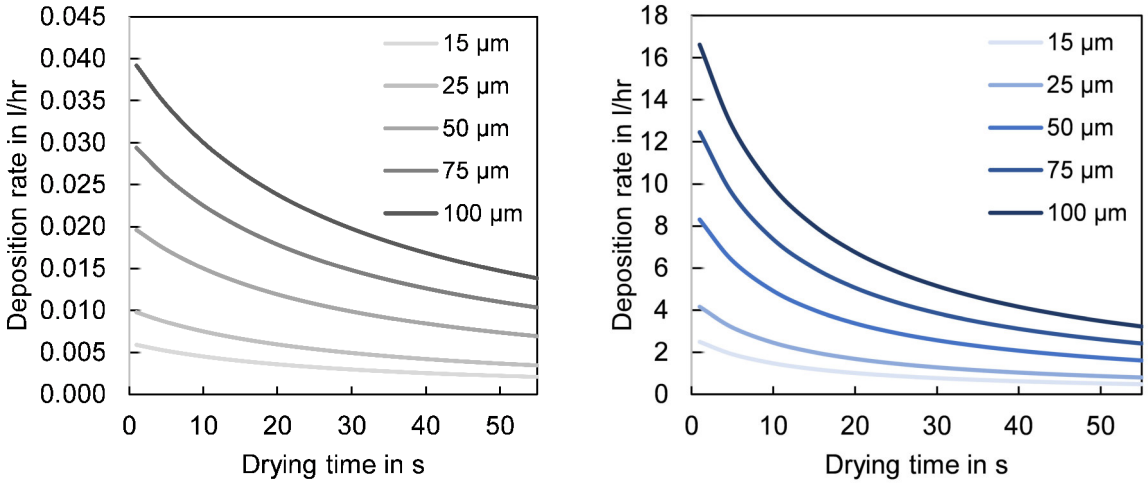

(a) Test setup (b) Industrial BJ machine

Figure 5.45: Performance analysis dependent on drying time and layer thickness.

Figure 5.45 visualises the hyperbolic function of the deposition rate in dependence on the drying time for relevant layer thicknesses on the test setup (Figure 5.45a) and the exemplary industrial machine as described above (Figure 5.45b). It is thus apparent that the advancement in the process step of drying will play an immensely important role in transfer to industrial application.

Still, since the feasibility of applying drying periods of only 15 s has been demonstrated herein using a simple IR heater assembly, and further improvements can be forecasted when advanced measures are taken (e.g. supporting moisture transport by convection currents or warming up the slurry prior to its processing to accelerate evaporation), the enormous potential of the process can be derived.

In particular, when analysing the process efficiency in binder jetting, scalability must be taken into account. Figure 5.46 visualises the deposition rate in dependence on the layer thickness used and the machine type at an estimated drying time of 15 s. The grey line shows the performance of the test setup utilised herein that is equipped with only one printhead and whose control does not allow for parallelisation of the process steps. Conversely, an industrial machine with a printing area of 1000 x 600 mm that is generously equipped with printheads would be capable of delivering a throughput of 1 – 10 l/hr on layer thicknesses between 20 and 100 µm. For comparison, the recently launched laser-induced slipcasting (LIS) machine CeraMax Vario V900 (Lithoz GmbH, Vienna, Austria) as an alternative laser-based additive manufacturing technology for large-size ceramic greenbodies (layer time of 40 s) is additionally plotted (Lithoz GmbH, 2022). In terms of productivity, a binder jetting machine of equivalent size (250 x 250 mm) is calculated to show a noticeably higher deposition rate at 15 s drying time.

Overall, it is demonstrated that adjusting the machine's printing area size significantly affects the part throughput. Hence, the choice of printer size in slurry-based 3D printing must be made based on the business case of the individual application.

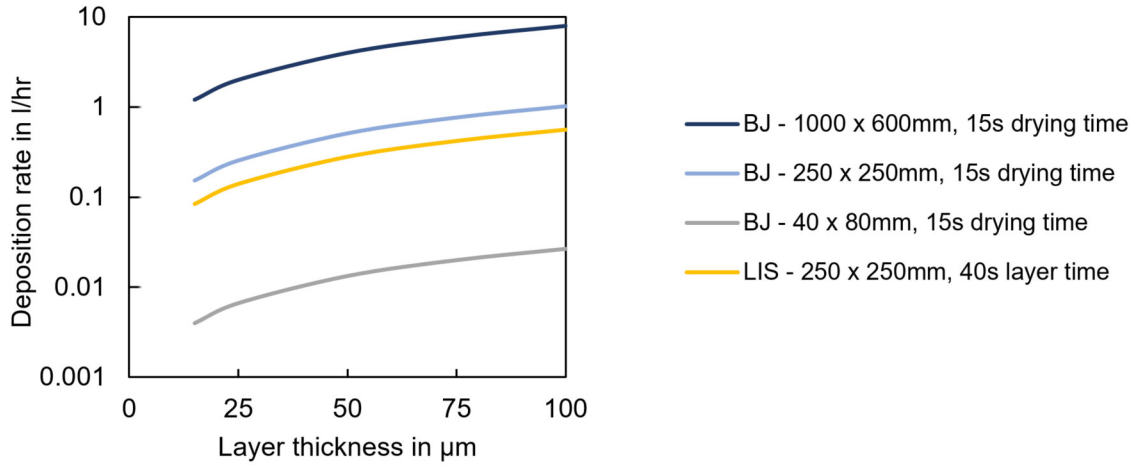

Figure 5.46: Demonstration of the scalability of the slurry-based 3D printing process.

6 Prospects for Advanced Casting

This chapter aims to outline the prospects of the slurry-based 3D printing technology for advanced casting applications based on the findings within this work. First, investigations on the extended process chain of ceramic casting core production are performed. A survey on the post-processing of 3D printed green bodies enables a deeper insight into various requirements within interdependent process steps and demonstrates the demand for a diligent configuration of the overall process. Chapter 6.1 includes studies on the wash-out process essential for damage-free part retrieval and the sintering behaviour of the material system used in consideration of anisotropic properties. In chapter 6.2, the knowledge derived from this work's results is applied in an overall process demonstration based on the example of a highly industrial-relevant close-contour cooling system. It shows the application of high-strength casting cores with imprinted predetermined breaking points fabricated in consideration of the overall elaborated knowledge. A second exemplary casting application is presented in chapter 6.3, employing the slurry-based 3D printing technology and its attributes of high resolution, low surface roughness and flexibility by additively manufacturing a matrix barcode insert for part marking purposes. Finally, chapter 6.4 summarises the potentials and challenges for technology deployment throughout the foundry environment.

6.1 Post-processing of 3D Printed Green Bodies

Complex and filigree as-printed structures that do not exhibit their final properties in the green state call for intelligent process management. Below, the crucial post-processing treatments of wash-out and sintering are investigated to assess the application potentials and boundaries in the overall process chain.

6.1.1 Specification of the Curing Cycle

During upscaling of the printing volume (increasing specimens' height from 2 mm to up to 12 mm), it is observed that the previously set curing cycle (280 °C, 1h) is to be modified to account for the higher thermal inertia related to its total mass and heat capacity, as well as the increased proportion of enclosing compacted powder material providing thermal insulation. In particular, the enclosed powder bed's appearance and texture change by enlarging the material surrounding the printed green bodies without adjusting the curing cycle. Even though the green bodies' strength has not been investigated in this respect, redispersion is found to be inhibited. By performing tests on the slurry's thermal composition, the thermal removal of organics that

make up approx. 1.05 wt.-% of the compacted and dried powder bed is investigated. Thereby, six specimens cut from dry and compacted powder beds of around 5 g each are weighed using Secura 125-1S analytical balance (Sartorius AG, Göttingen, Germany) and klined at 300 °C in the muffle furnace LE14/11/R7 (Nabertherm GmbH, Lilienthal, Germany). One specimen is removed from the furnace every hour, cooled down, and weighed again. Figure 6.1 shows the weight loss as measured, the calculated total organic portion, and the LOI reference value measured at 900 °C.

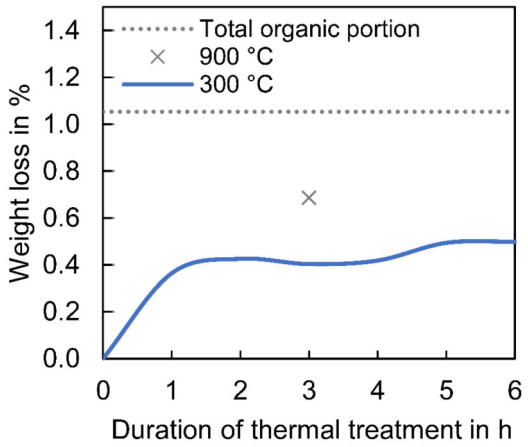

Figure 6.1: Determination of the slurry's thermal decomposition over time.

The weight loss determined during the first hour of thermal treatment, equalling 0.36 wt.-%, is found by far the highest. During the second hour, the specimen loses another 0.06 wt.-%. Only at 5 h, the next clear increase in weight loss (around 0.06 wt.-%) is detected. Thus, it is concluded that 1 h of thermal treatment of the powder compact at 300 °C presents the lower limit of curing time for a specimen's mass of ~ 5 g. Since powder compacts weighing between 10 and 30 g are fabricated in this chapter, a curing cycle time of 3 h is prescribed. A simultaneous thermogravimetric analysis (TG) and differential scanning calorimetry (DSC) of compacted powder (courses [3.1]-[3.3]) and a 1:4 mixture of binder and already cured compacted powder (courses [3.1]-[3.3]) is conducted (appendix A2) on STA 449 F3 Jupiter (Netzsch-Gerätebau GmbH, Selb, Germany) to assess the thermal stability of the binder during this longer thermal cycle. The evaporation of the solvent, an endothermic reaction accompanied by major weight loss, is already completed at 80 °C. No major degradation of the phenolic resin is observed during a holding time of 3 h at 300 °C (see the transition of TG-curve from [4.1] to [4.3] in the lower right). Conversely, when curing the powder compact, a weight loss of 0.45 % is detected, complying well with the results shown in Figure 6.1.

It has been shown that the slurry's organics slowly decompose during curing. Enhanced decomposition of the slurry additives is known to facilitate redispersion since an advanced degree of disintegration weakens the strength of the interparticle bonds. However, even though no thermal decomposition can be determined from the binder's weight loss, the prescribed course operates within a temperature range potentially critical for binder decomposition. The effect of the modified curing cycle on the green strength of 3D printed bodies has not yet been investigated. In future slurry material developments, one should preferably add organics that can be volatilised at temperatures below the respective onset temperature of binder degradation.

6.1.2 Wash-Out of Complex and Filigree Structures

As already noted, the disintegration of the green body and the consolidated powder bed is challenging in slurry-based 3D printing. The unprinted regions must be redispersed carefully to retrieve the green part without damage. During redispersion, the dried consolidated powder bed is crushed into small aggregates via reimmersion in a solvent. Parameters influencing the interparticle interactions and, thus, the redispersion of the powder bed are particularly the powder type, the redispersing medium, and polymeric additives. (Moon et al., 2000, p. 1) Since this thesis does not aim to optimise the slurry's chemistry, part retrieval and redispersion are assessed solely by performing practical tests.

Specimens' Geometries

The challenges and possibilities of the wash-out process are demonstrated on the basis of two specimens: specimen D (Figure 6.2) is used to evaluate the effectiveness of different wash-out methods and demonstrate the risk of part damage during wash-out. Furthermore, an u-shaped test geometry designed in the style of a cooling channel core's segment (Figure 6.3) is applied to showcase the enormous interference of the slurry's composition, the wash-out procedure and the damage-free fabrication of complex core structures.

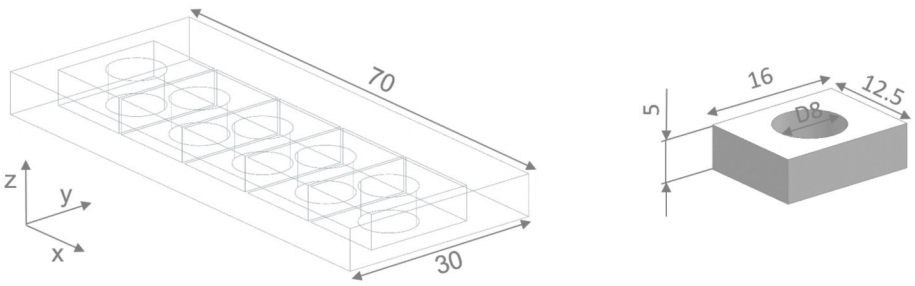

Figure 6.2: Dimensions of specimen D in mm, used for evaluating the effectiveness of the wash-out process and observing damages caused by wash-out and their orientation within the building volume.

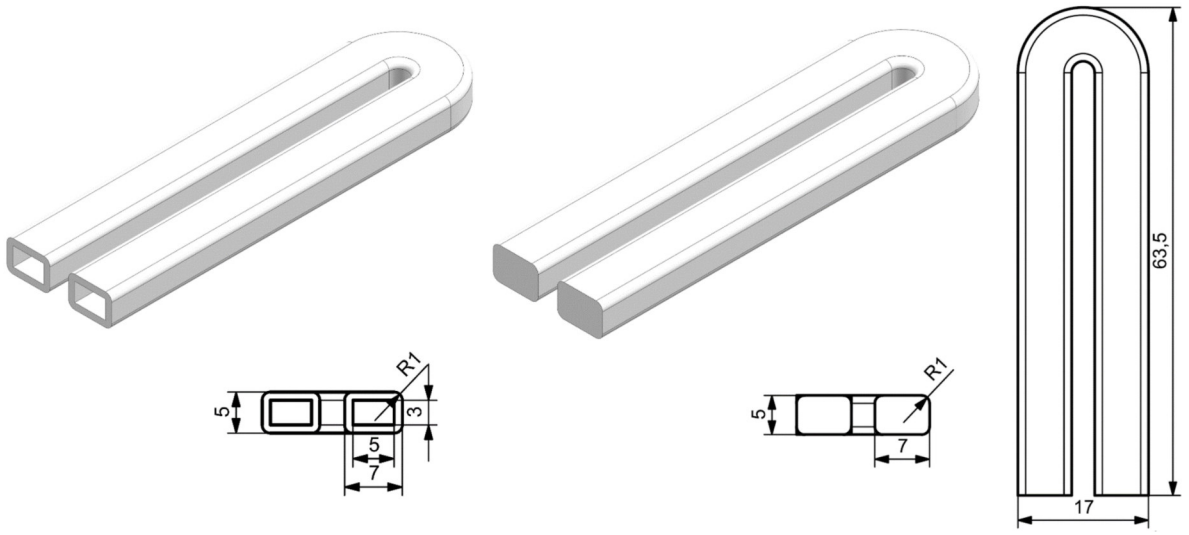

Figure 6.3: Designs of a hollow (left) and solid (right) u-shaped test geometry in the style of the water coolant jacket shown in Figure 6.13. The dimensions in mm are scaled to the available build volume of the test setup.

Specification of the Redispersion Medium

The slurry-based 3D printing method investigated herein allows for processing smaller particle sizes and achieving increased packing densities. Those material characteristics lead to a high number of particle-particle contacts, which is favourable with regard to sinterability but obstructive for redispersion.

Figure 6.4 shows the results from investigations on the redispersion behaviour. Figure 6.4a-c demonstrate the significantly differing separation of the u-shaped geometry using the redispersing media water, IPA and a mixture (1:1 by volume) thereof. Without being subjected to external forces, the powder bed is found to disintegrate into small flakes within seconds in water. Bigger flakes are created using the mixture of water and IPA as a redispersing medium. Only the coarse part structure is slowly separated from the surrounding material in larger chunks when using IPA. Hence, the powder bed is shown to remain cohesive in IPA but can be spontaneously redispersed in water. Moon et al. (2000) report the inhibition of redispersion by decreasing surface tension, that in turn reduces capillary forces (Moon et al., 2000, p. 2404). IPA exhibits a surface tension of only approximately one-third of water and is thus presumed to possibly enable slow but gentle part retrieval.

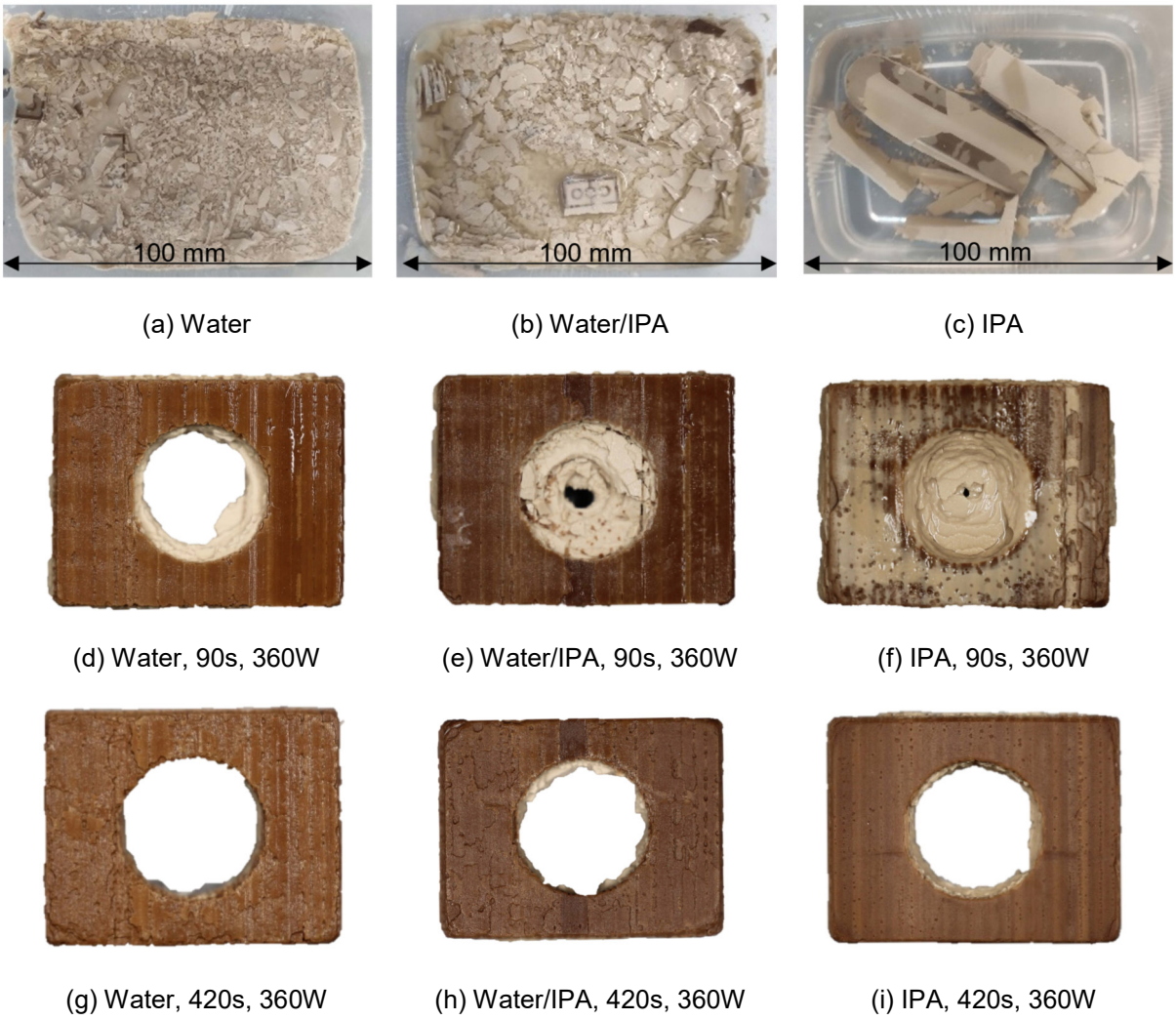

Figure 6.4: Investigations on cleaning efficiency and part damage during ultrasonic cleaning.

Figure 6.4d-f displays the cleaning progress observed on specimen D at a retention time of 90 s in an ultrasonic treatment (Emmi 55, EMAG AG, Mörfelden-Walldorf, Germany). The photographs confirm the increased cleaning efficiency of water as a redispersion medium. The decrease in specimens' volume over time in the ultrasonic bath is quantified in Figure 6.5. 100 % equals the target volume without any residuals on the specimens' surface or spallings. Together with Figure 6.4g-i, it reveals the challenges of damage-free but efficient cleaning. Water is shown to be an aggressive redispersion medium highly sensitive to the time of exposure to ultrasound. In contrast, the course of the water/IPA mixture approaches the target value slowly. Spallings are clearly visible when excessively cleaning parts with water or the mixture of water and IPA, whereas a nearly damage-free surface is shown for the treatment in IPA.

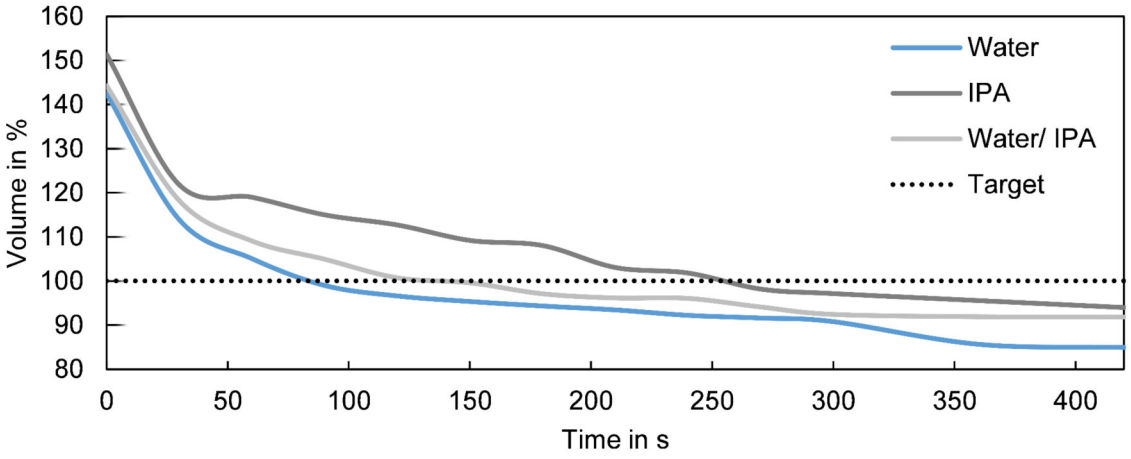

Figure 6.5: Quantification of residuals on the surfaces of specimens D for ultrasonic treatments in different redispersion media.

Specification of the Washout-Method

Moreover, the effect of the ultrasonic power is investigated. However, only minor effects of the ultrasonic output on the cleaning efficiency are found. Damages also occur likewise for all levels of ultrasonic output at treatment periods above 90 s.

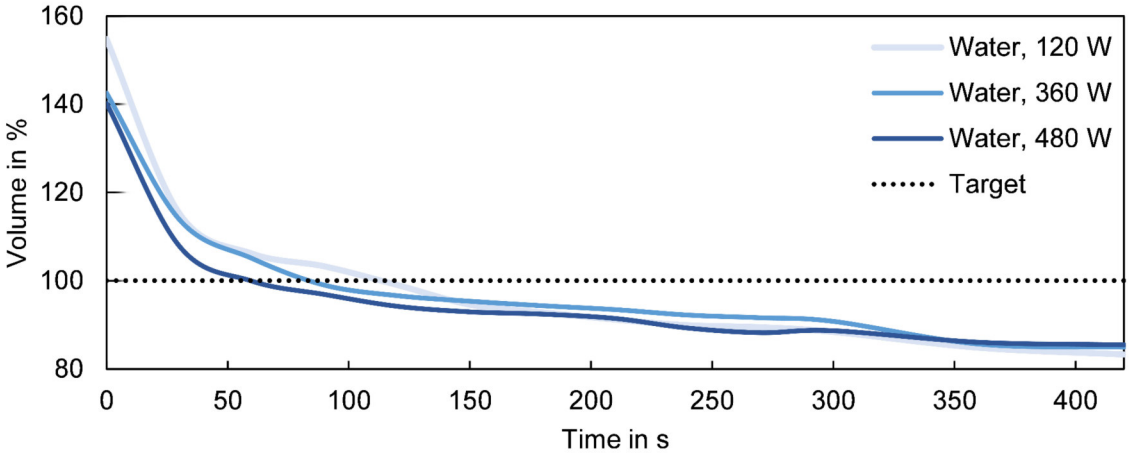

Figure 6.6: Quantification of residuals on the surfaces of specimens D for treatments of different ultrasonic outputs in water.

A rapid expansion of powder compacts in building direction by approximately 150 % can be observed (Figure 6.7). Swelling followed by solvent ingress is a known issue in part retrieval (Mühler et al., 2015a, p. 115). Thereof, it might be presumed that the redispersion medium ingresses the interlayer areas first due to their low density, whereas the dense plane may act as a diffusion barrier leading to an inhomogeneous expansion only in the z-direction. However, the colouration of the powder compact after wetting with water indicates a connection with the rheology modifier used in the slurry that is originally processed as a yellowish liquid. The

dispersing agent, a carboxylic acid preparation, hinders sedimentation by providing a gel-like network associated with swelling. Thus, it is assumed that this additive causes reversible swelling even after drying.

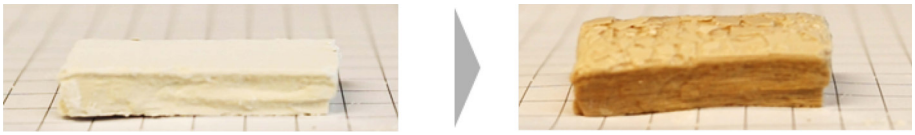

Figure 6.7: Demonstration of the expansion of a powder compact in the z-direction and its colouration followed by the saturation of the pores with water.

The effect of the explosive expansion is visualised in Figure 6.8a. The swelling starts from the inner core structure's opening, which constitutes a horizontal break's origin. On the contrary, the solid u-shaped core structure is retrieved smoothly in an ultrasonic bath. These experiences clearly show the need for further customisation of the slurry formulation with special respect to the additives used. Even though it might not be feasible to completely prevent swelling, enabling a less pronounced and more homogeneous instead of plate-like redispersion is believed to allow for local and smooth dissolution without causing forces on green bodies' walls. A relief hole is mechanically inserted into the core presented in chapter 6.2 to account for the unfavourable swelling of the powder compact during wash-out, which is considered a solvable problem in future applications.

Figure 6.8: Outcome of the part retrieval – (a) horizontal break in hollow u-shape due to explosive expansion of non-bound material after a water bath for 5 s, (b) solid u-shaped core with major adhesions after a water bath for 5 s, (c) core (b) treated in an ultrasonic bath for 60 s, (d) core (c) after finishing manually by brushing.

6.1.3 Shrinkage-free Sintering

Once a green body is removed from the environing consolidated powder, it is sintered to its final density and strength. Thus, the sintering behaviour, particularly the shrinkage behaviour, is crucial with respect to the implementation of printed parts in the individual designated application. As previously noted, the series of tests analysed in chapter 5.2 do not show any shrinkage but a slight expansion during sintering. First, the cause of this effect is discussed from

a material science perspective. Moreover, measurements of the density, porosity and thermal diffusivity of 3D printed specimens are shown. Thermooptical measurements reveal the 3D printed green bodies' anisotropic sintering behaviour.

Fundamentals on the Phase Transitions of Silica Polymorphs

Silica can take various crystalline forms that only exhibit minimal structural energy differences. Investigating the phase transitions and the stability of phases in silica is thus a delicate challenge. (Demuth et al., 1999, pp. 3833–3834) The volume differences of the emerging polymorphs determine the volume changes during sintering. During heating, the crystal structure of quartz changes reversibly from trigonal to hexagonal symmetry during the α-β-quartz transition at 573 °C (Raman, Nedungadi, 1940). The high quartz (β-quartz) turns to tridymite at 870 °C and requires the presence of certain impurities. β-cristobalite is typically formed from 1470 °C and shows a face-centred cubic crystal structure with a significantly lower density (2.32 g/cm³ compared to 2.65 g/cm³ for quartz). However, β-cristobalite can also develop at lower temperatures above 1.000 °C. During cooling, the activation energy barrier for converting β-cristobalite into α-quartz (Figure 6.9a), the typically stable silica phase at room temperature, is too high. Hence, a tetragonal α-cristobalite forms (Figure 6.9b). (Pagliari et al., 2013, p. 1, Carter, Norton, 2016, pp. 83–109) The conversion speed depends largely upon temperatures and grain sizes (Telle et al., 2007, pp. 228–229).

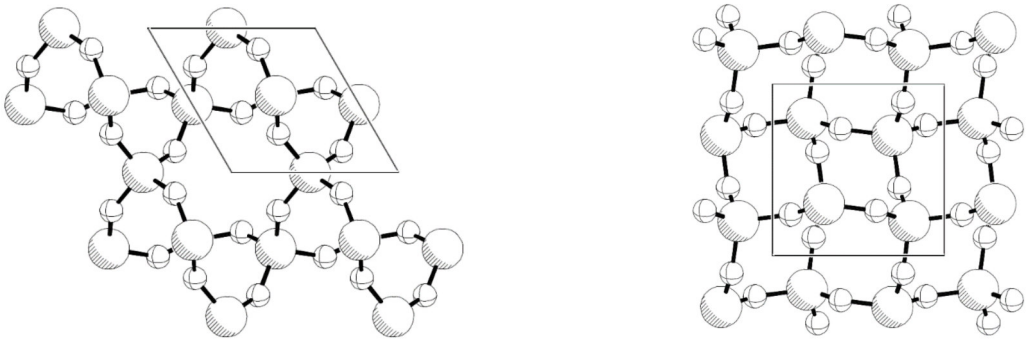

(a) α-quartz (b) α-cristobalite

Figure 6.9: Illustrations of the crystal structures of (a) α-quartz and (b) α-cristobalite. Large spheres represent Si atoms, and small spheres represent O atoms (Demuth et al., 1999, pp. 3838–3845).

The characteristic of significantly deviating bulk densities and thermal expansion values can be used to customise the expansion behaviour in firing technology, e.g. to match a ceramic body's thermal expansion with that of a glaze (Pagliari et al., 2013, p. 1). Herein, this effect is exploited to achieve zero net sintering shrinkage by superimposing regular sintering shrinkage with cristobalite formation associated with volume expansion. More precisely, the portion of the α-

cristobalite phase within the sintered specimen is set by promoting β-cristobalite transition until the desired content is reached, compensating for the concurrent shrinkage.

Determination of Density and Porosity

To demonstrate the high validity of density determinations on specimens A in chapter 5.2, the density and porosity of specimens B fabricated at a layer thickness of 50 µm, a drying intensity of 3.8 V, and a drying time of 55 s are determined using Archimedes' principle. Table 6.1 shows the results determined on low standard deviations. The density was further shown to be independent of the positioning on the printing platform by determining the density on specimens printed in orientations parallel or orthogonal to the printing direction. The bulk densities determined on specimens B using Archimedes' method fully correspond to those determined on specimens A based on DIN EN ISO 18754 (Figure 5.10a). Hence, the validity of density determinations by weight and volume measurements is proven. Moreover, the validness of the results shown in chapter 5.2 on a scaled build volume is confirmed by analysing more voluminous specimens that require a higher height of the building volume and, thus, a greater number of total layers. Overall, the prospect of achieving constant material properties over even greater build volumes using the 3D printing process developed herein can be held out.

Table 6.1: Results of the density determinations on specimens B using Archimedes' principle.

Orientation of the cylinders to the printing direction	**Particle density PD in g/cm³**	**Open porosity Φ in %**	**Bulk density ρ in g/cm³**
Parallel (n = 4)	2.56	45.05	1.40
Orthogonal (n = 4)	2.57	45.33	1.40
Standard deviation	$1.57 \cdot 10^{-2}$	$2.08 \cdot 10^{-1}$	$5.16 \cdot 10^{-3}$

Determination of Thermal Diffusivity

The thermal diffusivity evolving during heat-up can be monitored using thermooptical measurements. Figure 6.10 visualises the trend of thermal diffusivity and relative thickness during thermal treatment in a thermooptical measurement device. The major drop in thermal diffusivity up to 500 °C can be attributed to the debinding of the material. The binding bridges consisting of a polymer are removed, and the contact areas of the grains for heat conduction are narrowed since the polymer is replaced by air only. After 500 °C, the thermal diffusivity remains constant until approximately 1000 °C. Exponential growth is observed from here. The

growth in diffusivity points out the ongoing formation of sintering necks that again enlarge the contact areas of the grains. The heat-up is aborted at 1300 °C. Since the majority of growth in sintering necks occurs during the dwell time – which is not considered here – the thermal diffusivity is proposed to increase further, reflecting the ongoing sintering activities. Researchers on sintering technology, such as Saheb, Hayat (2017), reported an increase in thermal diffusivity with both sintering temperature and dwell time (Saheb, Hayat, 2017, pp. 124–125). In accordance with relevant literature (Buntebarth, 2020) and the heat penetration coefficient S (5.7) calculated above, a thermal diffusivity κ of 0.4 to 0.5 mm²/s is believed to be attainable using a complete sintering cycle.

The grey curve shows the sample expansion during heat-up. Here, the quartz inversion point (573 °C) is clearly recognisable. Furthermore, – consistent with the thermal diffusivity data – the onset of sintering accompanied by shrinkage is observed at around 1000 °C.

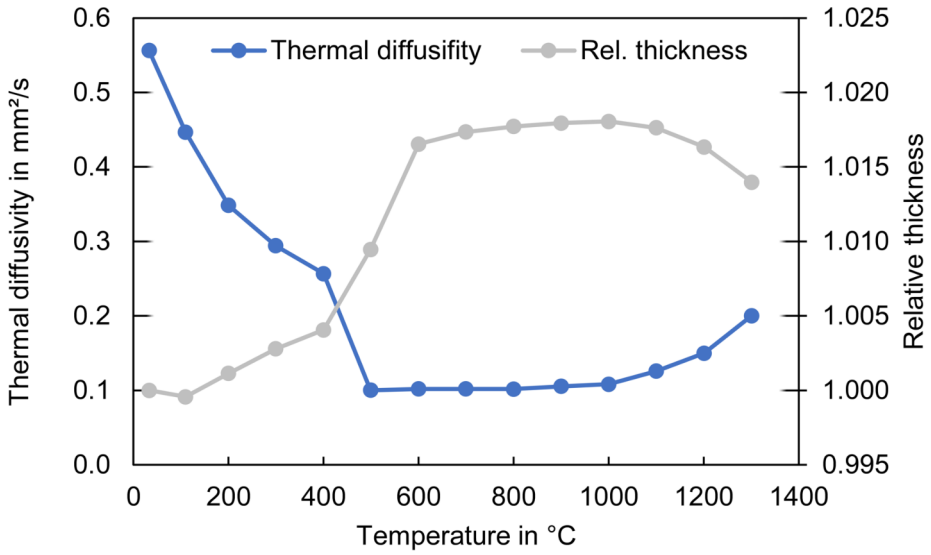

Figure 6.10: Trend of thermal diffusivity and relative thickness during heat up.

Consideration of Anisotropy during Sintering

Figure 6.11 shows the positioning of specimen B within the furnace and the results of the thermooptical measurements during a sintering cycle following the arrows. The relative width is determined parallel and orthogonal to the layer interfaces, as illustrated in Figure 4.13. During heat-up and cooling, the curves show a typical thermal expansion trend; in particular, the quartz transition point is depicted as to be expected (Telle et al., 2007, pp. 226–228).

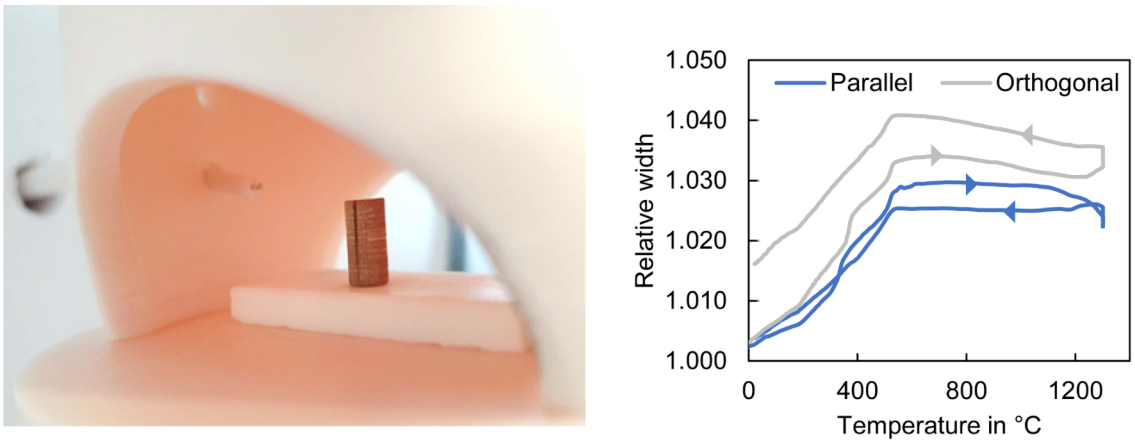

(a) (b)

Figure 6.11: (a) Positioning of a marked specimen B in the thermooptical measurement device; (b) Relative width parallel and orthogonal to the layers obtained during a sintering cycle.

From around 1000 – 1100 °C, relevant shrinkage is identifiable, even though shrinkage is measured noticeably less orthogonal to the layer interfaces. The expansion occurring at the sintering temperature points out the transition into cristobalite during the dwelling time. As stated above, unlike the α-β-quartz transition, this modification in the crystal structure can be irreversible. The expansion accompanied by cristobalite conversion is found to be more pronounced orthogonal to the layer interfaces than parallel. The reason for this effect may likely be the higher porosity and, thus, increased surface area next to the interfaces contributing to a higher kinetic reaction rate (Ringdalen, 2015, pp. 490–491).

6.1.4 Strengthening By Sintering Cycle Extension

Finally, the adjustability of the casting cores' mechanical strength via an adapted sintering curve is demonstrated. For this purpose, the experimental study, as specified in chapter 4.4, is repeated, and the specimens produced thereby are sintered using a varied sintering curve (Figure 6.12a). Series 1, whose corresponding results have been analysed in depth in chapter 5.2, and series 2, the comparison group, show an identical target dwelling time of 5 h but diverging control parameters. It is noted that the temperature curve associated with series 2 lies within the temperature range relevant for sintering (>1000 °C as determined in chapter 6.1.3) for around 2 h longer.

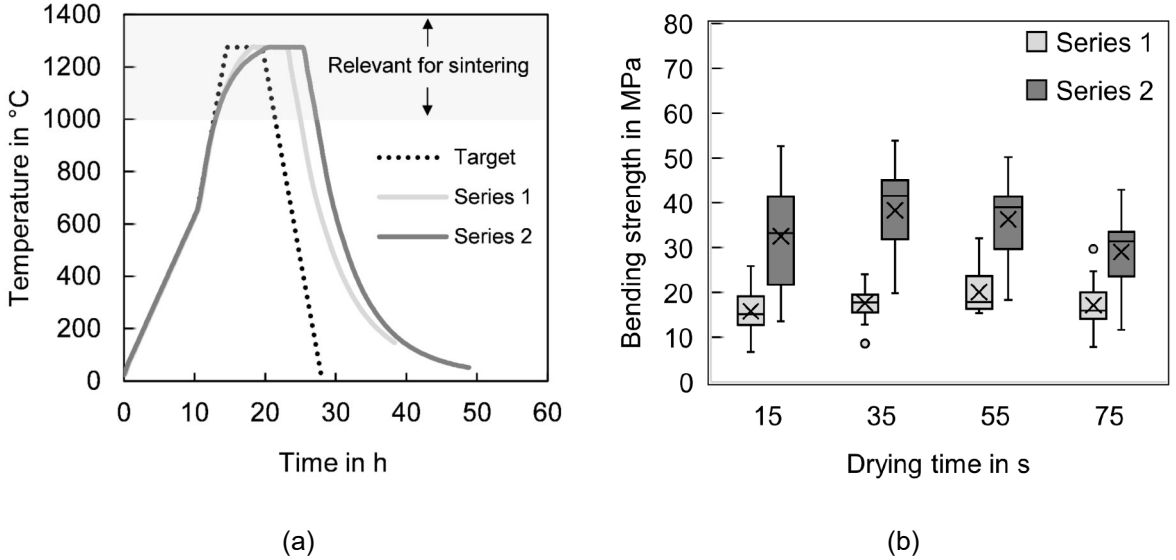

Figure 6.12: Demonstration of the effect of (a) deviating sintering curves on (b) the four-point bending strength.

Figure 6.12b shows exemplary results comparing the four-point bending strengths for the two series using the same 3D printing parameters but different sintering cycles. One can see that a significant increase in strength can be achieved by extending the sintering cycle. All compared parameter sets showed significantly increased strengths at a likewise increased spread. When increasing the retention time in the sintering relevant temperature range by only 2 h, the four-point bending strength and its spread are approximately doubled: while series 1 showed a mean strength of 17.6 MPa at an average deviation from the mean of 3.8 MPa, series 2 exhibits an average strength of 34.1 MPa at a deviation of 8.3 MPa. Hence, it can be concluded that an only slightly deviating sintering process results in significantly higher strengths – a P-value of $6.53 \cdot 10^{-31}$ quantifies the extremely high significance level. In contrast, the highest P-value achieved by varying the drying conditions comparing the bending strength among specimens of series 1 lies in the order of 10^{-5}.

From these provisions, the potential in industrial implementation is evident: One appropriately configured 3D printing machine optimised regarding short process times may be used for 3D printing different casting cores' green bodies. Various geometries can be easily arranged within the build volume. Depending on the requirements, particularly the fineness of the casting core and the respective load case, the post-processing route can be exploited for an easy and cost-effective adjustment of the mechanical strength.

6.2 Collapsible Cores for Contour-Close Coolings

6.2.1 Motivation

In order to meet environmental objectives and reduce carbon emissions, electrification policies and programs increasingly encourage green mobility concepts. In recent years, the usage of electric motors has thus risen dramatically. For efficiency reasons, fluid-cooled electric motors with complexly designed water flow systems are preferably employed in high-performance vehicles. (Boopathi et al., 2022, pp. 1–2) E.g. Feikus et al. (2020) and Jahangirian et al. (2020) showed that the design of the cooling channels in an electric motor housing is of decisive importance with respect to cooling efficiency. Figure 6.13 shows an exemplary schematic of a liquid-cooled electric motor housing.

Casting technology is the preferred manufacturing method if both complexity and economic efficiency are required in medium and large part quantities. However, to fulfil the demands of high-quality castings, casting cores that enable forming of cavities within the casting call for meeting numerous requirements such as (Gyarmati et al., 2021, p. 2):

- Adequate strength to withstand the loads during handling and casting
- High thermal stability to allow for maintaining dimensional accuracy until the surrounding metal is solidified
- Collapsibility after solidification to enable easy core removal

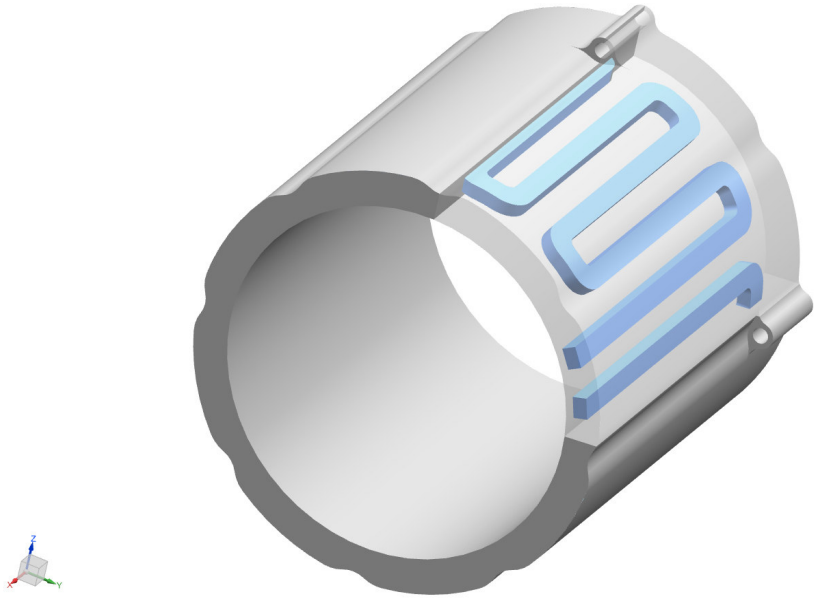

Figure 6.13: Schematic of a liquid-cooled electric motor housing.

When it comes to filigree, complex, and self-supporting geometries like the one shown in Figure 6.13, conventional casting cores reach their limits due to their low strength, thermal decomposition and distortion during casting, or core removability. The following subchapters show an application of slurry-based 3D printing on the example of a tubular self-collapsing geometry inspired by water coolant jackets in electrical motors.

6.2.2 Design of a Self-collapsing Core Structure

Casting cores produced via 3D printing allow an almost free design of inner cavities within a cast part. However, since the casting cores need to be stable enough to resist the high mechanical and thermal loads during casting but, concurrently, must be easily removable after solidification of the cast metal, the cores' stability and their collapsibility represent originally competing goals. Slurry-based 3D printing is considered a potential enabler technology for realising both filigree and easily collapsible casting cores by novel process-oriented designs.

The shrinking metal exerts forces on a fully enclosed casting core resulting in core compression and shrinkage constraint (Flemming, Tilch, 1993, pp. 28–29). The consequences are deformations and stress in the core and cast part, impeding the collapsibility of a solid core but enabling the self-collapsibility of a hollow core structure. The stress conditions are dependent on the wall thickness of the cast part.

A core structure specially designed for self-collapsibility is intended to withstand the mechanical and thermal loads during casting but collapse during solidification due to the cast metal's shrinkage. Depending on the load case applied, the core's wall thickness, the notches' cross-section, the number of notches and their orientation can be adjusted.

Figure 6.14 illustrates an exemplary design of a self-collapsing core structure and its enclosing cast as investigated herein: a cooling structure of a diameter of 8 mm cast in aluminium of 2 mm wall thickness. The core's global wall thickness is chosen to be 1.5 mm since thinner structures cannot be handled safely during wash-out. Four helical notches with tips of 90° complement the core's geometry dedicated to enabling its collapse during solidification. The helical orientation is chosen due to the fact that on the one side, hollow cylinders preferably break along their length when subjected to pressure, and, on the other side – since the casting cores are printed horizontally – the layer interfaces which are visible in the microstructure already represent vulnerabilities.

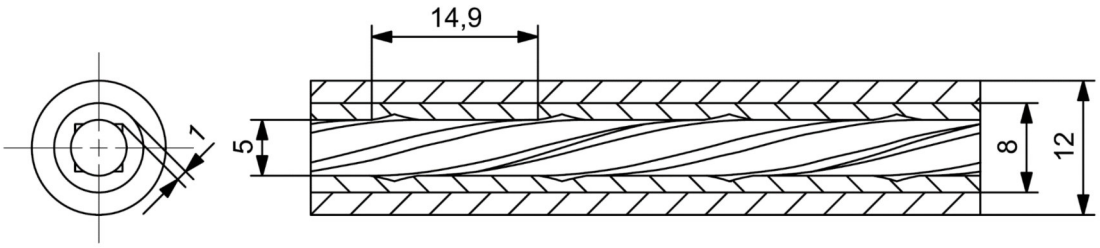

Figure 6.14: Design of a self-collapsing core structure (inner tube) enclosed by a thin-walled cast. Dimensions in mm.

6.2.3 Structural Analysis

The finite element method (FEM) solver Simcenter Nastran is utilised within the Siemens NX 12.0 environment (Siemens AG, Munich, Germany) to predict the build-up of stress during the shrinking of aluminium on the casting core.

Table 6.2 provides details on the material properties used for FEM simulation. The cast material's input properties originate from the material database of Siemens NX 12.0. The thermal expansion coefficient of the quartz core is derived from the literature (Recknagel, Dahlmann, 2009, p. 8), while the material density was determined experimentally (Table 6.1). The core's mechanical properties represent only estimates. The structural analysis results are thus to be regarded rather as a first indication to assess the physical behaviour during the solidification of the cast metal and the magnitude of evolving stresses. The crucial simulation settings are listed in Table 6.3. During the cooling of cast aluminium, mechanical strains develop from 350 °C downwards (Reihle et al., 2013, pp. 488–489). Thus, the cooling interval between 350 °C and 20 °C is prescribed in the simulation.

Table 6.2: Material properties for structural analysis.

Material property	**Cast material (aluminum A356)**	**Ceramic core (quartz)**
Thermal expansion coefficient in 1/K	$21.4 \cdot 10^{-6}$	$14 \cdot 10^{-6}$
Density in g/cm³	2.67	1.4
Young's modulus in GPa	70	2.5
Poisson's ratio	0.33	0.2

Table 6.3: Meshing parameters, boundary conditions and loads applied in the FEM simulation.

Type	Expression	Location
Global mesh element size	0.5 mm	Cast & Core
Mesh refinement	0.125 mm	Notch
Deformation constraint	Forced radial deformation	Outer surface of the cast
Initial stress-free temperature	350 °C	Entire workspace
Temperature load	20 °C	Entire workspace

Figure 6.15 visualises the result from structural analysis. For brittle materials, the maximum normal stress theory, also called Rankine's theory, is typically applied to determine the equivalent stresses resulting from mechanical strains. Hence, the maximum principal stress is assessed here. Figure 6.15a visualises the colour-coded model after cooling. Due to the radial deformation constraint that simplifies the load case, the outer shell of the solidifying metal shows excessive stresses. In reality, displacements can occur in all directions, compensating for the compressive and tensile stresses detected closeby. However, the aluminium shell is only implemented in the model to account for the thermal load case. The core itself is meshed finely, in particular in the notch. Notches can cause numerical singularities and eventually impede the converging of the solution (Niu et al., 2009).

Figure 6.15b shows the strongly scattering maximum principal stresses evolving within the notch and precisely mappable stresses on the inner surface between the notches along the casting core's length. The peripheral areas are hardly subjected to stress on the inner surface. However, the interior part shows tensile stresses around 10 MPa developing due to the cast material's shrinkage.

By structural analysis, it is thus shown exemplary that a hollow structure as designed herein can be subjected to tensile stresses during the solidification of the enclosing metal. In contrast, solid core structures only develop compressive stress during the shrinkage of the cast metal.

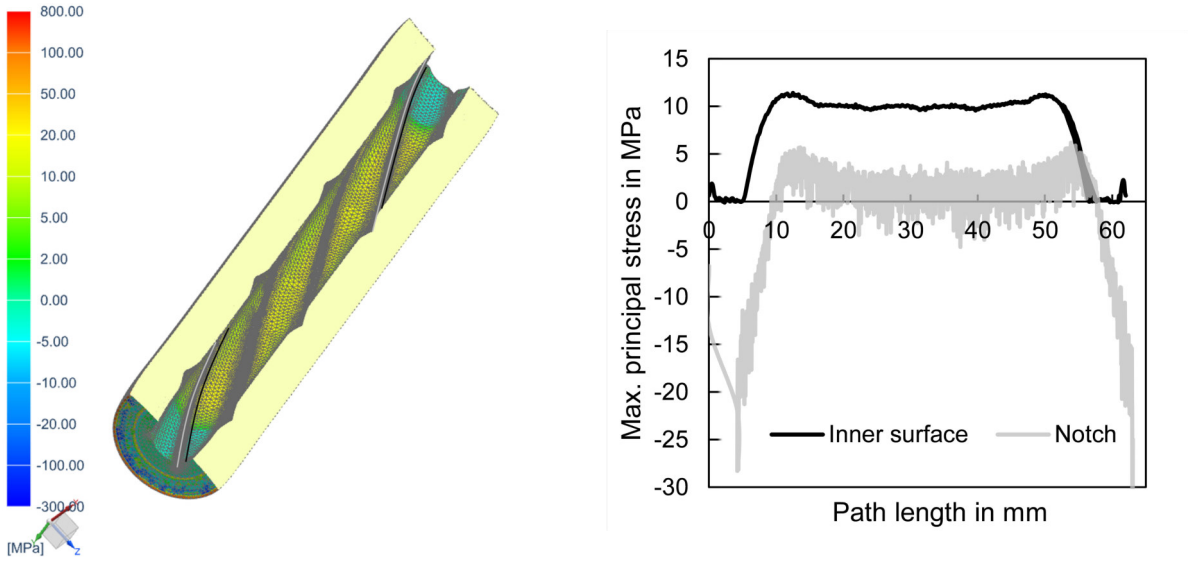

(a) (b)

Figure 6.15: Analysis of the stress development due to solidification of aluminium encapsulating the core structure – (a) visualisation of the inner core structure and the measuring paths, (b) maximum principal stress evolving along the measuring paths.

6.2.4 Core Production

The collapsible core design, as presented in Figure 6.14, is fabricated in duplicate using the test setup, a layer thickness of 50 µm, a drying intensity PAV of 3.8 V, and a drying period of 35 s. Figure 6.16 provides a detailed view of the printing process and the green part after wash-out.

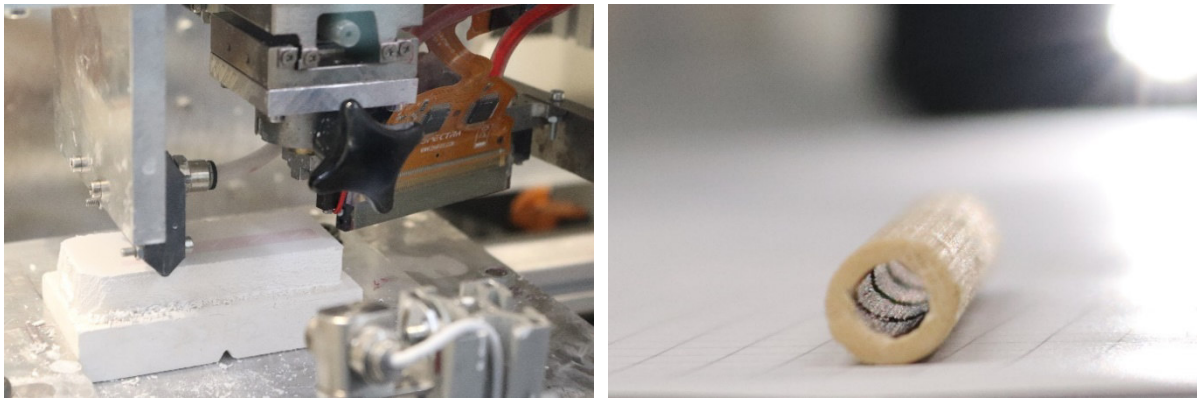

(a) (b)

Figure 6.16: Illustration of selected stages of the self-collapsible core fabrication process. (a) 3D printing utilising the test setup, (b) finished green body before sintering.

6.2.5 Casting

A 3D printed sand mould is utilised to produce a gravity-cast aluminium part. The cast part's minimum thickness conforms with the wall thickness used in the FEM analysis, even though

the cast part represents a cuboid. An alloy similar to A356 is cast to the mould at a casting temperature of 750 °C.

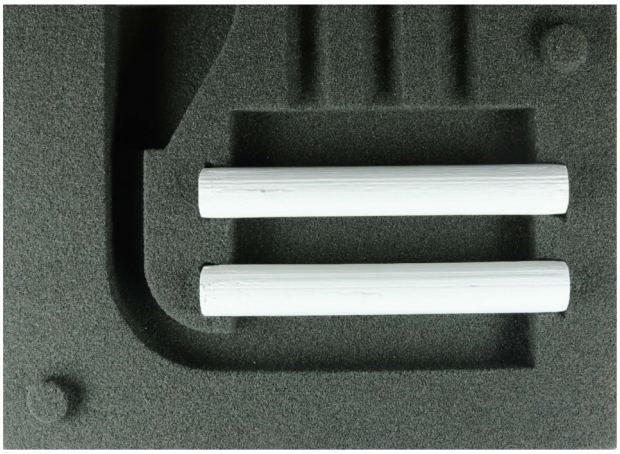

Figure 6.17: Insertion of two ceramic casting cores into a 3D printed sand mould.

6.2.6 Analysis of the Cast Part

Figure 6.18 shows a photograph of the part as cast, not yet subjected to external forces as usual in the process step of de-coring. One of the two self-collapsible cores produced with the same equipment and process parameters broke prematurely to solidification of the cast metal (Figure 6.18, left). The premature failure relates to the core arranged next to the sprue (Figure 6.17, bottom). The enhanced differential mechanical and thermal loads during casting are suspected of exceeding the core's load capacity. However, intrinsic material defects coincidentally occurring in a spot subjected to unfavourably high stresses or premature damage caused by manual wash-out are also conceivable explanations.

The second core (Figure 6.18, right) withstood the loads during casting and broke during the solidification of the cast metal. The photograph shows the arrangement of core fragments loosely enclosed by the cast metal. Different types of cracks are identified: Cracks following the course of the predetermined breaking line, cracks perpendicular to the predetermined breaking line, radial cracks, and interlayer cracks. The first three types comply with the loading situation presented in the sub-chapters 6.2.2 and 6.2.3. The interlayer cracks can be explained by the micrographic examinations conducted in chapter 5.2, showing highly porous interlayer structures with small, equally distributed flaws.

With the experiment performed herein, the concept of self-collapsible cores for casting applications has been proven for the first time. Fifteen mechanical impacts of approximately 3.3 J on the cast part are found sufficient for residue-free de-coring. By utilising slurry-based 3D printing, a procedure enabling complex and filigree structures that can be reliably de-cored

can thus be envisioned. Based on the process knowledge elaborated herein, the conventionally conflicting targets of casting cores' strength and collapsibility associated with both high processing efforts and restrictions in geometrical freedom may be transferred to a shared approach for high-performance cast parts, e.g. deployable in close-contour coolings for highly-efficient electrical motors or even aerospace components.

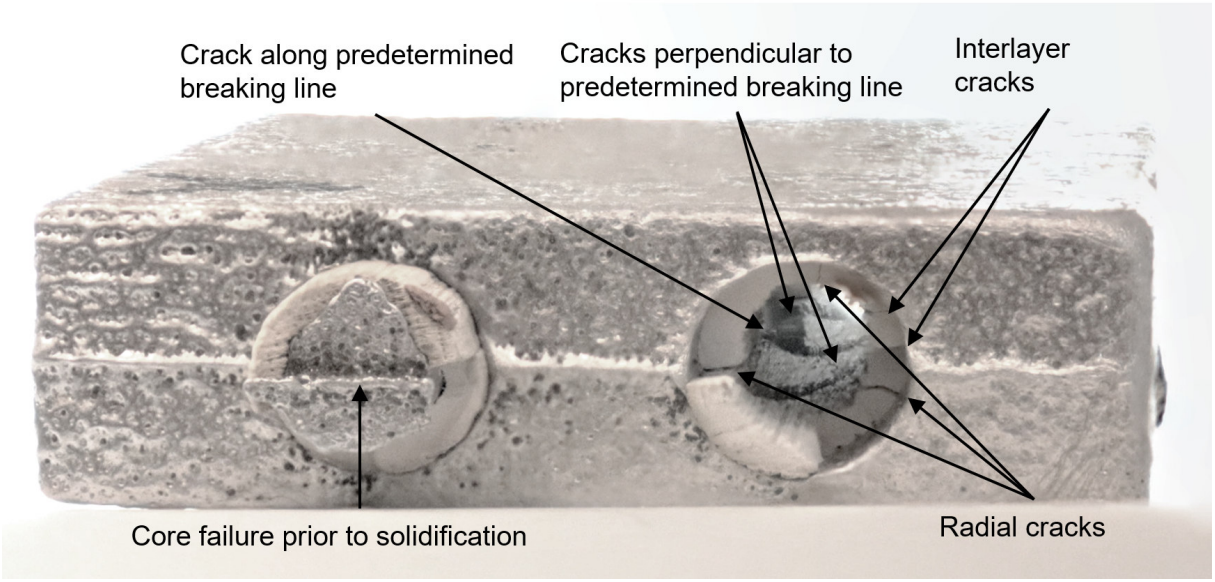

Figure 6.18: Analysis of the part as cast.

6.3 Additively Manufactured Digital Codes for Flexible Part Marking

6.3.1 Motivation

Quality control is of substantial importance in advanced production processes. Component traceability enables early identification of cause-effect chains and guarantees a solid foundation for effective quality assurance. Regardless of whether a casting process involves additive manufacturing of sand moulds or cores, or traditional sand casting procedures, the process chain comprises multiple steps prior to and after casting (e.g., mould/ core production, sandblasting). Employing marking methods allowing for component tracking during the whole complex casting process is desirable but challenging since post-treatments typically affect a cast component's surface topography (Deng et al., 2022, p. 1136). Assigning unique IDs to sand moulds may facilitate part tracking throughout the casting process and across the component's entire life cycle. With this intention, Vedel-Smith, Lenau (2012) suggested reconfigurable actuated pin-type tooling inserts applicable to green sand moulding machines. Uyan et al. (2022) studied the utilisation of 3D printed wax tags to be added to wooden patterns prior to moulding and burnt away during casting. Further developments include direct sand mould

labelling via laser cutting or ceramic stencils (Carlsson et al., 2022, p. 4). 3D printing of sand moulds and cores typically involves labelling using alphanumeric characters, e.g. to facilitate the assembly of mould segments (Meibodi et al., 2019, p. 140). However, subtle labels on sand moulds transferred to the cast component during casting are hardly feasible due to the coarse grains associated with a relatively low level of detail. QR codes are 2D matrix barcodes that store data in a smaller space than 1D barcodes. Advanced data processing techniques are available that allow for QR code embedment onto freeform CAD surfaces. (Kikuchi et al., 2018, p. 1) Placing a small digital code on the cast part's surface that is not machined or sandblasted after casting is thus considered achievable by inserting a slurry-based 3D printed QR code at an appropriate position into a sand core or mould. The principle procedure of additive manufacturing a high-resolution ceramic QR tag for part marking purposes in casting applications as an alternative to the just unveiled approaches ensuring traceability is described in the following section.

6.3.2 Production Sequence

The production sequence corresponds to the procedure developed in this thesis, as depicted in Figure 4.6, using the parameter set as listed in chapter 6.2.4, and comprises (1) 3D printing of the QR code via slurry-based additive manufacturing, (2) wash-out, (3) sintering, (4) mould assembly, (5) casting.

Figure 6.19 visualises different stages within the green body's fabrication. The tag's outer dimensions are 16 x 16 x 2 mm. The QR code protrudes 0.5 mm from the rectangular solid. The minimum feature of the code measures 0.76 mm square, which corresponds to only 5.4 fold the resolution perpendicular to the coating direction y, which is limited because of the printhead installation in the test setup. The resolution in coating direction x is higher (chapter 4.3.1). For this reason, the printing result is very sensitive to nozzle dysfunction in the y-direction, as can be seen in the form of line-shaped indents in Figure 6.19b and Figure 6.19c. Figure 6.19c also shows unwanted modifications on the geometry caused by wash-out: the contours are rounded off, and minor powder compact residuals remain on the edges. The geometry does not change during sintering (chapter 6.1.3). The residuals thus become permanently attached during sintering.

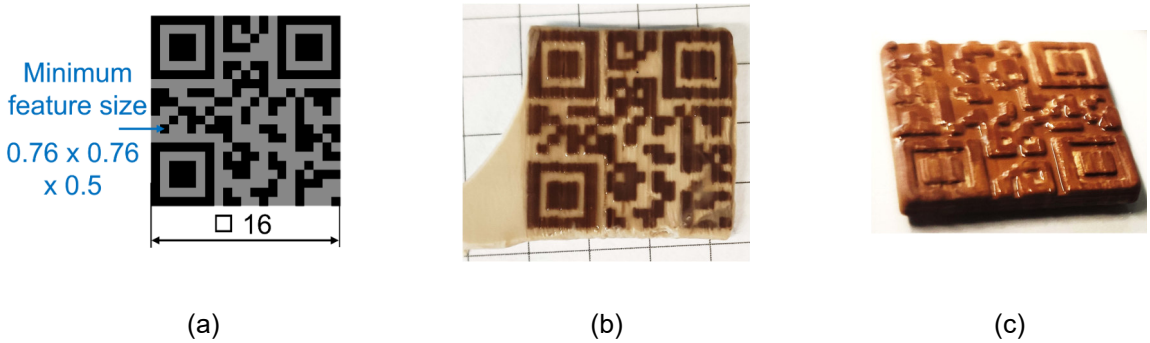

Figure 6.19: QR code tag. (a) CAD design, dimensions in mm, total depth of tag is 2 mm, (b) as printed state, wetted, (c) green body after wash-out.

The QR code tag is bonded into a 2 mm inlet within a sand mould (Figure 6.20a). An aluminium-silicon alloy is poured into the mould at a temperature of ~ 750 °C. Figure 6.20b shows the resulting cast part, including the casting system (gating system, feeders).

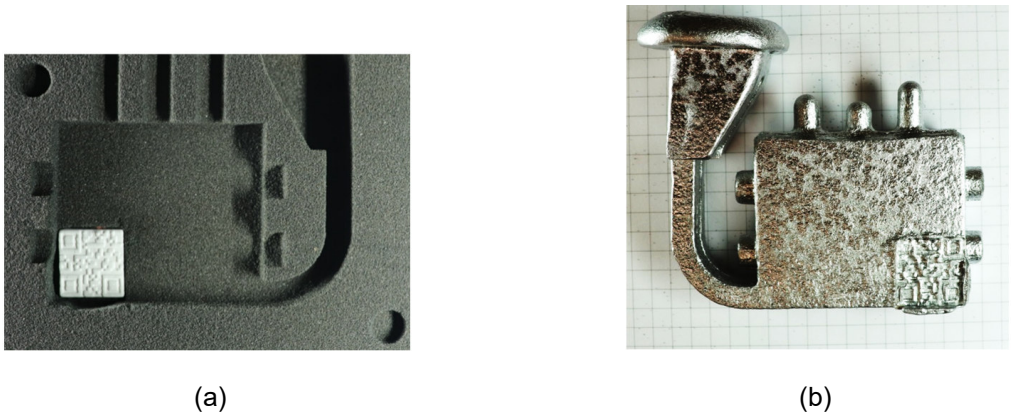

Figure 6.20: (a) Assembly of the QR tag and the mould. (b) Cast part.

6.3.3 Photographic Analysis and Discussion

Figure 6.21 visualises the result using frontal macro photographs. The additively manufactured insert shows the desired basic geometry containing rounded edges and vertical print errors both in the green and sintered stage (Figure 6.21a-b). Even larger roundings are observed on the casting's surface (Figure 6.21c). This effect is attributed to the poor wettability of the quartz ceramic with aluminium melt. Single features within the QR code broke during casting and moved slightly. However, taking into account the very small size of the QR tag of only 16 x 16 mm, the minimum feature size of 0.76 mm, and the low print resolution in the y-direction owed to the hardware setup, the precision of detail is considered promising. Hardware adjustments will allow for an increase in resolution in the y-direction. Improvements towards high-edge definitions are feasible by increasing the binder proportion and/ or replacing organic slurry additives that impair the wash-out process. The in-principle technological feasibility of

additive manufacturing digital code tags via slurry-based 3D printing in small sizes is thus demonstrated. The minimum feature size shown herein is physically impossible to realise in a sharp-contoured print using sands of common grain sizes. For slurry-based 3D printed digital tags, automatic code recognition after casting and sandblasting is rated as feasible using simple cameras and image processing methods (Figure 6.21d).

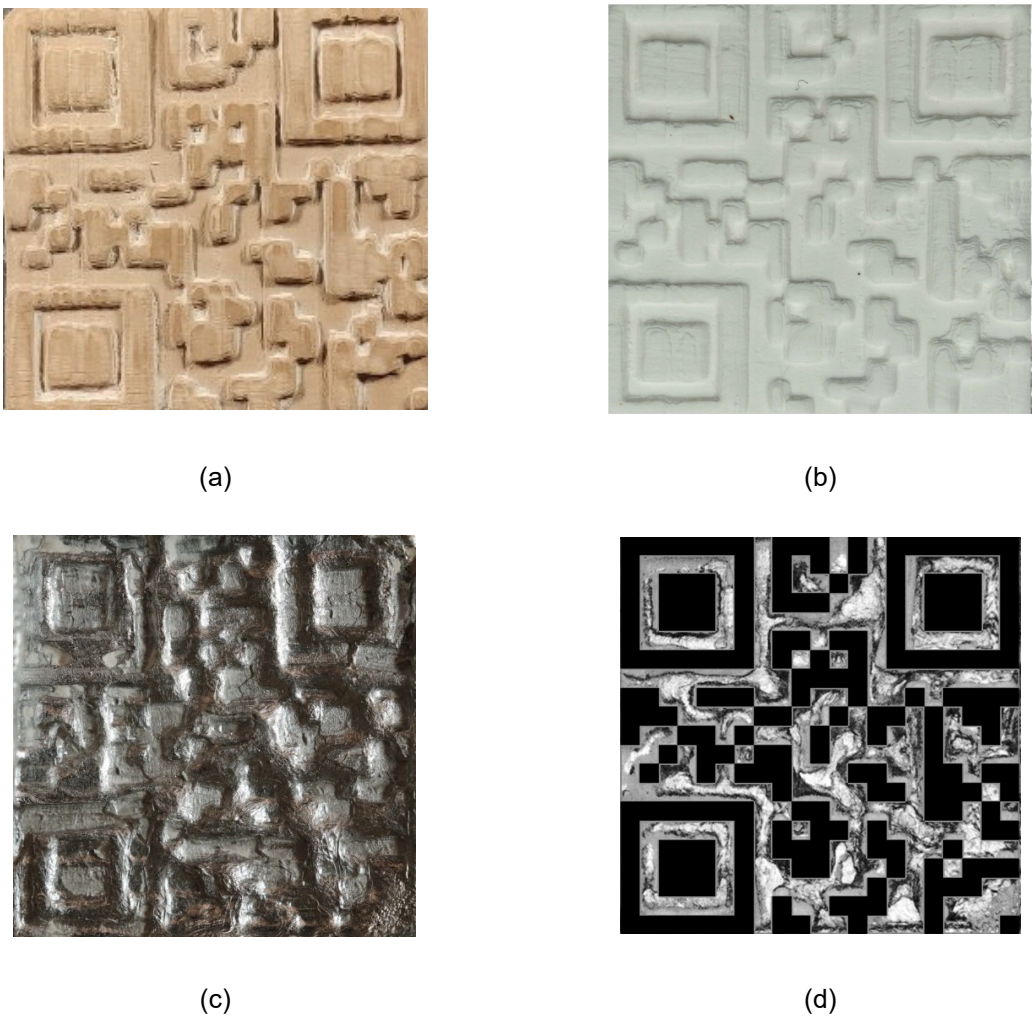

Figure 6.21: Frontal view of the QR code tag (a) in the green state, (b) in the sintered state, (c) on the surface of the cast part. (d) shows an overlay of the digital code data and the cast imprint's photograph.

6.4 Summary of the Technological and Economic Potentials and Challenges

The previous sub-chapters present exemplary use cases to envisage possible fields of application of slurry-based 3D printing in the foundry industry. As regards the industrial application of the technology, the primary potentials and challenges with relating to technology

and economy as identified in this thesis are summarised and accompanied by proposals for action briefly in Figure 6.22.

		Suggestions
Technology	**Potentials**	
	Material properties	
	- High surface quality	Application in high precision casting/ investment casting
	- High strength	Surface texturing (e.g. for medical implants)
	- Distortion-free sintering and casting	Functional integration
	- Abrasion resistance	Design freedom
	- High temperature stability	Conceivable eligibility in iron and steel casting
	Geometric flexibility	Individualisation/ part marking
	Challenges	
	Damage during wash-out process	Modification of the slurry and binder composition
	Prediction of core failure considering anisotropics	Development of a material model Coupling of casting process simulation and FEM
Economy	**Potentials**	
	Custom-tailored multi-material approach	Use of sintered ceramic only where advances are exploited
	Increasing productivity through larger machines/ build volume	Adaption of machine build volume to business case
	Production flexibility	
	Challenges	
	Reduced productivity through drying off the slurry's solvent	Development of efficient drying process (colouring, microwave, hot solvent, convection)
	High energy demand for sintering	Alignment of the sintering period to the required strength

Figure 6.22: Inferences on technological and economic potentials and challenges, including proposals for further action.

With respect to technological aspects, the expected superior material properties – being high surface quality, temperature stability and strength, and resistance to hot distortion and abrasion – provided the central impetus for the research conducted herein and were confirmed by utilising a collapsible high-strength casting core as required in aluminium casting of contour-close cooling structures. However, even individual properties may be exploited to open up the new application, as has been demonstrated by printing digital code tags to enable part traceability in casting. Equally, post-process surface finishing may be partially substituted by integrating surface textures into the core or mould. In particular, this might be of technological interest for inner contours that are not accessible for machining components or to realise functional surfaces, e.g. for medical implants. From an overall perspective, there are multiple further promising opportunities in utilising slurry-based 3D printing in the foundry industry, e.g. in high precision casting or investment casting where integrally cored ceramic moulds allow for enhanced process control, reduced lead times, and complexity compared to the conventional route of dipping wax patterns repeatedly in ceramic slurry (Bae, Halloran, 2011, pp. 1255–1256). Some product ranges in investment casting may already compete with 3D printed sand moulds and cores (Voigt, Manogharan, 2018, p. 13). However, incorporating

slurry-based 3D printing of integrally cored ceramic moulds into their infrastructure and business model offer investment casters the prospect of gaining production flexibility and long-term market shares on cast products meeting the most stringent quality requirements, e.g. in terms of dimensional accuracy or surface roughness, and processing sophisticated materials, e.g. steel or nickel-base alloys.

Wash-out was identified as a critical process step in the investigated process chain. The green bodies fabricated herein demanded a high exposure to ultrasound energy. Moreover, the non-bound compacted powder bed was found to swell tremendously. Thus, the green bodies were found susceptible to damages which are suggested to be mitigated by modifying the slurry composition. Moon et al. (2000) give valuable hints on the influencing factors on the redispersiblility of ceramic slurries. The binder, its mass proportion to be printed into the powder compact, and the printing parameters further contribute to improving the green bodies' structural integrity. The principle of realising self-collapsible ceramic casting cores that withstand the loads during casting and break as a result of the cast metal's shrinkage during solidification has been demonstrated. However, anisotropies were found to must be taken into account in the material model to predict core failure reliably.

Regarding economic expenses, various indicators must be likewise involved in decision-making, e.g. production flexibility, lead time, machine costs, energy consumption, or waste generation (Sivarupan et al., 2021, pp. 12–13). Incorporating AM in a hybrid casting process offers the prospect of improved resource utilisation and production efficiency in the foundry environment (Zheng et al., 2020, 6-11). Chapter 5.3.2 outlines considerations on the economic efficiency of the slurry-based 3D printing process itself, taking into account increased layer times due to the need to dry off a slurry's solvent. Increasing the machine's printing area size can significantly improve the part throughput. However, measures for more efficient layer-wise drying are advisable to save both energy and processing time. Sintering is a highly energy-consuming process (Ibn-Mohammed et al., 2019, pp. 5213–5214). Even though analysing the energy consumption of the overall process chain exceeds the scope of this work, it is obvious that including another energy-intensive process supplementary to metal smelting into the process chain comes with additional resource expenses. For this reason, those efforts need to be accompanied by earning benefits concerning the end product exploiting the aforementioned enhanced material properties to gain added value. It is suggested to realise moulding concepts tailored to the product and production environment. Multi-material core packages comprising sand and ceramic mould elements will possibly allow for an overall cost-effective and sustainable process route.

7 Conclusion and Future Work

Slurry-based 3D printing is a promising additive manufacturing technology as processing fine powders dispersed in suspension allows for the fabrication of sinterable ceramics of high surface qualities. Similar to powder-based binder jetting, virtually any powdery material can be processed at high deposition rates. Thus, a favourable efficiency compared to other AM methods is conceivable, which paves the way for future integration in the process chain of advanced castings. In metal casting, cores are used for shaping the internal cavities of the cast components. However, the production process faces a trade-off between a core's temperature resistance, its mechanical stability and its reliable removability subsequently to casting, leading to limitations in the exploitable design freedom. This work contributes to the fundamental understanding of the process characteristics of slurry-based binder jetting with a special emphasis on the requirements for future integration in casting technologies.

The slurry-based 3D printing process involves the repeating steps of casting a homogeneous layer from (for environmental reasons preferably aqueous) slurry, drying the layer to remove the suspension's solvent, and selectively applying binder onto the area that constitutes the respective part's cross-section. This technology's key challenges are allowing for reliable and homogeneous layer formation and controlling the formation of the microstructure by means of proper process management.

A 3D printing test setup enabling tailored process configuration and control options was developed to examine the slurry-based 3D printing process from those perspectives. By utilising CFD simulation methods, a coater geometry and appropriate process parameters for efficient, homogeneous and reliable layer formation were derived. Moreover, the influence of the layer-wise drying configuration on the material properties was studied. Finally, within the framework of an entire process chain demonstration, potentials and challenges for industrial implementation were revealed.

The most important achievements and proposals for further research are summarised in the following:

Homogeneous powder bed formation

The conditions necessary for a globally defect-free microstructure and scalability are created by achieving uniform macroscopic layer properties. A CFD approach enabled a computationally efficient surface reconstruction that has been carried out to enhance the coater design and determine appropriate process parameters. A 3D printing test setup and the basic process definitions required for reliable process control were developed based on the simulation

results and experiments. A tailored coater design allowed for extremely high surface qualities (Ra ~ 1.2 µm measured at the upper specimen's level) at coating speeds of as high as 100 mm/s and material feed on demand.

Control of material properties via drying configuration

It was shown that in slurry-based 3D printing, controlling material properties via drying configuration is feasible. Lower layer thicknesses and higher drying periods significantly improved material density, mechanical strength, ductility, dimensional accuracy, and surface quality. However, inverse behaviour was observed from a certain drying state (here above 55 s). Thus, it is evidenced that an over-drying state is attained when drying each layer excessively. While reducing the layer thickness and increasing the drying period is favourable with regard to materials' properties, those process parameters are economically disadvantageous since they result in lower deposition rates. Hence, it is suggested to optimise the drying setup, e.g. involve moisture transport via forced convection to achieve an advanced drying state in shorter times.

Potentials and challenges for industrial application

By studying the effect of the drying process, which is crucial for both part quality and process performance, comprehensive process knowledge on slurry-based 3D printing, and the achievable properties of future ceramic casting cores produced thereby were revealed. This thesis thus contributes to lowering the hurdles for the technology's industrial implementation in the foundry environment.

The concept of self-collapsible cores for casting applications was demonstrated. A tailored design of a hollow casting core – provided with predetermined breaking points – exhibiting superior mechanical and thermal stability was shown to break down due to forces caused by shrinkage of the solidifying cast metal. Thus it can be concluded that slurry-based 3D printing represents an advanced manufacturing method potentially enabling complex and filigree inner structures in future high-performance cast parts. A new strategy exploiting the potentials of slurry-based 3D printing may thus defy the conventional trade-off between casting cores' strength and their collapsibility and enable an elevation in design freedom for future cast parts.

Secondly, the superior surface properties in slurry-based 3D printing were shown to be exploitable by manufacturing ceramic digital code mould inserts for part tracking purposes.

However, this new approach demands further material and process developments prior to its industrial implementation. It was shown that the slurry material utilised herein enabled zero-shrinkage during sintering and thus superior dimensional accuracy but did not allow for appropriate redispersion due to the not-yet-optimised material composition. Redispersion,

however, is not only crucial to allow for part retrieval but also to enable full recyclability. Hence, future research on the slurry material, the process of part retrieval, and recycling is proposed.

A Appendix

A1 Advanced Coating Head Geometry

The advanced coating head geometry has been developed with a significant contribution of Alexander Seidel's master thesis (appendix A2) supervised by the author.

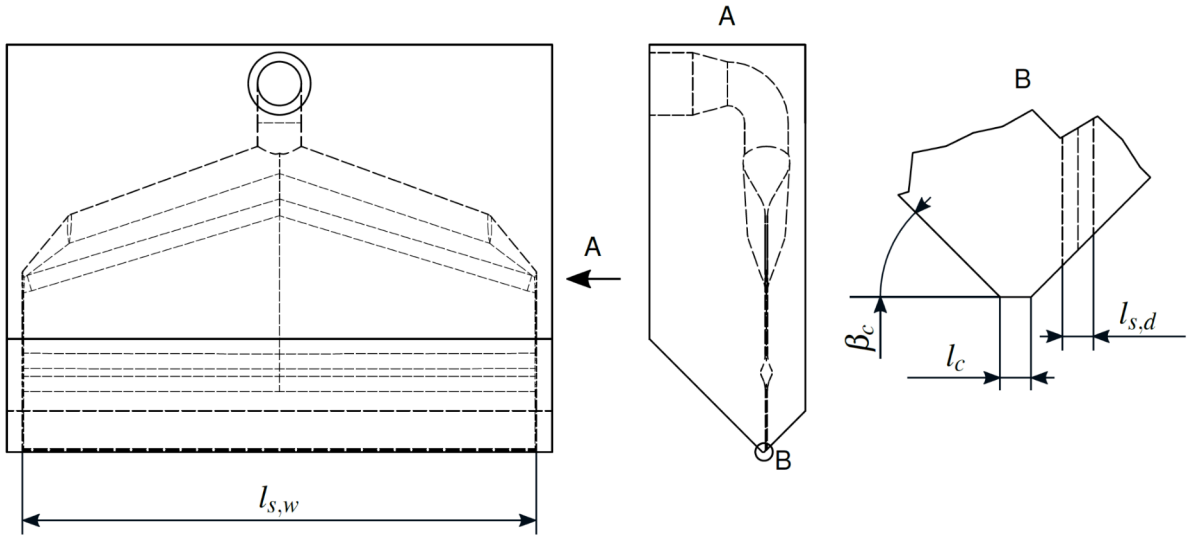

Figure A 1: Sketch of the final, advanced coating head geometry.

Table A 1: Geometry parameters of the final, advanced coating head geometry.

Geometry parameter	Variable	Value	Unit
Slurry tubing length	l_{tubing}	0.525	m
Slurry tubing diameter	d_{tubing}	$4 \cdot 10^{-3}$	m
Slot width	$l_{s,w}$	$3.3 \cdot 10^{-2}$	m
Slot depth	$l_{s,d}$	$1 \cdot 10^{-4}$	m
Chamfer distance	l_c	$1 \cdot 10^{-4}$	m
Chamfer angle	β_c	45	°

A2 Thermal Analysis

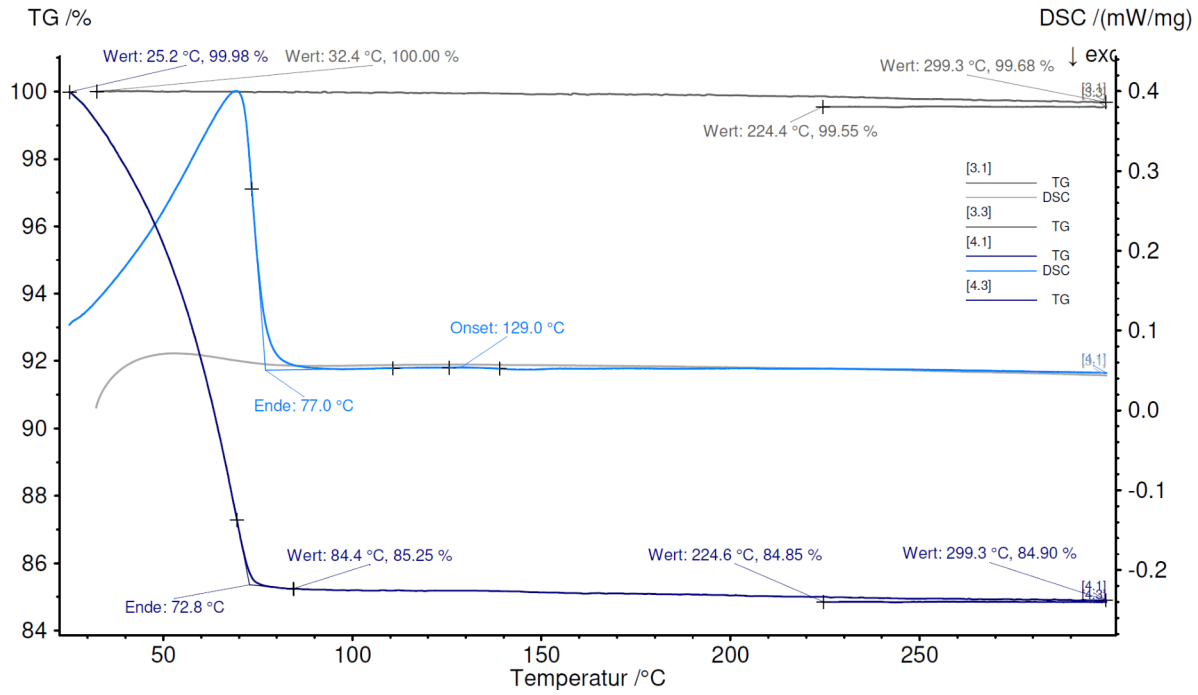

Figure A 2: Investigations of the thermal degradation of a compacted powder bed containing only slurry [3.1-3.3], or slurry and binder [4.1-4.3].

A3 Student Theses

Several student research projects were conducted within the scope of this work. The conception of the student theses, as well as the processing, analysis, interpretation, and illustration of results, was performed under my supervision and scientific guidance. I would like to express my gratitude and appreciation to all students for their essential contribution to this work.

Table A 2: List of Student Theses.

Name	Type of Thesis	Title (Year)
Simón Muzás, J.	Master's Thesis	Production and Characterization of Ceramic Layer Compounds (2020)
Seidel, A.	Master's Thesis	Numerical Simulation and Optimisation of the Slurry-based Layer Casting Process in Additive Manufacturing of Ceramic Parts (2020)
Angenoorth, J.	Student Thesis	Investigation of the Selective Binder Application to Ceramic Layers (2021)
Angenoorth, J.	Master's Thesis	Investigation of the Slurry-based Layer Coating Process in 3D Printing of Ceramic Casting Cores (2021)
Ding, H.	Student Thesis	Versagensgerechtes Design 3D-gedruckter keramischer Gießkerne (2022)
Zou, Y.	Master's Thesis	Influences of the Drying Process on the Properties of Ceramic Specimens Produced by Slurry-based Binder Jetting (2022)
Tanjavooru, V.	Master's Thesis	Development of a Numerical Simulation Tool for the Multiphase Flow in Binder-Jet 3D Printing using OpenFOAM (2022)
Rauch, J.	Master's Thesis	Thermische Simulationen zum Einfluss der Wärmeströme in Industrieöfen: Vorhersage der Dichteverteilung und Endform bei der Sinterung von Keramiken (2022)
Weileder, M.	Bachelor's Thesis	Untersuchungen zum Auslösen schlickerbasiert 3D-gedruckter keramischer Grünkörper aus dem konsolidierten Pulverbett (2022)

B List of Figures

C List of Tables

D Bibliography

AKPINAR, E.K., C. SARSILMAZ, and C. YILDIZ (2004). Mathematical modelling of a thin layer drying of apricots in a solar energized rotary dryer. In: *International Journal of Energy Research* **28**(8), 739-752.

AKSAY, I.A. and C.H. SCHILLING (1984). Colloidal Filtration Route to Uniform Microstructures. In: *Ultrastructure Processing of Ceramics, Glasses, and Composites*, 439-447.

ALGHUNAIM, A., S. KIRDPONPATTARA, and B.Z. NEWBY (2016). Techniques for determining contact angle and wettability of powders. In: *Powder Technology* **287**, 201-215.

ALMAGHARIZ, E.S., B.P. CONNER, L. LENNER, R. GULLAPALLI, G.P. MANOGHARAN, B. LAMONCHA, and M. FANG (2016). Quantifying the Role of Part Design Complexity in Using 3D Sand Printing for Molds and Cores. In: *International Journal of Metalcasting* **10**(3), 240-252.

ANSARI, S., M.A.I. RASHID, P.R. WAGHMARE, and D.S. NOBES (2020). Measurement of the flow behavior index of Newtonian and shear-thinning fluids via analysis of the flow velocity characteristics in a mini-channel. In: *SN Applied Sciences* **2**(11), 1-15.

ANTONY, J. (2014). *Design of experiments for engineers and scientists.* 2. ed., London: Elsevier.

ANWAR, N., T. SAPPINEN, K. JALAVA, and J. ORKAS (2021). Comparative experimental study of sand and binder for flowability and casting mold quality. In: *Advanced Powder Technology* **32**(6), 1902-1910.

ASTM International (2019). *ASTM C1161-18 - Test Method for Flexural Strength of Advanced Ceramics at Ambient Temperature*.

BAE, C.-J. and J.W. HALLORAN (2011). Integrally Cored Ceramic Mold Fabricated by Ceramic Stereolithography. In: *International Journal of Applied Ceramic Technology* **8**(6), 1255-1262.

BAI, Y., G. WAGNER, and C.B. WILLIAMS (2017). Effect of Particle Size Distribution on Powder Packing and Sintering in Binder Jetting Additive Manufacturing of Metals. In: *Journal of Manufacturing Science and Engineering* **139**(8).

BARUI, S., H. DING, Z. WANG, H. ZHAO, S. MARATHE, W. MIRIHANAGE, B. BASU, and B. DERBY (2020). Probing Ink-Powder Interactions during 3D Binder Jet Printing Using Time-Resolved X-ray Imaging. In: *ACS applied materials & interfaces* **12**(30), 34254-34264.

BASSOLI, E., A. GATTO, L. IULIANO, and M. GRAZIA VIOLANTE (2007). 3D printing technique applied to rapid casting. In: *Rapid Prototyping Journal* **13**(3), 148-155.

BENGISU, M. (2001). *Engineering ceramics,* Berlin: Springer.

BOOPATHI, N.G., M.S. MUTHURAMAN, R. PALKA, M. WARDACH, P. PRAJZENDANC, E. GUNDABATTINI, R.S. RASSIAH, and D.G. SOLOMON (2022). Modeling and Simulation of Electric Motors Using Lightweight Materials. In: *Energies* **15**(14), 5183.

BÖRGER, A., P. SUPANCIC, and R. DANZER (2002). The ball on three balls test for strength testing of brittle discs: stress distribution in the disc. In: *IOP Conference Series: Materials Science and Engineering* **22**(9-10), 1425-1436.

BOURELL, D.L., W. FRAZIER, H. KUHN, and M. SEIFI (2020). *Additive manufacturing processes,* Materials Park: ASM International. ASM handbook / prepared under the direction of the ASM International Handbook Committee. 24.

BRACKBILL, J.U., D.B. KOTHE, and C. ZEMACH (1992). A continuum method for modeling surface tension. In: *Journal of Computational Physics* **100**(2), 335-354.

BREINLINGER, T. (2015). *Entwicklung und Anwendung von Methoden zur Simulation des Trocknens von Suspensionen* (Dissertation, Karlsruhe Institute of Technology).

BRISCOE, B.J., G. LO BIUNDO, and N. ÖZKAN (1998). Drying kinetics of water-based ceramic suspensions for tape casting. In: *Ceramics International* **24**(5), 347-357.

BROSNAN, D.A. and G.C. ROBINSON (2003). *Introduction to drying of ceramics,* Westerville: American Ceramic Society.

BRYANT, N., T. FRUSH, J. THIEL, E. MACDONALD, and J. WALKER (2020). Influence of Machine Parameters on the Physical Characteristics of 3D-Printed Sand Molds for Metal Casting. In: *International Journal of Metalcasting* **11**(4), 3.

Bundesverband der Deutschen Gießerei-Industrie (1999). *BDG-Richtlinie P71 - Bindemittelprüfung - Biegefestigkeit von warmhärtenden, kunstharzgebundenen feuchten Formstoffen* (P71).

Bundesverband der Deutschen Gießerei-Industrie (1999). *BDG-Richtlinie P72 - Bindemittelprüfung - Prüfung von kalthärtenden, kunstharzgebundenen feuchten Formstoffen mit Härterzusatz* (P72).

BUNTEBARTH, G. (2020). Thermal properties of sand and mineral flours. In: *SN Applied Sciences* **2**(3), 1-9.

CARADONNA, M.A. (1997). *The fabrication of high packing density ceramic powder beds for the three dimensional printing process* (Master's Thesis, Massachusetts Institute of Technology).

CARLSSON, R., T. NEVZOROVA, and K. VIKINGSSON (2022). Long-Lived Sustainable Products through Digital Innovation. In: *Sustainability* **14**(21), 14364.

CARTER, C.B. and M.G. NORTON (2016). *Ceramic Materials - Science and engineering,* New York: Springer.

CHANTARAMEE, N., S. TANAKA, T. TAKAHASHI, and K. UEMATSU (2008). Evolution of Discontinuity in Particle Orientation in Ceramic Tape Casting. In: *Journal of the American Ceramic Society* **91**(10), 3181-3184.

CHAVEZ, L.A., P. IBAVE, B. WILBURN, D. ALEXANDER, C. STEWART, R. WICKER, and Y. LIN (2020). The Influence of Printing Parameters, Post-Processing, and Testing Conditions on the Properties of Binder Jetting Additive Manufactured Functional Ceramics. In: *Ceramics* **3**(1), 65-77.

CHEN, Q., E. JUSTE, M. LASGORCEIX, F. PETIT, and A. LERICHE (2022). Binder jetting process with ceramic powders: Influence of powder properties and printing parameters. In: *Open Ceramics* **9**, 100218.

CHIU, R.C. and M.J. CIMA (1993). Drying of Granular Ceramic Films: II, Drying Stress and Saturation Uniformity. In: *Journal of the American Ceramic Society* **76**(11), 2769-2777.

CHIU, R.C., T.J. GARINO, and M.J. CIMA (1993). Drying of Granular Ceramic Films: I, Effect of Processing Variables on Cracking Behavior. In: *Journal of the American Ceramic Society* **76**(9), 2257-2264.

CHUN, S.-Y., T. KIM, B. YE, B. JEONG, M. LEE, D.H. LEE, E.-S. KIM, H. LEE, and H.-D. KIM (2020). Capillary pressure and saturation of pore-controlled granules for powder bed binder jetting. In: *Applied Surface Science* **515**, 145979.

CHUN-CHIAO, W. and H. JIE (1988). A Study of Phenolic Novolak Resin Chemistry in Relation to the Hot Method of Coating Shell Sand. In: *Cast Metals* **1**(3), 171-175.

CIMA, M.J., M. OILVEIRA, H.R. WANG, E. SACHS, and R. HOLMAN (2001). Slurry-Based 3DP and Fine Ceramic Components. In: *International Solid Freeform Fabrication Symposium*, 216-223.

COLTON, T. and N.B. CRANE (2021). Influence of droplet velocity, spacing, and inter-arrival time on line formation and saturation in binder jet additive manufacturing. In: *Additive Manufacturing* **37**, 101711.

DANZER, R., P. SUPANCIC, J. PASCUAL, and T. LUBE (2007). Fracture statistics of ceramics – Weibull statistics and deviations from Weibull statistics. In: *Engineering Fracture Mechanics* **74**(18), 2919-2932.

DEMUTH, T., Y. JEANVOINE, J. HAFNER, and J.G. ÁNGYÁN (1999). Polymorphism in silica studied in the local density and generalized-gradient approximations. In: *Journal of Physics: Condensed Matter* **11**(19), 3833-3874.

DENESUK, M., G.L. SMITH, B. ZELINSKI, N.J. KREIDL, and D.R. UHLMANN (1993). Capillary Penetration of Liquid Droplets into Porous Materials. In: *Journal of Colloid and Interface Science* **158**(1), 114-120.

DENG, F., R. LI, S. KLAN, and W. VOLK (2022). Comparative Evaluation of Marking Methods on Cast Parts of Al–Si Alloy with Image Processing. In: *International Journal of Metalcasting* **16**(3), 1122-1139.

DERBY, B. (2010). Inkjet Printing of Functional and Structural Materials: Fluid Property Requirements, Feature Stability, and Resolution. In: *Annual Review of Materials Research* **40**(1), 395-414.

DESHPANDE, S.S., L. ANUMOLU, and M.F. TRUJILLO (2012). Evaluating the performance of the two-phase flow solver interFoam. In: *Computational Science & Discovery* **5**(1), 14016.

Deutsches Institut für Normung e.V. (2007). *DIN EN 843-2 - Hochleistungskeramik - Mechanische Eigenschaften monolithischer Keramik bei Raumtemperatur- Teil 2: Bestimmung des Elastizitätsmoduls, Schubmoduls und der Poissonzahl* (DIN EN 843-2:2007-03).

Deutsches Institut für Normung e.V. (2008). *DIN EN 843-1 - Advanced technical ceramics - Mechanical properties of monolithic ceramics at room temperature - Part 1: Determination of flexural strength* (DIN EN 843-1:2008-08).

Deutsches Institut für Normung e.V. (2017). *DIN 863-1 - Geometrical product specifications (GPS) - Micrometers - Part 1: Micrometers for external measurements; maximum permissible errors* (DIN 863-1:2017-02).

Deutsches Institut für Normung e.V. (2017). *DIN EN ISO/ASTM 52900 - Additive manufacturing - General principles - Fundamentals and vocabulary* (DIN EN ISO/ASTM 52900:2017-06).

Deutsches Institut für Normung e.V. (2020). *DIN 8580 - Manufacturing processes - Terms and definitions, division* (DIN 8580:2020-01).

Deutsches Institut für Normung e.V. (2020). *DIN EN ISO 13385-1 - Geometrical product specifications (GPS) - Dimensional measuring equipment - Part 1: Design and metrological characteristics of callipers* (DIN EN ISO 13385-1:2020-03).

Deutsches Institut für Normung e.V. (2022). *DIN EN ISO 18754 - Fine ceramics (advanced ceramics, advanced technical ceramics) - Determination of density and apparent porosity* (DIN EN ISO 18754:2022-06).

DIENER, S., A. ZOCCA, and J. GÜNSTER (2021). Literature review: Methods for achieving high powder bed densities in ceramic powder bed based additive manufacturing. In: *Open Ceramics* **8**, 100191.

DIENER, S., H. SCHUBERT, A. HELD, N. KATSIKIS, J. GÜNSTER, and A. ZOCCA (2022). Influence of the dispersant on the parts quality in slurry-based binder jetting of SiC ceramics. In: *Journal of the American Ceramic Society* **105**(12), 7072-7086.

DIENER, S., H. SCHUBERT, J. GÜNSTER, and A. ZOCCA (2023). Ink development for the additive manufacturing of strong green parts by layerwise slurry deposition (LSD-print). In: *Journal of the American Ceramic Society*.

DU, W., X. REN, Z. PEI, and C. MA (2020). Ceramic Binder Jetting Additive Manufacturing: A Literature Review on Density. In: *Journal of Manufacturing Science and Engineering* **142**(4).

EGELER, N., M. TORBUS, M. KNEZEVIC, G. BAE, R. LAITAR, D. TRINOWSKI, and W. SEELBACH (2012). *Silicic ester modified phenol/formaldehyde novolaks and their use for the production of resin coated substrates* (EP 2 522 683 A1).

ERHARD, P., A. SEIDEL, J. VOGT, W. VOLK, and D. GÜNTHER (2022). Evaluation and optimisation of a slurry-based layer casting process in additive manufacturing using multiphase simulations and spatial reconstruction. In: *Production Engineering* **16**(1), 43-54.

ERHARD, P., J. ANGENOORTH, J. VOGT, J. SPIEGEL, F. ETTEMEYER, W. VOLK, and D. GÜNTHER (2021). Characterization of Slurry-Cast Layer Compounds for 3D Printing of High Strength Casting Cores. In: *Materials* **14**(20), 6149.

ETTEMEYER, F. (2021). *Charakterisierung des Entkernverhaltens anorganisch gebundener Sand-Binder-Systeme* (Dissertation, Technical University of Munich).

FARKAS, I., M.J. LAMPINEN, and K. OJALA (1991). Water flow and binder migration during drying of coated paper. In: *Drying Technology* **9**(4), 1019-1049.

FEIKUS, F.J., P. BERNSTEINER, R.F. GUTIÉRREZ, and M. ŁUSZCZAK (2020). Weiterentwicklungen bei Gehäusen von Elektromotoren. In: *MTZ - Motortechnische Zeitschrift* **81**(3), 42-47.

FETZER, T., J. VANDERBORGHT, K. MOSTHAF, K.M. SMITS, and R. HELMIG (2017). Heat and water transport in soils and across the soil-atmosphere interface: 2. Numerical analysis. In: *Water Resources Research* **53**(2), 1080-1100.

FLEMMING, E. and W. TILCH (1993). *Formstoffe und Formverfahren.* 1. Aufl., Leipzig: Deutscher Verlag für Grundstoffindustrie.

FOCKE, W.W., M.S. SMIT, A.T. TOLMAY, L.S. VAN DER WALT, and W.L. VAN WYK (1991). Differential scanning calorimetry analysis of thermoset cure kinetics: Phenolic resole resin. In: *Polymer Engineering and Science* **31**(23), 1665-1669.

GAHLER, A., J.G. HEINRICH, and J. GÜNSTER (2006). Direct Laser Sintering of Al2O3–SiO2 Dental Ceramic Components by Layer-Wise Slurry Deposition. In: *Journal of the American Ceramic Society* **89**(10), 3076-3080.

GIBSON, I. (2021). *Additive Manufacturing Technologies.* 3rd ed., Cham: Springer.

GOKULDOSS, P.K., S. KOLLA, and J. ECKERT (2017). Additive Manufacturing Processes: Selective Laser Melting, Electron Beam Melting and Binder Jetting-Selection Guidelines. In: *Materials* **10**(6), 672.

GRAU, J.E. (1998). *Fabrication of engineered ceramic components by the slurry-based three dimensional printing process* (Ph.D., Massachusetts Institute of Technology).

GRAU, J.E., S.A. UHLAND, J. MOON, M.J. CIMA, and E.M. SACHS (1999). Controlled Cracking of Multilayer Ceramic Bodies. In: *Journal of the American Ceramic Society* **82**(8), 2080-2086.

GRIFFITH, A.A. (1921). The phenomena of rupture and flow in solids. In: *Philosophical Transactions of the Royal Society of London Series A, Containing Papers of a Mathematical or Physical Character* **221**(582-593), 163-198.

GÜNTHER, D. and F. MÖGELE (2016). Additive Manufacturing of Casting Tools Using Powder-Binder- Jetting Technology. In: I.V. SHISHKOVSKY, ed. *New Trends in 3D Printing:* InTech.

GÜNTHER, D., P. ERHARD, S. SCHWAB, and I. TAHA (2021). 3D Printed Sand Tools for Thermoforming Applications of Carbon Fiber Reinforced Composites-A Perspective. In: *Materials* **14**(16), 4639.

GYARMATI, G., I. BUDAVÁRI, G. FEGYVERNEKI, and L. VARGA (2021). The effect of sand quality on the bending strength and thermal distortion of chemically bonded sand cores. In: *Heliyon* **7**(7), e07624.

HACKNEY, P. and R. WOOLDRIDGE (2017). Optimisation of Additive Manufactured Sand Printed Mould Material for Aluminium Castings. In: *Procedia Manufacturing* **11**, 457-465.

HALLORAN, J.W. (2016). Ceramic Stereolithography: Additive Manufacturing for Ceramics by Photopolymerization. In: *Annual Review of Materials Research* **46**(1), 19-40.

HARTMANN, C., L. VAN DEN BOSCH, J. SPIEGEL, D. RUMSCHÖTTEL, and D. GÜNTHER (2022). Removal of Stair-Step Effects in Binder Jetting Additive Manufacturing Using Grayscale and Dithering-Based Droplet Distribution. In: *Materials* **15**(11).

HASBROUCK, C.R., J.W. FISHER, M.R. VILLALPANDO, and P.C. LYNCH (2020). A Comparative Study of Dimensional Tolerancing Capabilities and Microstructure Formation between Binder Jet Additively Manufactured Sand Molds and Olivine Green Sand Molds for Metalcasting of A356.0. In: *Procedia Manufacturing* **48**(1), 338-348.

HAWALDAR, N. and J. ZHANG (2018). A comparative study of fabrication of sand casting mold using additive manufacturing and conventional process. In: *The International Journal of Advanced Manufacturing Technology* **97**(1-4), 1037-1045.

HENDERSON, S.M. (1974). Progress in Developing the Thin Layer Drying Equation. In: *Transactions of the ASAE* **17**(6), 1167-1168.

HILPERT, M. and A. BEN-DAVID (2009). Infiltration of liquid droplets into porous media: Effects of dynamic contact angle and contact angle hysteresis. In: *International Journal of Multiphase Flow* **35**(3), 205-218.

HODDER, K.J. and R.J. CHALATURNYK (2019). Bridging additive manufacturing and sand casting: Utilizing foundry sand. In: *Additive Manufacturing* **28**, 649-660.

HOLMAN, R.K., M.J. CIMA, S.A. UHLAND, and E. SACHS (2002). Spreading and infiltration of inkjet-printed polymer solution droplets on a porous substrate. In: *Journal of Colloid and Interface Science* **249**(2), 432-440.

HU, M.S., M.D. THOULESS, and A.G. EVANS (1988). The decohesion of thin films from brittle substrates. In: *Acta Metallurgica* **36**(5), 1301-1307.

HUANG, S., C. YE, H. ZHAO, and Z. FAN (2019). Additive manufacturing of thin alumina ceramic cores using binder-jetting. In: *Additive Manufacturing* **29**, 100802.

IBN-MOHAMMED, T., C.A. RANDALL, K.B. MUSTAPHA, J. GUO, J. WALKER, S. BERBANO, S. KOH, D. WANG, D.C. SINCLAIR, and I.M. REANEY (2019). Decarbonising ceramic manufacturing: A techno-economic analysis of energy efficient sintering technologies in the functional materials sector. In: *IOP Conference Series: Materials Science and Engineering* **39**(16), 5213-5235.

JABBARI, M., R. BULATOVA, A. TOK, C. BAHL, E. MITSOULIS, and J.H. HATTEL (2016). Ceramic tape casting: A review of current methods and trends with emphasis on rheological behaviour and flow analysis. In: *Materials Science and Engineering: B* **212**, 39-61.

JAHANGIRIAN, S., A. HASSANPOUR, and S. KRISHNAN (2020). Demagnetization Simulations of High-Power Electric Motors for Reliable Electric Aircrafts. *AIAA Propulsion and Energy 2020 Forum.* Reston: American Institute of Aeronautics and Astronautics.

JAKUBSKI, J., M. DOBOSZ, and P. JELÍNEK (2005). The influence of the protective coating type on thermal deformation of casting cores. In: *Archiwum Odlewnictwa* **5**(15), 164-169.

JANETTI, B.M. and H. JANSSEN (2020). Impact of the drying rate on the moisture retention curve of porous building materials. In: *Construction and Building Materials* **258**, 119451.

JOSEPH, M.K., F. BANGANAYI, and D. OYOMBO (2017). Moulding Sand Recycling and Reuse in Small Foundries. In: *Procedia Manufacturing* **7**, 86-91.

KANG, J. and Q. MA (2017). The role and impact of 3D printing technologies in casting. In: *China Foundry* **14**(3), 157-168.

KANYO, J.E., S. SCHAFFÖNER, R.S. UWANYUZE, and K.S. LEARY (2020). An overview of ceramic molds for investment casting of nickel superalloys. In: *IOP Conference Series: Materials Science and Engineering* **40**(15), 4955-4973.

KHAN, M.A.A. (2017). *Evolution of Metal Casting Technologies - A Historical Perspective,* Cham: Springer.

KIKUCHI, R., S. YOSHIKAWA, P.K. JAYARAMAN, J. ZHENG, and T. MAEKAWA (2018). Embedding QR codes onto B-spline surfaces for 3D printing. In: *Computer-Aided Design* **102**, 215-223.

KLINOV, A. and I. ANASHKIN (2019). Diffusion in Binary Aqueous Solutions of Alcohols by Molecular Simulation. In: *Processes* **7**(12), 947.

KLOCKE, F. (2018). *Fertigungsverfahren 5 - Gießen und Pulvermetallurgie.* 5. Aufl. 2018, Berlin, Heidelberg: Springer.

KNEZEVIC, V. (1998). *Effect of binder drop placement strategy on surface finish of fine ceramic parts by 3D printing* (Master's Thesis, Massachusetts Institute of Technology).

KOCH, T., D. GLÄSER, K. WEISHAUPT, S. ACKERMANN, M. BECK, B. BECKER, S. BURBULLA, H. CLASS, E. COLTMAN, S. EMMERT, T. FETZER, C. GRÜNINGER, K. HECK, J. HOMMEL, T. KURZ, M. LIPP, F. MOHAMMADI, S. SCHERRER, M. SCHNEIDER, G. SEITZ, L. STADLER, M. UTZ, F. WEINHARDT, and B. FLEMISCH (2021). DuMux 3 – an open-source simulator for solving flow and transport problems in porous media with a focus on model coupling. In: *Computers & Mathematics with Applications* **81**, 423-443.

KUMAR, S. (2020). *Additive Manufacturing Processes.* 1st ed. 2020, Cham: Springer.

KUMAR, S. and D.B. KARUNAKAR (2021). Characterization and Properties of Ceramic Shells in Investment Casting Process. In: *International Journal of Metalcasting* **15**(1), 98-107.

LAKHDAR, Y., C. TUCK, J. BINNER, A. TERRY, and R. GOODRIDGE (2021). Additive manufacturing of advanced ceramic materials. In: *Progress in Materials Science* **116**, 100736.

LE NÉEL, T.A., P. MOGNOL, and J.-Y. HASCOËT (2018). A review on additive manufacturing of sand molds by binder jetting and selective laser sintering. In: *Rapid Prototyping Journal* **24**(8), 1325-1336.

LECHNER, P. (2021). *The Brittle Fracture Behaviour of Chemically-Bound Foundry Sands* (Dissertation, Technical University of Munich).

LIMA, P., A. ZOCCA, W. ACCHAR, and J. GÜNSTER (2018). 3D printing of porcelain by layerwise slurry deposition. In: *IOP Conference Series: Materials Science and Engineering* **38**(9), 3395-3400.

LITHOZ GMBH (2022). *Laser Induced Slipcasting*. Accessed: 16 August 2022. Available from: https://lithoz.com/de/technologie/lis-technologie.

LOHSE, D. (2022). Fundamental Fluid Dynamics Challenges in Inkjet Printing. In: *Annual Review of Fluid Mechanics* **54**(1), 349-382.

LÓPEZ DE SABANDO, A. (2019). *Pressure Die Casting (HPDC) Lost-Core (LC) technology for the production of Aluminium Closed Deck blocks for next generation Euro 7 engines - Core 4.0 - Public final report*. Accessed: 13 March 2022. Available from: https://ec.europa.eu/research/participants/documents/downloadPublic?documentIds=080166e5c59c3b69&appId=PPGMS.

MAJI, S., O. URAKAWA, and T. INOUE (2014). The structure and viscoelasticity of novolac resins. In: *Polymer Journal* **46**(9), 584-591.

MARTINEZ, D., C. BATE, and G. MANOGHARAN (2020). Towards Functionally Graded Sand Molds for Metal Casting: Engineering Thermo-mechanical Properties Using 3D Sand Printing. In: *JOM* **72**(3), 1340-1354.

MEIBODI, M.A., R. GIESECKE, and B. DILLENBURGER (2019). 3D Printing Sand Molds for Casting Bespoke Metal Connections - Digital Metal: Additive Manufacturing for Cast Metal Joints in Architecture. In: *CAADRIA proceedings*.

MERCHÁN, M., M.G. de CORTÁZAR, H. GALARRAGA, J. BÁRCENA, and A. ARTOLA (2019). Research on Coatings and Infiltration to Strengthen Ceramic Lost Cores Used in High-Pressure Die Casting Processes. In: *International Journal of Metalcasting* **13**(3), 597-603.

MITTERPACH, J., E. HRONCOVÁ, J. LADOMERSKÝ, and K. BALCO (2017). Environmental evaluation of grey cast iron via life cycle assessment. In: *Journal of Cleaner Production* **148**, 324-335.

MIYANAJI, H., M. ORTH, J.M. AKBAR, and L. YANG (2018a). Process development for green part printing using binder jetting additive manufacturing. In: *Frontiers of Mechanical Engineering* **13**(4), 504-512.

MIYANAJI, H., N. MOMENZADEH, and L. YANG (2018b). Effect of printing speed on quality of printed parts in Binder Jetting Process. In: *Additive Manufacturing* **20**, 1-10.

MIYANAJI, H., N. MOMENZADEH, and L. YANG (2019). Effect of powder characteristics on parts fabricated via binder jetting process. In: *Rapid Prototyping Journal* **25**(2), 332-342.

MONTGOMERY, D.C. (2009). *Design and analysis of experiments.* 7. ed., internat. student version, Hoboken: Wiley.

MOON, J., J.E. GRAU, M.J. CIMA, and E.M. SACHS (2000). Slurry Chemistry Control to Produce Easily Redispersible Ceramic Powder Compacts. In: *Journal of the American Ceramic Society* **83**(10), 2401-2408.

MOON, J., J.E. GRAU, V. KNEZEVIC, M.J. CIMA, and E.M. SACHS (2002). Ink-Jet Printing of Binders for Ceramic Components. In: *Journal of the American Ceramic Society* **85**(4), 755-762.

MORRELL, R., 2007. *Biaxial flexural strength testing of ceramic materials,* Teddington. Available from: https://eprintspublications.npl.co.uk/1569/.

MOSTAFAEI, A., A.M. ELLIOTT, J.E. BARNES, F. LI, W. TAN, C.L. CRAMER, P. NANDWANA, and M. CHMIELUS (2020). Binder jet 3D printing—Process parameters, materials, properties, modeling, and challenges. In: *Progress in Materials Science* **40**(1160), 100707.

MÜHLER, T., C. WIRTH, M. ASCHERI, D. NICOLAIDES, J. HEINRICH, and J. GÜNSTER (2015a). Slurry-based powder beds for the selective laser sintering of silicate ceramics. In: *Journal of ceramic science and technology* **6**(2), 113-118.

MÜHLER, T., C.M. GOMES, J. HEINRICH, and J. GÜNSTER (2015b). Slurry-Based Additive Manufacturing of Ceramics. In: *International Journal of Applied Ceramic Technology* **12**(1), 18-25.

MUNZ, D. (1999). *Ceramics - Mechanical Properties, Failure Behaviour, Materials Selection.* 1st ed., Berlin, Heidelberg: Springer Berlin / Heidelberg. Springer Series in Materials Science Ser. v.36.

MURRAY, M. (2009). *Cracking in coatings from colloidal dispersions - An industrial perspective*. Accessed: 5 March 2022. Available from: https://www.soci.org/-/media/files/conference-downloads/2009/rideal-lectures-apr-09/murray.ashx.

MYERS, K., A. PATERSON, T. IIZUKA, and A. KLEIN (2019). The Effect of Print Speed on Surface Roughness and Density Uniformity of Parts Produced Using Binder Jet 3D Printing. In: *International Solid Freeform Fabrication Symposium*, 122-133.

NAGASAWA, Y., M. UEMATSU, Y. TAKAHASHI, Z. KATO, K. UEMATSU, and S. TANAKA (2015). Observation of Particle Motion in High-Concentration Ceramic Slurries Under Low Shear Rate. In: *Journal of the American Ceramic Society* **98**(5), 1429-1436.

NIEVES-REMACHA, M.J., L. YANG, and K.F. JENSEN (2015). OpenFOAM Computational Fluid Dynamic Simulations of Two-Phase Flow and Mass Transfer in an Advanced-Flow Reactor. In: *Industrial & Engineering Chemistry Research* **54**(26), 6649-6659.

NIU, Z., D. GE, C. CHENG, J. YE, and N. RECHO (2009). Evaluation of the stress singularities of plane V-notches in bonded dissimilar materials. In: *Applied Mathematical Modelling* **33**(3), 1776-1792.

OBERKAMPF, W.L. (2010). *Verification and Validation in Scientific Computing,* Cambridge: Cambridge University Press.

OLIVEIRA, M.A. (2002). *Slurry based Three Dimensional Printing (S-3DP) of tungsten carbide cobalt* (Master's Thesis, Massachusetts Institute of Technology).

PAGLIARI, L., M. DAPIAGGI, A. PAVESE, and F. FRANCESCON (2013). A kinetic study of the quartz–cristobalite phase transition. In: *IOP Conference Series: Materials Science and Engineering* **33**(15-16), 3403-3410.

PARAB, N.D., J.E. BARNES, C. ZHAO, R.W. CUNNINGHAM, K. FEZZAA, A.D. ROLLETT, and T. SUN (2019). Real time observation of binder jetting printing process using high-speed X-ray imaging. In: *Scientific Reports* **9**(1), 2499.

PARTELI, E.J.R., J. SCHMIDT, C. BLÜMEL, K.-E. WIRTH, W. PEUKERT, and T. PÖSCHEL (2014). Attractive particle interaction forces and packing density of fine glass powders. In: *Scientific Reports* **4**(1), 6227.

PATIRUPANUSARA, P., W. SUWANPREUK, T. RUBKUMINTARA, and J. SUWANPRATEEB (2008). Effect of binder content on the material properties of polymethyl methacrylate fabricated by three dimensional printing technique. In: *Journal of Materials Processing Technology* **207**(1-3), 40-45.

PIVINSKII, Y.E., V.F. TSAREV, Z.E. TERESHCHENKO, and L.S. KONEVA (1973). The slip casting rate for quartz ceramics. In: *Refractories* **14**(7-8), 509-512.

PÖHLMANN, M. (2006). *Thermisch härtende Polymerverbundmaterialien als Basis für neue Befestigungssysteme* (Dissertation, Technical University of Dresden).

QUITTER, D. (2019). *Umweltverträgliche Sandkerne für den Aluminiumguss*. Accessed: 16 August 2022. Available from: https://www.konstruktionspraxis.vogel.de/umweltvertraegliche-sandkerne-fuer-den-aluminiumguss-a-790252/.

RADJAI, F., J.-N. ROUX, and A. DAOUADJI (2017). Modeling Granular Materials: Century-Long Research across Scales. In: *Journal of Engineering Mechanics* **143**(4), 4017002.

RAHAMAN, M.N. (2003). *Ceramic Processing and Sintering.* 2nd ed., Hoboken: Marcel Dekker Inc.

RAHAMAN, M.N. (2007). *Sintering of Ceramics,* Boca Raton: CRC Press.

RAMAN, C.V. and T. NEDUNGADI (1940). The α-β Transformation of Quartz. In: *Nature* **145**(3665), 147.

RECKNAGEL, U. and M. DAHLMANN, 2009. Spezialsande - Formgrundstoffe für die moderne Kern- und Formherstellung. In: *Giesserei Rundschau* **56**, 9-17.

REIHLE, M., M. HOFMANN, U. WASMUTH, W. VOLK, H. HOFFMANN, and W. PETRY (2013). In Situ Strain Measurements during Casting Using Neutron Diffraction. In: *International Conference on Residual Stresses 9* **768-769**, 484-491.

REYES, Y., J. CAMPOS-TERÁN, F. VÁZQUEZ, and Y. DUDA (2007). Properties of films obtained from aqueous polymer dispersions: study of drying rate and particle polydispersity effects. In: *Modelling and Simulation in Materials Science and Engineering* **15**(3), 355-368.

RINGDALEN, E. (2015). Changes in Quartz During Heating and the Possible Effects on Si Production. In: *JOM* **67**(2), 484-492.

SACHS, E.M., J.S. HAGGERTY, M.J. CIMA, and P.A. WILLIAMS (1993). *Three-dimensional printing techniques* (US5204055 A).

SACHS, E.M., M.J. CIMA, M.A. CARADONNA, J. GRAU, J.G. SERDY, P.C. SAXTON, S.A. UHLAND, and J. MOON (2000). *Jetting layers of powder and the formation of fine powder beds thereby* (EP1009614 A1).

SADARANG, J., R.K. NAYAK, and I. PANIGRAHI (2021). Challenges and Future Prospective of Alternative Materials to Silica Sand for Green Sand Mould Casting: A Review. In: *Transactions of the Indian Institute of Metals* **74**(12), 2939-2952.

SAHEB, N. and U. HAYAT (2017). Temperature-dependent thermal properties of spark plasma sintered alumina. In: *Science of Sintering* **49**(2), 117-128.

SAMA, S.R., T. BADAMO, and G. MANOGHARAN (2020). Case Studies on Integrating 3D Sand-Printing Technology into the Production Portfolio of a Sand-Casting Foundry. In: *International Journal of Metalcasting* **14**(1), 12-24.

SCHERER, G.W. (1990). Theory of Drying. In: *Journal of the American Ceramic Society* **73**(1), 3-14.

SCHMIDT, J.-S. and R. OSEBOLD (2017). Environmental Management Systems as a Driver for Sustainability. State of Implementation, Benefits and Barriers in German Construction Companies **23**(1), 150-162.

SCHUBERT, H. (2012). *Handbuch der Mechanischen Verfahrenstechnik - Partikeleigenschaften, Mikroprozesse, Makroprozesse, Schüttgut,* Weinheim: Wiley.

SCHULZE, D. (2008). *Powders and bulk solids - Behavior, characterization, storage and flow,* Berlin: Springer.

SHI, Y., J. ZHANG, S. WEN, B. SONG, C. YAN, Q. WEI, J. WU, Y. YIN, J. ZHOU, R. CHEN, W. ZHOU, H. JIA, H. YANG, and H. NAN (2021). Additive manufacturing and foundry innovation. In: *China Foundry* **18**(4), 286-295.

SIVARUPAN, T., N. BALASUBRAMANI, P. SAXENA, D. NAGARAJAN, M. EL MANSORI, K. SALONITIS, M. JOLLY, and M.S. DARGUSCH (2021). A review on the progress and challenges of binder jet 3D printing of sand moulds for advanced casting. In: *Additive Manufacturing* **40**, 101889.

SNELLING, D., H. BLOUNT, C. FORMAN, K. RAMSBURG, A. WENTZEL, C. WILLIAMS, and A. DRUSCHITZ (2013). The Effects on 3D Printed Molds on Metal Castings. In: *International Solid Freeform Fabrication Symposium*, 827-845.

SNELLING, D., Q. LI, N. MEISEL, C.B. WILLIAMS, R.C. BATRA, and A.P. DRUSCHITZ (2015). Lightweight Metal Cellular Structures Fabricated via 3D Printing of Sand Cast Molds. In: *Advanced Engineering Materials* **17**(7), 923-932.

SOHN, H.Y. and C. MORELAND (1968). The effect of particle size distribution on packing density. In: *The Canadian Journal of Chemical Engineering* **46**(3), 162-167.

SPIERINGS, A.B., M. SCHNEIDER, and R. EGGENBERGER (2011). Comparison of density measurement techniques for additive manufactured metallic parts. In: *Rapid Prototyping Journal* **17**(5), 380-386.

SPIERINGS, A.B., M. VOEGTLIN, T. BAUER, and K. WEGENER (2016). Powder flowability characterisation methodology for powder-bed-based metal additive manufacturing. In: *Progress in Additive Manufacturing* **1**(1-2), 9-20.

STAAT, H.J.J., A. VAN DER BOS, M. VAN DEN BERG, H. REINTEN, H. WIJSHOFF, M. VERSLUIS, and D. LOHSE (2017). Ultrafast imaging method to measure surface tension and viscosity of inkjet-printed droplets in flight. In: *Experiments in Fluids* **58**(1), 1-8.

STAUDER, B.J., H. KERBER, and P. SCHUMACHER (2016). Foundry sand core property assessment by 3-point bending test evaluation. In: *Journal of Materials Processing Technology* **237**, 188-196.

SUN, S.-C., B. YUAN, and M.-P. LIU (2012). Effects of moulding sands and wall thickness on microstructure and mechanical properties of Sr-modified A356 aluminum casting alloy. In: *Transactions of Nonferrous Metals Society of China* **22**(8), 1884-1890.

TELLE, R., H. SALMANG, and H. SCHOLZE (2007). *Keramik.* 7th ed., Berlin, Heidelberg: Springer.

TIAN, X., D. LI, and J.G. HEINRICH (2012). Rapid prototyping of porcelain products by layer-wise slurry deposition (LSD) and direct laser sintering. In: *Rapid Prototyping Journal* **18**(5), 362-373.

TIAN, X., J. GÜNSTER, J. MELCHER, D. LI, and J.G. HEINRICH (2009). Process parameters analysis of direct laser sintering and post treatment of porcelain components using Taguchi's method. In: *Journal of the European Ceramic Society* **29**(10), 1903-1915.

TRAVERS, J.C., B.G. COOK, and L. COOK (2017). Null Hypothesis Significance Testing and p Values. In: *Learning Disabilities Research & Practice* **32**(4), 208-215.

UPADHYAY, M., T. SIVARUPAN, and M. EL MANSORI (2017). 3D printing for rapid sand casting—A review. In: *Journal of Manufacturing Processes* **29**(6), 211-220.

UTELA, B., D. STORTI, R. ANDERSON, and M. GANTER (2008). A review of process development steps for new material systems in three dimensional printing (3DP). In: *Journal of Manufacturing Processes* **10**(2), 96-104.

UYAN, T., K. JALAVA, J. ORKAS, and K. OTTO (2022). Sand Casting Implementation of Two-Dimensional Digital Code Direct-Part-Marking Using Additively Manufactured Tags. In: *International Journal of Metalcasting* **16**(3), 1140-1151.

VAEZI, M. and C.K. CHUA (2011). Effects of layer thickness and binder saturation level parameters on 3D printing process. In: *The International Journal of Advanced Manufacturing Technology* **53**(1-4), 275-284.

VASKOVÁ, I., L. VARGA, I. PRASS, V. DARGAI, M. CONEV, M. HRUBOVČÁKOVÁ, M. BARTOŠOVÁ, B. BUĽKO, and P. DEMETER (2020). Examination of Behavior from Selected Foundry Sands with Alkali Silicate-Based Inorganic Binders. In: *Metals* **10**(2), 235.

VEDEL-SMITH, N.K. and T.A. LENAU (2012). Casting traceability with direct part marking using reconfigurable pin-type tooling based on paraffin–graphite actuators. In: *Journal of Manufacturing Systems* **31**(2), 113-120.

Verein Deutscher Giessereifachleute e.V. (1999). *VDG-Merkblatt P26 - Prüfung von Formgrundstoffen - Bestimmung der Stoffeigenschaften von Quarzsand* (P26).

VOCK, S., B. KLÖDEN, A. KIRCHNER, T. WEIßGÄRBER, and B. KIEBACK (2019). Powders for powder bed fusion: a review. In: *Progress in Additive Manufacturing* **4**(4), 383-397.

VOGT, J., G. SEIFERT, and F. RAETHER (2021a). Towards Ceramic Production via Digitalization and Additive Manufacturing. In: *Ceramic Applications* (9), 33-44.

VOGT, J., H. FRIEDRICH, M. STEPANYAN, C. ECKARDT, M. LAM, D. LAU, B. CHEN, R. SHAN, and J. CHAN (2022). Improved green and sintered density of alumina parts fabricated by binder jetting and subsequent slurry infiltration. In: *Progress in Additive Manufacturing* **7**(2), 161-171.

VOGT, J., M. STEPANYAN, P. ERHARD, D. GÜNTHER, S. GARCHING, F. SCHMALZL, and S. GLÄSER (2021b). Slurry-based 3-D-printing of Casting Cores. In: *Casting Plant & Technology* (3), 30-35.

VOGT, J., M. STEPANYAN, P. ERHARD, D. GÜNTHER, S. SCHMALZL, and S. GLÄSER. Slurry-based additive manufacturing of casting cores. *InCeight Casting C8,* pp. 123-130.

VOIGT, R.C. and G.P. MANOGHARAN (2018). 3D Printed Sand Molds-An Opportunity for Investment Casters.

WAGNER, W., H.-J. KRETZSCHMAR, R. SPAN, and R. KRAUSS (2010). D2 Properties of Selected Important Pure Substances. *VDI Heat Atlas.* Berlin, Heidelberg: Springer, pp. 153-300.

WANG, J., S.R. SAMA, and G. MANOGHARAN (2019a). Re-Thinking Design Methodology for Castings: 3D Sand-Printing and Topology Optimization. In: *International Journal of Metalcasting* **13**(1), 2-17.

WANG, J., S.R. SAMA, P.C. LYNCH, and G. MANOGHARAN (2019b). Design and Topology Optimization of 3D-Printed Wax Patterns for Rapid Investment Casting. In: *Procedia Manufacturing* **34**, 683-694.

WASHBURN, E.W. (1921). The Dynamics of Capillary Flow. In: *Physical Review* **17**(3), 273-283.

WESTERMAIER, S. and W. KOWALCZYK (2020). Implementation of Non-Newtonian Fluid Properties for Compressible Multiphase Flows in OpenFOAM. In: *Open Journal of Fluid Dynamics* **10**(02), 135-150.

WITH, G. and H.H.M. WAGEMANS (1989). Ball-on-Ring Test Revisited. In: *Journal of the American Ceramic Society* **72**(8), 1538-1541.

WOHLERS, T. (2022). *Wohlers Report 2022 - History of Additive Manufacturing*. Accessed: 28 August 2022. Available from: wohlersassociates.com/history2022.pdf.

WOHLERS, T., N. MOSTOW, I. CAMPBELL, O. DIEGEL, J. KOWEN, and I. FIDAN (2022). *Wohlers Report 2022 - 3D Printing and Additive Manufacturing: Global State of the Industry,* Washington, DC: Wohlers Associates.

YANEZ-SANCHEZ, S.I., M.D. LENNOX, D. THERRIAULT, B.D. FAVIS, and J.R. TAVARES (2021). Model Approach for Binder Selection in Binder Jetting. In: *Industrial & Engineering Chemistry Research* **60**(42), 15162-15173.

YEN, H.C. (2015). Experimental studying on development of slurry-layer casting system for additive manufacturing of ceramics. In: *The International Journal of Advanced Manufacturing Technology* **77**(5-8), 915-925.

YUASA, K., M. TAGAMI, M. YONEHARA, T.-T. IKESHOJI, K. TAKESHITA, H. AOKI, and H. KYOGOKU (2021). Influences of powder characteristics and recoating conditions on surface morphology of powder bed in metal additive manufacturing. In: *The International Journal of Advanced Manufacturing Technology* **115**(11-12), 3919-3932.

ZARETSKIY, L. (2016). Modified Silicate Binders New Developments and Applications. In: *International Journal of Metalcasting* **10**(1), 88-99.

ZHANG, C. and S. YANG (2019). Probabilistic Prediction of Strength and Fracture Toughness Scatters for Ceramics Using Normal Distribution. In: *Materials (Basel, Switzerland)* **12**(5).

ZHANG, J., J. TUOHEY, N. AMINI, D.A. MORTON, and K.P. HAPGOOD (2021). Liquid imbibition into 3D printed porous substrates. In: *Chemical Engineering Science* **245**, 116967.

ZHANG, Z. and A. PROSPERETTI (2005). A second-order method for three-dimensional particle simulation. In: *Journal of Computational Physics* **210**(1), 292-324.

ZHENG, J., A. CHEN, W. ZHENG, X. ZHOU, B. BAI, J. WU, W. LING, H. MA, and W. WANG (2020). Effectiveness analysis of resources consumption, environmental impact and production efficiency in traditional manufacturing using new technologies: Case from sand casting. In: *Energy Conversion and Management* **209**, 112671.

ZHU, W.-J., G.-Q. TIAN, Y. LU, K. MIAO, and D.-C. LI (2019). Leaching improvement of ceramic cores for hollow turbine blades based on additive manufacturing. In: *Advances in Manufacturing* **7**(4), 353-363.

ZOCCA, A., P. COLOMBO, C.M. GOMES, and J. GÜNSTER (2015). Additive Manufacturing of Ceramics: Issues, Potentialities, and Opportunities. In: *Journal of the American Ceramic Society* **98**(7), 1983-2001.

ZOCCA, A., P. LIMA, and J. GÜNSTER (2017). LSD-based 3D printing of alumina ceramics. In: *Journal of ceramic science and technology* **8**(1), 141-147.

ZOCCA, A., P. LIMA, S. DIENER, N. KATSIKIS, and J. GÜNSTER (2019). Additive manufacturing of SiSiC by layerwise slurry deposition and binder jetting (LSD-print). In: *IOP Conference Series: Materials Science and Engineering* **39**(13), 3527-3533.

Dissertationen des Lehrstuhls für Umformtechnik und Gießereiwesen, Prof. Dr.-Ing. Wolfram Volk

01 *Felix Zimmermann*
Generierung von maßgeschneiderten Bauteileigenschaften in PHS-Bauteilen durch Anlassen mittels Flamme;
2014; ISBN: 978-3-95884-007-2

02 *Christopher Joseph Thoma*
Simulationsgestützte Optimierung der Maßhaltigkeit in der Prozesskette Druckguss;
2015; ISBN: 978-3-73699-009-8

03 *Joung Sik Suh*
Verbesserung der Kaltumformbarkeit von AZ31 Mg-Blech durch Equal Channel Angular Pressing (ECAP);
2015; URN: http://nbn-resolving.de/urn/resolver.pl?urn:nbn:de:bvb:91-diss-20151215-1271570-1-8

04 *Robert Ramakrishnan*
3-D-Drucken mit einem anorganischen Formstoffsystem;
2016; URN: http://nbn-resolving.de/urn/resolver.pl?urn:nbn:de:bvb:91-diss-20160129-1276474-1-5

05 *Patrick Saal*
Quantitative Phasenanalyse von ausferritischem Gusseisen mithilfe der Neutronendiffraktometrie;
2017; URN: http://nbn-resolving.de/urn/resolver.pl?urn:nbn:de:bvb:91-diss-20170125-1304161-1-8

06 *Peter Sachnik*
Methodik für gratfreie Schnittflächen beim Scherschneiden;
2017; URN: http://nbn-resolving.de/urn/resolver.pl?urn:nbn:de:bvb:91-diss-20160406-1304184-1-8

07 *Thomas Martin Kopp*
Einfluss der Werkzeugsteifigkeit auf Scherschneidprozess und Werkzeugverschleiß beim offenen Schnitt;
2017; URN: http://nbn-resolving.de/urn/resolver.pl?urn:nbn:de:bvb:91-diss-20170426-1327352-1-7

08 *Simon Josef Maier*
Inline-Qualitätsprüfung im Presswerk durch intelligente Nachfolgewerkzeuge
2018; ISBN: 978-3-95884-004-1

09 *David Jocham*
Bestimmung der lokalen Einschnürung nach linearer und nichtlinearer Umformhistorie sowie Ermittlung dehnungs- und geschwindigkeitsabhängiger Materialkennwerte;
2018; ISBN: 978-3-95884-012-6

10 *Christoph Kaiser*
Effiziente Produkt- und Prozessabsicherung für gefalzte Karosseriebauteile durch ein metamodellbasiertes Assistenzsystem;
2018; ISBN: 978-3-95884-018-8

11 *Daniel Marian Opritescu*
Risikominimale Überbrückung von Kapazitätsengpässen im Presswerksverbund der Automobilindustrie;
2018; ISBN: 978-3-95884-020-1

12 *Maria Anna Hiller*
Fügen durch Clinchen mit rotierender Werkzeugbewegung;
2019; ISBN: 978-3-95884-024-9

13 *Hannes Alois Weiss*
Fertigung effizienter Elektromotoren;
2019; ISBN: 978-3-95884-037-9

14 *Wan-Gi Cha*
Formability Consideration in Bead Optimization to stiffen Deep Drawn Parts;
2019; ISBN: 978-3-95884-036-2

15 *Sven Peter Jansen*
Methodik zur Auslegung konturnaher Temperiersysteme in Druckgusswerkzeugen;
2019; ISBN: 978-3-95884-035-5

16 *Georg Baumgartner*
Das mikromechanische Verhalten von binären Aluminium-Silizium-Legierungen unter Last;
2019; ISBN: 978-3-95884-032-4

17 *Simon Vogt*
Entwicklung eines Verfahrens zur Herstellung von verpressten Spulen für effizientere E-Traktionsantriebe;
2019; URN: http://nbn-resolving.de/urn/resolver.pl?urn:nbn:de:bvb:91-diss-20191001-1483133-1-0

18 *Patrick Thomas Helmut Woisetschläger*
Beitrag zur Optimierung der Schichtanbindung bei thermisch gespritzten Zylinderlaufflächen im Verbrennungsmotor;
2020; ISBN: 978-3-95884-042-3

19 *Michael Walter Krinninger*
Ansätze zur Reduzierung der prozessbedingten Flitterbildung beim Scherschneiden von Aluminiumblechen im offenen Schnitt;
2020; ISBN: 978-3-95884-045-4

20 *Tim Benkert*
Blechradkörper für Leichtbauzahnräder – Eine Machbarkeitsstudie zur Herstellung von tiefgezogenen und feingeschnittenen Innenteilen mehrteiliger Zahnräder;
2020; ISBN: 978-3-95884-046-1

21 *Benjamin Himmel*
Material Jetting of Aluminium – Analysis of a Novel Additive Manufacturing Process;
2020; ISBN: 978-3-95884-049-2

22 *Florian Martin Hofbauer*
Großserientaugliche Umsetzung von dünnwandigem Stahlguss für den Automobilbau;
2020; ISBN: 978-3-95884-050-8

23 *Annika Weinschenk*
Simulative und experimentelle Untersuchungen zur Detektion und Prävention von Einfallstellen in Außenhautbauteilen;
2020; ISBN: 978-3-95884-052-2

24 *Florian Heilmeier*
Ermittlung schwindungsbedingter Gussteilspannungen mit Hilfe eingegossener, faseroptischer Dehnungssensoren;
2020; ISBN: 978-3-95884-053-9

25 *Ferdinand Neumayer*
Ermittlung und Auswirkung der Durchbruchkraft beim Scherschneiden;
2020; URN: http://nbn-resolving.de/urn/resolver.pl?urn:nbn:de:bvb:91-diss-20200729-1530885-1-5

26 *Manuel Pintore*
Gießtechnische Herstellung und technologische Charakterisierung von Kupfer-Aluminium Schichtverbunden;
2021; ISBN: 978-3-95884-059-1

27 *Tim Mittler*
Verbundstranggießen von Kupferwerkstoffen;
2021; ISBN: 978-3-95884-058-4

28 *Christoph Hartmann*
Spatio-Temporal Optical Flow Methods for Process Analysis – Robust Strain, Strain Rate, and Crack Propagation Measurement in Shear Cutting;
2021; ISBN: 978-3-95884-066-9

29 *Marco Raupach*
Simulationsbasierte Konstruktionsmethodik zur Herstellung markanter Bauteilradien im Karosseriebau;
2021; ISBN: 978-3-95884-068-3

30 *Fabian Zgoll*
Methodik zur maschinenoptimalen Werkzeugeinarbeitung durch virtuelle Kompensation der Werkzeug- und Pressendurchbiegung;
2021; ISBN: 978-3-95884-067-6

31 *Phillipp Johnathan Lechner*
A Material Model for Foundry Cores – The Brittle Fracture Behaviour of Chemically-Bound Foundry Sands;
2021; ISBN: 978-3-95884-073-7

32 *Martin Feistle*
Edge-Fracture-Tensile-Test – Neues Kantenrissprüfverfahren für duktile metallische Werkstoffe;
2021; ISBN: 978-3-95884-079-9

33 *Thomas Greß*
Vertical Continuous Compound Casting of Copper Aluminium Semi-Finished Products – Design of a Resource-Efficient Production Technology for the Formation of Metallurgically Bonded Bilayer Parts;
2021; URN: http://nbn-resolving.de/urn/resolver.pl?urn:nbn:de:bvb:91-diss-20210721-1579499-1-7

34 *Jens-Michael Stahl*
Residual stresses induced by shear cutting – Targeted use for manufacturing functional surfaces with an improved fatigue behavior;
2021; URN: http://nbn-resolving.de/urn/resolver.pl?urn:nbn:de:bvb:91-diss-20210802-1593943-1-2

35 *Florian Ettemeyer*
Charakterisierung des Entkernverhaltens anorganisch gebundener Sand-Binder-Systeme;
2021; URN: http://nbn-resolving.de/urn/resolver.pl?urn:nbn:de:bvb:91-diss-20211011-1601398-1-3

36 *Lucas Schulte-Vorwick*
In-Line-Richten von Fahrzeugstrukturteilen aus Leichtmetalldruckguss;
2021; ISBN: 978-3-95884-075-1

37 *Martin Günther Landesberger*
Characterization and Design of Enhanced Ductile Irons;
2022; ISBN: 978-3-9820746-9-6

38 *Nikolas Viktor Beulich*
Entwicklung einer Methodik zur Auslegung und Absicherung des Freiformbiegens mit bewegter Matrize für dreidimensionale Biegegeometrien;
2022; URN: http://nbn-resolving.de/urn/resolver.pl?urn:nbn:de:bvb:91-diss-20221219-1652106-1-5

39 *Philipp Maximilian Tröber*
Adhäsionsentstehung beim Scherschneiden und Tiefziehen unter Berücksichtigung von Temperatur und thermoelektrischen Strömen;
2023; URN: http://nbn-resolving.de/urn/resolver.pl?urn:nbn:de:bvb:91-diss-20230130-1688200-1-4

40 *Matthias Eder*
Validierung von Materialmodellen – Der MUC-Test als Methodik zur Qualifizierung von Materialmodellen für Blechwerkstoffe;
2023; ISBN: 978-3-9820746-8-9

41 *Simon Josef Vitzthum*
In-situ Analysis of Elastic-Plastic Characteristics of Steel Sheets;
2023; ISBN: 978-3-9820746-7-2

42 *Patricia Erhard*
Slurry-based 3D printing of ceramic casting cores;
2023; ISBN 978-3-9820746-6-5